Surface Acoustic Wave Devices using Coupled Resonance with Nano- and Microstructures for Biosensing Applications

A thesis submitted
for the award of the degree of

DOCTOR OF PHILOSOPHY

by

SHYAM TRIVEDI

CENTER FOR NANOTECHNOLOGY
INDIAN INSTITUTE OF TECHNOLOGY GUWAHATI
GUWAHATI -781039, ASSAM, INDIA
NOVEMBER 2018

'The journey of a thousand miles begins with one step.'

Lao Tzu

Dedicated to my
Parents Shail Trivedi, Krishna Chandra Trivedi,
Brother Manish
&
Beloved **'Dadu'**

Certificate

This is to certify that the thesis entitled **"Surface Acoustic Wave Devices using Coupled Resonance with Nano- and Microstructures for Biosensing Applications"** submitted by Shyam Trivedi (126153005), a research scholar in the Center for Nanotechnology, Indian Institute of Technology Guwahati, for the award of the degree of Doctor of Philosophy, is a record of an original research work carried out by him under my supervision and guidance. The thesis has fulfilled all requirements as per the regulations of the institute and in our opinion has reached the standard needed for submission. The results embodied in this thesis have not been submitted to any other University or Institute for the award of any degree or diploma.

Dated:

Guwahati

Prof. Harshal B. Nemade
Department of Electronics and Electrical Engineering,
Indian Institute of Technology Guwahati,
Guwahati - 781039, Assam, India

Declaration

This is to declare that the thesis entitled **"Surface Acoustic Wave Devices using Coupled Resonance with Nano- and Microstructures for Biosensing Applications"** submitted by me to the Indian Institute of Technology Guwahati for the award of the degree of Doctor of Philosophy is a bonafide record of research work carried out by me under the supervision of Prof. Harshal B. Nemade. Hereby I declare that the contents of this thesis, in full or in parts, have not been submitted to any other University or Institute for the award of any degree or diploma.

Dated:

Guwahati

Shyam Trivedi

Abstract

Surface acoustic wave (SAW) is an elastic wave that propagates on the surface of a material with its energy mainly confined to a depth of about one wavelength at the surface. Usually, SAW devices are realized on polished piezoelectric substrates with metallic interdigital transducer (IDT) made on the surface for the transduction of electrical energy to acoustic energy and vice versa. SAW is generated in the substrate by applying an alternating voltage to the IDT. The operating frequency of the SAW device depends on the dimensions of the IDT structure and acoustic velocity in the substrate. SAW devices are microelectromechanical systems (MEMS) that are used in the design of compact and inexpensive RF filters, correlators, analog signal processing units, and electronic communication systems.

In the last few years, the demand for low cost, compact and sensitive biosensors for the detection of disease-causing pathogens has increased. SAW biosensor is an analytical device that comprises IDT on a piezoelectric substrate as transducer and a chemically functionalized active area that selectivity detects a specific biological analyte. SAW biosensors are helpful because they offer real-time, label-free detection with high sensitivity and selectivity. They are a promising low-cost alternative to the conventional fluoroimmunoassay, radioimmunoassay and surface plasmon based optical biosensing techniques. Acoustic wave devices such as quartz crystal microbalance (QCM) and acoustic plate mode (APM) have been used for biosensing purposes, but they are limited by the low frequency of operation and low mass sensitivity. Rayleigh wave SAW devices used for gas sensing applications are not employed for biosensing because the wave gets attenuated in the presence of liquid medium usually present in biosensors. Of all the SAW-based biosensing systems, Love wave (LW) devices are the most promising choice for biosensor design. Guiding layer of the LW devices keeps the energy of the wave at the surface providing high mass sensitivity and also shields the IDT from liquids. Finite element (FE) simulation of LW device considering different guiding layer materials to calculate mass sensitivity, insertion loss and the coupling coefficient of the device are presented in the thesis.

The thesis mainly focuses on the investigation of coupled resonance effect in LW and shear-horizontal (SH) SAW device with micro or nanostructures made on the top surface of the device for high mass sensitivity biosensing applications. The first major contribution of the thesis is analysis of coupled resonance in an LW device with ZnO nanorods and an SH-SAW device with SiO_2 micro-ridges designed on the surface via 3D FE simulation for both resonator and delay line geometries. At a particular size of the nanorods, both the substrate and nanorods vibrate in unison causing a sharp swing in the resonance frequency of the device, leading to a

transition between inertial and elastic loading regimes. Simulation results show that at coupled resonance the device offers high mass sensitivity because of increase in the stiffness of the contact between nanorods and the device surface. However, coupled resonance leads to a decrease in the electromechanical coupling coefficient of the device and an increase in the insertion loss of the device.

The second major contribution in this research work is the fabrication of LW resonator and delay line devices by a standard UV-photolithography. The devices are characterized by connecting them to a network analyzer via an appropriate matching circuit. ZnO nanorods were grown on the surface of the devices by low temperature hydrothermal solution method and an attempt was made to control the height and orientation of the nanorods by using the direct growth, polyethylenimine (PEI) assisted growth, and template growth aided by e-beam lithography. As the nanorods tend to merge, it is difficult to control the orientation and uniformity of rods on the device surface required to achieve coupled resonance.

The third major contribution of the thesis is FE simulation of SH-SAW resonator with S1813 micro-ridges followed by fabrication of the devices, verification of coupled resonance, and biosensing experiment. Polymer ridges of fixed width and various heights are designed along the wave propagation direction on the surface of the resonator. The coupled resonance effect showing a sharp decrease and an increase in the resonance frequency of the device is attained at a critical ridge height and the same configuration is used for specific detection of biotin. The S1813 ridges are silanized by aminopropyltriethoxysilane (APTES) and the subsequent protein attachment is confirmed by confocal microscopy. Different concentrations of biotin solution are applied on the sensing and reference devices immobilized with avidin and bovine serum albumin (BSA), respectively. The device gives high mass sensitivity, three times greater than the mass sensitivity offered by a conventional layered SH-SAW device.

Acknowledgment

I express my deepest and most sincere gratitude to my thesis supervisor Professor Harshal B. Nemade for his excellent guidance throughout my study. His kindness, dedication, hard work, and attention to detail have been a great inspiration to me. I thank him for the unlimited support, invaluable guidance and utmost patience he has shown to me.

I am thankful to my doctoral committee members Professor Roy P. Paily, Professor Parameswar Krishnan Iyer and Professor Arun Chattopadhyay for their precious suggestions and time to improve the quality of my research work. My special thanks to the technical staff of the Centre for Nanotechnology for their support in various tasks. I would also like to thank Ministry of Human Resource and Development (MHRD) for providing scholarship during my Ph.D. work.

I am highly thankful to Indian Nanoelectronics User Program (INUP), and Centre for Nano Science and Engineering (CeNSE), IISc., Bangalore, for providing the fabrication facility to carry out my experimental work. I would like to thank Dr. Sanjiv Srivastav, INUP coordinator for his tremendous help during my stay at IISc, Bangalore. I would like to thank Dr. Prabhakar Rao, Project instructor, sparing his precious time for the execution of my project work. I am very grateful to Professor K. N. Bhat and Professor M. M. Nayak for their help and useful suggestions during the fabrication of devices. Most importantly, I offer my gratitude to the INUP staff of CeNSE, IISc, Bangalore for their sincere efforts and precious time to execute my project.

My special thanks to my seniors Mandar Maitra, Dr. Sai Krishna Santosh, Dr. Basudeba Behera, Jitendra Kumar, Vivek Lukose, and Sushanta Kundu for their help, support, and all the useful technical discussions. I would also like to thank my colleagues and labmates Ashish Singh, Dipjyoti Das, Namami Goswami, Ujjwol Barman, Shatrudhan Palsaniya, Siddhanta Roy, Thomas T. Daniel, Monica Naorem, and Paromita Bhattacharjee for their unconditional care, love, and support.

When one stays at a residential campus like IITG for an extended period of time, one ends up creating a big circle of friends comprising fellow research scholars and campus residents. This is true in my case too. My acknowledgment would be incomplete without mentioning their contributions towards successful completion of my Ph.D. journey. I would like to thank my entire badminton *play-group*, Anand, Basant, Subrat, Pankaj, Mukul, Shatrughan, Ram, Rajendra, Vinod, Uttam, Siddesh, Kishor and Subhasis from various departments of IIT. Playing badminton with you all has been one of the most enriching experiences of my life. We went

on to win *Spardha* tournaments three times consecutively. I will always cherish those winning moments and countless match analysis that ensued those victories. I was fortunate to represent IITG in Badminton in the All India Inter-IIT Sports meet at IIT Kanpur (2016) and IIT Madras (2017). I will also forever remember those cycling trips that we took on weekends which were always rejuvenating and refreshing after tiring and exhaustive weekdays academic activities. I would like to acknowledge Dr. Anamika Barua mam from HSS department of IITG and Swapnali Bora mam for their love and support. I will forever cherish the dinner parties we had at your quarter. I am extremely thankful to Mrs. Leena Nemade for the care and support given to me during my stay at IITG and I always enjoyed special sweets and dishes prepared by her on the occasion of Diwali.

During these six years at IITG, I have had several friends that have helped me in several ways, I would like to say a big thank you to all of them for their friendship and support. Finally, My deepest gratitude goes to my parents and brother for their unconditional love, support, and encouragement throughout my studies and help me go through the rigors of Ph.D.

Contents

List of Figures

List of Tables

List of Abbreviations

AFM	Atomic Force Microscopy
APM	Acoustic Plate Mode
APTES	Aminopropyltriethoxysilane
BAW	Bulk Acoustic Wave
BGS	Bleustein–Gulyaev-Shimizu
BHF	Buffered Hydrofluoric Acid
BSA	Bovine Serum Albumin
CEA	Carcinoembryonic Antigen
CENSE	Center For Nanoscience & Engineering
CMOS	Complementary Metal Oxide Semiconductor
COM	Coupling-of-mode
CVD	Chemical Vapour Deposition
DI	Deionized
DOF	Degrees Of Freedom
EBL	E-beam Lithography
ELISA	Enzyme-linked Immunosorbent Assay
EM	Electromagnetic
FBAR	Film Bulk Acoustic Resonator
FEM	Finite Element Method
FESEM	Field Emission Scanning Electron Microscope
FFT	Fast Fourier Transform
FIA	Fluoroimmunoassay
FPW	Flexural Plate Wave
GSG	Ground-source-ground
HIV	Human Immunodeficiency Virus
HMDS	Hexamethyldisilazane
HMTA	Hexamethylenetetramine
IDT	Interdigital Transducer
IF	Intermediate-frequency
IL	Insertion Loss
IL-6	Interleukin-6
INUP	Indian Nanoelectronics User Program
IPA	Isopropyl Alcohol

IUPAC	International Union Of Pure And Applied Chemistry
LB	Langmuir–blodgett
LG-APM	Layer Guided Acoustic Plate Mode
LIL	Laser Interference Lithography
LOD	Limit Of Detection
LW	Love Wave
MEMS	Microelectromechanical Systems
MIBK	Methyl Isobutyl Ketone
MOCVD	Metal-organic Chemical Vapour Deposition
NIL	Nanoimprint Lithography
PECVD	Plasma Enhanced Chemical Vapour Deposition
PEI	Polyethylenimine
PMMA	Polymethylmethacrylate
QCM	Quartz Crystal Microbalance
RF	Radio-frequency
RIA	Radioimmunoassay
S-FBAR	Shear Mode Thin Film Bulk Acoustic Resonator
SAM	Self Assembled Monolayer
SAW	Surface Acoustic Wave
SGAW	Surface Generated Acoustic Wave
SH	Shear-horizontal
SNRD	Surface Nanorod Density
SNV	Sin Nombre Virus
SPR	Surface Plasmon Resonance
SSBW	Surface Skimming Bulk Wave
STW	Surface Transverse Wave
TCF	Temperature Coefficient Of Frequency
TSM	Thickness Shear Mode
TTI	Triple Transit Interference
VNA	Vector Network Analyzer
XRD	X-ray Diffraction

List of Symbols

A_{dm}	Mass proportional damping coefficient
$B_a(f)$	Susceptance of the IDT
B_{dk}	Stiffness proportional damping coefficient
C_0	Capacitance of one periodic section of the IDT per unit length
C_T	Total capacitance of the IDT
C_s	Capacitance of one periodic section of the IDT
D	Delay line path length
E_j	Electric field vector
F_T	Total force at the sensor surface
F_x	Net force at the sensor surface in the x direction
F_y	Net force at the sensor surface in the y direction
F_z	Net force at the sensor surface in the z direction
$G_a(f)$	Radiation counctance of the IDT
$G_a(f_0)$	Radiation counctance of the IDT at center frequency
IL_{min}	Minimum insertion loss
K^2	Electromechanical coupling coefficient
K^2_{max}	Maximum value of coupling coefficient
L	Center to center distance between input and output IDT
L_c	Cavity length of the resonaor
L_g	Total length of the reflector grating
L_p	Penetration depth of SAW in reflector grating
L_t	IDT transducer length
N	Number of fingers in the IDT.
N_g	Number of fingers in the reflector grating
N_p	Number of finger pairs in the IDT
S_{11}	Input port reflection coefficient

S_{21}	Forward voltage gain
S_ϕ	Phase mass sensitivity
$S_{f_{max}}$	Maximum value of mass sensitivity
S_f	Frequency mass sensitivity
S_{kl}	Strain tesnor component
T	Temperature
T_0	Room or reference temperature
T_d	Time delay of the surface wave propagating from input IDT to output IDT in a delay line device
V_{in}	Voltage applied at the input port
V_{out}	Voltage obtained at the output port
W	IDT aperture
Y_f	Admittance of device
Z_0	Characterisitc impedance
Z_L	Load impedance
Z_{aL}	Acoustic load impedance
Z_c	Acoustic impedance of the substrate
$\Delta\Gamma$	Shift in half-band-half-width of resonance
$\Delta\phi$	Phase shift in the output waveform due to mass loading
Δf	Frequency shift due to mass loading
Δf^*	Complex frequency shift
Δm	Incremental mass loading per unit area on the device surface
Δt	Time delay in the output waveform due to mass loading
Γ	Total reflection coefficient
Γ_{back}	Back surface of the SAW device geometry
Γ_{bottom}	Bottom surface of the SAW device geometry
Γ_{front}	Front surface of the SAW device geometry
Γ_{left}	Left surface of the SAW device geometry
Γ_{right}	Right surface of the SAW device geometry
α	Transduction coefficient
α_1	First order tempearture coefficient
β	Propagation constant
β_l	Propagation constant of the guiding layer
β_s	Propagation constant of the substrate
δ	Detuning parameter
ϵ	Dielectric constant
ϵ_{ij}^s	Permittivity tensor for constant stress
$\frac{\Delta f}{f_0}$	Relative shift in frequency of SAW

$\frac{\Delta v}{v_0}$	Relative shift in velocity of SAW
κ	Reflectivity due to perturbations
λ	Wavelength of SAW
μ_l	Shear modulus of the guiding layer
μ_s	Shear modulus of the substrate
ω	Angular frequency
$\overline{\sigma}_T$	Area-averaged total stress at the sensor surface
ϕ	First euler angle denoting rotation about z axis
ϕ_r	Phase associated with reflection coefficient of individual metal finger
ψ	Third euler angle denoting rotation about $z^{'}$ axis
ρ	Material density
$\rho_e(x)$	Electrostatic charge density on metal fingers when unit voltage is applied
ρ_l	Density of the guiding layer
ρ_s	Density of the substrate
σ	Standard deviation in the frequency measured over a given period of time in stable conditions
τ_g	Delay of the wave reflected by reflector grating
θ	Second euler angle denoting rotation about $x^{'}$ axis
θ_R	Rayleigh angle
ζ_r	Damping ratio
a	Width of each finger of the IDT
a_{max}	Size of the maximum element used to mesh the simulation geometry
c^E_{ijkl}	Stiffness tensor for constant electric field
d_c	Separation between two reflector gratings in a resonant cavity
e_{ijk}	Piezoelectric tensor relating elastic to electric fields
f	Frequency of SAW
f_0	Unperterbed frequency of SAW
f_{ar}	Anti-resonance frequency of SAW device
f_r	Resonance frequency of SAW device
h	Thickness of the guiding layer
h_{ZnO}	ZnO nanord height

h_t	Height of SiO_2 ridge
p	Pitch of the IDT
r_s	Reflection coefficient of a single finger of the IDT or grating
u_x	Displacement component in x direction
u_y	Displacement component in y direction
u_z	Displacement component in z direction
v_f	Velocity of SAW for a free surface
v_g	Group velocity of the Love wave
v_{liq}	Velocity of SAW in liquid
v_l	Shear velocity of the guiding layer
v_m	Velocity of SAW for a metallized surface
v_p	Phase velocity of the Love wave
v_{solid}	Velocity of SAW in solid
v_s	Shear velocity of the substrate
w	Width of SiO_2 ridge

Chapter 1

Introduction

Every new beginning comes from some other beginning's end.

Lucius Annaeus Seneca

In the fields of healthcare, disease control, environmental monitoring and biotechnology there has been an increasing demand for high-quality sensors and components. A tremendous growth is seen in the microelectromechanical systems (MEMS) industry producing compact micro-fabricated devices with high sensitivity, rapid response, reliability along with size and cost reductions. Biosensor design is one of the fastest growing multidisciplinary research area. In the last decade, the demand for sensors that detect the presence of specific biomolecules at low concentration levels, for the early detection of diseases has increased [1]. Potentially harmful micro-organisms and pathogens such as fungi, bacteria and viruses often cause infectious diseases worldwide causing nearly 40% of the total 50 million annual estimated deaths along with loss of millions of dollars to health and food industry [2]. There is an urgent requirement of novel, inexpensive, reliable and small-sized sensors that provide large sensitivity and selectivity to a minute amount of analyte present in the liquid media.

Surface acoustic wave (SAW) devices are an important part of the MEMS family and have emerged as a key component in radio-frequency (RF) and intermediate-frequency (IF) stages of communication systems such as radio receivers, satellite phones, television and mobile phones. SAW filters particularly are most popular in communication systems. SAW devices are also used as resonators, correlators and delay lines for signal processing and sensing applications in the areas of electronic and telecommunication industry [3]. SAW is an acoustic wave traveling along the surface of a material exhibiting linear elasticity. The concentration of energy of these waves is higher at the surface and decreases exponentially with the depth of the substrate. SAW devices provide geometrical freedom near the surface for physical interaction with the propagating wave permitting use of SAW devices for a broad range of applications. Conventionally, SAW devices are realized on a polished piezoelectric substrate in conjunction with an interdigital transducer (IDT) as the transduction element for excitation of various types of surface waves such as Rayleigh wave, shear-horizontal (SH) wave, Bleustein–Gulyaev-Shimizu (BGS) wave, and Love wave (LW).

Of all the available biosensing techniques such as enzyme-linked immunosorbent assay (ELISA), surface plasmon resonance (SPR), electrochemical biosensing, radioimmunoassay (RIA) and fluoroimmunoassay (FIA), the electromechanical based SAW is one of the most promising bio-sensing platform [4], [5]. A SAW biosensor requires very little pre/post processing of the analyte and offers label-free, quick and real-time analysis of biomolecule interactions with high sensitivity [6]. The velocity of SAW is 10^{-5} times that of electromagnetic waves, and it enables designing small wavelength compact devices operating at high frequencies and low power levels [7]. SAW biosensors are quite cost effective compared to optical sensing techniques as they offer label-free and direct detection of the bio-analyte. SAW devices can be mass produced because the IDT can be lithographically patterned on the substrate and they can also be integrated with microfluidic systems to enable flow control of liquid bio-analyte on the sensor surface. Any perturbation occurring on the active region of the device due to mass loading of the analyte produces a shift in the frequency and velocity of the wave that can be monitored and measured in real-time using electronic equipment such as a network analyzer [8], [9].

1.1 Generation of waves in elastic medium

A solid body gets deformed when subjected to a mechanical, thermal, electrical or magnetic force. If the solid object returns to its original shape after removal of force, it is said to be an elastic body [10]. An elastic or acoustic wave is generated in the solid material whenever there is a strain producing changes in the relative position of the particles. In the presence of strains, internal forces are created in the material as particles tend to return to their equilibrium state or unstrained state. The propagation of acoustic wave involves stresses and strains. For example, a localized displacement, such as a hammer blow on a material will cause strains which in turn induce stresses, the stresses generate further strains at distant points, and the disturbance propagates away from the excitation source in the form of acoustic waves [11].

From the perspective of the concentration of energy, elastic waves can be classified into bulk waves and surface waves [12]. Bulk waves propagate into the medium and are classified as longitudinal and transverse waves. A longitudinal wave is a type of wave that involves compressions and rarefactions with particle displacements along the direction of wave propagation as shown in Fig. 1.1a. The other type of bulk wave is the transverse wave or shear wave, in which the particle displacements are perpendicular to the direction of wave propagation as shown in Fig. 1.1b. Surface waves are elastic waves propagating along the surface of a semi-infinite solid (bounded medium). There are two main types of surface waves, viz. Rayleigh waves and Love waves. Rayleigh waves were first identified by Lord Rayleigh in 1885. The wave amplitude decays exponentially with depth and becomes negligible after a depth of one wavelength. The particles near the surface possess an elliptical motion along the sagittal plane with anti-clockwise movement as shown in Fig. 1.1c [11]. However, the motion of particles turn clockwise with increasing depth. In the case of Love waves, the particle displacements are in the plane of the surface and transverse to the direction of wave propagation, as shown in Fig. 1.1d. In general, Love waves are generated when a guiding layer with lower acoustic velocity than the substrate is present on

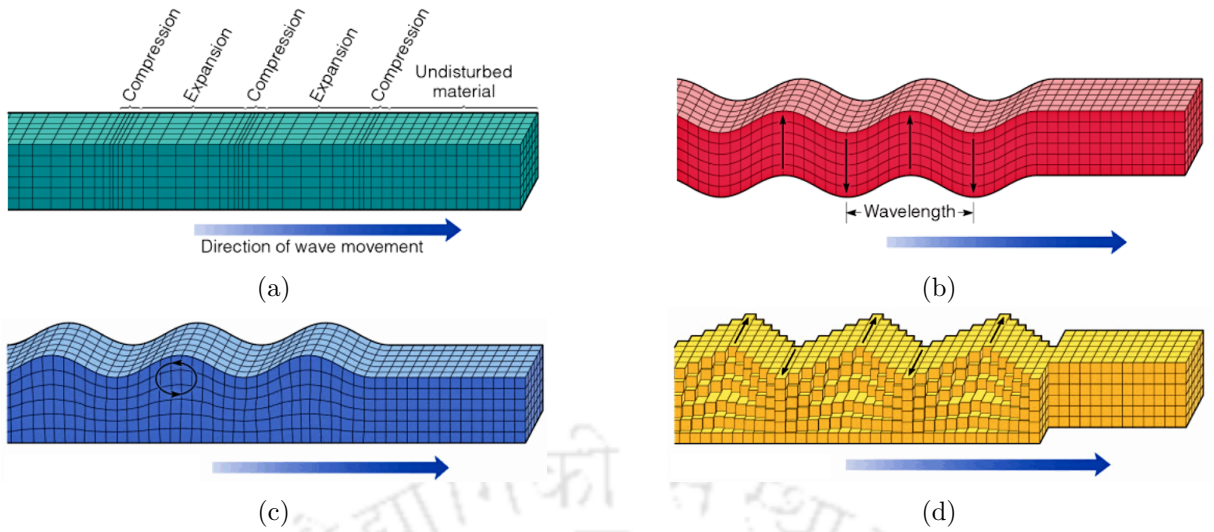

Figure 1.1: Schematic of elastic wave propagation in perturbed medium : (a) longitudinal or compressional wave, (b) shear or transverse wave, (c) Rayleigh wave, and (d) Love wave (adapted from [14]).

the substrate surface causing confinement of a major fraction of wave energy in the overlayer [13].

1.2 SAW device

SAW is a mechanical vibration generated at the free surface of an elastic solid. One of the most efficient ways to excite this type of wave was devised by White and Voltmer in 1965 [15]. Thin comb-like metallic stripes known as interdigital transducer (IDT) was fabricated by a lithographic process on the surface of the piezoelectric substrate such as quartz and was excited by applying an alternating voltage. The invention of IDT ultimately led to the design of analog electrical filters and sensors that operate in the frequency range of 10 MHz to 1 GHz or above. The shape of a typical IDT is shown in Fig. 1.2a. It consists of alternating metal fingers of width a, pitch p, and aperture W. The ratio a/p is called as the metallization ratio, generally kept at a value of 0.5. The IDT consists of large number of repeating vertical metallic bars (fingers) and a pair of horizontal metallic bars. The odd numbered vertical bars are connected to one horizontal bar and the even numbered vertical bars are connected to the other horizontal bar.

When an alternating voltage of period T is applied to the IDT, an electric field is produced between the fingers generating regions of compression and expansion near the surface on account of inverse piezoelectric effect. At time instant t, for a given polarity of the voltage, a stress wave is generated that travels a distance of $\lambda/2$ in period $T/2$ at a certain velocity v, depending on the type of piezoelectric substrate used. At time $t + T/2$, the elastic disturbance reaches the neighboring finger, just when the polarity of the voltage at the IDT fingers change as shown in Fig. 1.2b, leading to emission of stress wave from the second pair of fingers which adds constructively to the first wave. Vibrations add up constructively only when the IDT pitch p is

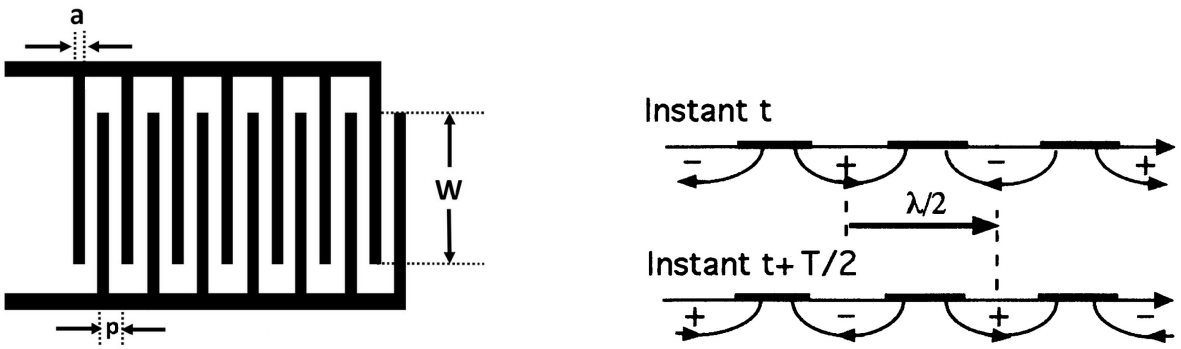

(a) (b)

Figure 1.2: (a) IDT with finger width a, pitch p, and aperture W. (b) Excitation of SAW on piezoelectric substrates using IDT (adapted from [16]).

equal to half the wavelength of the emitted surface wave. The resonance frequency of SAW is given as,

$$f = \frac{v}{2p} = \frac{v}{\lambda} \tag{1.1}$$

where v is the phase velocity of SAW and λ is the acoustic wavelength.

1.2.1 SAW device configurations

SAW devices are usually fabricated on a polished single crystal piezoelectric substrate such as lithium niobate, lithium tantalate, quartz, and langasite. SAW devices are also realized on various non-piezoelectric materials such as silicon, diamond, sapphire, and silicon dioxide using piezoelectric thin films like ZnO and AlN in conjunction with the IDT. In general, SAW devices are operated in two configurations: resonator and delay line as shown in Fig. 1.3. The metallic IDTs employed in SAW devices are fabricated on a piezoelectric substrate using well-established lithography techniques used in semiconductor industry.

In a SAW resonator, the wave propagates within a resonant cavity such that the wave is reflected back to the generating IDT by the reflector gratings. The resonator devices are mainly of two types: one port resonator and two port resonator. A one port SAW resonator can be made by using a large number of IDT fingers without reflectors as shown in Fig. 1.3a. In this device, multiple reflections within the IDT lead to the formation of standing waves and the device resonates at a particular frequency. One port resonators usually contain a pair of reflector gratings that are fabricated on either side of the bi-directional IDT (Fig. 1.3b). The reflector gratings act as mirrors to confine the generated surface wave between them by forming a standing wave pattern. The reflectors are made in the shape of shorted metal strips or grooves. Surface waves are completely reflected from the gratings when $N_g|r_s| \approx 1$, where N_g is the number of fingers in reflector grating and r_s is the reflection coefficient of each finger. In a grating, each finger reflects weakly (r_s is in the range of 1–3%), but if a sufficient number of fingers are used then the total reflection coefficient Γ reaches the unity value [11]. Considering practical aspect of the device, the length of the grating structure must be greater than the penetration depth L_p which is the distance that the surface wave propagates into the grating

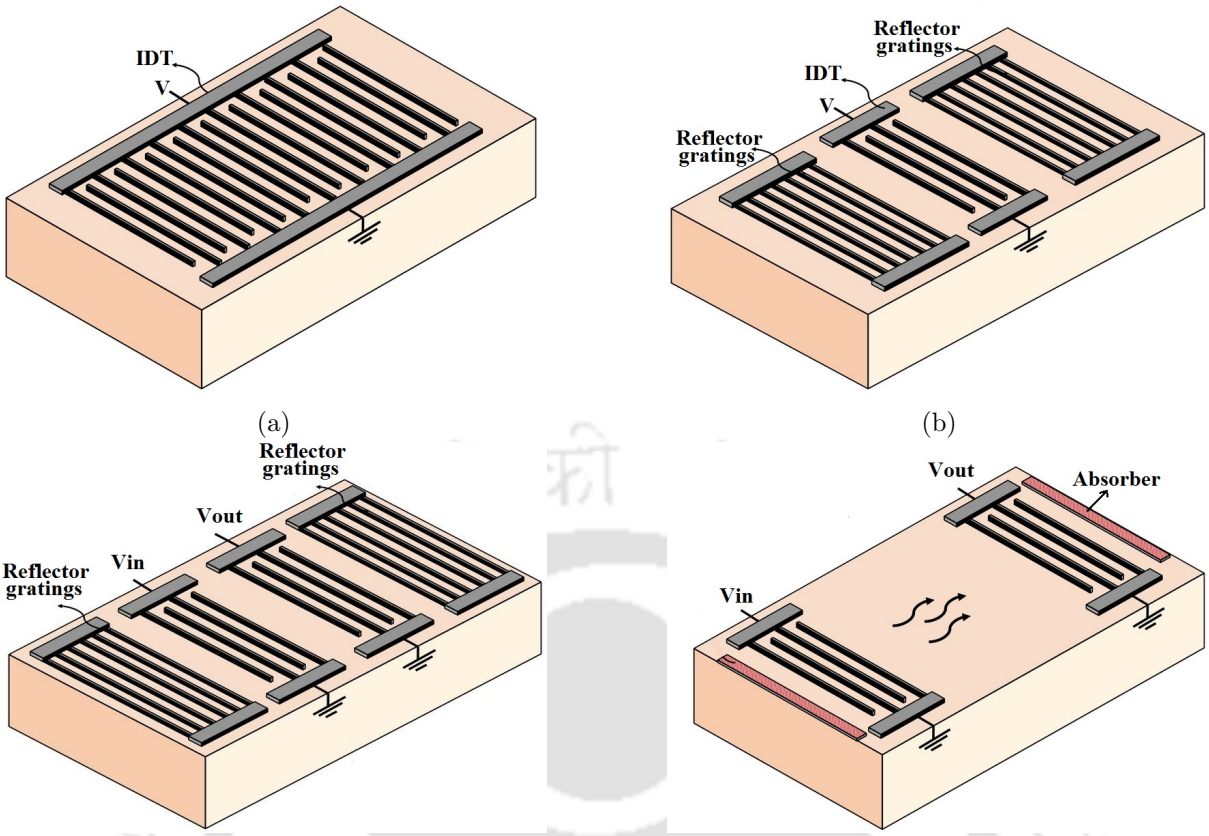

Figure 1.3: SAW device configurations : (a) one-port SAW resonator with large number of IDT fingers, (b) one-port resonator with reflector gratings, (c) two-port SAW resonator, and (d) SAW delay line device with absorbers.

structure. A two-port SAW resonator consists of a set of IDTs arranged in between two reflectors gratings as shown in the Fig. 1.3c. Two port resonators are used as a controlling element for designing high stability oscillators [17]. Resonators offer the advantages of high Q values and low insertion losses making them suitable for designing oscillator circuits [9]. Fig. 1.3d shows a SAW delay line device with a certain distance between the input and output IDTs deciding the delay time. Since SAWs travel 10^{-5} times slower than electromagnetic waves, longer delays are attainable within a compact device size [7]. The bi-directional IDT emits surface wave on either side, and an absorber material is put at the ends of the device so that there are no reflections from the edges. The waves are generated on either side of the IDT, and subsequently, only half of the power reaches the output IDT. At the output IDT, only half of the received power is reconverted into electrical energy since the other half is again used up in the generation of SAW that is sent back towards the input IDT due to the piezoelectric effect. It causes a 6 dB loss and together with the other second order effects, such as triple transit interference (TTI) (loss due to multiple SAW reflections between bidirectional input and output IDTs) and load mismatch the losses typically increase to about 15–20 dB [18]. The delay line is mainly used to implement band pass filters, designing oscillators and sensors [11].

1.2.2 SAW device parameters

SAW devices find use in the design of electrical filters and sensors. The relevant parameters employed for characterization of SAW devices are listed below:

- **SAW frequency** (f) : The frequency of the generated SAW ($f = v/2p = v/\lambda$) depends on the geometry of the IDT structure (pitch p and finger width a of the IDT fingers) and the type/orientation of the piezoelectric material used as a substrate.

- **Electromechanical coupling coefficient** (K^2) : It is a measure of the efficiency of a given piezoelectric material in converting an applied electrical signal into mechanical energy associated with a surface acoustic wave. A high K^2 value can help in designing low insertion loss (IL) devices. The wave velocities for metallized and free surface are denoted by v_m and v_f, respectively. The metallized surface velocity is obtained when the surface has an ideal metal coating that does not cause any mechanical loading but shorts the parallel component of the electric field of the wave [11]. The K^2 values are usually expressed as percentages and is obtained by the formula-

$$K^2(\%) = 2\left(\frac{v_f - v_m}{v_f}\right) \times 100 \tag{1.2}$$

  Piezoelectric crystals such as lithium niobate, lithium tantalate and, langasite offer higher K^2 values in comparison to quartz.

- **Input port reflection coefficient** (S_{11}) : The S_{11} is a measure of the amount of power that gets reflected back when the signal source is connected to the input port and a matched load ($Z_L = Z_0$) is connected to the output port. It is calculated from the total reflection coefficient Γ once the characteristic impedance Z_0 and load impedance Z_L of the system is known.

$$\Gamma = \frac{Z_L - Z_0}{Z_L + Z_0} \tag{1.3}$$

$$S_{11}(\text{dB}) = 20\log|\Gamma| \tag{1.4}$$

- **Insertion loss** (IL) : In a two port SAW device, application of source voltage V_{in} at the input port results in the generation of SAW that travels a certain distance and undergoes propagation loss before getting detected as a signal V_{out} at the output port. This loss is often measured with the help of network analyzer as scattering parameter S_{21}. The insertion loss in dB is expressed as [18]

$$IL(\text{dB}) = 20\log\left|\frac{V_{out}}{V_{in}}\right| \tag{1.5}$$

- **Relative shift in frequency or velocity** ($\Delta f/f_0$, $\Delta v/v_0$) : Change in mass Δm_0, conductivity $\Delta\sigma$, and temperature ΔT etc. near the active area of the SAW sensor causes

a relative change in velocity $\frac{\Delta v}{v_0}$ and frequency $\frac{\Delta f}{f_0}$ which is expressed as [19],

$$\frac{\Delta f}{f_0} = \frac{1}{f_0}\left[\frac{\partial f}{\partial m}\Delta m_0 + \frac{\partial f}{\partial \sigma}\Delta\sigma + \frac{\partial f}{\partial T}\Delta T + ...\right] \tag{1.6}$$

The frequency shift is given as $\Delta f = f - f_0$, where f_0 is the unperturbed frequency.

- **Mass sensitivity** (S_f, S_ϕ) : Mass sensitivity of a SAW device is defined as the relative change in frequency or phase occurring as a result of application of incremental surface mass density (Δm) on the active area of the sensor. The frequency mass sensitivity S_f and the phase mass sensitivity S_ϕ are defined as [20],

$$S_f = \lim_{\Delta m \to 0} \frac{\Delta f / f_0}{\Delta m} \tag{1.7}$$

$$S_\phi = \lim_{\Delta m \to 0} \frac{\Delta \phi / kD}{\Delta m} \tag{1.8}$$

$$S_f = \frac{D}{L} S_\phi \tag{1.9}$$

where $k = 2\pi/\lambda$ is the wavenumber, $\Delta\phi$ is the phase shift, D is the delay line path length and L is the center to center distance between input IDT and output IDT. The units of gravimetric mass sensitivity are $\mathrm{m^2\,kg^{-1}}$ or $\mathrm{cm^2\,g^{-1}}$ [21].

- **Limit of detection (LOD)** : The detection limit is an important characteristic of acoustic biosensors as it determines the minimum amount of surface mass that can be detected. It is obtained from the mass sensitivity of the device once the standard deviation σ in the frequency of the reference channel measured over a given period of time in stable conditions is known. The detection limit is given by [22]

$$LOD = \frac{3\sigma}{S_f} \tag{1.10}$$

- **Temperature coefficient of frequency (TCF)** : Most of the SAW devices such as sensitive filters and sensors are required to meet precise specifications over a wide range of temperatures. For this reason, temperature stability needs to be considered for the design of the device. TCF is given as [23],

$$TCF = \frac{1}{T - T_0}\frac{\Delta f}{f_{r,T_0}} \tag{1.11}$$

where f_{r,T_0} is the resonant frequency at the reference temperature T_0 usually 20 °C and temperature T is varied from -20 °C to 100 °C. The slope of the graph plotted between relative change in frequency $\Delta f/f_{r,T_0}$ and difference in temperature (T-T_0) represents the calculated value of TCF. It is expressed in units of ppm $\mathrm{°C^{-1}}$, and for a device, it should be as low as possible. In general, piezoelectric materials with larger K^2 possess a poor TCF because larger $\mathrm{K^2}$ indicates that mechanical properties are more sensitive to perturbations.

1.3 Biosensors

In healthcare, medical and consumer applications small, reliable, and low-cost sensors are required that can detect the presence of specific biomolecules or disease causing pathogens. According to the International union of pure and applied chemistry (IUPAC), biosensors are defined as a type of chemical sensor that specifically detects a biologically relevant analyte by recording its presence with the help of a transducer [24].

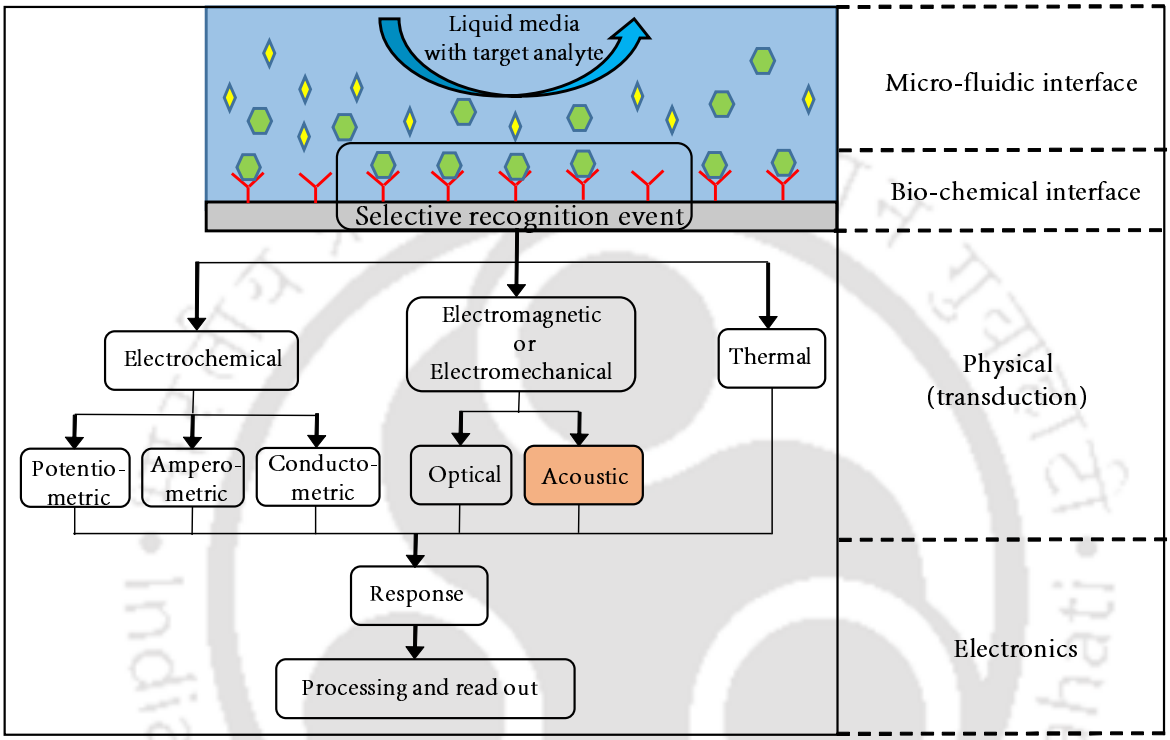

Figure 1.4: Biosensing platform showing recognition of specific bio-analyte at the sensor surface through various physical transduction mechanisms followed by processing and read out by an electronic system (adapted from [25]).

Fig. 1.4 shows a typical biosensing platform. It consists of a microfluidic interface with proper flow control that brings the sample fluid containing the analyte towards the surface. The surface of the sensor is coated with an appropriate film or immobilized protein that can selectively bind the required analyte and ignore the other non-specific proteins that might be present in the sample. Surface chemistry decides how a particular protein can be immobilized on the device surface to detect a specific analyte. There are various techniques for biofunctionalization and immobilization of proteins such as physisorption involving electrostatic and weak van-der-walls forces [26], chemisorption that involves formation of densely packed self assembled monolayer (SAM) through thiol-gold interactions [27], covalent attachments using silanization and cross-linkers [28] or affinity coupling involving the well known streptavidin and biotin linkages on surfaces [29]. Among them, covalent binding is most advantageous as it ensures stable attachments and retains the biological activity of biomolecules after immobilization. The selective recognition of the analyte at the biochemical interface produces a signal based on

electrochemical, electromechanical, optical or thermal change at the sensor surface, and the signal is processed and read out by an electronic setup.

Depending on the transduction mechanism different biosensing techniques exist. Electrochemical sensing mostly employs enzymatic reaction with the chemical species to be detected at the interface of an electronic conductor operating in amperometric or potentiometric mode. Amperometric systems measure the short-circuit current while the potentiometric systems measure the open-circuit voltage [25]. The glucose sensor is one of the commercialized examples of amperometric systems [30]. Optical sensing is the most used technique for designing biosensors. They are mainly based on measuring absorption/scattering of light, interferometry, fluorescence, and SPR. Fluorescence is highly sensitive but needs labeling and complicated read out systems. SPR sensors detect the change in refractive index, causing a shift in reflection angle of the incident wave when the analyte gets bound to the surface. SPR sensors are label-free but are costly and require high-quality light source [31]. Common to most electrochemical techniques is the requirement of a label like in the case of ELISA, which increases cost and complexity of analysis.

1.4 Acoustic biosensors

Acoustic wave sensors mainly use the change in properties of elastic waves (frequency, phase, and velocity) as the transduction mechanism. The gravimetric technique for mass sensing was first used by Sauerbrey in 1959, when he showed the occurrence of frequency shift due to mass loading in a quartz crystal microbalance (QCM) device. This technique opened an entirely new method for mass sensing using the mechanical properties of waves and vibrations [32]. Piezoelectric materials and MEMS based devices are already used in the design of RF filters and oscillators, but now with advancement of technology, they are also used as chemical and biosensors [33]. A few advantages of acoustic wave sensors are listed below-

- Mass loading due to attachment of bio-analyte on the sensor surface causes real time change in frequency or phase of the wave leading to quantitative detection.
- Acoustic wave sensors are cost effective alternative to optical sensing techniques [34], [35].
- They offer label free detection of analyte with high sensitivity and selectivity.
- Widely used SPR based systems use a gold layer for immobilization of analyte and rely on the change in refractive index of the material. Acoustic wave sensors, on the other hand, can be designed on different surfaces and rely on mass change (gravimetric) which is independent of the material's optical properties [36].
- Acoustic wave sensors respond upon real direct binding of the analyte to the receptor while SPR sensors may produce a signal even at the proximity of analyte to receptor [36].
- Acoustic sensors can be integrated with microfluidic channels for easy flow control of the analyte on the sensor surface. The change in frequency or phase of the wave upon mass loading can be easily monitored using electronic systems such as oscillators and network analyzers.

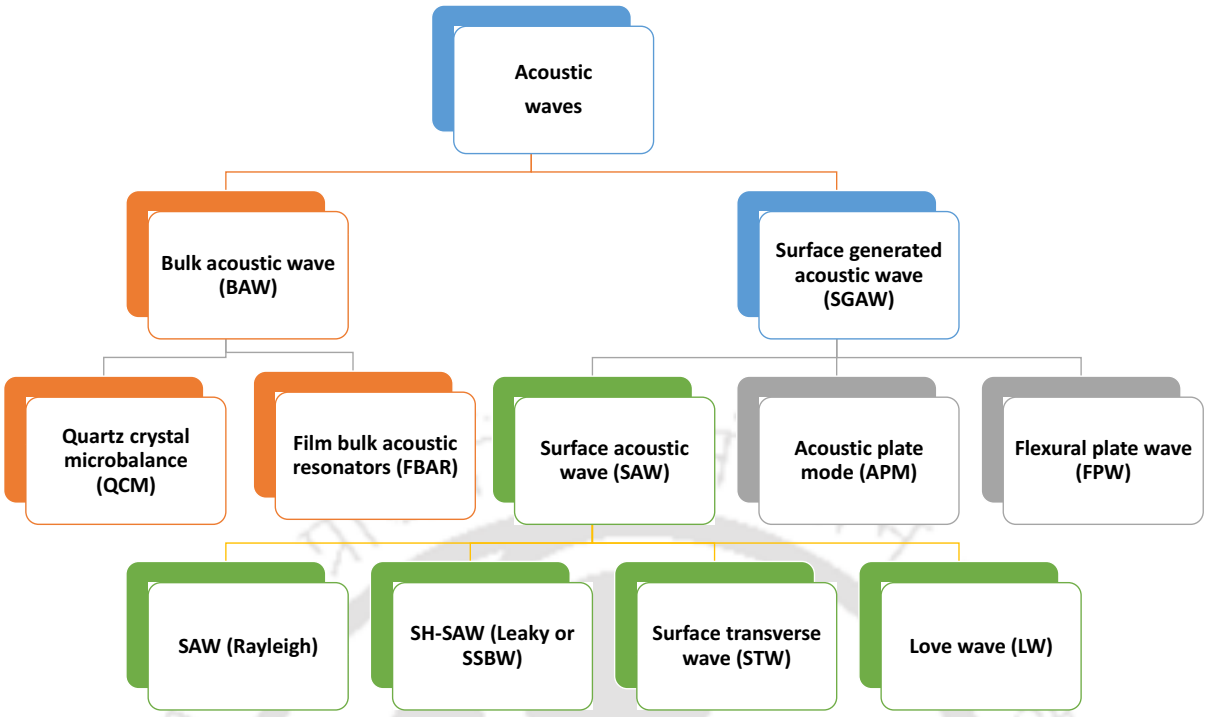

Figure 1.5: Classification of acoustic wave devices.

- Acoustic sensors often use metal electrodes and IDTs that can be batch fabricated using photolithography. Since the speed of the acoustic wave is 10^5 times less than electromagnetic (EM) wave, significant delays are attainable in compact device sizes with less power consumption.

There are different types of acoustic wave devices as shown in Fig. 1.5. They can be broadly divided into two categories depending on the mode of wave propagation. Bulk acoustic wave (BAW) devices where the wave propagates through the entire body of the substrate in an unguided manner. QCM and thin film bulk acoustic resonator (FBAR) are two major types of BAW device. The other category is the surface generated acoustic wave (SGAW) where the wave generation and detection happen at the surface of the substrate using IDTs. The SGAW can be further divided into SAW devices and plate mode devices. In a SAW device, the wave travels mainly at the surface of the substrate in a guided or unguided way. Rayleigh wave, SH-SAW, surface skimming bulk wave (SSBW), surface transverse wave (STW) and LW are major types of SAW. In plate mode devices such as acoustic plate mode (APM) and flexural plate wave (FPW), the wave is generated at the surface but guided by multiple reflections from top and bottom of the substrate.

In general, the acoustic waves can also be classified depending on the particle displacements with respect to the direction of wave propagation. If the particle motion is in the direction of wave propagation, it is termed as a longitudinal wave. If the particle motion is perpendicular to the direction of wave propagation, then it is called as shear or transverse wave. Further shear wave with particle displacements parallel to the substrate surface is called as SH-SAW, while wave having elliptical particle motion in the sagittal plane at the surface is called as Rayleigh

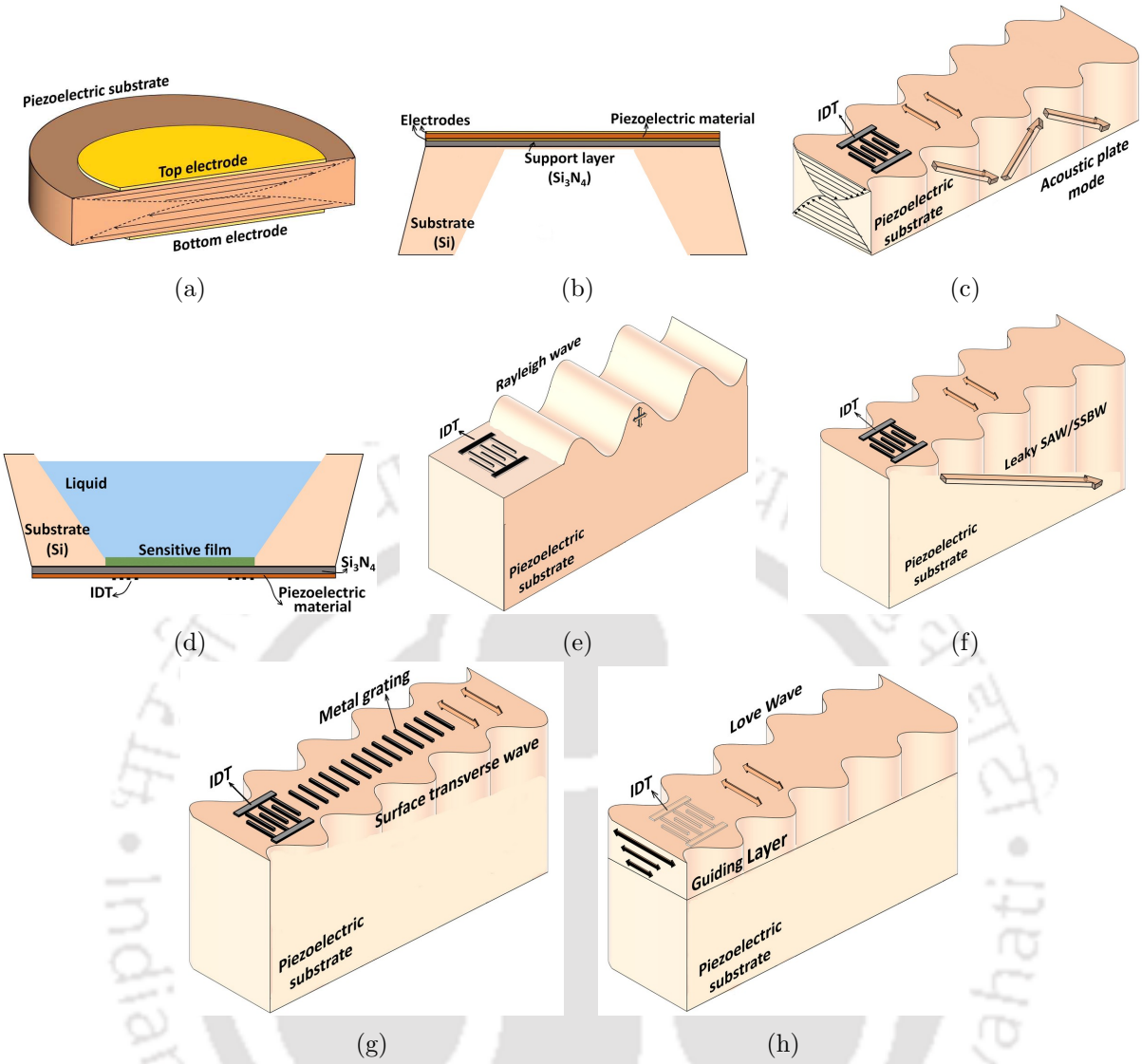

Figure 1.6: Various types of acoustic wave devices : (a) QCM (b) FBAR (c) APM (d) FPW (e) Rayleigh (f) Leaky SAW or SSBW (g) STW, and (h) LW.

wave. SAW devices tend to have higher sensitivity than BAW devices as any perturbation occurring on the surface causes a maximum change in wave velocity of SAW in comparison to BAW which travels through the entire body of the material. The various acoustic wave devices are shown in Fig. 1.6.

1.4.1 Quartz crystal microbalance

QCM device consists of a thin piezoelectric substrate (usually AT-quartz) sandwiched between two electrodes as shown in Fig. 1.6a. Application of voltage to the electrodes results in the generation of SH vibration which travels across the entire thickness of the substrate. It is usually operated in a thickness shear mode (TSM) in which stationary wave gets generated if the thickness of the substrate is integral multiple of half wavelength. It is called as a microbalance because frequency tends to decrease when the surface of the substrate gets loaded by mass and

is mainly employed to monitor thin films in microelectronics [32]. The mass sensitivity of QCM is proportional to the square of the resonant frequency given as,

$$S_f = -\frac{2}{\sqrt{\rho_q v_q}} {f_0}^2 \tag{1.12}$$

where ρ_q and v_q are material density and SH velocity of AT-cut quartz. The above relation is correct only when the deposited mass layer is very thin such that its elastic properties do not affect the resonance frequency of the crystal and the frequency variations are only due to mass change effect. The mass sensitivity can be improved by operating the QCM at higher frequencies by making the substrate thinner. However, handling of thin wafers is extremely difficult and limits the maximum frequency of operation.

The QCM technology is well researched and established. QCM devices can be operated in liquid media and have been used for the detection of proteins [37], pesticides [34], bacteria and viruses [38], [39] and even for detection of DNA [40]. Typically they are operated in the frequency range of 1–20 MHz. QCM operating at high frequencies of 30 MHz can provide mass sensitivity and LOD up to $6\,\mathrm{m^2\,kg^{-1}}$ and $10\,\mathrm{ng\,cm^{-2}}$, respectively [41].

1.4.2 Thin film bulk acoustic resonator

FBAR devices consist of a thin film of a piezoelectric material such as AlN or ZnO sandwiched between two metal electrodes fabricated on a silicon substrate as shown in Fig. 1.6b [42]. Depending on the orientation of the piezoelectric thin film, the device may generate either a longitudinally polarized wave or shear wave upon electrical excitation of the metal electrodes. Since the thickness of the piezoelectric film is between 100 nm and a few µm, the acoustic energy is efficiently concentrated in the layer thereby allowing the device to be operated in GHz regime. Hence FBAR devices provide mass sensitivity higher than QCM and SAW devices. The other advantage is that the device fabrication is compatible with complementary metal oxide semiconductor (CMOS) and silicon manufacturing techniques allowing miniaturization of devices.

The high-frequency operation of FBAR device often introduces considerable noise in read out and characterization systems that reduce the LOD even when mass sensitivity is high [43]. Although fabrication of FBAR device is compatible with CMOS processes, the manufacturing is still challenging and increases the research cost. FBAR sensors that generate high-velocity longitudinal vibration radiate a significant part of the wave energy upon liquid loading that leads to a reduction in Q factor of the device [44]. To overcome the losses in the presence of liquids, shear mode thin film bulk acoustic resonator (S-FBAR) have been fabricated that can be operated at near GHz frequencies with high mass sensitivity and LOD. Weber *et al.* [45] reported a S-FBAR device resonating at 790 MHz, consisting of ZnO thin film as the piezoelectric layer, which gave a high mass sensitivity of $75\,\mathrm{m^2\,kg^{-1}}$ and LOD of $2.3\,\mathrm{ng\,cm^{-2}}$ [45].

1.4.3 Acoustic plate mode device

Fig. 1.6c shows an APM device consisting of IDT fabricated on a thin piezoelectric substrate. The device generates a plate wave that undergoes multiple reflections from the top and bottom surfaces of the substrate with SH vibrations. The main advantage of this configuration is that the sensing surface can be on the opposite side of IDTs, that helps to isolate the IDTs from liquids used in biosensing. Similar to QCMs, mass sensitivity of the device can be improved by decreasing the substrate thickness and operating the device at a higher frequency [46]. Typically this device is operated in the frequency range of 20–200 MHz and offers mass sensitivity between 2–5 $m^2\,kg^{-1}$. ST-cut quartz and $LiNbO_3$ are commonly used as a substrate for APM devices. Mechanical and electrical loading tend to reduce the APM response if high K^2 material like $LiNbO_3$ is used as substrate [47]. Designing oscillator with APM devices is difficult because several plate modes get excited with very less frequency separation between them, that results in frequency hopping between one mode to another [48]. Some improvement in sensitivity of tradition SH-APM devices can be obtained if a guiding layer is put on the substrate surface, making it a layer guided acoustic plate mode (LG-APM) device [49].

1.4.4 Flexural plate wave device

FPW device consists of a thin plate having thickness just about a fraction of the acoustic wavelength. Confinement of acoustic energy in such thin membranes leads to high mass sensitivity. Fig. 1.6d shows a FPW device with thin Si_3N_4 plate present between a silicon substrate and piezoelectric layer. When thickness of the plate is less than the penetration depth of the wave, guided modes across both the substrate surfaces interact with each other leading to the production of *Lamb* modes. A Lamb wave can be regarded as two Rayleigh wave propagating on either side of the plate edge with a thickness less than one wavelength. Plate waves propagate in two mode types: anti-symmetric or symmetric with latter having lower propagation velocities [50]. The mass sensitivity of the device is given as [51],

$$S_f = -1/2\rho d \tag{1.13}$$

where ρ is the plate density and d is the plate thickness. FPW devices are typically operated in the frequency range of 2–20 MHz with reported mass sensitivities of about 20–100 $m^2\,kg^{-1}$ [52]. The device offers fairly high mass sensitivity at lower operational frequencies. The main advantage of the device is that the FPW velocity is less than the compressional velocity of sound in liquid leading to very less energy radiation and loss in liquid media. However, having thin plates makes fabrication challenging and increases the fragility of the device [53].

1.4.5 Rayleigh wave device

Lord Rayleigh first proposed the existence of Rayleigh wave in 1885 [54]. These types of wave have elliptical particle motions in a plane perpendicular to the surface and along the wave propagation direction as described in section 1.1. Displacements decay exponentially with the

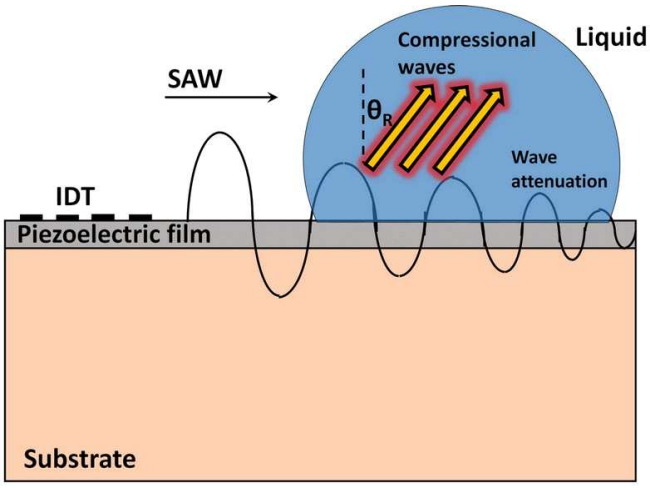

Figure 1.7: Attenuation of Rayleigh waves in liquid.

depth of the substrate, and a major fraction of wave energy is concentrated within a depth of one wavelength from the free surface of the substrate. The first SAW device operating in Rayleigh mode was made by White and Voltmer in 1965 by making IDTs over quartz substrate [15]. Since then, Rayleigh wave devices have been successfully used in telecommunication industry as signal filters and delay lines [11] and also for gas sensing applications [55]. These device operate between 40–400 MHz and give mass sensitivity in the range of 10–20 $m^2\,kg^{-1}$, in gaseous media. Commonly used crystals are quartz, $LiTaO_3$, $LiNbO_3$ and langasite [56]. The attenuation of Rayleigh wave in the liquid is illustrated in Fig. 1.7. The particle displacement in Rayleigh wave has a component perpendicular to the substrate surface. As the wave encounters a liquid region, it launches compressional components, radiating at a particular angle given by,

$$\theta_R = \sin^{-1}\left(\frac{v_{liq}}{v_{solid}}\right) \tag{1.14}$$

where θ_R is the Rayleigh angle that depends on the ratio of wave velocity in liquid v_{liq} and wave velocity in solid substrate v_{solid} [57]. It leads to loss of a major fraction of the wave energy and momentum into the liquid. To avoid the high damping caused by the aqueous environment, the acoustic waves must have particle displacements parallel to the sensor surface, hence SH waves are suitable for biosensing.

1.4.6 Shear horizontal surface acoustic wave device

A shear horizontal surface wave has particle vibrations parallel to the substrate surface and perpendicular to the direction of wave propagation. The advantage of this type of wave motion is that it can be used for biosensing in liquid media. The shear horizontal wave produced by Y-cut crystals of $LiNbO_3$ and $LiTaO_3$ is called as the *leaky wave* [58] while on quartz substrates they are known as SSBW [59], [60]. As shown in Fig. 1.6f, IDT launches a surface wave with SH vibrations, but as it propagates further, it starts to leak its energy into the depth of the substrate. The wave is termed as a leaky wave because it is only partially confined to the surface which tends to reduce the mass sensitivity. In addition, the IDTs need to be protected from

the liquid by covering it with polyimide or polystyrene. A SSBW falls into the category of shallow longitudinal bulk wave with shear horizontal polarization that is mostly generated by Y-cut quartz as well as $LiTaO_3$/$LiNbO_3$ crystals. With distance, the amplitude of the wave decays proportional to x^{-P} ($0.5 \leq P \leq 1.5$). On the other hand, leaky SAW falls into the category of surface wave consisting of SH vibrations. The wave starts at the surface and penetrates into the depth of the substrate at a larger angle than SSBW. With distance, the amplitude of the wave decays proportional to $e^{-\alpha x}$ where α is the decay constant of the wave. It is mainly generated by Y-cut $LiTaO_3$/$LiNbO_3$ crystals. SH-SAW devices are used for both gas and liquid sensing applications. The typical operating frequency is 30–500 MHz with sensitivities between 10–20 $m^2\,kg^{-1}$. ST quartz, 36°-YX $LiTaO_3$, 64°-YX $LiNbO_3$, 41°-YX $LiNbO_3$, $KNbO_3$, and langasite have been used as crystal materials. For a SH-SAW sensor, $LiTaO_3$ or $LiNbO_3$ is more advantageous than quartz as a substrate since it provides high electromechanical coupling coefficient. In addition, compared to quartz ($\epsilon = 4.5$), the dielectric constant of $LiTaO_3$ ($\epsilon = 47$) is closer to the dielectric constant of liquid solution ($\epsilon = 75$) placed above it which helps to confine the electric field to the surface by reducing the dielectric mismatch [47], [61].

1.4.7 Surface transverse wave device

STW device shown in Fig. 1.6g consists of a substrate generating SSBW with metal grating made on the propagation path that slows down and traps the wave energy at the surface. The STW can also be termed as grating-affected SSBW [62]. Gratings can be matched to the transducer to minimize reflections and provide much stronger guiding of the wave [63]. They can be used for sensing applications both in gaseous and liquid media [64], [65]. Since the wave energy stays at the surface, they outperform Rayleigh devices regarding mass sensitivity and propagation loss. They are typically operated between 30–300 MHz and offer mass sensitivity in the range of 10–20 $m^2\,kg^{-1}$. The problem with STW devices is that the IDTs are exposed to liquid media, and they suffer from bulk losses which lead to their limited use in biosensing applications.

1.4.8 Love wave device

LW was first mathematically discovered by Edward Love in 1911 [66]. They are generated during an earthquake when the wave energy passes through the stratified geological layer and cause maximum damage because of the slow decay of the wave. LW devices consist of a substrate that primarily excites a SSBW or leaky SAW, which is subsequently confined by a thin guiding layer located above the substrate and IDTs as shown in Fig. 1.6h. The condition for the existence of LW modes is that the shear velocity of the overlay material should be less than that of the substrate [13]. The difference between mechanical properties of the guiding layer and substrate causes confinement of acoustic wave in the guiding layer by keeping the wave energy near the surface and reducing the wave propagation velocity. Thus, the LW can be defined as *layered-affected SSBWs* [67].

In LW devices there is very less penetration of wave in the substrate, making them very

sensitive to any perturbations occurring on the sensor surface such as added mass, changes in conductivity, viscosity, and temperature. The greater the confinement of wave in the guiding layer, the larger is the sensitivity [9]. The device can be used both in gaseous and liquid media. It is typically operated in the frequency range of 80–300 MHz and reported mass sensitivity is between 20–100 $m^2\,kg^{-1}$ [48], [68]. Mainly rotated Y-cut quartz, 36°-YX $LiTaO_3$, 64°-YX $LiNBO_3$, and 41°-YX $LiNbO_3$ are used as substrates while SiO_2, ZnO and polymers are used as guiding layer materials [9], [68].

1.4.9 Comparison of acoustic wave sensors

Apart from sensitivity, limit of detection and selectivity, the robustness of device, ease of handling and low cost also play a vital role in success, selection, and commercialization of the sensors. Miniaturization of the devices offers the possibility of creating an array of sensors in small space. Each of the acoustic wave devices has its advantages and disadvantages, and a comparison between them can help in making the correct selection for sensor design. Table 1.1 lists all the main features of different acoustic wave sensors. QCM is a well-established technology, but it suffers from poor sensitivity and low frequency of operation. APM devices do not offer any significant improvement in mass sensitivity. Fabrication of FBAR is CMOS compatible, and it has high operational frequency and mass sensitivity, but production of the device is costly and complicated. FPW devices have the advantage that it can provide high sensitivity at low frequencies, but its sensitivity decreases in liquids because of losses.

Among all the SGAW devices, SH-SAW and LW are most promising. LW devices have found considerable interest in biosensor design because they provide high sensitivity as guiding layer keeps the energy of the wave at the surface. They can be operated at high frequencies, allow shielding of IDTs from liquids and are robust. LW devices have particular challenges like fabrication complexity, selection of appropriate guiding layer as per requirement, correct interpretation of frequency shift due to mass or viscoelastic loading, and proper design of flow cell and microfluidic channels over the device. Although, after QCM, they are most likely to get commercialized and can be very competitive to other biosensing techniques.

1.5 LW biosensors - state of the art

SH-SAW and LW devices are most promising candidates to be used as acoustic biosensors. In 1992, the first attempt to design an LW biosensor was made by Kovacs *et al.* [104]. The author discussed fundamental properties of LW delay line such as dispersion relation, phase velocity, group velocity and attempted to calculate mass sensitivity by coating different thicknesses of photoresist. In the same year, Gizeli *et al.* [105] calculated the sensitivity of polymer coated device by coating different thicknesses of langmuir–blodgett (LB) film and tested protein attachment on the surface. Since then LW sensors have evolved and used for detection of proteins and immunoglobulins [69], [72], [73], detection of disease causing bacteria like anthrax [77] and E. coli [78] and also viruses such as Ebola [87], HIV [88], influenza [86] and hepatitis B [80]. LW

Device	Wave motion	f (MHz)	S_f ($m^2\,kg^{-1}$)	Substrate material	Advantages and disadvantages
QCM	bulk SH	1–20	1–5	AT-quartz	• cheap, robust and commercially established • low frequency and low mass sensitivity • thin, fragile device at high frequency
S-FBAR	bulk SH	500–2000	75	Si, ZnO, AlN	• CMOS compatible fabrication • high fabrication complexity and cost
APM	bulk SH plate mode	20–200	2–5	ST-quartz, $LiNbO_3$	• IDTs can be made on the back side • mode hopping • low mass sensitivity
FPW	shear vertical lamb mode	2–20	20–100	Si, Si_3N_4, ZnO, $LiNbO_3$	• high sensitivity at low frequencies • sensitivity decreases in liquid • fabrication complexity
SAW	surface shear vertical	40–400	10–20	$LiNbO_3$, $LiTaO_3$ quartz, langasite	• high operational frequency • attenuation in liquid media
SH-SAW	surface SH	30–500	10–20	$LiNbO_3$, $LiTaO_3$, quartz, langasite, $KNbO_3$	• high operational frequency than QCM • mass sensitivity less than STW and LW
STW	surface SH	30–300	10–20	ST-quartz	• high frequency and sensitivity than QCM • low propagation loss than SH-SAW • bulk losses can occur
LW	surface SH	80–300	20–100	$LiNbO_3$, $LiTaO_3$, quartz	• high frequency and sensitivity • robust, IDT not exposed to liquids • high cost

Table 1.1: Comparison of various acoustic wave sensors.

devices have also been reported for DNA hybridization detection [91]and detection of pesticides and chemicals [98], [99]. Table 1.2 lists various LW devices with reported sensitivity and limit of detection values that have been used for different biological and chemical sensing purposes over the years.

1.6 SAW biosensor measurement techniques

A SAW biosensor consists of two identical delay line or resonator type devices, one acting as a sensing channel and the other as a reference as shown in Fig. 1.8a. The active area of the sensor is coated with a suitable sensitive film that can specifically attach the analyte to be detected while the reference channel is immobilized with a blocking protein. The sensor surface on both the devices is incubated with the liquid sample containing the analyte for a given period and washed. After washing, the analyte will remain attached only on the sensing channel resulting in phase/frequency shift between the two devices.

SAW sensor characterization could be performed by using a closed loop oscillator arrangement or an open loop network analyzer measurement. Fig. 1.8b shows an oscillator configuration where the delay line device is placed in the feedback loop of the RF amplifier which compensates for the insertion loss generated by delay line. The total time delay T_d of the device is given by [106],

$$T_d = \frac{D}{v_p} + \frac{L - D}{v_{idt}} \tag{1.15}$$

where D is the delay line path length, L is the center-to-center distance between the IDTs, v_p, and v_{idt} are the phase velocities of the wave in sensing area and IDT region respectively. The

Year	Device	f (MHz)	Sensitivty(S) or limit of detection (L)	Detection	Ref.
			Immunosensors		
1997	SiO_2/ST-quartz	110	S = 38 $m^2 kg^{-1}$ L = 1 ng ml^{-1}	Sheep IgG	[4]
2003	(ZnO & SiO_2)/ST-quartz	89	S = 40-95 $m^2 kg^{-1}$ L = 500 pg ml^{-1}	Rat IgG	[69]
2003	ZnO/SiO_2/ST-quartz	747 & 1586	S = 4.5 & 8.5 $\mu m^2 pg^{-1}$	interleukin-6 (IL-6)	[70]
2011	PMMA/36°-YX $LiTaO_3$	208	S = 7 kHz ml mg^{-1}	IgG	[71]
2011	Gold/PMMA/41°-YX $LiNbO_3$	440	S = 45 to 168 ° $\mu g^{-1} ml^{-1}$	Rabbit IgG	[72]
2015	Gold/PMMA/ST-quartz	70	S = 0.15 $nmol^{-1}$ L = 0.6 nmol	AFB1-BSA bioconjugate	[73]
2016	SiO_2/ST-quartz	120	L = 10 pg ml^{-1}	Rabbit IgG	[74]
			Bacteria/Virus/Cancer biomarkers		
2000	SiO_2/ST-quartz	124	L = 10^5 cells/ml	Legionella & E. coli	[75]
2002	SiO_2/ST-quartz	88	S = 18 $m^2 kg^{-1}$	M13 bacteriophage	[76]
2004	(Polyimide & Polystyrene)/36°-YX $LiTaO_3$	103	L = 1-2 ng cm^{-2}	bacillus anthracis	[77]
2007	SiO_2/AT-quartz	118	L = 10^6 bacteria/ml	E-coli	[78], [79]
2008	SiO_2/36°-YX $LiTaO_3$	325	-	sin nombre virus (SNV) & Coxsackie virus	[6]
2009	SiO_2/36°-YX $LiTaO_3$	199	S = 0.74 Hz µl pg^{-1} L = 10 pg μl^{-1}	Hepatitis B virus	[80]
2010	CMOS-SAW Gold/ZnO/SiO_2/Si	321	S = 2810 $m^2 kg^{-1}$ L = 8.7 pg Hz^{-1}	breast cancer biomarker hMAM	[81]
2012	SiO_2/ST-quartz	150	S = 515 ° $cm^2 \mu g^{-1}$ L = 5-15 ng cm^{-2}	circulating tumor cells	[82]
2013	SiO_2/ST-quartz	163	S = 32 $m^2 kg^{-1}$ L = 10^8 pfu ml^{-1}	M13 bacteriophage	[83]
2014	Gold/SiO_2/36°-YX $LiTaO_3$	165	S = 0.48 ° ml ng^{-1} L = 1.25 ng ml^{-1}	carcinoembryonic tumor antigen	[84]
2015	Gold/SiO_2/36°-YX $LiTaO_3$	198	L = 10 ng ml^{-1} $m^2 kg^{-1}$ L = 10^8 pfu ml^{-1}	prostate cancer biomarker PSA	[85]
2015	SiO_2/41°-YX $LiNbO_3$	120	L = 1 ng ml^{-1}	Influenza A viral antigen	[86]
2015	SiO_2/36°-YX $LiTaO_3$	325	L = 1.9× 10^4 $pfuml^{-1}$	Ebola antigen	[87]
2017	SiO_2/36°-YX $LiTaO_3$	325	L = 12-87 ng ml^{-1}	human immunodeficiency virus (HIV) type 1 & 2	[88]
			DNA/Nucleic acids		
2004	Gold/SiO_2/ST-quartz	142	S = 419±64 ° $cm^2 \mu g^{-1}$ L = 75 pg cm^{-2}	thrombin aptamers, probe/target DNA strands	[89]
2006	ZnO nanotips on SiO_2/YZ-$LiNbO_3$	328	L = 1.5-2.2 mg cm^{-2}	probe and complementary strands	[90]
2007	Gold/36°-YX $LiTaO_3$	200	L = 135 pg ml^{-1} Hz^{-1}	probe/target DNA strands	[91]
2008	SiO_2/Gold/36°-YX $LiTaO_3$	121	S = 6 Hz cm^2 ng^{-1} L = 1 ng cm^{-2}	DNA-gold nanoparticle conjugate	[92]
2008	Gold/PMMA/ST-Quartz	155	-	DNA structure bending	[93]
2009	Gold/PMMA/ST-Quartz	155	-	conformal arrangement of DNA	[94]
2009	Gold/36°-YX $LiTaO_3$	104	S = 6.3 Hz ng^{-1}	probe/target DNA strands	[95]
2014	Gold/128°-YX $LiNbO_3$	100	L = 1.2 pg ml^{-1} Hz^{-1}	probe/target DNA strands	[96]
			Chemicals/Others		
1996	Gold/Novolac/ST-quartz	110	-	lipid monolayer & bilayer	[97]
1997	Gold/PMMA/ST-quartz	80	S = 31.3 ° $cm^2 \mu g^{-1}$ L = 400 ppb	Atrazine (pesticide)	[98]
2001	(PMMA & CEC)/36°-YX $LiTaO_3$	103	S = 1500 Hz mm^2 ng^{-1} L = 20 pg mm^{-2}pg/l	toluene, trichloroethane etc.	[99]
2009	SiO_2/ST-quartz	125	S = 25 $m^2 kg^{-1}$ L = 60 ng cm^{-2}	avidin functionalized gold nanoparticles	[100]
2010	SiO_2/AT-quartz	118	L = 10^{-12} mol l^{-1}	heavy metal detection using E. coli	[101]
2010	SiO_2/AT-quartz	117	L = 0.02 ppm	okadaic acid (toxin)	[102]
2016	Graphene oxide/SiO_2/ST-quartz	164	S = 760-3087 Hz ppm^{-1} L = 9-40 ppb	chemical warfare agents	[103]

Table 1.2: Literature survey of different LW sensors.

circuit oscillates at a fixed frequency f, and the total phase shift in the circuit loop is an integral multiple of 2π represented as,

$$2\pi f T_d + \phi_{amp} = n(2\pi) \tag{1.16}$$

where ϕ_{amp} is the phase shift introduced by the RF amplifier. Upon mass loading the phase velocity v_p is changed, that leads to variation in time delay T_d and frequency of oscillation. Relative change in phase velocity introduces a relative change in oscillation frequency given as, $\Delta f/f_0 = \Delta v_p/v_{p0}$, where v_{p0} and f_0 are the unperturbed wave velocity and frequency. The frequency shift can be measured with the help of a frequency counter. The oscillator setup is advantageous as it is low cost and allows real time monitoring of frequencies. However, stabilizing the oscillation is challenging as the device needs to be operated between one phase cycle of 2π. If the insertion loss of the device exceeds the gain offered by amplifier, the oscillations cease [107]. Fig. 1.8c shows an *open loop* configuration of SAW device with measurements performed using a network analyzer. The main advantage of network analyzers is that they provide complete characterization of the device with frequency, phase measurements, impedance information, and S-parameters.

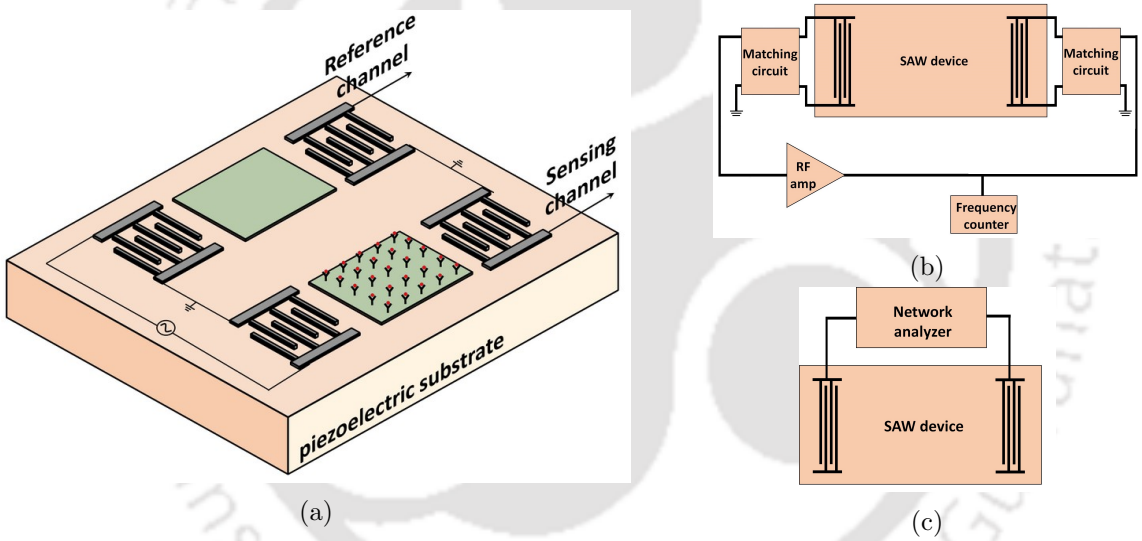

Figure 1.8: (a) Typical SAW biosensor setup with sensing and reference channels, (b) closed loop oscillator arrangement for frequency measurement, and (c) measurement using network analyzer (adapted from [51]).

1.7 Problem definition and scope of the thesis

In the last few years, LW devices have garnered much interest for biosensor design. Researchers have tried to increase the mass sensitivity and improve LOD of the device by employing different substrates (quartz, $LiNbO_3$, $LiTaO_3$, langasite, etc.) along with various combinations of guiding layer materials (SiO_2, ZnO, AlN, gold, polymers, etc.). Nanostructures made on top of the overlayer could enhance the sensitivity by increasing the available surface area for the analyte to attach. Li *et al.* [22] detected carcinoembryonic antigen (CEA) using a SiO_2 based LW device by immobilizing the corresponding antibody. An improvement in LOD of 2–3 orders of

magnitude was obtained by using gold nanoparticles conjugates to attach on the captured antigens and increasing the mass loading on the device. Zhang *et al.* [90] have shown experimentally that ZnO nanotips of 500 nm height over $SiO_2/LiNbO_3$ SAW sensor can enhance the immobilization of DNA by a factor of 200 compared to a flat ZnO film. Reyes *et al.* [108] reported tenfold increase in the mass sensitivity of a conventional QCM by growing ZnO nanorods on the device surface by metal-organic chemical vapour deposition (MOCVD) method. Although there are a variety of nanostructures in materials science, ZnO nanorods are most promising because they can be easily fabricated at low temperatures without affecting the properties of the underlying piezoelectric substrate and their aspect ratio can also be controlled [109], [110]. A vertically aligned array of ZnO nanorods can be grown over large areas by hydrothermal solution growth on a pre-deposited ZnO seed layer covered by lithographically patterned photoresist acting as a template [111].

In 1985 Dybwad explained a system of *coupled resonator* where gold particles of 10-50 µm diameter size were put over a quartz substrate vibrating in a shear horizontal way [112]. At a certain size, the resonant frequency of the sphere matches with the substrate, giving negative (inertial loading) and positive (elastic loading) frequency shifts. Ramakrishnan *et al.* [113] further investigated coupled resonance by employing high aspect ratio palladium resonant nanopillars over a SAW device using FE simulation to detect a small concentration of hydrogen. Coupled resonance with SU-8 and polymethylmethacrylate (PMMA) micro-pillars have also been used in QCM to enhance the sensitivity of the device for humidity detection [114], [115]. The presence of ZnO nanorod of a certain aspect ratio over Love wave device can form a *Dybwad system of coupled resonance*. Such a system can be very sensitive to the mass loading and is the motivation of current study.

The main objective of this thesis work is to simulate and fabricate LW and SH-SAW devices by growing nano or microstructures of appropriate size on the top surface of the sensor as it not only provides an increase in the surface area for the analyte to attach but also cause *coupled resonance* leading to an increase in mass sensitivity. The thesis work mainly involves finite element method (FEM) based simulation of LW device with ZnO nanorods, and micro ridges of SiO_2 or polymer made on SH-SAW device, fabrication of the proposed devices, and biosensing experiments. LW and SH-SAW devices are particularly suited for biosensing, however, utilizing coupled resonance to increase sensitivity of the biosensors to our knowledge have not been attempted either by simulations or through experiments. The scope of the thesis includes the following-

- Simulation of SH-SAW devices based on piezoelectric substrates such as 36°-YX $LiTaO_3$, 41°-YX $LiNbO_3$, 90°-ST and AT quartz to calculate and compare surface velocity, coupling coefficient, and TCF.
- Analytical calculation of phase velocity, group velocity and mass sensitivity of LW device considering different guiding layers and comparison with FE simulation results.
- FE simulation of LW resonator and delay line devices to investigate coupled resonance with ZnO nanorods and its effect on mass sensitivity, coupling coefficient, stress, and insertion

loss. The study is also carried out for SH-SAW devices with SiO_2 micro-ridges.

- Fabrication of LW devices using photolithography followed by design of matching circuit and characterization using the network analyzer.
- ZnO nanorod grown by hydrothermal methods for controlling the height and orientation of the nanorods.
- Simulations and experiments of SH-SAW resonator comprising S1813 polymer micro-ridges designed along the wave propagation direction that utilizes the coupled resonance phenomenon for high mass sensitivity biosensing.
- Biosensing experiment using SH-SAW resonator comprising S1813 polymer micro-ridges by detection of biotin on avidin functionalized micro-ridges.

1.8 Organization of thesis

The thesis is organized into eight chapters, and their contents are briefly outlined as follows.

Chapter 1 introduces SAW devices and their essential parameters and characteristics. The fundamental working principle of the biosensor is explained and the advantages of acoustic wave sensors over other conventional methods are listed. Different types of acoustic sensors are discussed. Extensive literature survey of LW and SH-SAW biosensors is presented along with a discussion of problem definition and scope of the thesis.

In chapter 2, various modeling and simulation techniques of SAW devices such as the equivalent circuit method, the coupling of modes (COM) model, P-matrix approach and impulse response method are presented. Modeling technique for delay line, resonant cavity, one-port and two port resonators is described. 3D FE simulation of substrates generating SH-SAW is carried out by optimizing the mesh and applying appropriate boundary conditions. 36°-YX $LiTaO_3$, 41°-YX $LiNbO_3$, 90°-ST and AT quartz are used as substrates and both resonator and delay line geometries are considered in the simulation. The free surface velocity, metalized surface velocity, electromechanical coupling coefficient, TCF, and insertion loss for each substrate are calculated and compared.

Chapter 3 presents the solution of LW dispersion equation using bisection method for the calculation of phase velocity, group velocity and mass sensitivity considering SiO_2, ZnO, gold, SU-8, PMMA, and polyimide guiding layers. The results are compared with those obtained by FE simulation. The frequency response of LW device along with depth displacement calculation for the fundamental mode and the next higher order mode is carried out. 3D FE simulation of SiO_2 based LW delay line is performed to calculate the time response, mass sensitivity, and insertion loss. The mass sensitivity of delay line device is calculated by applying incremental surface mass density on the surface and noting the corresponding values of time and phase delays in the output voltage. The insertion loss of delay line is obtained by taking the fast Fourier transform (FFT) of the impulse response of the delay line device.

Chapter 4 presents the 3D FE simulation of SiO_2 based LW resonator and delay line geometries containing ZnO nanorods of various values of height and packing density on the top surface of the device. The effect of coupled resonance on frequency response, mode transitions, mass sensitivity, coupling coefficient, stress, and insertion loss of the device is studied.

Chapter 5 presents the 3D FE simulation of SH-SAW resonator and delay line geometries containing SiO_2 micro-ridges of fixed width and various values of height made on the top surface of the device. The effect of coupled resonance on frequency response, mode transitions, mass sensitivity, coupling coefficient, stress and insertion loss of the device is studied.

In chapter 6, the fabrication of LW resonator and delay line devices using standard photolithography and mask-alignment procedures is described. The devices are connected to a network analyzer via an appropriate matching circuit, and S_{11} for the resonator and S_{21} for the delay line are measured. The growth rate and orientation control of ZnO nanorods are attempted using the low-temperature hydrothermal fabrication method.

Chapter 7 describes the fabrication of SH-SAW resonator containing S1813 polymer micro-ridges patterned along the direction of wave propagation on top of the device. Ridges of fixed width and various values of height are designed on the surface by varying the spin speed during spin coating the resist. Coupled resonance is studied through FE simulation and experiment. The polymer ridges were biofunctionalized by silanization, and different concentrations of biotin is detected on avidin immobilized micro-ridges. The mass sensitivity and LOD of the device is measured.

Chapter 8 lists the conclusions of the research work and recommendations for future work.

Chapter 2

Modeling and simulation of SAW devices

> We have no idea about the 'real' nature of things ... The function of modeling is to arrive at descriptions which are useful.
>
> Richard Bandler

The development and evolution of modern SAW devices have been possible because of simultaneous efforts put in the fabrication as well as theoretical modeling and simulation of devices. To describe the function of IDT fabricated on the piezoelectric substrate in a SAW device, several methods of modeling are available such as delta function method, impulse response method, equivalent circuit method, coupling-of-mode (COM) method, and P-matrix method [11], [16]. This chapter presents these modeling techniques in brief followed by calculation of frequency response and admittance characteristics of SAW delay line, resonant cavity and one/two port resonators. This chapter also presents the results of 3D FE simulations of SH-SAW resonator and delay line based on 36°-YX $LiTaO_3$, 41°-YX $LiNbO_3$, 90°-AT quartz, and 90°-ST quartz substrates using COMSOL Multiphysics. Phase velocities, coupling coefficient, and TCF of different substrates are calculated and compared with the reported values using the Eigenmode analysis. Time response of SH-SAW delay line is performed to calculate output voltage and displacement. The insertion loss of delay line is calculated and compared to different substrates.

2.1 Piezoelectricity and constitutive equations

A solid subjected to external force gets deformed and returns to its original form when the force is removed, such a body is said to be elastic. Various types of forces like, mechanical, thermal, electrical and magnetic can be employed for the generation of elastic waves in an elastic medium. However, it is more suitable to choose materials in which the stress varies linearly with the applied electric field. The elasticity of a solid is concerned with the internal

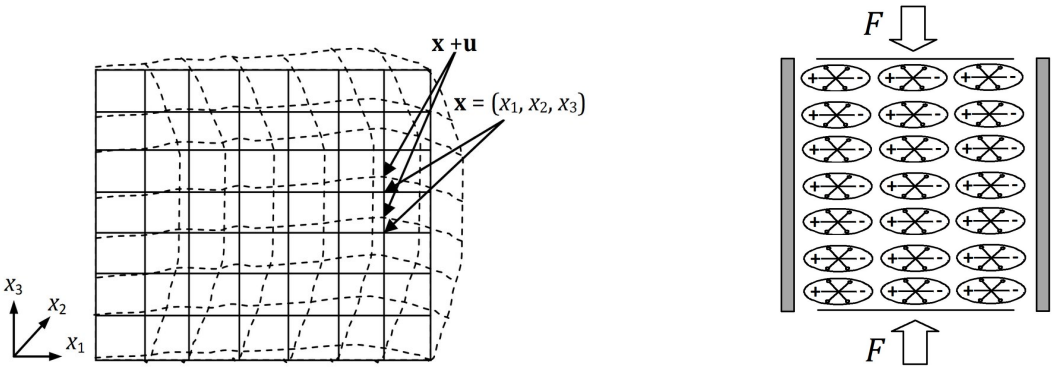

(a) (b)

Figure 2.1: (a) Particle positions in equilibrium and deformed states of a solid body (The deformation of the solid is shown in broken lines.). (b) Polarization of molecules upon application of external deforming force in a piezoelectric material. [116].

forces within the solid and its particle displacement from equilibrium position [10]. The particle is an elementary region of a material much larger than the inter-atomic distance and much smaller than any characteristic elastic dimensions such as wavelength. Consider an equilibrium state of the solid, with particle located at point $\boldsymbol{x} = (x_1, x_2, x_3)$ and displaced by an amount $\boldsymbol{u} = (u_1, u_2, u_3)$, where the components u_1, u_2 and u_3 are the general components of coordinates x_1, x_2, x_3 respectively. Thus the particle has been displaced to a new position $\boldsymbol{x} + \boldsymbol{u}$ as shown in Fig. 2.1a. If $\boldsymbol{u}$ is independent of $\boldsymbol{x}$ there will be no internal force since this simply shows a displacement of a material as a whole, and also there will be no force if the material is rotated. The strain at each point can be defined as

$$S_{ij}(x_1, x_2, x_3) = \frac{1}{2}\left(\frac{du_i}{dx_j} + \frac{du_j}{dx_i}\right), \qquad i, j = 1, 2, 3. \tag{2.1}$$

Thus the strain is related to the internal forces. The strain is a second rank symmetrical tensor as $S_{ij} = S_{ji}$. The stress T is defined as internal stress in the material, i.e., force per unit area. The second-rank symmetric stress tensor is defined as $T_{ij}(x_1, x_2, x_3)$ with $T_{ij} = T_{ji}$. According to Hooke's law, each component of stress is given by the linear combination of the strain components, and it is expressed as,

$$T_{ij(mech)} = \sum_k \sum_l c_{ijkl} S_{kl}, \qquad i, j, k, l = 1, 2, 3 \tag{2.2}$$

where c_{ijkl} is the fourth-rank stiffness tensor. These elements represent the physical properties of the material under consideration. Pierre & Jacques Curie discovered piezoelectricity phenomenon in 1981. The piezoelectricity is a Greek word which means *electricity by pressure*. The external force exerted on piezoelectric material results in the generation of electric field at the surface of the material [56]. Without application of any force, the centers of positive and negative charges of each molecule of the piezoelectric material coincide. Thus the external effects of charges reciprocally cancel, and electrically neutral molecules appear. By applying an external force to the material, the internal reticular structures of the molecules deform that results in the

separation of positive and negative charges of the molecules, creating the electric dipoles. The facing dipoles are mutually canceled, and a distribution of linked charges appears at the surface of the piezoelectric materials as shown in Fig. 2.1b. Piezoelectricity is defined as a phenomenon which couples the elastic stresses and strains to the electric fields and displacements and occurs only in anisotropic materials, whose internal structure lacks a center of symmetry [11]. The stress, $T_{ij(elec)}$ produced by the piezoelectric effect is given by,

$$T_{ij\,(elec)} = \sum_{k} e_{kij} E_k, \qquad i,j,k,l = 1,2,3. \tag{2.3}$$

where electric field $E_k = -\frac{\partial V}{\partial x_k}$. Total stress T_{ij} is the sum of stresses due to the electric field and mechanical strain and can be expressed as

$$T_{ij} = \sum_{k}\sum_{l} c^{E}_{ijkl}\, S_{kl} - \sum_{k} e_{kij} E_k. \tag{2.4}$$

The electric displacement can be expressed by electric field and permittivity tensor ϵ_{ij} of the dielectric medium. In case of piezoelectric material, an additional electric field displacement caused by the strain is developed due to the piezoelectric effect. The total electric displacement can then be given as

$$D_i = \sum_{j} \varepsilon^{s}_{ij} E_j + \sum_{j}\sum_{k} e_{ijk} S_{jk} \tag{2.5}$$

where, c^{E}_{ijkl} is the stiffness tensor for constant electric field ($\mathrm{N\,m^{-2}}$), S_{kl} is the strain component, e_{ijk} is the piezoelectric tensor relating elastic to electric fields ($\mathrm{C\,m^{-2}}$), ϵ^{s}_{ij} is the permittivity tensor for constant stress ($\mathrm{F\,m^{-1}}$), and E_j is the electric field vector ($\mathrm{V\,m^{-1}}$) [11]. Equations (2.4-2.5) are known as *piezoelectric constitutive relations*. The tensor components in the equations can be reduced to matrix elements and are written in the form of convenient matrix based equations as [18],

$$\begin{aligned} [T] &= [c][S] - [e^t]E \\ D &= [e][S] + [\epsilon]E \end{aligned} \tag{2.6}$$

where $[T]$ and $[S]$ are stress and strain matrices respectively of size 6×1. The piezoelectric matrix of size 3×6 is denoted by $[e]$. Stiffness matrix $[c]$ is of size 6×6. Electric field E and electric displacement density D are vectors of size 3×1. If the stress and strain are functions of time and position, then the mechanical equation of motion can be expressed using Newton's laws as,

$$\rho \frac{\partial^2 u_i}{\partial t^2} = \sum_{j} \frac{\partial T_{ij}}{\partial x_j}. \quad i,j = 1,2,3 \tag{2.7}$$

where ρ is the density of the material and T_{ij} is the stress tensor and u_i is the displacement. In case of piezoelectric medium, elastic waves travel much slower than the electromagnetic waves. Hence the electric field can be expressed using quasi-static approximation

$$E_i = -\frac{\partial V}{\partial x_i} \tag{2.8}$$

Using (2.8) in (2.4) along with (2.1) for the strain, the equation of motion for piezoelectric material can be expressed as [11]

$$\rho \frac{\partial^2 u_i}{\partial t^2} = \sum_j \sum_k \left\{ e_{kij} \frac{\partial^2 \phi}{\partial x_j \partial x_k} + \sum_l c^E_{ijkl} \frac{\partial^2 u_k}{\partial x_j \partial x_l} \right\}. \tag{2.9}$$

In addition, the material is taken to be an insulator there are no free charges. Thus div $\boldsymbol{D} = 0$. Using (2.5) the relation is written as

$$\sum_i \sum_j \left\{ \epsilon^S_{ij} \frac{\partial^2 \phi}{\partial x_i \partial x_j} + \sum_k e_{ijk} \frac{\partial^2 u_j}{\partial x_i \partial x_k} \right\} = 0. \tag{2.10}$$

The degrees of freedom (dependent variables) are the global displacements u_1, u_2, and u_3 in the global x_1, x_2, and x_3 directions, respectively, and the electric potential V can be obtained by solving the equations (2.9 and 2.10) using appropriate boundary conditions [11].

2.2 SAW models

To describe the function of IDT fabricated on a piezoelectric substrate in SAW device, several methods of modeling are available such as delta function method, impulse response method, equivalent circuit method, COM method, and P-matrix method. This section describes each of these techniques in brief.

2.2.1 Delta function model

The delta function model is one of the earliest and basic SAW models developed for prediction of IDT response. The model does not consider energy, capacitance, and the electromechanical coupling coefficient of the materials, and cannot predict input/output impedance levels, circuit factor loading, and harmonic response. It can only determine the transfer function of the IDT, giving relative insertion loss as a function of the frequency [16]. In this approach, the complex electric field distribution between adjacent fingers of an excited IDT is modeled as a discrete number of delta function sources at the metal finger edges as shown in 2.2a. Each finger has two delta function sources of electric field intensity, with amplitude proportional to the applied voltage. The voltage on the electrode fingers alternate in polarity with their centers spaced $\lambda/2$ apart. The model can be further simplified by replacing the two delta sources at the edges of the fingers with one equivalent source at the center of each finger (see Fig. 2.2b).

A reference point at the center of the finger ($x = 0$) is assumed for summing the delta function contributions. The amplitudes of delta sources are assumed to be constant but the phase contribution changes for each finger according to the distance from the reference point [18]. The frequency response for the IDT modeled using the delta function approximation is

given by,

$$H_i(f) = \sum_{-N_p}^{N_p} (-1)^{N_p} A_n \exp^{-j\beta x_{N_p}} \tag{2.11}$$

where $H_i(f)$ is the frequency response of the IDT, N_p is the number of finger pairs, $(-1)^{N_p}$ denote the alternating polarity of the IDT fingers, β is the propagation constant, A_n is the amplitude parameter proportional to the finger apodization overlap, and x_n is the distance from the reference point. For a uniformly apodized IDT (constant overlapping aperture W), A_n is normalized to unity. The IDT response is approximated in the form of a *sinc* function given as,

$$|H_i(f)| \simeq N \left| \frac{sinX}{X} \right| \tag{2.12}$$

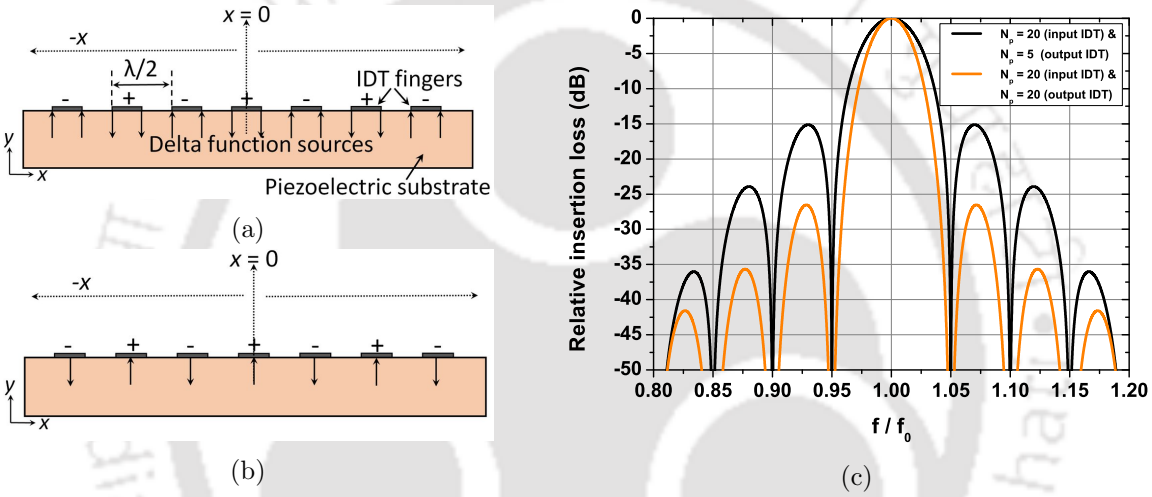

Figure 2.2: (a) Delta function model showing electric field lines approximated as delta function sources at each edge of the IDT finger. (b) Simplified delta function model with one source at the center of each excited finger. (c) Calculated magnitude response of SAW filter with uniform IDT for two cases viz, one with $N_p = 20$ and $N_p = 5$ in the input and output IDTs respectively and the other with $N_p = 20$ in both input and output IDTs using the delta function model.

where f_0 is the center frequency, $X = N_p\pi(f - f_0)/f_0$, and N is the total number of fingers in the IDT such that $N_p = (N-1)/2 \simeq N/2$ for large odd N and $N_p = N/2$ for even N. The overall amplitude response $H_T(f)$ of SAW filter with input and output IDTs pairs is given by the relationship,

$$|H_T(f)| = |H_i(f)| \cdot |H_o(f)| \tag{2.13}$$

where $H_o(f)$ is the frequency response of output IDT. Fig. 2.2c illustrates the computation of relative insertion loss of SAW filter containing input and output IDTs with constant finger overlap. Two cases are considered, one with $N_p = 20$ in the input IDT and $N_p = 5$ in the output IDT, and the other with $N_p = 20$ in both the input and output IDTs. Increasing the number of pairs of electrodes in the output IDT causes a reduction in the magnitude of side lobes. The overall response also becomes narrower.

2.2.2 Impulse response model

The impulse response method predicts the absolute amplitude, hence the power of SAW by considering the energy of the wave [16]. It provides additional information on the SAW transducer response over that given by the delta function model, in that matching networks and circuit impedance can be included [18], [117]. It provides insight into frequency scaling that must be used in the determination of apodization quantities for SAW filters. The impulse response model uses the Fourier transform pair relations to determine the impulse response $h(t)$ of a SAW filter, given its desired frequency response $H(f)$. A unit step signal is applied to the IDT fabricated on the piezoelectric substrate, and the output response is shown in Fig. 2.3. If the IDT electrodes are short circuited at $t = 0$ the response of the device with unit step signal for duration of N_p/f_0 can be expressed as,

$$a_u(t) = \begin{cases} -a_0 sin(2\pi f_0 t), & \text{for } 0 \leq t \leq N_p/f_0 \\ a(t) = 0, & \text{for other t values} \end{cases} \tag{2.14}$$

$$a_0 = K\sqrt{f_0 C_1/2} \tag{2.15}$$

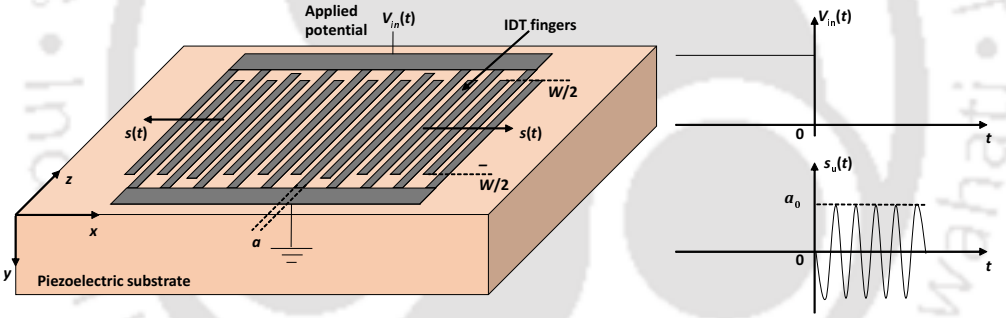

Figure 2.3: IDT on piezoelectric substrate with response to a unit step voltage input.

where $C_1 = \epsilon_p + \epsilon_0$ is the capacitance per pair per unit length of IDT fingers and K is a measure of the surface wave coupling efficiency. Thus the impulse response from (2.14) and (2.15) can be expressed as

$$h(t) = \begin{cases} 4\sqrt{(K^2 C_s)} f_0^{3/2} sin(2\pi f_0 t), & \text{for } 0 \leq t \leq N_p/f_0 \\ 0, & \text{otherwise} \end{cases} \tag{2.16}$$

where f_0 is the synchronous frequency and C_s is the capacitance per finger pair. The Fourier transform of (2.16) is given by,

$$|H_f| \simeq 2\sqrt{(K^2 C_s f_0)} N_p \frac{sin(N_p\pi(f - f_0)/f_0)}{N_p\pi(f - f_0)/f_0} \tag{2.17}$$

showing that it has the same *sinc* function dependence as delta function model.

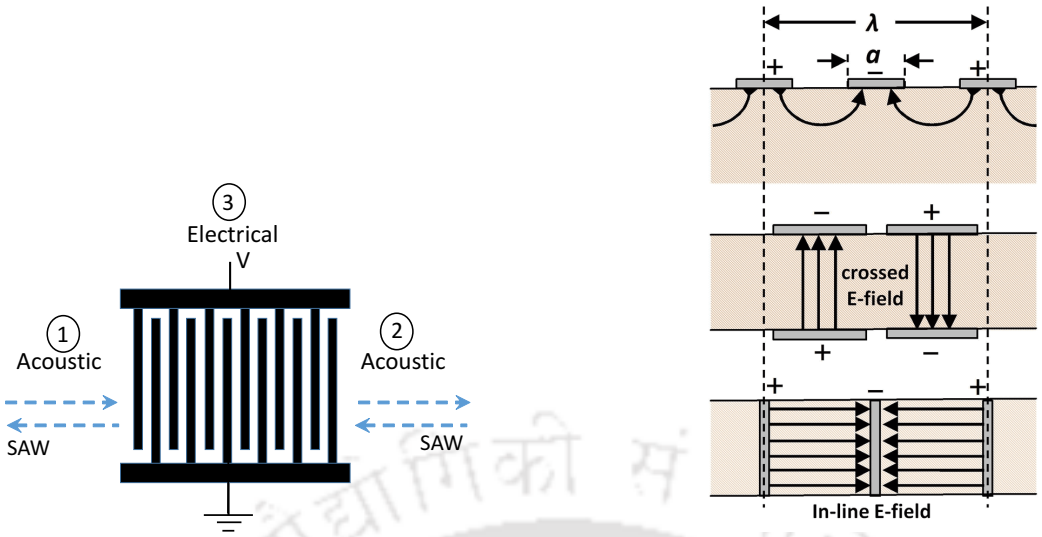

Figure 2.4: (a) IDT represented as a three port network. Port 1 and 2 are electrical equivalents of acoustic port while port 3 is a true electrical port. (b) Electric field line directions in an electrically excited IDT with *cross-field* and *in-line* field approximations [18].

2.2.3 Equivalent circuit model

The equivalent circuit model used to describe the response of SAW device is essentially a three port model, consisting of two acoustic ports and one electric port as shown in Fig. 2.4a. Port 1 and 2 are the electrical equivalents of acoustic port represented in the form of a passive SAW transmission line, while port 3 is a true electrical port where voltages are applied and sensed. Fig. 2.4b shows the electric field generated in a SAW device upon electrical excitation of IDTs. The electric field distribution can be approximated by a *cross-field* model, in which electric field lines are perpendicular to the substrate surface, similar to the electric field between plates of a capacitor. In the *in-line* field model the field lines are parallel to the substrate surface. In 1969 Smith *et al.* [118] used Mason's cross field model for launch and detection of BAW and formulated an equivalent circuit model for SAW device operation. In this model, the acoustic forces are represented in the form of electric voltages and SAW velocities in terms of equivalent currents. The IDT can be represented in the form of a equivalent three port admittance network as shown in Fig. 2.5a. G_0 is the electrical characteristic admittance of SAW transmission line given as,

$$G_0 = K^2 C_s f_0 \tag{2.18}$$

where C_s is the capacitance of one periodic section of IDT. C_s is also expressed as $C_s = C_0 W$, where C_0 is the capacitance of one periodic section of IDT per unit length. The total capacitance of the IDT, depends on the number finger pairs given as $C_T = N_p C_s$. The Y parameters of the 3-port network using the equivalent circuit of a period of an IDT can be expressed as,

$$\begin{bmatrix} I_1 \\ I_2 \\ I_3 \end{bmatrix} = \begin{bmatrix} -jG_0\cot(N_p\theta) & jG_0\csc(N_p\theta) & -jG_0\tan(\theta/4) \\ jG_0\csc(N_p\theta) & -jG_0\cot(N_p\theta) & jG_0\tan(\theta/4) \\ -jG_0\tan(\theta/4) & jG_0\tan(\theta/4) & j\omega C_T + j4N_pG_0\tan(\theta/4) \end{bmatrix} \begin{bmatrix} V_1 \\ V_2 \\ V_3 \end{bmatrix} \tag{2.19}$$

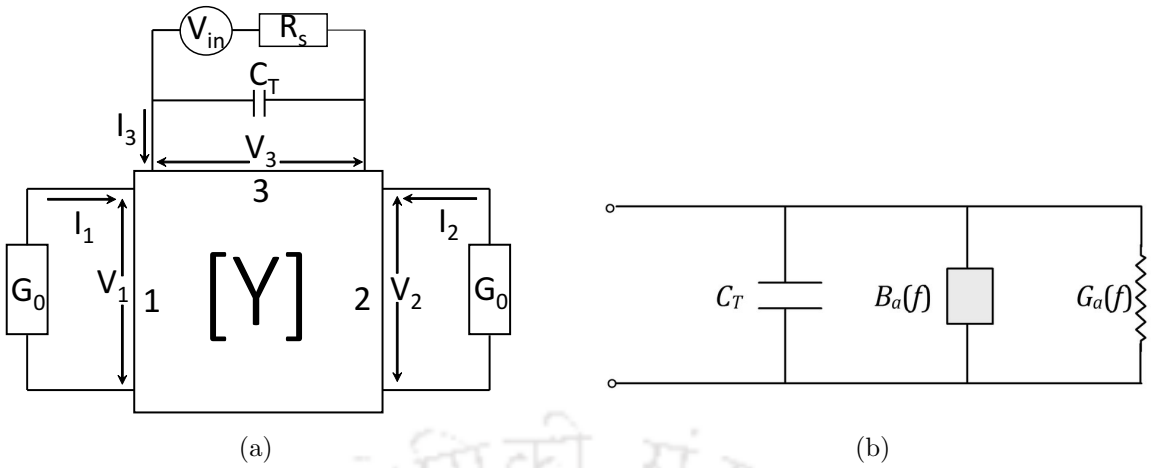

(a) (b)

Figure 2.5: (a) Three-port equivalent admittance network representation for an IDT in the crossed-field model. (b) Equivalent circuit representation of SAW IDT [18].

where $\theta = 2\pi f/f_0$ is the electrical transit angle in radian through one finger pair. Fig. 2.5b shows the overall equivalent circuit representation of SAW IDT. The input admittance Y_f is written as,

$$Y(f) = G_a(f) + B_a(f) + j\omega C_T \tag{2.20}$$

$G_a(f)$ and $B_a(f)$ are the radiation conductance and susceptance respectively, given by the following relations

$$G_a(f) = G_a(f_0)\left|\frac{\sin X}{X}\right|^2 \tag{2.21}$$

$$B_a(f) = G_a(f_0)\frac{(\sin(2X) - 2X)}{2X^2} \tag{2.22}$$

$$G_a(f_0) = 8K^2 f_0 C_s N_p^2 \tag{2.23}$$

where $X = N_p\pi(f - f_0)/f_0$ and $G_a(f_0)$ is the radiation conductance at the center frequency f_0. Fig. 2.6a shows plot of normalized radiation conductance and susceptance versus normalized frequency with $\lambda = 20$ µm, $N_p = 20$, $W = 80\lambda$, $f_0 = 208$ MHz, and $v = 4160$ m/s for a $LiTaO_3$ substrate. The radiation conductance accounts for the electrical power from the voltage source carried by the acoustic wave away from the IDT. The susceptance accounts for the current induced by the acoustic waves passing beneath the fingers of the IDT [119]. The conductance becomes maximum at the center frequency while the susceptance crosses through zero. The equivalent circuit approach is often used to design SAW devices so that the IDTs are well matched to a 50 Ω source. At the center frequency, the reactance is zero, so the overall impedance becomes

$$Z(f_0) = \frac{1}{Y(f_0)} = \frac{G_a(f_0) - j2\pi f_0 C_T}{(G_a(f_0))^2 + (2\pi f_0 C_T)^2} \tag{2.24}$$

$$Re[Z(f_0)] \simeq \frac{G_a(f_0)}{(2\pi f_0 C_T)^2} \tag{2.25}$$

The IDTs are designed with appropriate values of N_p and W so that the real part of impedance, $Re[Z(f_0)]$ is close to 50 Ω. From (2.23) and (2.25) it is noted that $Re[Z(f_0)]$ is inversely proportional to the IDT aperture. Fig. 2.6b shows the variation of real part of IDT impedance

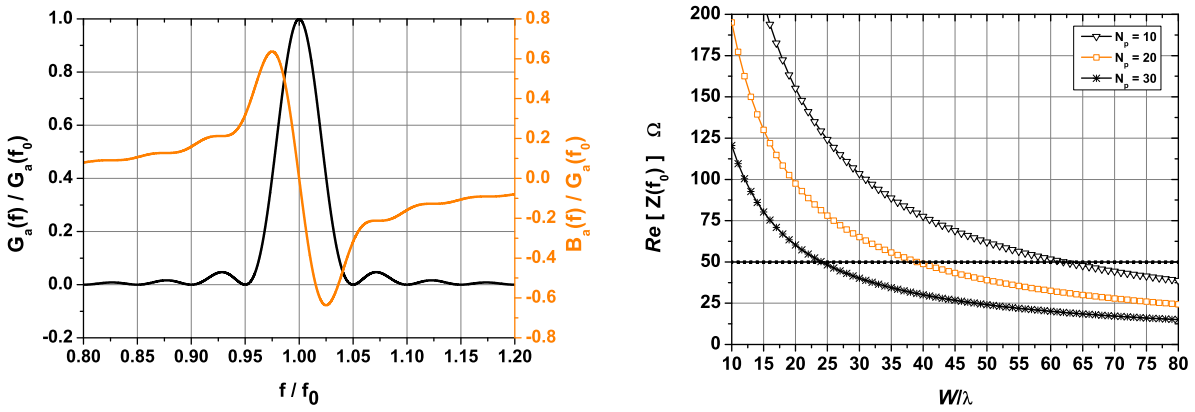

(a) (b)

Figure 2.6: (a) Plot of normalized radiation conductance and susceptance versus normalized frequency for a SAW IDT with $\lambda = 20$ µm, $N_p = 20$, $W = 80\lambda$, $f_0 = 208$ MHz, and $v = 4160$ m/s on a $LiTaO_3$ substrate. (b) Variation in real part of IDT impedance with normalized IDT aperture for $\lambda = 20$ µm.

with normalized IDT aperture for three different values of N_p. The matching is achieved at W/λ = 24, 39, and 62 at corresponding values of $N_p = 10$, 20 and 30 respectively, for $\lambda = 20$ µm on $LiTaO_3$ substrate. Sometimes, if the matching is difficult to achieve then, a series inductor is used to tune out the capacitive reactance of the IDT or an L-C type of circuit can be used as matching circuit placed in-between IDT and source.

2.2.4 COM model and P-matrix approach

Coupling-of-modes model is widely used in designing SAW devices. It represents the coupling of two counter-propagating surface waves in the form of differential equations [120]. The model considers wave amplitudes, acoustic properties and coupling interactions between the waves but does not include depth of penetration of the wave in the substrate. Propagation of one-dimensional wave equation on a free surface without electrical coupling is given as,

$$\frac{d^2}{dx^2}\phi(x,t) = \frac{1}{v^2}\frac{d^2}{dt^2}\phi(x,t) \tag{2.26}$$

where v is the SAW velocity, and $\phi(x,t)$ represents displacement or electric potential of the wave normalized to power flow. Fig. 2.7a shows two counter-propagating modes in the x direction with $\phi_+(x)$ and $\phi_-(x)$ denoting the forward and backward components respectively. Presence of transducers or periodic perturbations cause reflections leading to coupling of the forward and backward propagating waves. The equation of the loaded wave is given by,

$$\left(\frac{d^2}{dx^2} + \beta_0^2\right)\phi(x) = -\zeta(x)\beta_0^2\phi(x) \tag{2.27}$$

where $\beta_0 = \omega/v_0$ is the propagation constant and $\zeta(x)$ is the periodic load density. Solutions to the equation are Eigenmodes with an infinite set of discrete harmonics. It can be reduced to a finite system of equations with the differential approach involving a transformation of the

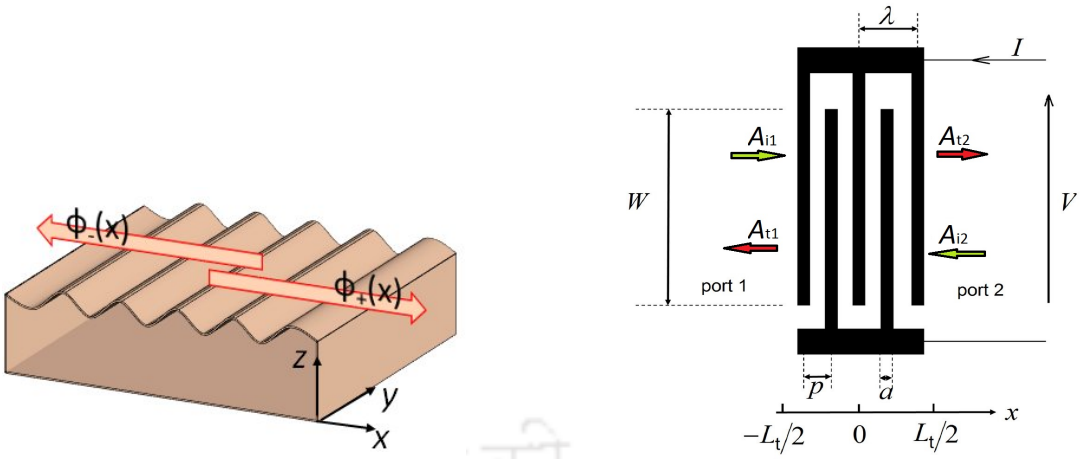

(a) (b)

Figure 2.7: (a) Counter-propagating waves in COM model (b) P-matrix representation of the IDT. The IDT aperture is W. The pitch p of the IDT is given as, $p = a/4 = \lambda/2$. A_i and A_t denote the amplitudes of incident and transmitted waves.

reduced algebraic equations into linear differential equations. The counter-propagating waves get reflected by the periodic grating and undergo constructive and destructive interference at two discrete frequencies forming a stopband. It happens when the period of the grating (p) is half of the SAW wavelength ($\lambda = 2p$). This condition is called as Bragg relation. The two counter-propagating modes $\phi_+(x)$ and $\phi_-(x)$ are composed of slow ($R(x)$ and $S(x)$) and fast (exponential terms) varying phase oscillations.

$$\begin{aligned} \phi_+(x) &= R(x)e^{-j\pi x/p} \\ \phi_-(x) &= S(x)e^{j\pi x/p} \end{aligned} \tag{2.28}$$

Generation of SAW due to piezoelectric effect adds the electrical coupling term to the differential equation. As SAW propagates, because of inverse piezoelectric effect, charges are induced on the electrodes, and it leads to a current $I(x)$, flowing through the electrode which is written in a differential form. The final three differential equations of the COM model are written as,

$$\begin{aligned} \frac{dR(x)}{dx} &= -j\delta R(x) + j\kappa S(x) + j\alpha V \\ \frac{dS(x)}{dx} &= -j\kappa^* R(x) + j\delta S(x) - j\alpha^* V \\ \frac{dI(x)}{dx} &= -2j\alpha^* R(x) - 2j\alpha S(x) + j\omega C V \end{aligned} \tag{2.29}$$

where δ is the detuning parameter given as $\delta = 2\pi(f - f_0)/v - j\gamma$. In the above equations δ, κ, α, v, γ, and C are the detuning parameter, reflectivity due to perturbations, transduction coefficient, saw velocity, attenuation and capacitance per unit length respectively. Most of these COM parameters are dependent on width, the height of electrodes, and orientation/type of substrate. Thus, cannot be determined from the theory itself. They are often evaluated by fabricating the device and performing experiments or through numerical simulations. The COM

analysis along with P-matrix formulation is often used for modeling the response of SAW devices, such as delay line and resonators. The P-matrix is a type of scattering matrix commonly used to describe the behavior of SAW gratings and transducers [121]. Fig. 2.7b shows an uniform IDT transducer and its P-matrix representation. A_{i1} and A_{i2} represent the amplitudes of wave incident at ports 1 and 2 respectively. The amplitudes of waves leaving the transducer at these ports are represented by A_{t1} and A_{t2} . W is the IDT aperture, N is the number of fingers in the IDT and $L_t = (2N-1)\lambda/4$ is the length of the transducer. Current and voltage are denoted by I and V respectively. The P-matrix is defined as,

$$\begin{bmatrix} A_{t1} \\ A_{t2} \\ I \end{bmatrix} = \begin{bmatrix} P_{11} & P_{12} & P_{13} \\ P_{21} & P_{22} & P_{23} \\ P_{31} & P_{32} & P_{33} \end{bmatrix} \begin{bmatrix} A_{i1} \\ A_{i2} \\ V \end{bmatrix} \tag{2.30}$$

where $A = \phi_s\sqrt{\omega W/(2\Gamma_s)}$ is the amplitude of the wave, related to the surface potential ϕ_s and IDT aperture W. The constant Γ_s is defined as, $\Gamma_s = (\Delta v/v)/\epsilon_\infty$, where $\epsilon_\infty = 50\epsilon_0$ and $\epsilon_\infty = 5.6\epsilon_0$ for 36°-YX $LiTaO_3$ and ST-quartz, respectively [11]. For a lossless non reflective transducer, with conditions of reciprocity, the elements of the P-matrix are

$$P_{11} = P_{22} = 0 \tag{2.31}$$
$$P_{12} = P_{21} = e^{-jkL_t} \tag{2.32}$$
$$P_{13} = -P_{31}/2 = j\overline{\rho_e}(k)\sqrt{\omega W\Gamma_s/2}e^{-jkL_t/2} \tag{2.33}$$
$$P_{23} = -P_{32}/2 = j\overline{\rho_e}(-k)\sqrt{\omega W\Gamma_s/2}e^{-jkL_t/2} \tag{2.34}$$
$$P_{33} = Y(\omega) = G_a(\omega) + jB_a(\omega) + j\omega C_T. \tag{2.35}$$

Assuming that $V = 0$ and no waves arrive from the right side of the IDT ($A_{i2} = 0$), $P_{11} = A_{t1}/A_{i1}$ is the reflection coefficient of the IDT. Since the transducer is assumed to be non-reflective, P_{11} and P_{22} both are zero. $P_{12} = A_{t1}/A_{i2}$ is the ratio of two waves traveling across distance L_t of the transducer. Thus, $P_{12} = P_{21} = e^{-jkL_t}$ simply represents the phase. P_{33} is the IDT admittance Y, which is same as given in (2.20). Other elements like P_{13} and P_{23} are computed using $\overline{\rho_e}(k)$, which is the Fourier transform of the electrostatic charge density $\rho_e(x)$ in the IDT [122]. Equations (2.31–2.35) are valid only for non-reflective transducers. Transducers do reflect and the entries of the P-matrix change. As per the COM model, for a reflective transducer, the elements P_{11} and P_{22} become

$$P_{11} = \Gamma_1 = -c_{12}^* \frac{\sin(sL_t)}{D} \tag{2.36}$$
$$P_{22} = \Gamma_2 = c_{12}\sin(sL)\frac{e^{-2jk_0L_t}}{D} \tag{2.37}$$

where $c_{12} = r_s/p$, $s^2 = \delta^2 - |c_{12}^2|$, $\delta = 2\pi(f - f_0)/v$ is the detuning factor and $D = s\cos(sL_t) + j\delta\sin(sL_t)$. The reflection coefficient of one finger is r_s. Equations (2.36–2.37) are important for designing reflector gratings and resonators.

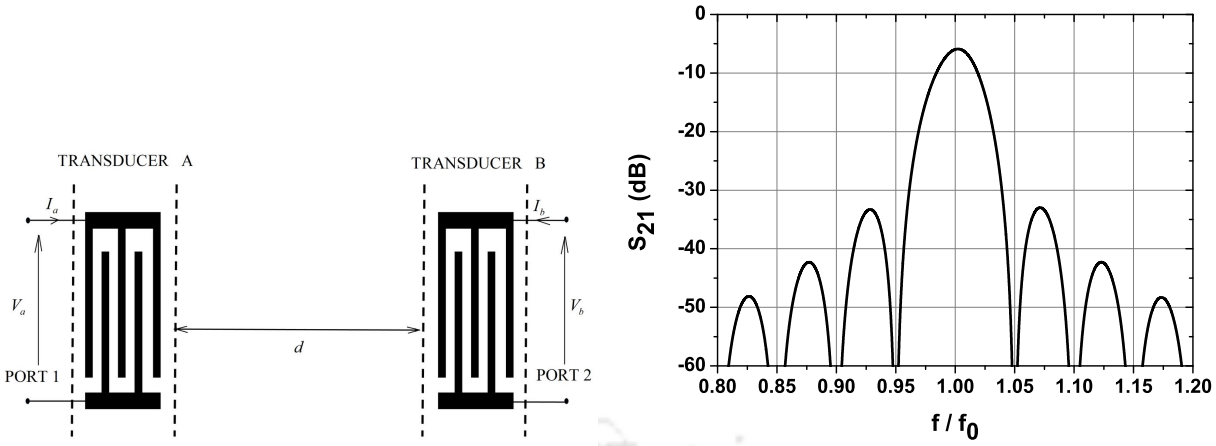

(a) (b)

Figure 2.8: (a) Delay line device with input and output IDTs. (b) Typical response of a delay line showing S_{21} in dB.

2.3 SAW device modeling using P-matrix

P-matrix method is a convenient modeling technique to study the response of SAW devices. The section presents modeling of basic delay line device, resonant cavity, one port and two port resonators by assuming the simple case of loss-less, and non-reflective IDTs.

2.3.1 Delay line

A basic delay line device, consisting of two IDTs separated by a distance d apart is shown in Fig. 2.8a. Voltage V_a is applied to input IDT that results in the generation of SAW which induces a voltage V_b at the output IDT. Y_{11} is the admittance looking into port 1 when the output port is shorted (i.e. $V_b = 0$). Since both transducers are identical and non-reflective in nature, the admittance is given by (2.20) with $Y_{11} = Y_{22} = Y$. The trans-admittance Y_{12} is the ratio of current I_b induced in the shorted output port when voltage V_a is applied at the input port. It is given by the product of amplitude responses of both the IDTs as,

$$Y_{21}\big|_{V_b=0} = \frac{I_b}{V_a} = -2P_{13}^a P_{13}^b e^{-jkd} = H_t^a(\omega) H_t^b(\omega) e^{-jkd} \tag{2.38}$$

where superscripts a and b represent the transmitting and receiving transducers respectively. The scattering parameter S_{21} of the two port device with matched resistances R_S and R_L at source and load respectively is written as [11]

$$S_{21} = \frac{2Y_{12}\sqrt{R_S R_L}}{R_S R_L Y_{12}^2 - (1 + Y_{11}R_S)(1 + Y_{22}R_L)}. \tag{2.39}$$

The insertion loss in dB is given by $IL = 20\log|S_{21}|$. Each IDT produces a 3 dB loss in generation and reception of SAW, leading to a total of 6 dB loss as shown in Fig. 2.8b.

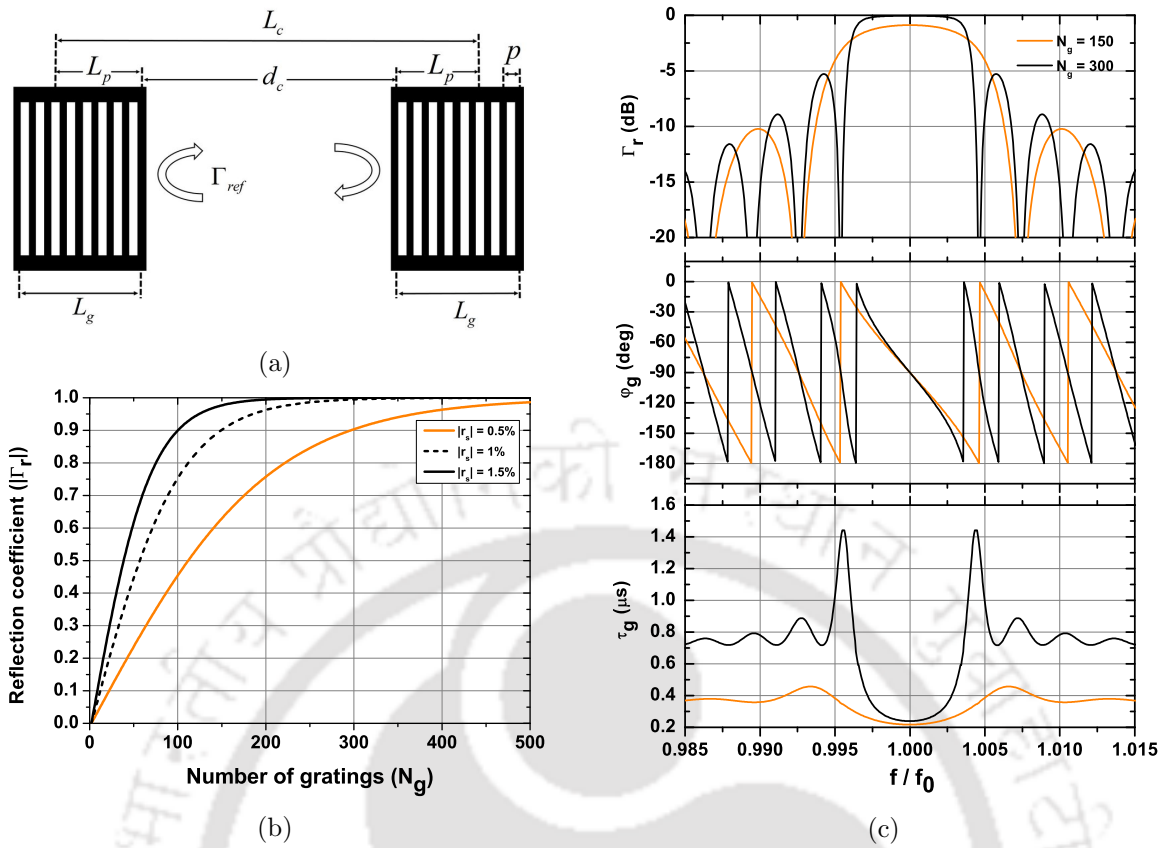

Figure 2.9: (a) Resonant cavity consisting of two identical reflector gratings with shorted metal fingers. (b) Variation in reflection coefficient $|\Gamma|$ with the number of gratings for different values of strip reflection coefficient r_s, considering $\lambda = 20$ µm. (c) Frequency response showing the magnitude, phase and delay of the resonant cavity with $r_s = 1\%$, $\phi_r = -\pi/2$ and $\lambda = 20$ µm for $N_g = 150$ and 300.

2.3.2 Resonant cavity

Similar to optical resonators, the essential requirement of a SAW resonator is a properly designed resonant cavity that can efficiently reflect the waves. A resonant cavity is formed by two reflector gratings, consisting of either shorted fingers, open fingers or grooves made on the substrate. In a grating, each strip reflects weakly, but if there are many strips, the total reflection coefficient can be close to unity when the pitch p is equal to half the wavelength ($p = \lambda/2$) [11]. Fig. 2.9a shows a resonant cavity structure with two identical reflector gratings separated by a distance d_c. Each reflector grating consists of N_g strips with total grating length of $L_g = (N_g - 1)p$. The reflection coefficient of a single finger is denoted by r_s, which typically depends on the height of metal finger and type of the piezoelectric material used as a substrate. Typically r_s is given as, $r_s = |r_s|e^{j\phi_r}$. Its magnitude is typically between 1–3% with phase ϕ_r being $\pm\pi/2$. The reflection coefficient of each grating is given by Γ, and its associated phase is denoted by ϕ_g. As the wave strikes the reflector grating, each strip reflects a certain portion of the energy. The wave is effectively reflected at a penetration depth L_p given by, $L_p = \tau_g v/2$ where τ_g is the delay of the reflected wave. The total length of the resonant cavity, L_c is given by $L_c = 2L_p + d_c$.

The resonance in the cavity can occur only when the wave undergoes a phase shift of 2π during the round trip between the gratings. The condition is given as

$$d_c = (n + \phi_g/\pi)\,\lambda/2. \tag{2.40}$$

At Bragg frequency, $\phi_g = \phi_r = \pm\pi/2$, so the condition for resonance becomes

$$d_c = (n \pm 1/2)\,\lambda/2. \tag{2.41}$$

The reflection coefficient of the grating is calculated using (2.36) as

$$\Gamma = -c_{12}^{*}\frac{\sin(sL_g)}{s\cos(sL_g) + j\delta\sin(sL_g)} \tag{2.42}$$

where $c_{12} = r_s/p$, $s^2 = \delta^2 - |c_{12}^2|$, and $\delta = 2\pi(f - f_0)/v$. At resonance condition $f = f_0$ and $\delta = 0$ then,

$$\Gamma = |\Gamma|e^{j\phi_g} = -\frac{c_{12}^{*}}{j|c_{12}|}\frac{\sin(j|c_{12}|L_g)}{\cos(j|c_{12}|L_g)} = -e^{-j\phi_r}\tanh(|c_{12}|L_g) \tag{2.43}$$

Therefore, $|\Gamma| = \tanh(|c_{12}|L_g) \approx \tanh(r_s N_g)$. It shows that reflection coefficient depends on the number of gratings and reflectivity of each finger. Fig. 2.9b indicates the variation of reflection coefficient with the number of gratings, at resonance, for three different values of r_s with $\lambda = 20$ µm. As the number of fingers in the gratings increase, the reflection coefficient also increases. For $N_g = 200$, $\Gamma = 0.76$, 0.96 and 0.99 is obtained for $r_s = 0.5$, 1 and 1.5 respectively. Typically in a resonator 100-300 fingers are used in the design of reflector grating. The phase of the reflection coefficient ϕ_g and time delay of reflected wave τ_g are given as

$$\tan(\phi_g - \phi_r) = -(\delta/\sigma_k)\tanh(\sigma_k L_g) \tag{2.44}$$

$$\tau_g = -(1/v_f)d\phi_g/d\delta. \tag{2.45}$$

where $\sigma_k = s/j$. Fig. 2.9c shows the variation of magnitude, phase and delay of grating reflection coefficient with normalized frequency for $\lambda = 20$ µm, and $N_g = 150$ and 300. The magnitude of reflectivity $|r_s|$ and phase ϕ_r of each finger is kept at 1% and $-\pi/2$ respectively. The magnitude of reflection coefficient increases with N_g and is maximum at the center frequency f_0. At resonance $f = f_0$, the grating reflection coefficient has the same phase as the reflection coefficient of one finger ($\phi_g = \phi_r = -\pi/2$) because all the possible path lengths of the reflected waves are in multiples of the wavelength. The time delay of the reflected wave is minimum at resonance. Compared to $N_g = 150$, the $N_g = 300$ case shows a much sharper response with a large difference in delay times between center frequency and other frequency components.

2.3.3 One port resonator

One port resonator consists of a transducer placed between two reflector gratings. The device is shown in Fig. 2.10a. The length of the transducer IDT is L_t and the separation between IDT and reflector grating is d_s. When an alternating voltage is applied to the transducer, the IDT

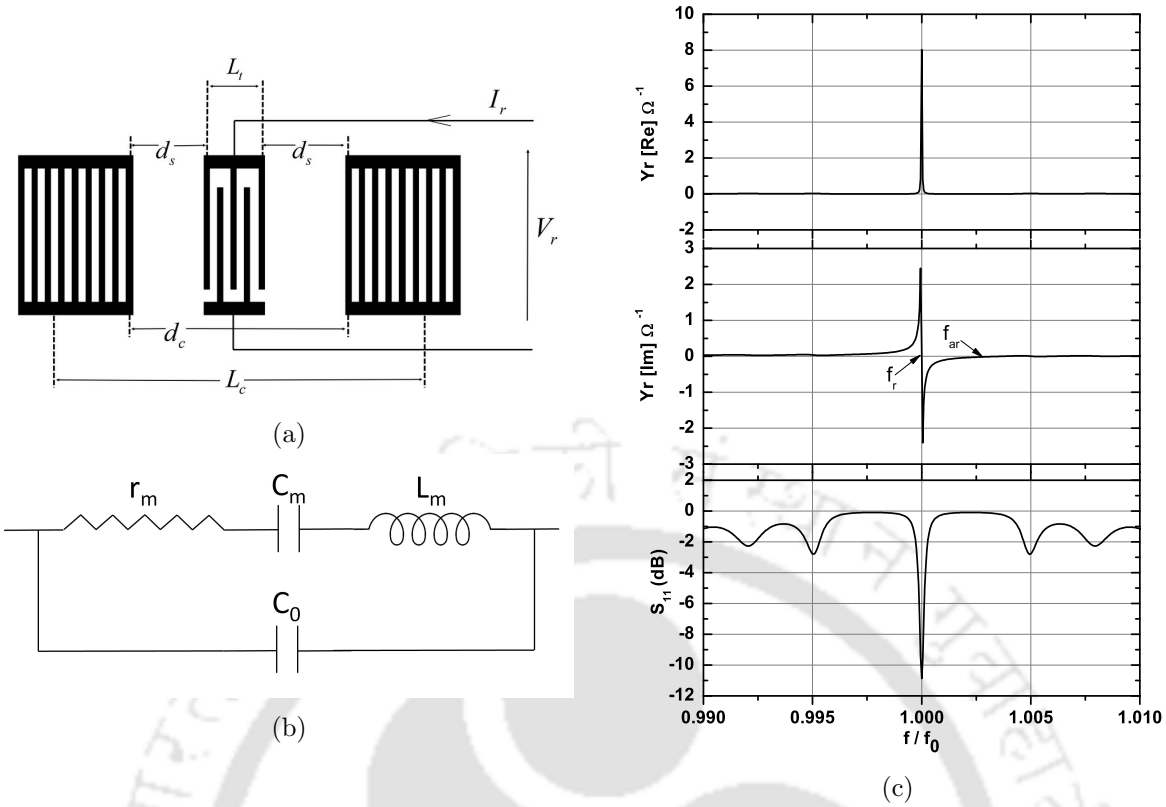

Figure 2.10: (a) Design of one port resonator showing transducer IDT of length L_t, placed in the center of two identical reflector gratings. (b) Equivalent circuit representation of one port resonator. (c) Frequency response of resonator showing the variation of admittance and S_{11} with normalized frequency. Response is obtained for $LiTaO_3$ substrate with $v = 4160\ \mathrm{m\,s^{-1}}$, $\lambda = 20\ \mu\mathrm{m}$, $N_g = 300$, $N_p = 20$ and $r_s = 1\%$. The resonance frequency $f_r = f_0 = 208$ MHz and anti-resonance frequency $f_{ar} = 208.75$ MHz are marked with arrows.

generates SAW in opposite directions, which strike the two gratings on either side, get reflected and create standing waves in the resonant cavity. Fig. 2.10b shows the L-C equivalent circuit representation of one port resonator consisting of a series connection of resistance r_m, motional capacitance C_m and inductance L_m, in parallel with capacitance C_0. The voltage and current applied to the resonator is V_r and I_r respectively. The distance between the reflector gratings is given by $d_c = 2d_s + L_t$. For constructive interference of SAW, d_c is given as

$$d_c = (2n \pm 1/2)\lambda/2, \tag{2.46}$$

which is different from the resonance condition (2.41) given for a resonant cavity. The admittance of one port resonator, $Y_{1P} = I_r/V_r$ is calculated from the P-matrix element P_{33}. Due to the presence of spacing between IDT and reflector grating, the reflection coefficient of the resonant cavity gets modified as, $\Gamma' = \Gamma e^{-2jkd_s}$. The admittance of the resonator is written as [11],

$$Y_{1P} = P_{33} + \frac{4P_{13}^2\Gamma'}{\Gamma'(P_{11} + P_{12}) - 1} \tag{2.47}$$

where P_{33} is the admittance of the isolated transducer (without gratings). The input port reflection coefficient S_{11} is expressed in dB as,

$$S_{11}(\text{dB}) = 20\log_{10}\frac{Y_0 - Y_{1P}}{Y_0 + Y_{1P}} \tag{2.48}$$

where $Y_0 = 0.02\ \Omega^{-1}$ is the characteristic admittance. The real and imaginary parts of Y_{1p} calculated from (2.47) along with S_{11}(dB) are shown in Fig. 2.10c. The frequency at which the Re$\{Y_{1P}\}$ becomes maximum and Im$\{Y_{1P}\}$ crosses through zero is called as the resonance frequency f_r. The second zero crossing of Im$\{Y_{1P}\}$ is called as the anti-resonance frequency f_{ar}. In terms of equivalent circuit representation, the total admittance Y_{1P} is

$$Y_{1P} = j\omega C_0 + \frac{1}{r_m + j\omega L_m + \frac{1}{j\omega C_m}} \tag{2.49}$$

where the individual circuit elements are given as,

$$\begin{aligned} C_0 &\approx C_t \\ r_m &= \frac{1 - |\Gamma|}{2G_a(\omega_r)} \\ L_m &= \left(\frac{L_c}{v}\right)\frac{1}{4G_a(\omega_r)} \\ C_m &\approx 1.8C_0\left(\frac{L_t}{L_c}\right)\left(\frac{\Delta v}{v}\right) \end{aligned} \tag{2.50}$$

where L_c/v is the cavity length in time units and L_t/L_c is the ratio of transducer length to cavity length.

2.3.4 Two port resonator

A two port resonator consists of two identical transducer IDTs placed in between the reflector gratings. The analysis of two port resonator is more complicated than the one-port resonator, but a simplified approach assuming non-reflective and loss-less transducers can be used to represent the device in terms of equivalent circuits [11], [18], [123]. Fig. 2.11a shows a two port resonator. The center of the IDTs is separated by a distance Δ such that the resonance condition given by (2.41) holds. The distance between the reflector gratings is d_c. Voltage V_1 is applied to the left transducer, and the right one is shorted. The admittance of the device can be calculated using the P-matrix relations. P_{33} represents the admittance of each of the transducer without gratings. G_a is the acoustic conductance, and parameter γ is defined as, $\gamma = \Gamma e^{-jkd_c}$. Resonances occur when $\gamma = \pm 1$. The mode is said to be symmetric if $\gamma = 1$ and asymmetric if $\gamma = -1$. For the asymmetric mode, the equations are given as,

$$Y_{11} = P_{33} - \frac{2\gamma G_a}{\gamma + 1}; \qquad Y_{12} = G_a\frac{\gamma - 1}{\gamma + 1} \tag{2.51}$$

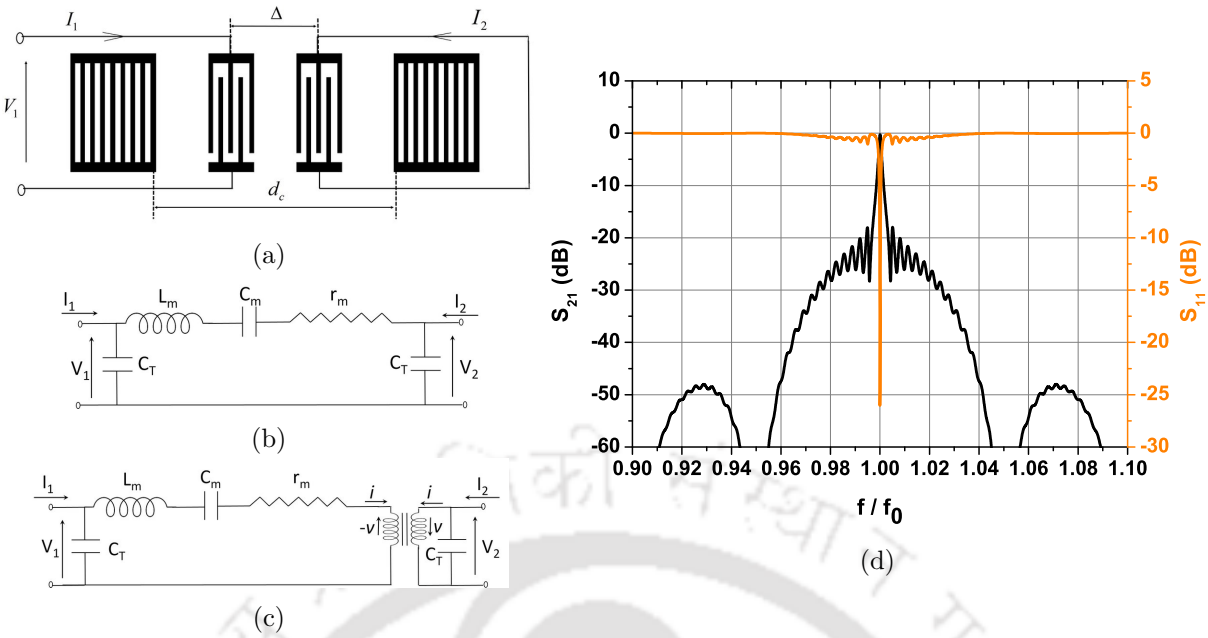

Figure 2.11: (a) Design of a two port resonator showing two identical transducers separated by Δ, placed in between a resonant cavity formed by two identical reflector gratings. Equivalent circuit representation of two port resonator for (b) asymmetric mode and (c) symmetric mode. (d) Typical response of a two port resonator with $N_g = 300$, $N_p = 20$, $\lambda = 20$ µm and $r_s = 1\%$.

and for the symmetric mode

$$Y_{11} = P_{33} + \frac{2\gamma G_a}{1-\gamma}; \qquad Y_{12} = G_a \frac{1+\gamma}{1-\gamma}. \tag{2.52}$$

By symmetry of the design Y_{11}=Y_{22}. Once the Y parameters are known. The S_{11} the device can be calculated as

$$S_{11} = \frac{(1 - R_S Y_{11})(1 + R_L Y_{22}) + R_S R_L Y_{12}^2}{(1 + R_S Y_{11})(1 + R_L Y_{22}) - R_S R_L Y_{12}^2} \tag{2.53}$$

where R_S and R_L are the matched value of resistances connected to the source and load side respectively. S_{21} can be calculated from relation (2.39). The equivalent circuit arrangements for the asymmetric and symmetric modes are shown in Fig. 2.11b and 2.11c respectively. The values of motional capacitance and inductances are calculated from (2.50). For the asymmetric mode, the typical response of two port resonator (S_{21} and S_{22}) with $N_g = 300$, $N_p = 20$, $\lambda = 20$ µm and $r_s = 1\%$ is shown in Fig. 2.11d.

2.4 FEM

The FEM is a numerical technique for solving differential equations associated with almost every discipline of engineering, particularly in the areas of stress/strain analysis of solid structures, heat conduction analysis, and fluid dynamics. The finite element method provides numerical solutions to such problems defined by differential equations. The propagation of SAW governed by differential equations given in (2.9) and (2.10) are solved along with the complexities in the geometry of the device, materials used in the device, and proper boundary conditions.

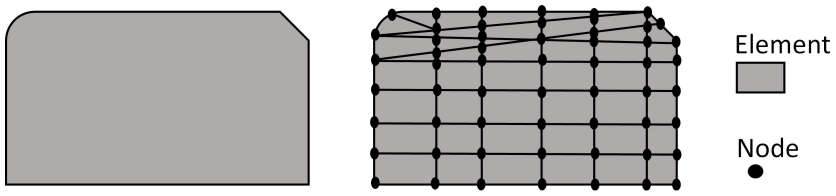

Figure 2.12: FEM involves discretization of problem into small mesh elements and nodes.

This section gives a brief outline of the procedures used in finite element method formulations. The detailed descriptions can be found in [124].

In FEM, 2D or 3D geometry of the structure is first designed. The properties of materials used in the simulation, such as elastic constants, density, Young's modulus, Poisson's ratio, permittivity values and piezoelectric coefficients, etc. are correctly applied. Boundary conditions at the boundaries of the structure are to be provided. For example in case of stress/strain analysis for piezoelectric material, the boundary conditions can be displacement constraints and electrical boundary conditions such as electric potential, charge etc. Further, the geometry domains are to be divided into smaller domains called elements which are connected at specific points called nodes as shown in Fig. 2.12. The elements created in the geometry can be in the shape of triangular, quadrilateral, tetrahedral, or brick depending on the dimensions. The output information in the case of stress/strain analysis in piezoelectric material involves nodal and elemental information, the solution to the primary unknown quantities, the displacements in all directions, and voltage to be determined at nodes. These unknowns are called as degrees of freedom (DOF). The continuum has infinite degrees of freedom, whereas the discretized domain has finite number of DOF, contributing to the name finite element method. In this thesis, the simulations and analysis of SAW devices are carried out by FEM using piezoelectric module of COMSOL Multiphysics software [125]. The software has well developed solvers, graphical user interface (GUI) and post-processing capabilities.

2.4.1 Approximations used in FEM

Consider a one port resonator with IDT and reflector gratings. Typically the length, width, and depth of such a device in terms of wavelength are 500λ, 50λ, and 100λ respectively. For basic accuracy of results in FEM, at least ten linear elements per wavelength are required for meshing the geometry. For piezoelectric problems, there are four unknowns namely three displacement components (u_x, u_y and u_z) and potential (ϕ). So the total number of unknowns in the problem would be $(500\times50\times100)\times(10)\times(4) = 10^8$. Solving such large number of equations is possible only by powerful computers whose cost and time required (to solve) is not justified. Some valid approximations are often needed to reduce the size of the model to a manageable level.

- Reduction of geometry from three to two dimensions: SAW (Rayleigh waves), can be simulated considering only the length and depth of the substrate and ignoring the width because the profile of the wave is similar in the lateral direction.
- Reduction of depth in the model geometry: Since SAW carry energy mostly near the

surface, only 5 to 10 wavelengths of the substrate depth can be considered. It would reduce the number of unnecessary calculations in solving a model with full depth.

- Using periodic and anti-periodic boundary conditions: The IDT consists of a large number of repeating electrodes that emit SAW in either direction. To reduce model geometry infinite periodic boundary conditions with only one wavelength of the wave (λ) or anti-periodic boundary conditions with the half wavelength of the wave ($\lambda/2$) can be used for device characterization.

2.4.2 SAW device simulation using FEM

Finite element (FE) simulation plays a major role in studying the various aspects and characteristics of SAW device before fabrication. Many researchers have reported simulations of different types of SAW devices using FEM. Lerch *et al.* [126] presented a FEM scheme to calculate Eigenmodes and dynamic response to mechanical and electrical excitation of 2D and 3D piezoelectric transducer for any geometry. Abdollahi *et al.* [127] evaluated the mass sensitivity of SAW device considering different piezoelectric materials using 3D-FE simulation by calculating wave propagation speeds and energy distributions. Ippolito *et al.* [128] carried out the FE simulation of a two port SAW delay line device composed of XY-$LiNbO_3$ substrate with ZnO guiding layer to calculate displacements, electromagnetic feed-through, and insertion loss. Wang *et al.* [129] used FEM carry out a study on the effects of change in film properties on the mass sensitivity of SAW sensors. FE simulation was used to simulate SAW delay line device coated with Palladium thin film for H_2 gas sensing [130], [131]. Rahman *et al.* [132] performed FEM simulation to study SAW based quantum devices. Micro-cavities filled with different materials, designed on SH-SAW delay line path for the reduction in insertion loss, improvement in power efficiency and enhancement of mass sensitivity were also studied through simulations and experiments in [133]–[135]. Simulations involving evaluation of mass sensitivity of layer guided SH-SAW (Love wave) devices were also reported in [21], [136], [137].

2.5 FE simulation of SH-SAW resonator

This section presents the results of FE analysis of SH-SAW resonator. Piezoelectric crystals that generate shear waves such as $LiTaO_3$, $LiNbO_3$, and quartz are considered. Firstly, the euler angle representation of the orientation of these crystals is explained. Next, the 3D geometry used for the simulation of the resonator with appropriate boundary conditions and mesh refinement process is described. Analysis of a rotated Y-cut $LiTaO_3$ is performed to study leaky and non-leaky SAW generated by the substrate. Eigenmode study is done to calculate free surface velocity v_f, metallized surface velocity v_m, K^2, and TCF. Lastly, the frequency response of SH-SAW resonator is performed to calculate admittance and total displacement of the device.

2.5.1 Crystal orientation and Euler angles

The orientation of the piezoelectric substrate and its Euler angle representation is of prime importance in the design and modeling of SAW devices as it dictates the material properties and ultimately the device response. The local coordinate axes are represented by (x, y, z) while the crystal axes are denoted by (X, Y, Z). A particular crystal cut is defined by three euler angles (ϕ, θ, ψ) with three consecutive rotations about z, x', and z' as shown in Fig. 2.13a. Initially, the local coordinate axes are aligned with the crystal axes. First rotation is done with respect to the z axis by an angle ϕ creating new local axes as x' and y'. Now the second rotation is done about x' axis by an angle θ generating new axis z'. The last rotation is done about z' axis by an angle ψ. The final orientation of the crystal plane is achieved after completing the three Euler angle rotations. The *line of nodes* N shown in Fig. 2.13a represents the intersection between unrotated and rotated crystal plane.

Four different crystal types that are often used for designing SH-SAW and LW devices are selected for FE simulation and are listed below:

- 36°-YX $LiTaO_3$ represents a Y-cut crystal, rotated by 36° about the crystallographic X axis generates SH wave polarized in the z axis and propagating in the x axis.
- 41°-YX $LiNbO_3$ represents a Y-cut crystal, rotated by 41° about the crystallographic X axis generates SH wave polarized in the z axis and propagating in the x axis.
- 90° rotated AT quartz represents a Y-cut crystal, rotated by 35.25° about the crystallographic X axis, with an additional rotation of 90° along the y axis generating SH wave polarized in the x axis and propagating along the z axis.
- 90° rotated ST quartz represents a Y-cut crystal, rotated by 42.75° about the crystallographic X axis, with an additional rotation of 90° along the y axis generating SH wave polarized in the x axis and propagating along the z axis.

Fig. 2.13b shows an x propagating Y-cut crystal with the cut face perpendicular to the Y direction piezoelectric substrate, rotated by an angle θ about the crystallographic X axis.

Since piezoelectric substrates are anisotropic, their properties change with the orientation of the crystal. Thus, the properties of the piezo-substrate need to be properly implemented in the FEM for different crystal cuts. The properties that need to be input for successful finite element solution are 6×6 stiffness matrix [c], 3×6 piezoelectric matrix [e], 3×3 permittivity matrix [ϵ], and density ρ. When the orientation of the substrate is changed, the density remains unchanged, but all other properties get changed. Elastic, piezoelectric and dielectric constants of crystals viz. $LiTaO_3$, $LiNbO_3$ and quartz, and material properties of ZnO, gold, SiO_2 and polymers used in simulation are listed in Appendix A. The material constants are taken from COMSOL material library and are also available in [116], [138].

There are two ways to implement a particular orientation of the piezoelectric substance in FE software. In the first method, the original non-rotated properties of the substrate are taken and transformed by matrix rotation method using the Euler angles [139]. The process of getting the

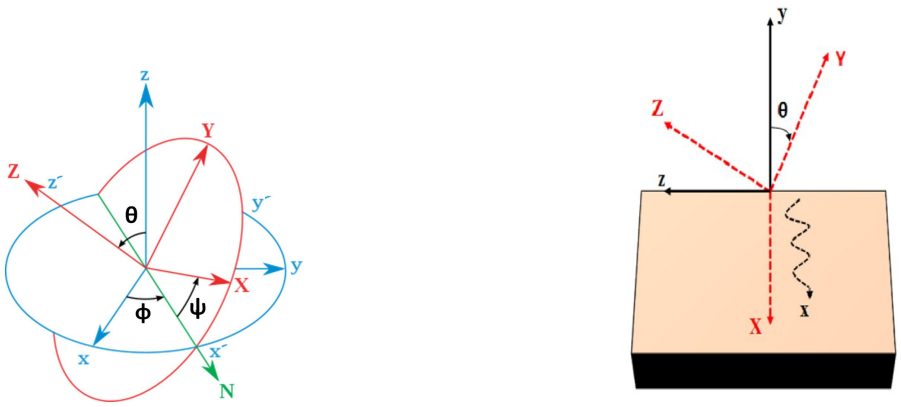

(a) (b)

Figure 2.13: (a) Orientation of piezoelectric crystal cut is defined by three Euler angles (ϕ, θ, ψ). (b) A rotated Y-cut piezoelectric substrate with wave propagating in x axis.

transformed matrices is also explained in detail by Auld [116] and is described in Appendix B. A simple program can be written in MATLAB software for the transformation of the matrices which then can be used as input in FE software. The second and more convenient method involves directly inputting the Euler angles of the piezoelectric substrate in the model geometry. In this thesis, COMSOL was employed for FE simulation, and correct Euler angles were used in the defined *rotated coordinate system* of the simulation geometry.

2.5.2 Simulation geometry and mesh refinement

3D FE simulation is performed for a conventional one port SH-SAW resonator with an infinite number of IDT fingers on a piezoelectric substrate. Owing to the periodic nature of IDT structure, only one finger of the IDT is used in the simulation geometry, and appropriate boundary conditions are applied to the surfaces. A rotated coordinate system is defined by applying the specific Euler angles associated with the piezoelectric substrate. The resonator can be regarded as an infinitely extended periodic structure of which one unit cell is shown in Fig. 2.14a. The resonator operates at a wavelength $\lambda = 12$ µm. Massless aluminum finger of length $\lambda/4$ is made on top of the resonator surface. A substrate depth of 5λ is kept in the simulation with the bottom surface (Γ_{bottom}) kept fixed. A resonator length of $\lambda/2$ is sufficient to perform the simulation by applying anti-periodic boundary conditions across the left and right surfaces (Γ_{left} and Γ_{right}), given as,

$$\begin{aligned} u_l &= -u_r \\ V_l &= -V_r \end{aligned} \tag{2.54}$$

where u_l and V_l are the displacement and potential at the left surface of the geometry respectively, and u_r and V_r denote the displacement and potential at the right surface of the geometry respectively. The front and back surfaces of the geometry (Γ_{front} and Γ_{back}) are applied with periodic boundary conditions, which makes the resonator effectively of infinite aperture. The

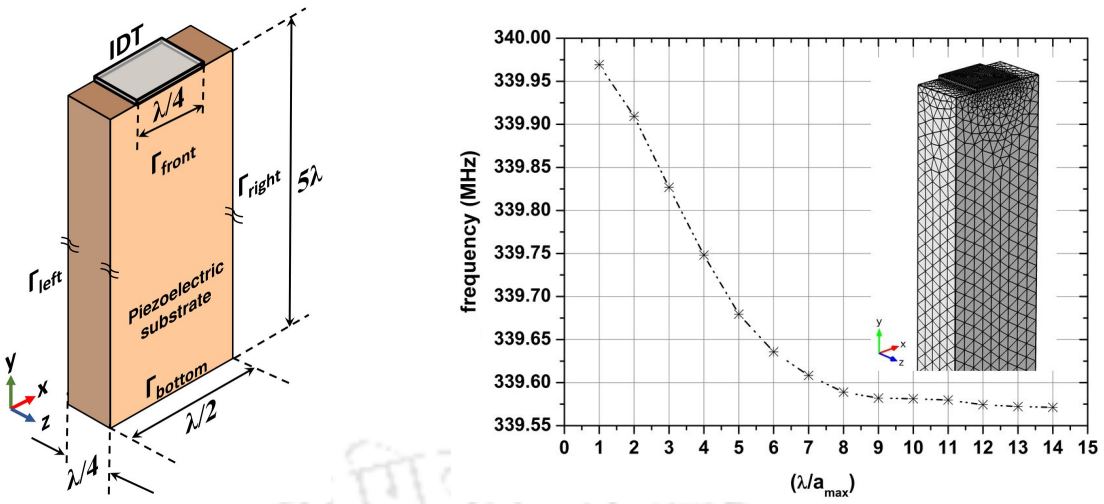

(a) (b)

Figure 2.14: (a) Geometry used for 3D FE simulation of SH-SAW resonator. (b) Graph showing variation in Eigenmode frequency of 36°-YX $LiTaO_3$ based SH SAW resonator with the ratio of wavelength to maximum element size (λ/a_{max}). Meshed geometry for the case when maximum element size is one-tenth of the wavelength is also shown.

expressions for the periodic boundary conditions are given below.

$$\begin{aligned} u_f &= u_b \\ V_f &= V_b \end{aligned} \tag{2.55}$$

where u_f and V_f are the displacement and potential at the front surface of the geometry respectively, and u_b and V_b denote the displacement and potential at the back surface of the geometry.

Eigenmode analysis is used to calculate the natural frequencies of vibration of a given structure. In this case, the external loads (drive voltage) are not applied to the structure with the electrodes kept either shorted or open. It calculates the homogeneous solutions of the differential equations involved and is used as a starting point for other detailed analysis such as transient or frequency response of the device. By applying the open and short circuit conditions at the surface, the Eigenmode study is used to calculate the free and metallized surface velocities of the device, respectively. The electromechanical coupling coefficient K^2 is then computed by (1.2.)

Once the frequency around which the required Eigenmode exists is determined, a parametric sweep of frequencies is done to determine the response of the device around those frequencies. A sinusoidal driving voltage is applied to the electrode, and a steady state response is obtained as an output. The frequency response study calculates the particular solution of the differential equation and is highly useful in determining the resonance frequency, admittance and displacement of the device. The total displacement of SAW is given by $\sqrt{(|u_x|^2 + |u_y|^2 + |u_z|^2)}$ where u_x, u_y, and u_z are the particle displacements in the x, y, and z directions respectively.

The Eigenmode analysis is carried out on the 3D model to study the effect of mesh density on the resonance frequency of the SH-SAW. Free tetrahedral elements are used to mesh the

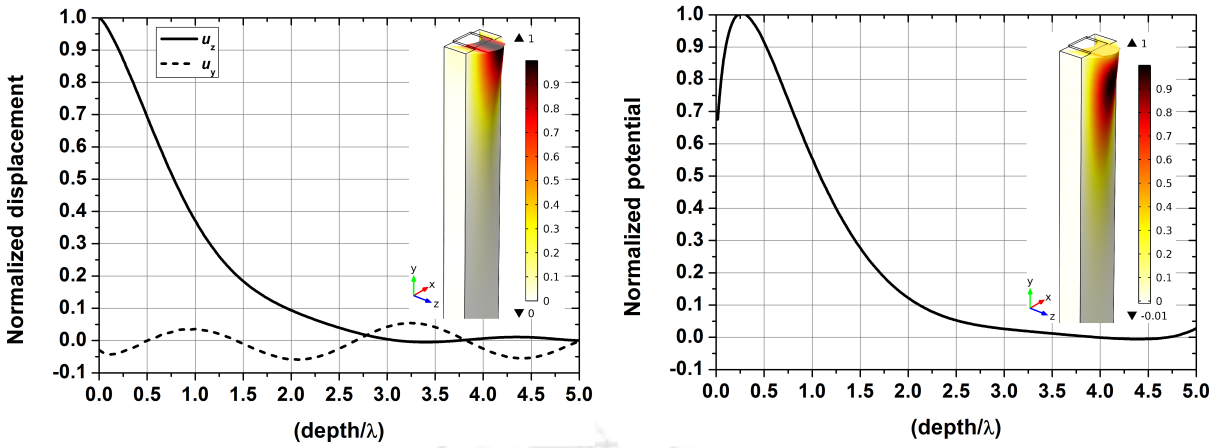

(a) (b)

Figure 2.15: (a) Variation in normalized displacement component u_z and u_y with normalized substrate depth. The 3D profile in the inset shows the normalized total displacement. (b) Variation in potential with normalized substrate depth. The 3D profile in the inset shows the normalized potential.

geometry. A parametric sweep of maximum element size a_{max} is carried out by keeping the other mesh parameters fixed. An element growth rate of 1.2, minimum element size of 10 nm, and resolution of narrow regions is maintained at 0.9. The obtained resonance frequency of SH wave for 36°-YX $LiTaO_3$ substrate is plotted with the ratio of wavelength to maximum element size (λ/a_{max}) as shown in Fig. 2.14b. When a_{max} is large, the geometry is sparsely meshed, and the obtained resonance frequencies are higher. As a_{max} becomes smaller, the meshing becomes denser and resonance frequency values tend to stabilize. The fact that the displacements are maximum near the substrate surface for SAW, the domain is discretized to higher densities near the surface than near the bottom. Also, the electrode regions are meshed to higher degrees of density. When the maximum element size is about one-tenth of wavelength of SAW, the geometry is optimally meshed considering accuracy, time, and memory usage.

Fig. 2.15a presents the variation in normalized displacement (showing shear component u_z and vertical component u_y) with normalized device depth for a 36°-YX $LiTaO_3$ substrate. The displacement profile shows that the device generates SH wave with maximum shear displacement at the surface. Also, the shear displacement component is about 20 times greater than the vertical displacement component. Fig. 2.15b shows the variation in potential with depth of the substrate. The potential becomes maximum at about 0.27λ depth inside the substrate. Both the displacements and the electric potential die down within 2–3 wavelengths, which is typical for a SAW.

2.5.3 FE analysis of a rotated Y-cut $LiTaO_3$ crystal

The variation in mode shape, phase velocity, and coupling coefficient with Euler angle θ for a Y-cut $LiTaO_3$ crystal is studied. The rotated coordinate system was used, and θ was varied from 0° to 180°, to examine the effect of crystal rotation on the substrate velocity. The $LiTaO_3$

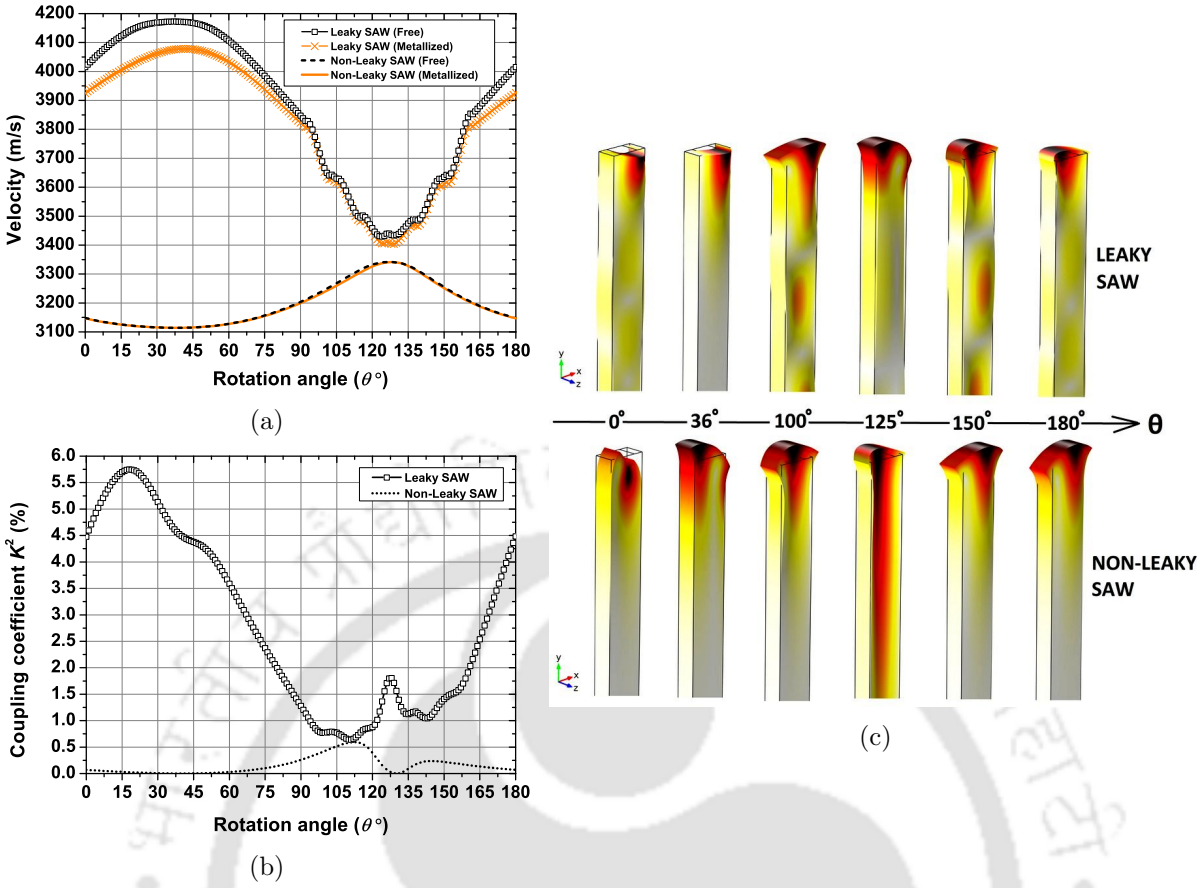

Figure 2.16: Variation in (a) free and metallized surface velocities and (b) electromechanical coupling coefficient with crystal rotation angle θ for leaky and non-leaky SAW modes in the $LiTaO_3$ crystal. (c) Change in the mode shapes of leaky and non-leaky SAW as Euler angle θ is varied from 0° to 180°. At $\theta = 36°$ the leaky SAW is reduced to a near perfect shear horizontal surface wave while the non-leaky SAW at the same angle gets transformed to a Rayleigh wave.

substrate mainly excites two types of wave, one is the dominant leaky SAW with high K^2, and the other is a non-leaky SAW with low K^2. As the rotational angle θ is varied, the free surface and metallized surface velocities for both types of wave vary as shown in Fig. 2.16a. The electromechanical coupling coefficient is calculated using (1.2) and is shown in Fig. 2.16b. A rotation angle of $\theta = 36°$ is widely used in mobile communications and is commercially available for device fabrication because 36°-YX $LiTaO_3$ provides low insertion loss and high coupling coefficient. At $\theta = 36°$ the leaky SAW is reduced to a near perfect shear horizontal surface wave as observed in the mode shape shown in Fig. 2.16c, and the associated free surface velocity and coupling coefficient are 4172 m/s and 4.7% respectively. At $\theta = 125°$, the leaky SAW gets transformed into a Rayleigh type surface wave with a free surface velocity of 3439 m/s and coupling coefficient 1.71%. On the other hand, the non-leaky SAW displays a Rayleigh type behavior at $\theta = 36°$ with a low K^2 of 0.006%, and it changes into a bulk-type shear horizontal wave as θ approaches 125° as shown in Fig. 2.16c. The low K^2 value of non-leaky SAW will cause negligible spurious responses in devices intended to use leaky SH-type surface wave. The results obtained for crystal rotation are listed in Table 2.1 and are consistent with the results reported in [58].

Rotation angle ($\theta°$)	Leaky SAW			Non-Leaky SAW		
	v_m ($\mathrm{m\,s^{-1}}$)	v_f ($\mathrm{m\,s^{-1}}$)	K^2 (%)	v_m ($\mathrm{m\,s^{-1}}$)	v_f ($\mathrm{m\,s^{-1}}$)	K^2 (%)
36	4075	4172	4.7	3115.2	3115.3	0.006
125	3410	3439	1.7	3341	3341.6	0.036

Table 2.1: Free and metallized surface velocities and electromechanical coupling coefficient for leaky and non-leaky SAW in the $LiTaO_3$ SH-SAW device for two unique rotation angles.

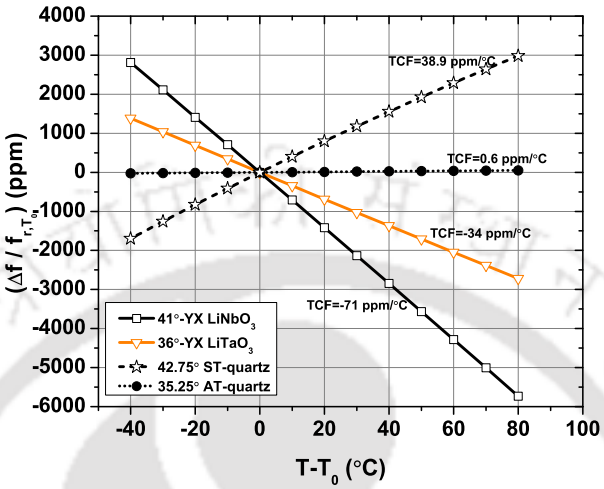

Figure 2.17: Plot showing the variation in relative shift in frequency with temperature for four different substrates.

2.5.4 Eigen frequency and frequency response studies

Eigenmode analysis is performed for $LiTaO_3$, $LiNbO_3$, and quartz based SH-SAW resonator by applying the correct values of Euler angles in the simulation geometry. For each of these devices, metallized velocity v_m and free surface velocity v_f are calculated by applying an electrical short and open boundary conditions at the substrate surface respectively. Table 2.2 shows the four different crystal-cuts with their Euler angles and wave propagation directions. It also shows the calculated and reported values of velocities, coupling coefficient, and TCF. The 41°-YX $LiNbO_3$ and 36°-YX $LiTaO_3$ offer high K^2 calculated values of 18.2% and 4.7% respectively while the 90°-AT and ST quartz have low K^2 of 1.75% and 1.25% respectively.

TCF of the piezoelectric SH-SAW device is calculated by using the relation given in (1.11). The material parameters of the substrate such as the stiffness and piezoelectric constants change with temperature and are given by the relationship [140],

$$C' \approx C_0(1 + \alpha_1(T - T_0)) \tag{2.56}$$

where C' and C_0 refer to the material constant at various temperature of T and room temperature T_0 respectively. The first order temperature coefficient is denoted by α_1, usually given in units of $°C^{-1}$. The material constants of the piezoelectric substrate at room temperature and the first order temperature coefficients are shown in Table A.1 and A.2 of Appendix A respectively. The variation of the relative shift in frequency $(\Delta f/f_{r,T_0})$ is plotted versus the temperature $(T - T_0)$ for different substrates, as shown in Fig. 2.17. The slope of the graph represents the

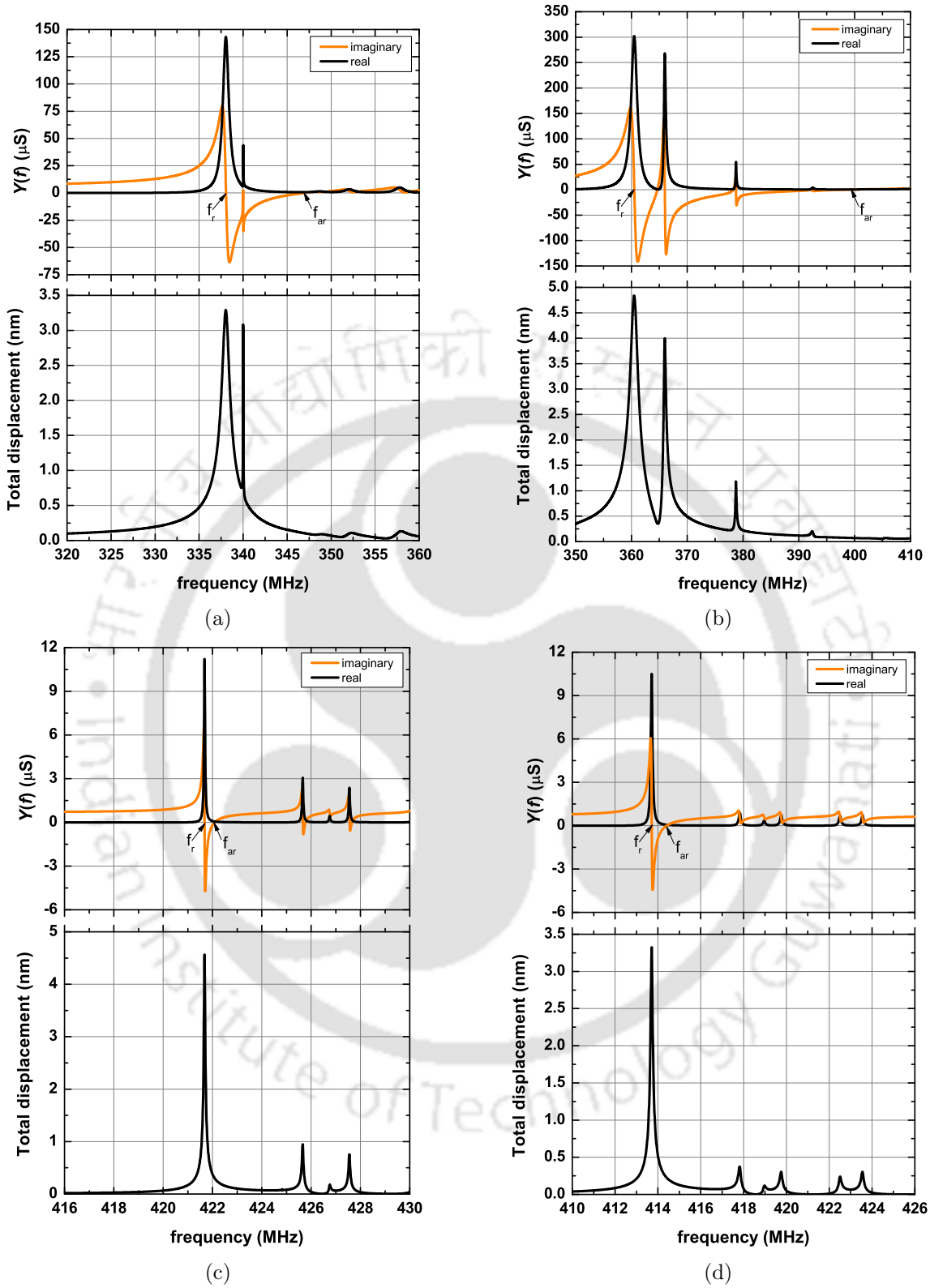

Figure 2.18: Frequency response of SH-SAW resonator showing the admittance and total displacement plots for (a) 36°-YX $LiTaO_3$ with f_r = 338.07 MHz and f_{ar} = 346.95 MHz, (b) 41°-YX $LiNbO_3$ with f_r = 360.53 MHz and f_{ar} = 398.44 MHz, (c) 90°-AT quartz with f_r = 421.69 MHz and f_{ar} = 422.09 MHz, and (d) 90°-ST quartz with f_r = 413.71 MHz and f_{ar} = 414.41 MHz.

Substrate	Propagation	Euler angles(°)	Calculated values				Reported values		
			v_m	v_f	K^2	TCF	v_f	K^2	TCF
		(ϕ, θ, ψ)	($m\,s^{-1}$)	($m\,s^{-1}$)	(%)	($ppm°C^{-1}$)	($m\,s^{-1}$)	(%)	($ppm°C^{-1}$)
36°-YX LT	polarized in z propagating in x	(0,-54,0)	4075	4172	4.7	-34	4160[141]	4.8[11]	-32 to -45[142]
41°-YX LN	polarized in z propagating in x	(0,-49,0)	4375	4813	18.2	-71	4792[11]	17[11]	-70 to -90[143]
90°-AT quartz	polarized in x propagating in z	(0,-125.15,0)	5077	5109	1.25	0.6	5100[18]	1.43[18]	0 to 1[142]
90°-ST quartz	polarized in x propagating in z	(0,-132.75,0)	4980	5024	1.75	38.9	5050[144]	1.89[18]	40[145]

Table 2.2: Calculated and reported values of velocities, coupling coefficient and TCF for different substrates along with their associated Euler angles and wave propagation direction.

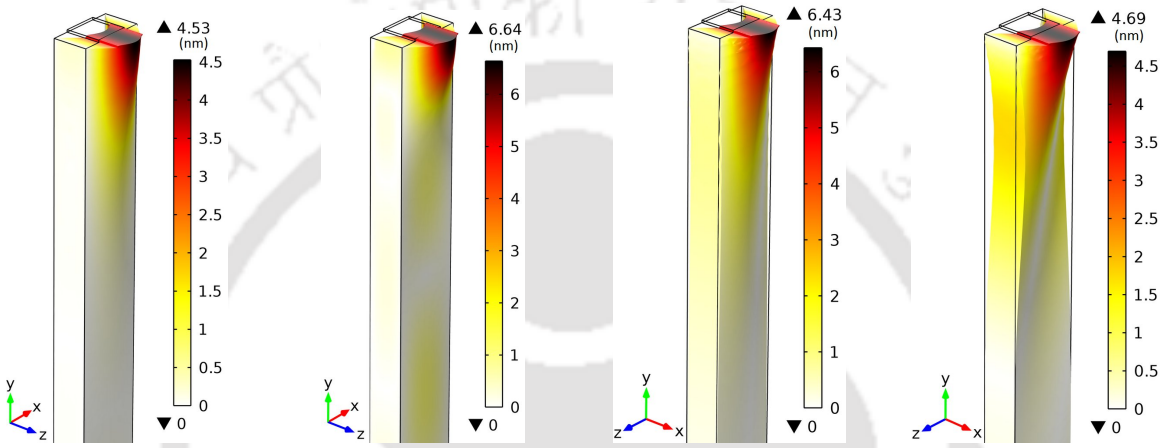

(a) (b) (c) (d)

Figure 2.19: Total displacement profile (in nm) of the SH-SAW mode at resonance frequency f_r, obtained through frequency response is shown for (a) 36°-YX $LiTaO_3$, (b) 41°-YX $LiNbO_3$, (c) 90°-AT quartz and (d) 90°-ST quartz.

TCF value. $LiNbO_3$ and $LiTaO_3$ possess high K^2 but have poor TCF with large negative values of -71 $ppm°C^{-1}$ and -34 $ppm°C^{-1}$ respectively. ST quartz is also very sensitive to temperature variations and has large positive TCF of about 40 $ppm°C^{-1}$. Although the coupling coefficient of AT quartz is lowest in comparison to other crystals, it has the highest thermal stability and thus can offer high mass sensitivity and better LOD [9].

Frequency response is performed for the SH-SAW resonator. For each of the four piezoelectric substrates, the frequency is varied in steps of 0.01 MHz to calculate admittance $Y(f)$, and the total displacement of the device. The frequency at which the $\mathrm{Re}\{Y(f)\}$ becomes maximum and the $\mathrm{Im}\{Y(f)\}$ crosses through zero is called as the resonance frequency f_r while the corresponding second zero crossing of $\mathrm{Im}\{Y(f)\}$ is called as the anti-resonance frequency f_{ar}. Fig. 2.18 shows the frequency response of 36°-YX $LiTaO_3$, 41°-YX $LiNbO_3$ and AT/ST quartz substrates with the calculated admittance and total displacement of SH-SAW resonator. The resonator operates at a wavelength of 12 µm. For 36°-YX $LiTaO_3$ substrate, the f_r and f_{ar} are obtained at 338.07 MHz and 346.95 MHz respectively, and for 41°-YX $LiNbO_3$, the corresponding values are 360.53 MHz and 398.44 MHz. The 90°-AT quartz substrate offers the f_r and f_{ar} at 421.69 MHz and 422.09 MHz respectively, and for 90°-ST quartz the, corresponding values

are obtained at 413.71 MHz and 414.41 MHz. The total displacement profile of the SH wave for different piezoelectric substrates at the resonance frequency is shown in Fig. 2.19. For 36°-YX $LiTaO_3$ and 41°-YX $LiNbO_3$ substrates, the y axis is normal to the substrate surface (Y-cut), with wave polarized in the z axis and propagating along the x direction. On the other hand, the 90°-AT/ST quartz substrates are also Y-cut with wave polarized in the x axis and propagating along the z direction

2.6 FE simulation of SH-SAW delay line

This section presents the SH-SAW delay line characteristics considering 36°-YX $LiTaO_3$, 41°-YX $LiNbO_3$, and 90°-AT/ST quartz substrates. Firstly, the simulation geometry and its associated boundary conditions are described. Next, time response simulation is performed to study the variation in voltage and displacement. The electrostatic solver is used to compute the charge density on the surface of IDT and the substrate. Lastly, the impulse response of SH-SAW delay line is used to calculate and compare the insertion loss values obtained for different substrates.

2.6.1 Simulation geometry

The 3D geometry used for simulation of the SH-SAW delay line is shown in Fig. 2.20a. Massless input and output IDT fingers of aluminum with zero thickness and 3 µm width are made on the piezoelectric substrate that generates SAW of $\lambda = 12$ µm. The center-to-center separation L between the input and output IDT is 5λ. The delay line path length D is 39 µm. Periodic boundary conditions are kept along the z axis to realize IDTs of an infinite aperture that helps to minimize the size of simulation geometry.

A critically damped region of size 2λ is made on the either sides and bottom of the device so that no reflections occur from the edges of the device. The damping ratio at resonance ζ_r is given by

$$\zeta_r = \frac{A_{dm} + B_{dk}\omega^2}{2\omega} \tag{2.57}$$

where ω is the angular frequency of operation and A_{dm} and B_{dk} are the mass and stiffness damping parameters respectively [146]. The critical damping ($\zeta_r = 1$) can be achieved by keeping $A_{dm} = 0$ and $B_{dk} = 1/\pi$f where f is the frequency of operation. The even fingers of input IDT are connected and given a sinusoidal input voltage of $V_{in} = 5\sin(\omega t)$ while the odd fingers are connected and grounded. The even fingers of output IDT are connected and are used as output terminal V_{out} while the odd fingers are connected and grounded. The time response is obtained for 50 ns with a time step of 1 ps. The total displacement of SAW is given by $\sqrt{(|u_x|^2 + |u_y|^2 + |u_z|^2)}$ where u_x, u_y, and u_z are the particle displacements in x, y and z directions respectively. The insertion loss of the device is calculated by taking Fourier transform of the impulse response as per the equation (1.5). A mesh refinement study was performed by plotting the magnitude of the maximum stable output voltage V_{out} (at t > 40 ns)

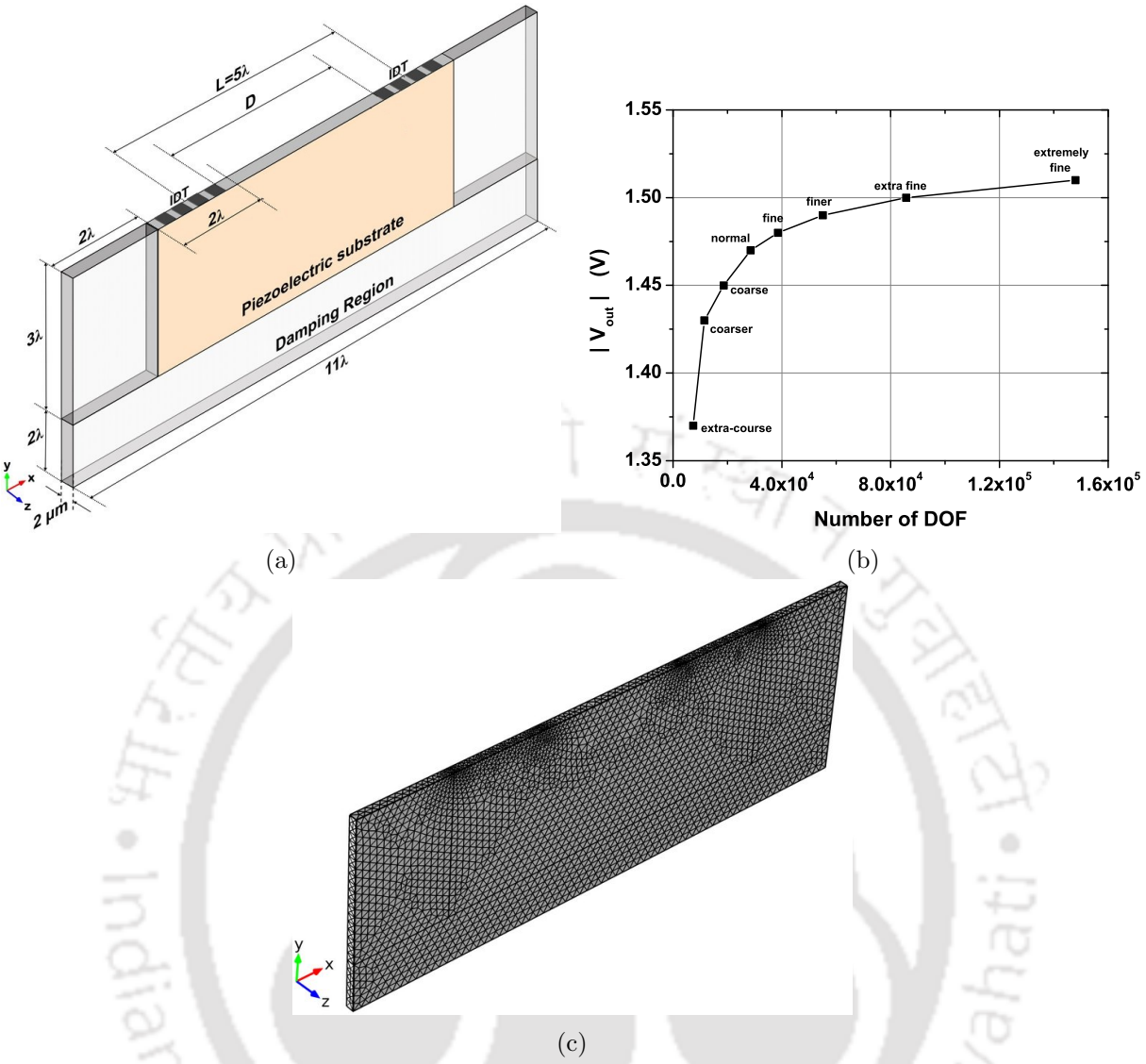

Figure 2.20: (a) 3D simulation geometry of a SH-SAW delay line device. (b) Mesh refinement study showing the plot of magnitude of the maximum stable output voltage V_{out} (at t > 40 ns) versus number of degrees of freedom (DOF) for the device obtained by progressively increasing the physics-controlled mesh from *extra-coarse* to *extremely-fine*. (c) Geometry meshed using the *extra-fine* option.

versus number of degrees of freedom (DOF) of the device obtained by progressively increasing the physics-controlled mesh from *extra-coarse* to *extremely-fine*. The output voltage value tends to stabilize as DOF increases and the convergence of the solution was observed with respect to the mesh refinement. Considering time, memory usage and sufficient accuracy of the simulation, an extra-fine mesh of tetrahedral elements is kept resulting in about 11000 elements and more than 80000 solvable degrees of freedom during simulation. The minimum element quality of the 3D mesh was above 0.1. Fig. 2.20b and 2.20c show the mesh-refinement plot and the meshed geometry, respectively.

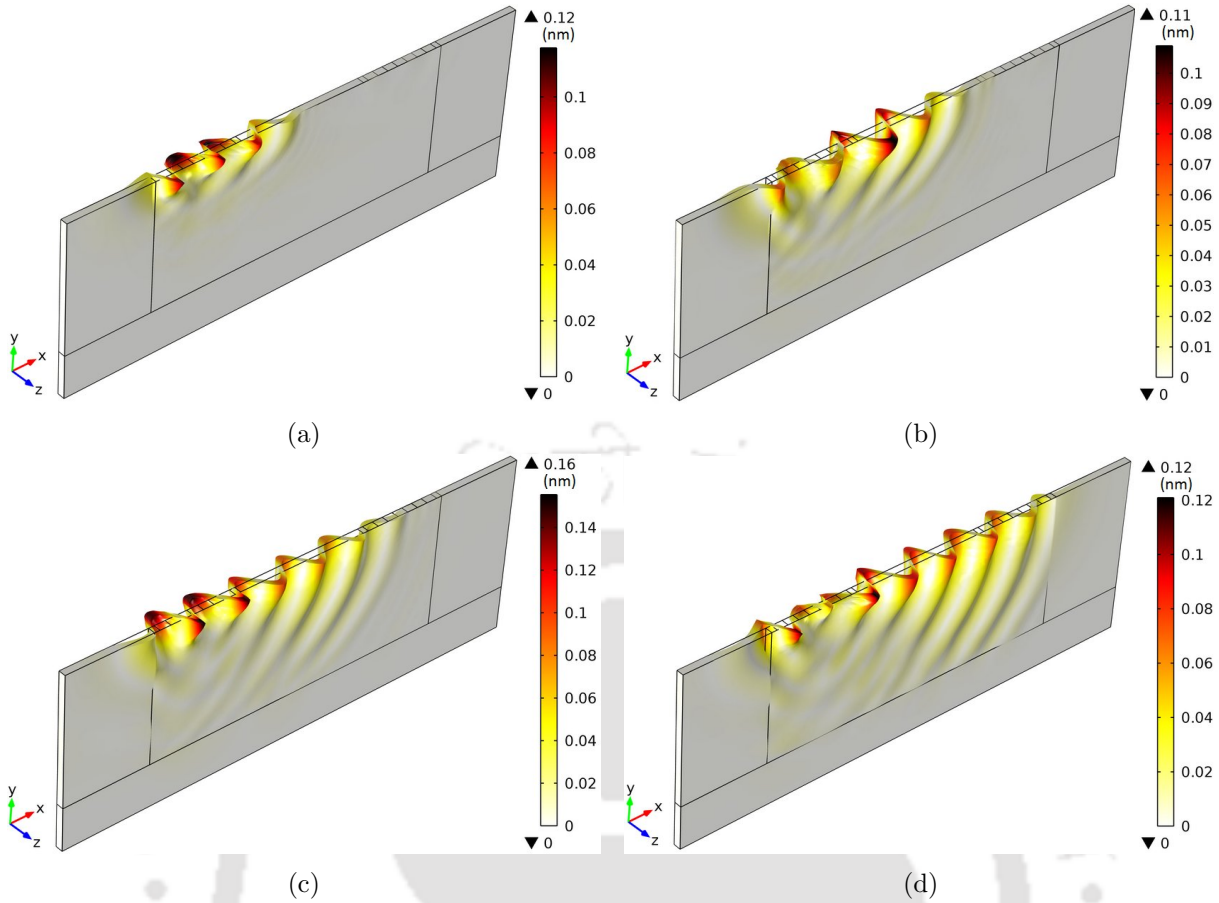

Figure 2.21: Time response simulation showing displacement profile and propagation of SH-SAW at (a) 4 ns (b) 8 ns (c) 12 ns, and (d) 16 ns for 36°-YX $LiTaO_3$ substrate.

2.6.2 Time response

Time response simulation showing the 3D displacement profile and propagation of SH-SAW at different times for 36°-YX $LiTaO_3$ is shown in Fig. 2.21. The wave is generated at the input IDT, travels through the delay line path in shear horizontal manner and reaches the output IDT. The damping conditions at the boundaries of the device ensure that the reflection from edges is minimized and does not affect the propagation of the wave. The variation of shear displacement component, vertical displacement component and voltage with time for a SH-SAW delay line device considering different substrates is shown in Fig. 2.22a, 2.22b, and 2.22c respectively. The SH nature of the wave is confirmed from the observation that the shear displacement components are larger than the vertical displacement components as shown in Fig. 2.22a and 2.22b. Different input frequency is applied to each of the substrate, depending on the shear velocity supported by the crystal (Table 2.2) to achieve SH-SAW of wavelength of 12 µm. Application of sinusoidal input of 5 V at the input IDT results in the generation of a stable sinusoidal voltage at the output IDT. The 41°-YX $LiNbO_3$ substrate generates a maximum sinusoidal output voltage of 4.8 V while 36°-YX $LiTaO_3$ produces an output voltage of 1.5 V. Quartz crystals generate very less output voltage of 0.03 V because of large insertion losses. Table 2.3 lists the values of maximum output voltage, shear and vertical displacement, charge density and minimum insertion loss of each of the substrates. Although all these crystals generate wave with particle displacements

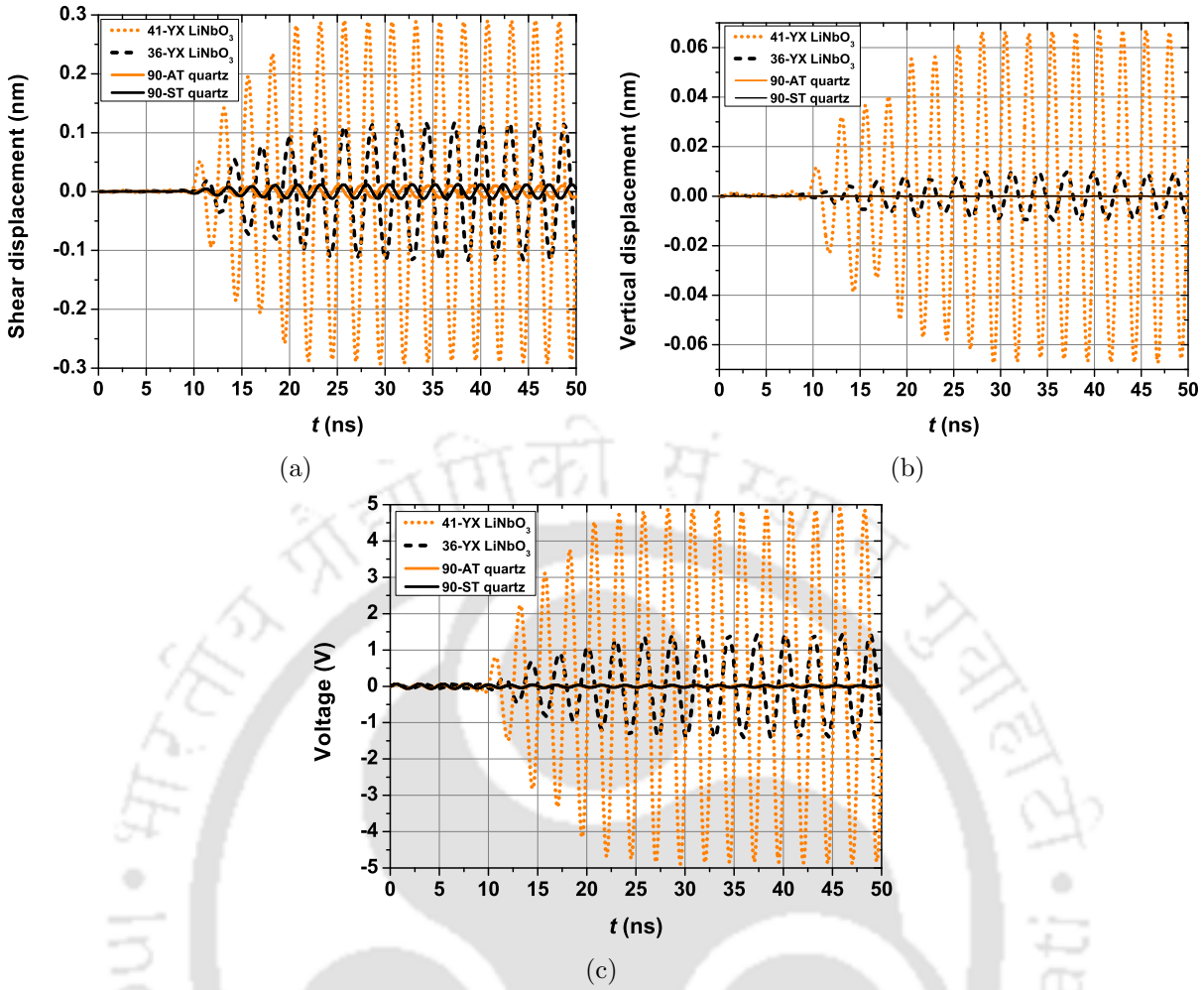

Figure 2.22: Time response of SH-SAW delay line device showing variation in (a) shear displacement component, (b) vertical displacement component, and (c) output voltage with time for different substrates.

mainly of SH nature, it can be noted that the difference between SH and vertical displacements is much greater for ST and AT substrates. Thus, ST and AT substrates generate a much purer SH wave than $LiTaO_3$ and $LiTaO_3$ substrates.

2.6.3 Charge density

For calculation of charge density, a simulation geometry similar to Fig. 2.20a was considered with IDT fingers designed on the entire delay line path. Electrostatic stationary solver was used to calculate the charge density by applying alternating voltages of 1 V and 0 V on the fingers of IDT. Fig. 2.23 shows the spread of static charge density across the length of the device. The charge density on the IDT finger is either positive or negative, depending on the polarity of the applied voltage on each finger. It is noted that the charge density is maximum near the electrode edges and diverges as $1/\sqrt{(x)}$ [123]. Since coupling coefficient of $LiNbO_3$ is largest, it provides the highest charge density, followed by $LiTaO_3$. ST/AT quartz generates a low value of charge density because of their low K^2 values [11].

Substrate	V_{out} (V)	Shear displacement (nm)	Vertical displacement (nm)	IL_{min} (dB)	Charge density ($\mu C\,cm^{-2}$)
36°-YX $LiTaO_3$	1.5	0.12	0.01	-27.1	200
41°-YX $LiNbO_3$	4.8	0.29	0.07	-15.6	250
90°-AT quartz	0.031	0.010	5.8×10^{-5}	-37.8	20
90°-ST quartz	0.030	0.012	4.3×10^{-5}	-38.4	19.5

Table 2.3: Maximum values of output voltage, shear displacement, vertical displacement, charge density, and minimum insertion loss obtained for SH-SAW delay line device considering different substrates.

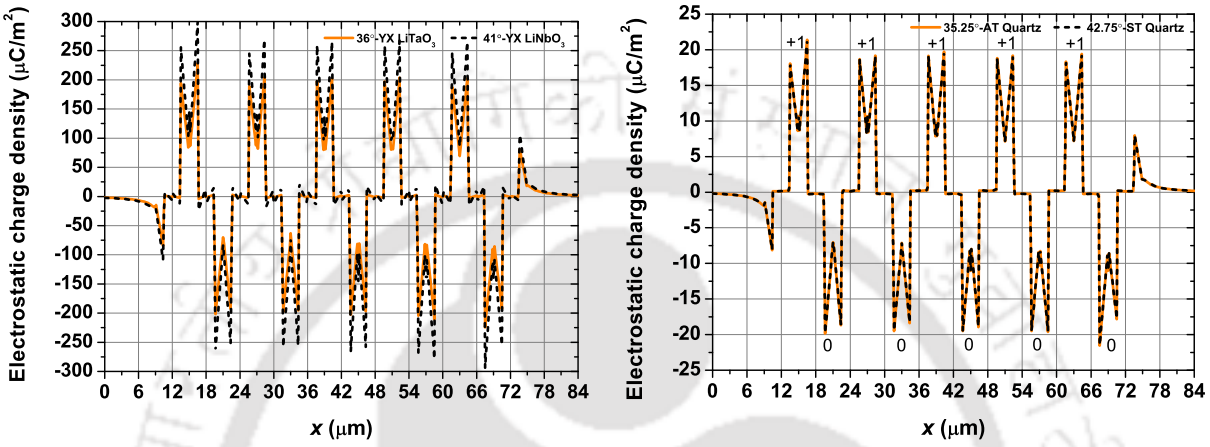

(a) (b)

Figure 2.23: Variation in electrostatic charge density with device length for (a) 36°-YX $LiTaO_3$ and 41°-YX $LiNbO_3$ and, (b) 90°-AT quartz and 90°-ST quartz.

2.6.4 Insertion loss

The input IDT is excited with a unit impulse input of 1.5 ns duration. Fig. 2.24a shows the impulse response of the device. The electromagnetic feed-through effect seen at the beginning of the impulse response is about 100 times less than the applied unit impulse signal. The feed-through can be further reduced if device length is increased, but it would enhance the number of elements required for meshing, thus increasing the time and memory usage. The frequency response of the delay line was obtained by taking the Fourier transform of the impulse response voltage at the output IDT and is shown in Fig. 2.24b. Since the time response simulation contained a limited number of data points, the frequency response signal was improved by zero padding the output voltage signal [127]. The 41°-YX $LiNbO_3$ substrate gives a minimum IL of -15.6 dB while 36°-YX $LiTaO_3$ provides a minimum IL of -27.1 dB. In comparison, the ST/AT quartz because of their poor K^2, gives large IL of about -38 dB. The obtained results of IL of SH-SAW device is consistent with results reported in [147], [148]

2.7 Summary

In this chapter, a brief introduction to basics of piezoelectric constitutive equations and modeling of SAW devices using delta function model, impulse response model, equivalent circuit

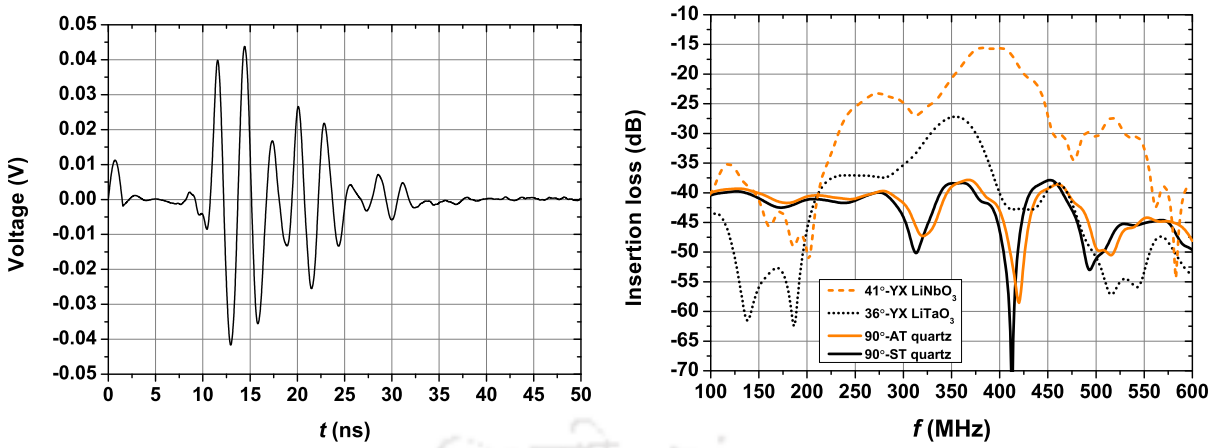

(a) (b)

Figure 2.24: (a) Impulse response of 36°-YX $LiTaO_3$ SH-SAW delay line. (b) Comparison of insertion loss of SH-SAW delay line devices considering different substrates.

model and P-matrix based COM model is presented. Assuming loss-less non-reflective transducers, SAW delay line, resonant cavity, and one and two port resonators were modeled using the useful P-matrix based approach. It helps to calculate the frequency response and admittance characteristics of the device by designing an appropriate number of IDT finger pairs and reflector gratings. The chapter also presented a brief outline of FEM based simulation technique describing the basic principle, limitations, approximations and boundary conditions used for simulation of the structure.

FE simulation of SH-SAW resonator and delay line was performed using COMSOL Multiphysics software by applying appropriate boundary conditions and Euler angles to the simulation geometry. The rotation of a Y-cut $LiTaO_3$ crystal by an angle θ about the crystallographic X axis is investigated using FE simulation. The Leaky SAW has high coupling coefficient than the non-leaky SAW. Leaky SAW at $\theta = 36°$ takes the form of a near perfect shear horizontal surface wave which gets transformed to a Rayleigh type wave at $\theta = 125°$. Eigenmode analysis of SH-SAW resonator based on 36°-YX $LiTaO_3$, 41°-YX $LiNbO_3$, 90°-AT quartz, and 90°-ST quartz was performed to calculate surface velocities, coupling coefficient, and TCF of the device. Quartz based devices suffer from low coupling coefficient but offer high phase velocities. 90°-AT quartz provides the highest temperature stability. $LiNbO_3$ substrate gives highest K^2 but has the least temperature stability. The frequency response of SH-SAW resonators considering different substrates was performed to study the mode shape and to calculate the total displacement and admittance of device. Simulations of SH-SAW delay line was carried out to investigate the wave propagation, time response and electrostatic charge density of the device. The insertion loss of SH-SAW delay line was calculated for different substrates and compared. $LiNbO_3$ gives the lowest insertion loss followed by $LiTaO_3$. Quartz because of low their K^2 values suffer from high insertion losses.

Chapter 3

Finite element analysis of Love wave devices

> Every once in a while, a new technology, an old problem, and a big idea turn into an innovation.
>
> Dean Kamen

The Love wave (LW) devices were introduced in section 1.4.8. A LW device essentially consists of a guiding layer present on a substrate that generates SH-SAW. This chapter presents basic operation and principle of working of the LW device, analytical calculations of phase velocity, group velocity and mass sensitivity by solving the dispersion equation of LW, and 3D FE simulation of LW resonator to calculate mass sensitivity and coupling coefficient for the first two modes. Different guiding layers such as SiO_2, gold, ZnO, SU-8, PMMA and polyimide are considered, and the results of FE simulation are compared with the analytically obtained values. Selection of appropriate guiding layer is necessary for the proper design of LW device, and a comparison between different layers is presented. The frequency response of LW device along with depth displacement calculation for mode-0 and mode-1 is carried out. Comparison of SiO_2 based LW device considering different substrates such as 36°-YX $LiTaO_3$, 41°-YX $LiNbO_3$, 90°-AT quartz and 90°-ST quartz is performed by calculating the variation in S_f, K^2 and TCF with the thickness of guiding layer. Lastly, 3D FE simulation of SiO_2 based LW delay line is performed to calculate the time response, mass sensitivity, and insertion loss. The mass sensitivity of delay line device is calculated by applying incremental surface mass density on the surface and noting the corresponding values of time and phase delays in the output voltage. The insertion loss of delay line is obtained by taking the FFT of the impulse response of the delay line device. The variation in minimum insertion loss of device with SiO_2 and PMMA guiding layer thickness is also studied.

3.1 Love wave

LW is an elastic wave that propagates in a layered structure consisting of a substrate and a guiding layer on top of it. LW has pure shear horizontal vibrations with particle movement parallel to the surface and perpendicular to the wave propagation direction (perpendicular to the sagittal plane) [104]. The propagation of LW is possible only if the shear velocity in the layer is less than the shear velocity in the substrate. Thus, LW is a type of shear horizontally polarized wave that can be produced in an SSBW device or leaky SAW device when an overlayer with an acoustic shear velocity less that in bulk is deposited on the surface of the substrate [68]. The guiding layer slows down the propagating acoustic shear mode, thus decreasing the penetration depth and confining the energy of the wave in the layer.

The variation in the power flow of the fundamental LW mode as a function of the guiding layer thickness is shown in Fig. 3.1. LW device consists of a piezoelectric substrate with IDT fabricated on the surface. A guiding layer of thickness h is coated on top of the device. When the thickness of the guiding layer is much smaller than the wavelength ($h \ll \lambda$), most of the wave energy is located in the piezoelectric substrate, and the LW propagates with a velocity close to the velocity in the substrate. When thicker layers are applied, with thickness still smaller than the wavelength ($h < \lambda$), the energy is concentrated in the overlayer, and the velocity of LW tends towards the velocity in the layer. At a certain thickness, the wave is maximally confined in the layer, with a large normalized wave amplitude (normalized to the total energy of the wave) at the surface [149], [150]. This thickness corresponds to the maximum mass sensitivity of the device. The guiding layer not only confines the wave energy to the surface and increases mass sensitivity but also serves to lower the insertion loss of the device. In addition, the guiding layer shields the metal electrodes from the liquid medium typically used for biosensing. SiO_2, ZnO, gold and polymers are often used as guiding layer in LW sensors.

Piezoelectric substrates like 36°-YX $LiTaO_3$, 41°-YX $LiNbO_3$, 90°- ST and AT quartz are some of the crystals that generate SH wave [9]. Quartz substrates generate pure SH wave, provide good temperature stability and high mass sensitivity, but they suffer from low K^2 and high insertion losses. $LiNbO_3$ has high coupling coefficient but has poor thermal stability. 36°-YX $LiTaO_3$ provides better thermal stability than $LiNbO_3$, sufficiently high K^2 (higher than quartz but lower than $LiNbO_3$), and lower insertion loss in comparison to quartz substrates [77], therefore it is often preferred for designing LW sensors.

3.2 Theoretical background

Analytical modeling and FEM are often used to calculate the mass sensitivity of a LW device. An approximate formula for mass sensitivity of Love mode gravimetric sensors assuming a non-piezoelectric semi-infinite substrate was first given by Wang *et al.* [151] using the dispersion equation of LW. McHale *et al.* [152] used the Maxwell model of viscoelasticity to derive the theoretical sensitivity of LW and layer-guided SH-APM sensors considering polymer guiding layers. Liu *et al.* [153] presented a general dispersion equation of LW devices for analytical investiga-

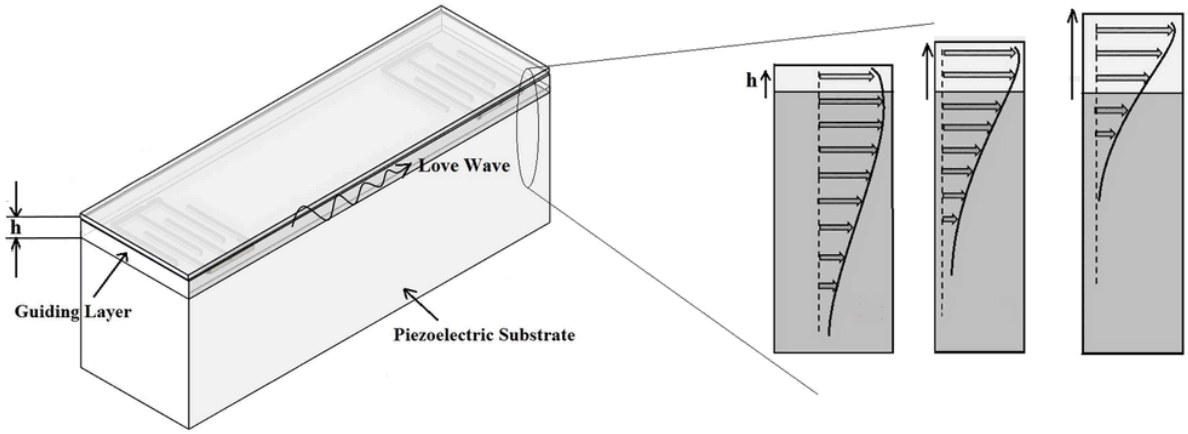

Figure 3.1: Schematic representation of LW device showing the power flow in the guiding layer and piezoelectric substrate as a function of the guiding layer thickness (adapted from [149]).

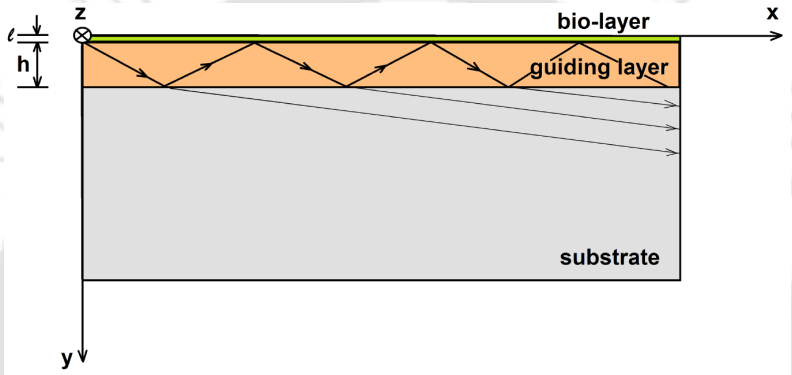

Figure 3.2: The configuration of the Love wave device showing the guiding layer and mass loading bio-layer (adapted from [150]).

tion of phase velocity, electromechanical coupling coefficient and mass sensitivity of a layered structure with SiO_2 on quartz substrate. Abdollahi *et al.* [127] evaluated the mass sensitivity of SAW devices considering different piezoelectric materials by calculating wave propagation speeds and energy distributions through 3D FE simulation. Calculation of mass sensitivities of LW devices using wave velocity and displacements obtained from FE simulation have also been reported in [21], [136].

The configuration of the Love wave device is shown in Fig. 3.2. It shows a semi-infinite substrate of density ρ_s overlaid with a guiding layer of thickness h and density ρ_l. The y axis is normal to the surface of the substrate, and the wave propagates in the x direction with SH displacement in the z direction. The phase velocity and mass sensitivity of the Love wave device depend on the density and thickness of the guiding layer present on the substrate. The dispersion equation of Love wave is given as [151]

$$\tan(\beta_l h) = \frac{\mu_s}{\mu_l}\sqrt{\frac{1-(v_p^2/v_s^2)}{(v_p^2/v_l^2)-1}} \tag{3.1}$$

where μ_s and v_s are the shear modulus and shear velocity of the substrate while μ_l and v_l are the

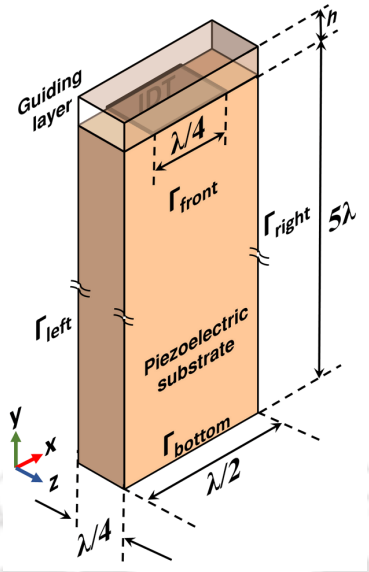

Figure 3.3: Geometry used for 3D FE simulation of Love wave resonator.

corresponding values of the guiding layer. The phase velocity of the LW and angular frequency of the propagating wave in the layered media are denoted by v_p and ω, respectively. β_l and β_s are the transverse propagation constant of the waveguiding layer and substrate respectively given as

$$\beta_l = \sqrt{\frac{\omega^2}{v_l^2} - \frac{\omega^2}{v_p^2}} \qquad \beta_s = \sqrt{\frac{\omega^2}{v_p^2} - \frac{\omega^2}{v_s^2}} \tag{3.2}$$

The required condition for LW mode propagation is that β_l and β_s should be real and $v_s \geq v_p \geq v_l$. Once the phase velocity of Love wave is obtained by solving the dispersion equation, the group velocity v_g is calculated by the relation [141]

$$v_g = v_p \left(1 + \frac{h/\lambda}{v_p} \frac{dv_p}{d(h/\lambda)}\right) \tag{3.3}$$

In the sensor configuration shown in Fig. 3.2, a uniform thin film representing a chemical or biological species of thickness l, density ρ_b and shear velocity v_b present on the waveguiding layer causes mass loading of the device. Mass sensitivity S_f is obtained from the relative change in frequency as a result of the deposition of incremental mass per unit area Δm uniformly distributed on the sensor surface [67] as

$$S_f = \lim_{\Delta m \to 0} \left(\frac{\Delta f / f_0}{\Delta m}\right). \tag{3.4}$$

where f_0 is the unperturbed frequency of the device and $\Delta f = f - f_0$ is the change in the frequency due to the mass loading of the thin film. If the thickness of mass loading layer is much less than the SAW wavelength, then first-order perturbation theory can be applied by ignoring the elastic effects of the thin mass loading layer ($v_b = 0$), to get the theoretical mass sensitivity of the

device given by [151]

$$|S_m| = \frac{1}{\rho_l h}\left(1 + \frac{sin(\beta_l h)cos(\beta_l h)}{\beta_l h} + \frac{\rho_s}{\rho_l}\frac{cos^2(\beta_l h)}{\beta_s h}\right)^{-1} \tag{3.5}$$

3.3 Love wave resonator

The 3D FE simulation of a LW resonator, composed of a guiding layer made on 36°-YX $LiTaO_3$ substrate is performed using COMSOL software. The resonator operates at a wavelength of $\lambda = 12$ µm and can be considered as an infinitely extended periodic structure of which one unit cell is shown in Fig. 3.3. Periodic and anti-periodic boundary conditions are applied along the z and x axes respectively with bottom boundary kept fixed. Massless aluminum IDT of zero thickness and 3 µm finger width is made on the piezoelectric substrate. Since the wave is confined mostly to one-wavelength depth, a substrate depth of 5λ is used in the simulation. SiO_2, ZnO, gold, PMMA, polyimide and SU-8 are considered as guiding layers, and their material properties are listed in Table A.3 of Appendix A. Eigenmode analysis is used to calculate the electromechanical coupling coefficient of the device from the metallized surface velocity v_m and free surface velocity v_f using the relation given in (1.2). The total displacement of SAW is given by $\sqrt{(|u_x|^2 + |u_y|^2 + |u_z|^2)}$ where u_x, u_y, and u_z are the particle displacements in the x, y, and z directions respectively. Frequency response is used to calculate the resonance frequency and device displacements. As discussed in section 2.5.2 about SH-SAW resonator, mesh setting with maximum element size about one-tenth of the wavelength of SAW is used to perform the simulations.

A double-stranded DNA of length 150 base pairs (about 50 nm long) can be roughly treated as an elastic cylindrical rod of 1 nm radius [154], [155] having a material density of 1210 $\mathrm{kg\,m^{-3}}$ [156]. A surface mass density of $2{\times}10^{-5}$ $\mathrm{kg\,m^{-2}}$ is equivalent to the presence of double-stranded DNA of length 50 base pairs present uniformly over the sensor surface. The *added mass* feature of COMSOL is used to simulate the mass loading of device by applying surface mass density Δm on the sensor surface, increasing from $2{\times}10^{-5}$ $\mathrm{kg\,m^{-2}}$ to $6{\times}10^{-5}$ $\mathrm{kg\,m^{-2}}$ corresponsding to a DNA length of about 17 to 50 nm. The slope of the graph of relative change in frequency against change in surface mass density as per (3.4) gives the mass sensitivity value.

3.3.1 Mass sensitivity and coupling coefficient

The mass sensitivity and the coupling coefficient of LW device are calculated by both analytical and FE methods considering 36°-YX $LiTaO_3$ substrate and SiO_2, ZnO, gold, PMMA, SU-8 and polyimide as guiding layer materials. The dispersion relation (3.1) is solved numerically in MATLAB using the bisection method to calculate the LW phase velocity v_p. Once the phase velocity is obtained, the group velocity is calculated using (3.3). Fig 3.4a shows the variation in phase velocity and group velocity with the normalized thickness of PMMA guiding layer for the fundamental LW mode (mode-0) and the next higher order mode (mode-1). When h/λ is small, the velocity of the LW tends toward the velocity of the substrate (4170 $\mathrm{m\,s^{-1}}$), but as the

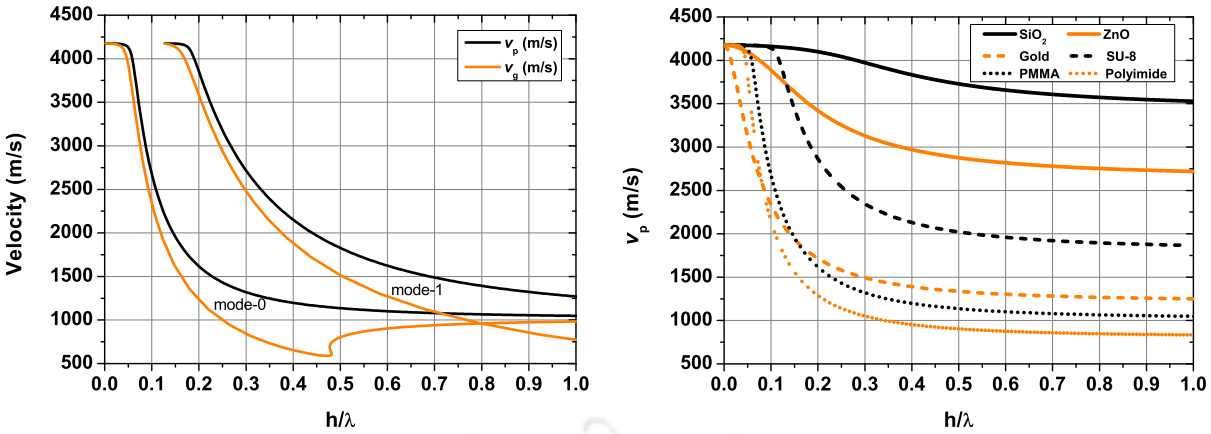

(a) (b)

Figure 3.4: (a) Plot showing the variation in phase velocity v_p and group velocity v_g with the normalized thickness of PMMA guiding layer for the fundamental LW mode (mode-0) and the next higher order mode (mode-1) considering 36°-YX $LiTaO_3$ substrate. (b) Variation in phase velocities of the fundamental LW mode with normalized thickness of SiO_2, ZnO, gold, PMMA, polyimide and SU-8 guiding layers considering 36°-YX $LiTaO_3$ substrate.

thickness of the layer increases, the phase velocity of LW starts to decrease. When h/λ is large, the velocity of LW tends toward the velocity of the PMMA guiding layer (1017 $\mathrm{m\,s^{-1}}$). It shows that when the overlayer is thin, major fraction of the wave energy is concentrated at the top surface of the substrate. As the thickness of the guiding layer increases, the wave gets trapped in the layer and wave velocity tends towards the shear velocity of the guiding layer. At $h/\lambda \approx 0.15$, the next higher order mode starts to appear. Fig. 3.4b shows the variation in phase velocities of the fundamental LW mode with the normalized thickness of SiO_2, ZnO, gold, and the three polymer guiding layers. For all the layers, v_p decreases with increasing thickness of the overlayer. It id noted that v_p starts from 4170 $\mathrm{m\,s^{-1}}$ and begins to decrease with increasing layer thickness. At $h/\lambda = 0.2$, for the SiO_2 case, v_p becomes 4099 $\mathrm{m\,s^{-1}}$ but for PMMA, at the same normalized thickness, v_p drops to 1300 $\mathrm{m\,s^{-1}}$. SiO_2 shows less dispersion in phase velocity in comparison to polymers because the shear velocities of $LiTaO_3$ and SiO_2 are close. PMMA, polyimide and gold layers display a sharp dispersion in phase velocity and even a small variation in the layer thickness would cause a large shift in the phase velocity of LW.

Equation (3.5) can be used to estimate the mass sensitivity of LW device if the density and shear velocity of the substrate and guiding layer are known. Fig. 3.5a shows the variation in mass sensitivity of LW device with the normalized thickness of polymer guiding layers while the Fig. 3.5b displays the mass sensitivity variation in LW device considering SiO_2, ZnO and gold layers. The mass sensitivities of SiO_2, ZnO and gold layers typically lie between 20–50 $\mathrm{m^2\,kg^{-1}}$ which is in the range of mass sensitivity values reported in [157], [158]. Polymer layers such as polyimide, PMMA, and SU-8 give maximum mass sensitivities of 868 $\mathrm{m^2\,kg^{-1}}$, 822 $\mathrm{m^2\,kg^{-1}}$, and 652 $\mathrm{m^2\,kg^{-1}}$ at corresponding normalized thicknesses of 0.06, 0.07, and 0.14 respectively. The low density and low shear velocity of polymers lead to a large (μ_s/μ_l) ratio which causes stronger entrapment of acoustic energy on the surface of the device leading to high mass sensitivity. The mass sensitivity of polymers is about 10–15 times greater than SiO_2 layer which is consistent

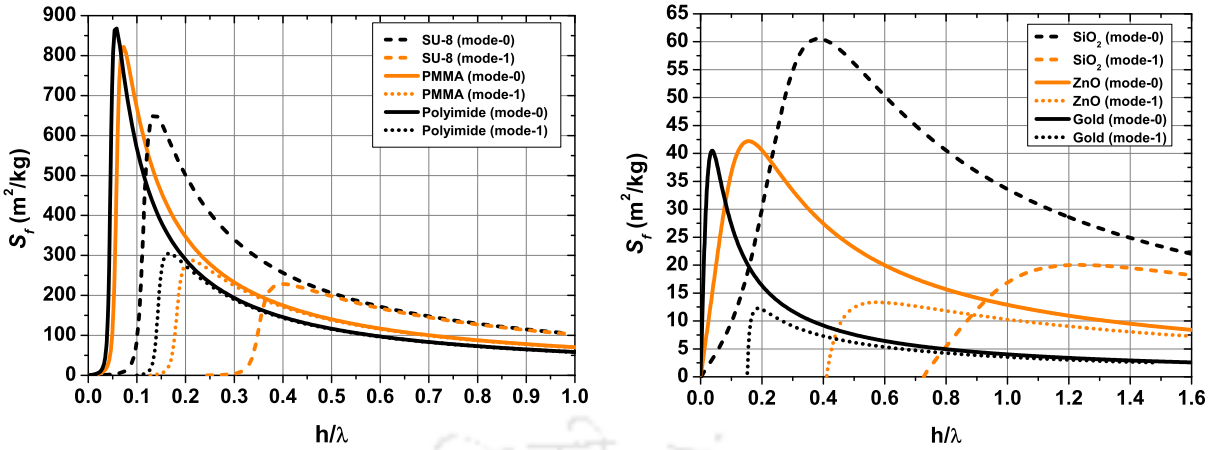

(a) (b)

Figure 3.5: Calculated values of mass sensitivities of LW device for mode-0 and mode-1 as a function of the normalized thickness of (a) Polyimide, PMMA, and SU-8, and (b) SiO_2, ZnO and gold as guiding layer.

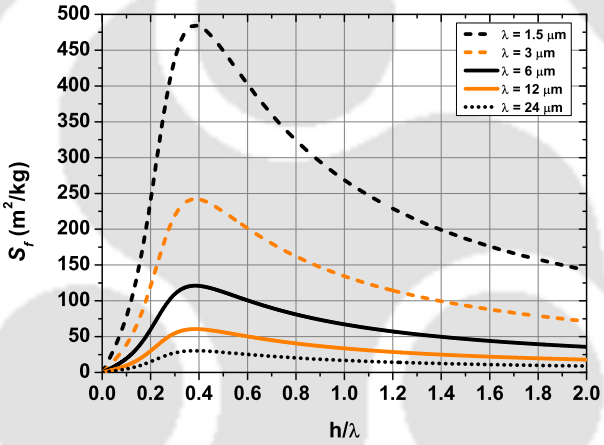

Figure 3.6: Plot showing variation in mass sensitivity of LW device with normalized thickness of SiO_2 guiding layer considering different wavelengths.

with the result obtained by Han *et al.* [136]. It is also noted that the mass sensitivity of the fundamental mode (mode-0) is about three times greater than the value obtained by the next higher order mode (mode-1). Fig. 3.6 shows the mass sensitivity plot of LW device with SiO_2 as guiding layer, operating at different wavelengths. At $\lambda = 24$ µm, the maximum mass sensitivity $S_{f_{max}} = 30$ m^2 kg^{-1} is obtained, while at $\lambda = 1.5$ µm the $S_{f_{max}}$ increases to 484 m^2 kg^{-1}. It shows that if the device is operated at high frequency (low wavelengths) high mass sensitivity can be achieved, but the fabrication of device becomes difficult. Considering error-free practical resolution limit of standard photolithography, fabricating the device with $\lambda = 12$ µm with a large number of uniform IDT having an electrode width of 3 µm is quite challenging. Fig 3.7 shows the mass sensitivity values of LW resonator device with different layers obtained through FEM. The results are comparable with the values obtained by the analytical method as shown in Fig. 3.5. The maximum values of mass sensitivities $S_{f_{max}}$ obtained through analytical and FEM at respective normalized thicknesses for different guiding layer materials are listed in Table 3.1.

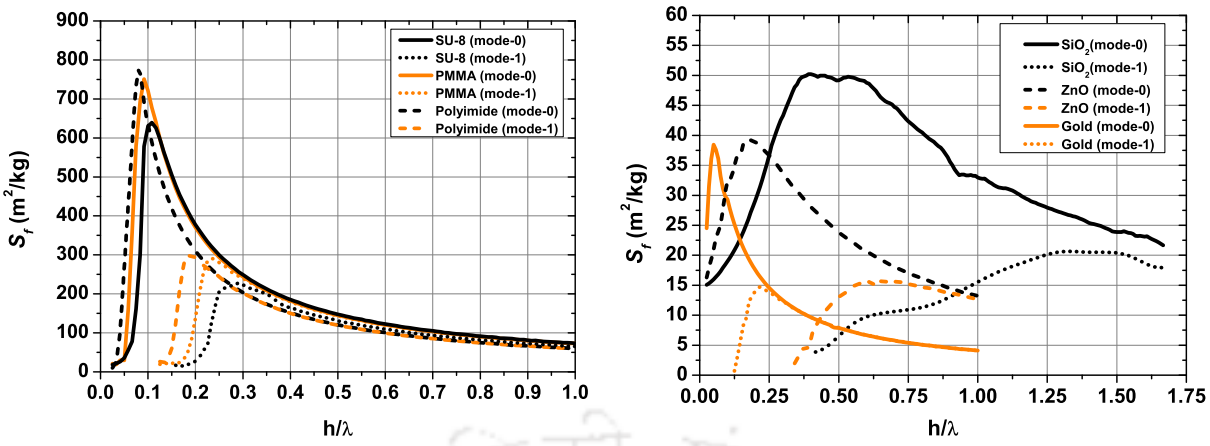

Figure 3.7: Plot showing mass sensitivities S_f of LW device for mode-0 and mode-1 as a function of normalized thickness of (a) Polyimide, PMMA, and SU-8, and (b) SiO_2, ZnO and gold as guiding layer, obtained using FE simulation.

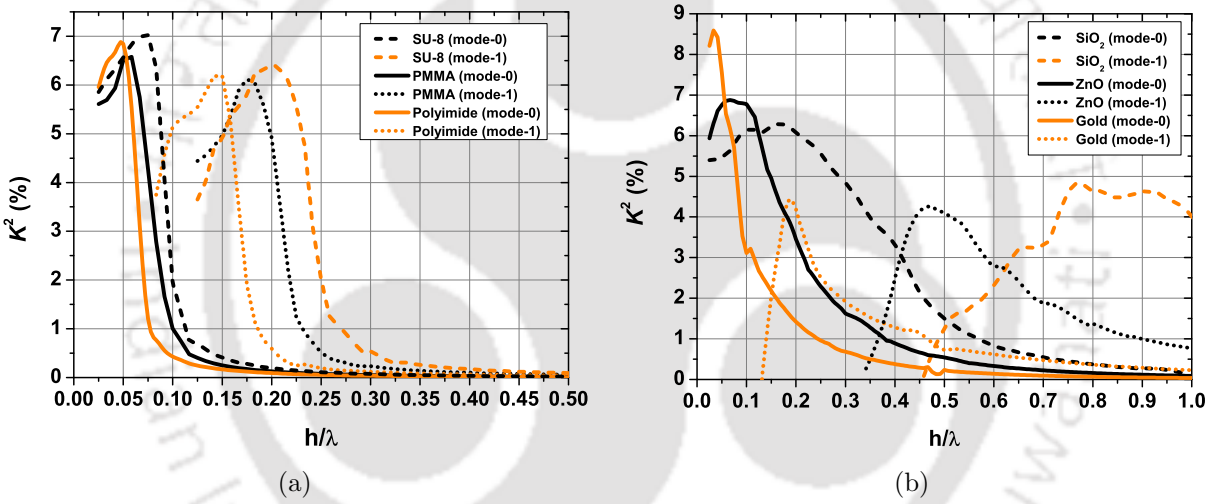

Figure 3.8: Variation in K^2 of LW device for mode-0 and mode-1 as a function of normalized thickness of (a) Polyimide, PMMA, and SU-8, and (b) SiO_2, ZnO and gold as guiding layer, obtained using FE simulation.

Material	Mass sensitivity ($m^2\,kg^{-1}$)							
	Analytical				FEM			
	mode-0		mode-1		mode-0		mode-1	
	$S_{f_{max}}$	h/λ	$S_{f_{max}}$	h/λ	$S_{f_{max}}$	h/λ	$S_{f_{max}}$	h/λ
SiO_2	61	0.39	20	1.24	50	0.39	21	1.3
ZnO	42	0.16	13	0.57	39	0.18	15	0.6
Gold	40	0.04	12	0.19	38	0.05	14	0.21
PMMA	822	0.07	288	0.21	752	0.09	291	0.23
Polyimide	868	0.06	306	0.17	770	0.08	298	0.19
SU-8	652	0.14	229	0.4	639	0.11	228	0.29

Table 3.1: The maximum values of mass sensitivity ($S_{f_{max}}$) for mode-0 and mode-1, attained at the specific values of normalized layer thickness for different guiding layer materials obtained by analytical and FEM.

Material	Coupling coefficient (%)			
	mode-0		mode-1	
	K^2_{max}	h/λ	K^2_{max}	h/λ
SiO_2	6.3	0.17	4.8	0.78
ZnO	6.9	0.07	4.3	0.47
Gold	8.5	0.03	4.4	0.19
PMMA	6.6	0.06	6.1	0.18
Polyimide	6.8	0.05	6.2	0.14
SU-8	7	0.08	6.5	0.2

Table 3.2: The maximum values of coupling coefficient (K^2_{max}) for mode-0 and mode-1, attained at the specific values of normalized layer thickness for different guiding layer materials obtained by FEM.

The K^2 values of LW device with different guiding layers is obtained by FEM. Fig. 3.8a shows the variation in K^2 with the normalized thickness of polymer guiding layers for mode-0 and mode-1. Polymer layers exhibit a rapid rise in K^2 values, reaching a maximum of about 7%, then decrease sharply within a very narrow range of h/λ 0.03–0.1. It shows that to achieve large K^2 with polymers, they need to be coated precisely over a narrow range of thickness values. Fig. 3.8b shows variation in K^2 with the normalized thickness of SiO_2, ZnO and gold as guiding layer materials. For the fundamental mode, gold offers a maximum K^2 value of 8.5% at $h/\lambda = 0.03$. ZnO and SiO_2 layers provide maximum K^2 of 6.9% and 6.3% at h/λ of 0.07 and 0.17 respectively. They offer slow variation in K^2 over a wide range of h/λ 0.03–0.4. The maximum coupling coefficient K^2_{max} obtained through FEM at respective normalized thicknesses for different guiding layer materials are listed in Table 3.2.

3.3.2 Selection of guiding layer

Selecting appropriate material for guiding layer is necessary for the design of LW sensors. SiO_2, ZnO and PMMA are some of the materials that have been typically used as guiding layers [68]. Polymers like PMMA, polyimide, polystyrene, SU-8, PDMS, parylene-C have low density and low shear velocity. They confine the wave energy at the surface, provide excellent waveguiding capabilities and offer high mass sensitivity. They can be easily deposited on the device surface using spin coating methods. SU-8 is a polymer photoresist possessing low shear velocity and rigidity comparable to SiO_2 that is extensively used in microfabrication. Experimental and theoretical studies of SU-8 as a guiding layer material in LW devices have been reported in [159], [160]. Parylene-C is another polymer layer that can provide a biocompatible interface for sensor devices. Theoretical analysis of a LW device with parylene-C as guiding layer [161] and using GO (Graphene oxide) as a sensitive layer for vapor and humidity sensing have also been reported [162]. On the downside, polymers need to be coated very precisely otherwise the K^2 of the device becomes very low. They introduce more losses in wave propagation as their thickness is increased and also tend to swell in liquid media [163].

ZnO is another material that is often used as guiding layer. ZnO/ST-quartz device has been reported to provide high sensitivity, small TCF, and high K^2 [150]. ZnO has several

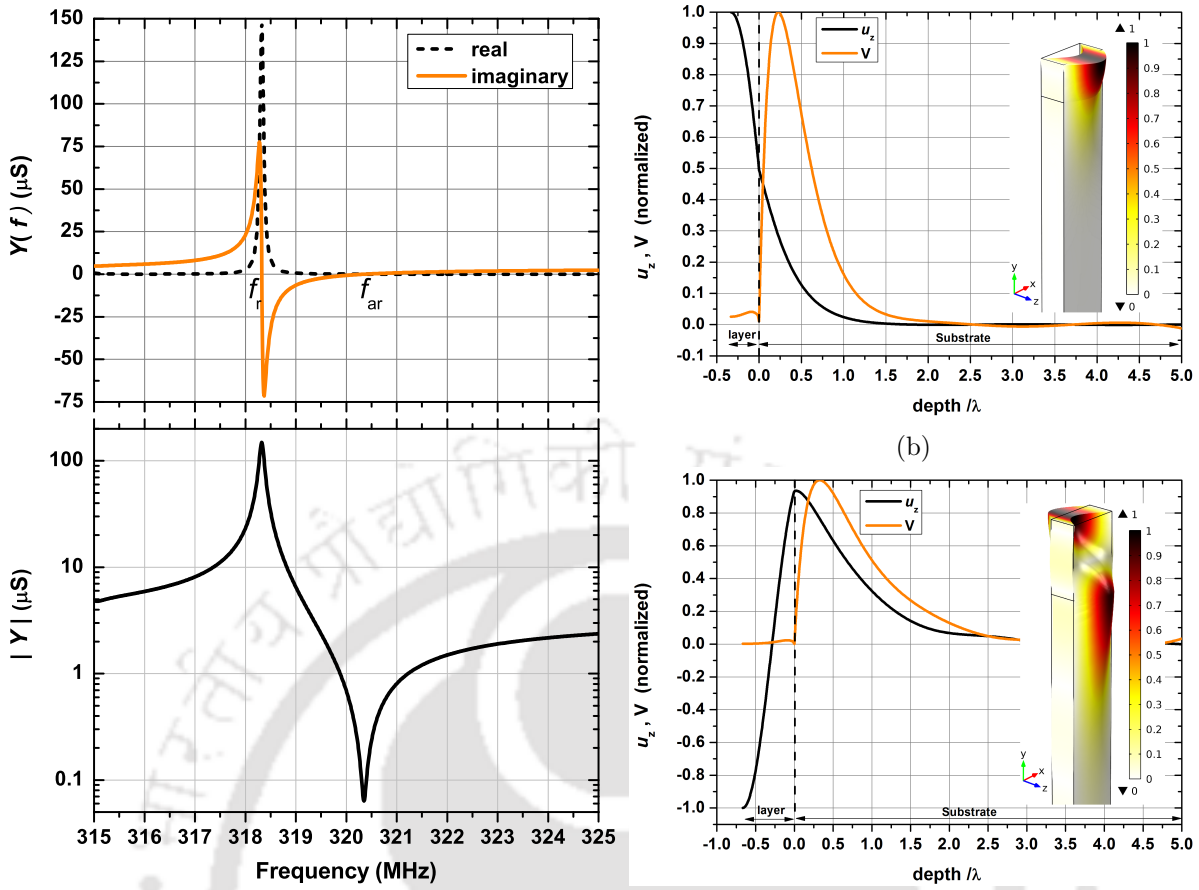

Figure 3.9: (a) The frequency response of Love wave resonator with 4.7 µm thick SiO_2 layer showing resonance frequency f_r and anti-resonance frequency f_{ar} at 318.32 MHz and 320.35 MHz respectively. Variation in normalized shear displacement u_z and potential V with normalized device depth along with the 3D displacement profile is shown for (b) LW resonator composed of 4 µm thick SiO_2 layer (displaying mode-0) (c) LW resonator composed of 8 µm thick SiO_2 layer (displaying mode-1).

disadvantages, it is considered as a CMOS contaminant and can deteriorate the efficiency of transducers. ZnO is reactive to acids, liquids, and moisture, and can negatively impact device performance in the presence of liquids. Gold has been extensively used as a guiding layer in LW devices for biosensor design [48]. It has low shear velocity, high density, provide good waveguiding capabilities and is bio-compatible. However, the material is costly and promotes unwanted coupling of RF signals between the two IDTs. SiO_2 is preferred as guiding layer material because of its inertness to chemicals, good mechanical stability, and sufficiently low shear velocity. It is stable in water, at elevated temperatures and is an excellent electrical insulator [164]. One of the shortcomings of SiO_2 is that the thickness required for attaining maximum mass sensitivity is high. In addition, a number of chemical processes are required to make the surface ready for biofunctionalization.

Substrate	Mass sensitivity ($m^2\,kg^{-1}$)		Coupling coefficient (%)	
	$S_{f_{max}}$	h/λ	K^2_{max}	h/λ
36°-YX $LiTaO_3$	50	0.39	6.3	0.17
41°-YX $LiNbO_3$	59	0.33	19.5	0.08
90°-AT quartz	100	0.15	1.1	0.09
90°-ST quartz	97	0.15	1.6	0.08

Table 3.3: Maximum values of mass sensitivity and the coupling coefficient of LW device obtained at specific values of the normalized thickness of SiO_2, considering different piezoelectric substrates.

3.3.3 Frequency response of LW resonator

The maximum mass sensitivity of 36°-YX $LiTaO_3$ based LW resonator with SiO_2 guiding layer for the fundamental mode is obtained at $h/\lambda = 0.39$ (Table 3.1). It corresponds to SiO_2 thickness of 4.7 µm for the device operating at $\lambda = 12$ µm. The frequency response of the device is performed in the frequency range of 315–325 MHz with a step size of 0.01 MHz. Frequency response displaying the variation in admittance of the resonator is shown in Fig. 3.9a. The resonance frequency f_r and the anti-resonance frequency f_{ar} are obtained at 318.32 MHz and 320.35 MHz, respectively.

The variation in normalized shear displacement u_z and normalized potential V with normalized depth of the LW resonator for SiO_2 layer of thickness 4 µm ($h/\lambda = 0.33$) and 8 µm ($h/\lambda = 0.66$) is presented in Fig. 3.9b and 3.9c, respectively. A thickness of 4 µm generates fundamental Love mode (mode-0) with maximum shear displacement at the device surface. The magnitude of shear displacement decrease with device depth and diminishes in about one or two wavelengths. The decrease in shear displacement is much faster in the guiding layer than in the substrate. A thickness of 8 µm generates the next higher order Love mode (mode-1) as shown in Fig. 3.9c. The shear displacements are maximum at the top and bottom surfaces of the guiding layer and are out of phase. In both the modes the electric potential remains low in the guiding layer but rises inside the substrate peaking at a depth of approximately $\lambda/4$ below the layer-substrate interface.

3.3.4 Comparison between different substrates

The variations in mass sensitivity and coupling coefficient of LW device with SiO_2 guiding layer, considering different substrates are shown in Fig. 3.10a and 3.10b, respectively. Quartz substrate provides higher shear wave velocity hence higher mass sensitivity than $LiTaO_3$ and $LiNbO_3$ substrates (Table 2.2) [68]. Quartz-based LW device with SiO_2 guiding layer offer high mass sensitivity of about 100 $m^2\,kg^{-1}$ at h/λ of 0.15, which is almost double the mass sensitivity offered by $LiTaO_3$ and $LiNbO_3$ based LW device. However, LW device based on $LiTaO_3$ and $LiNbO_3$ provide K^2_{max} of 6.3% and 19.5% at h/λ of 0.17 and 0.08 respectively, while quartz offers a low K^2_{max} of about 1.6%. Table 3.3 lists the normalized thickness of guiding layer at which $S_{f_{max}}$ and K^2_{max} are achieved for the LW device considering different substrates.

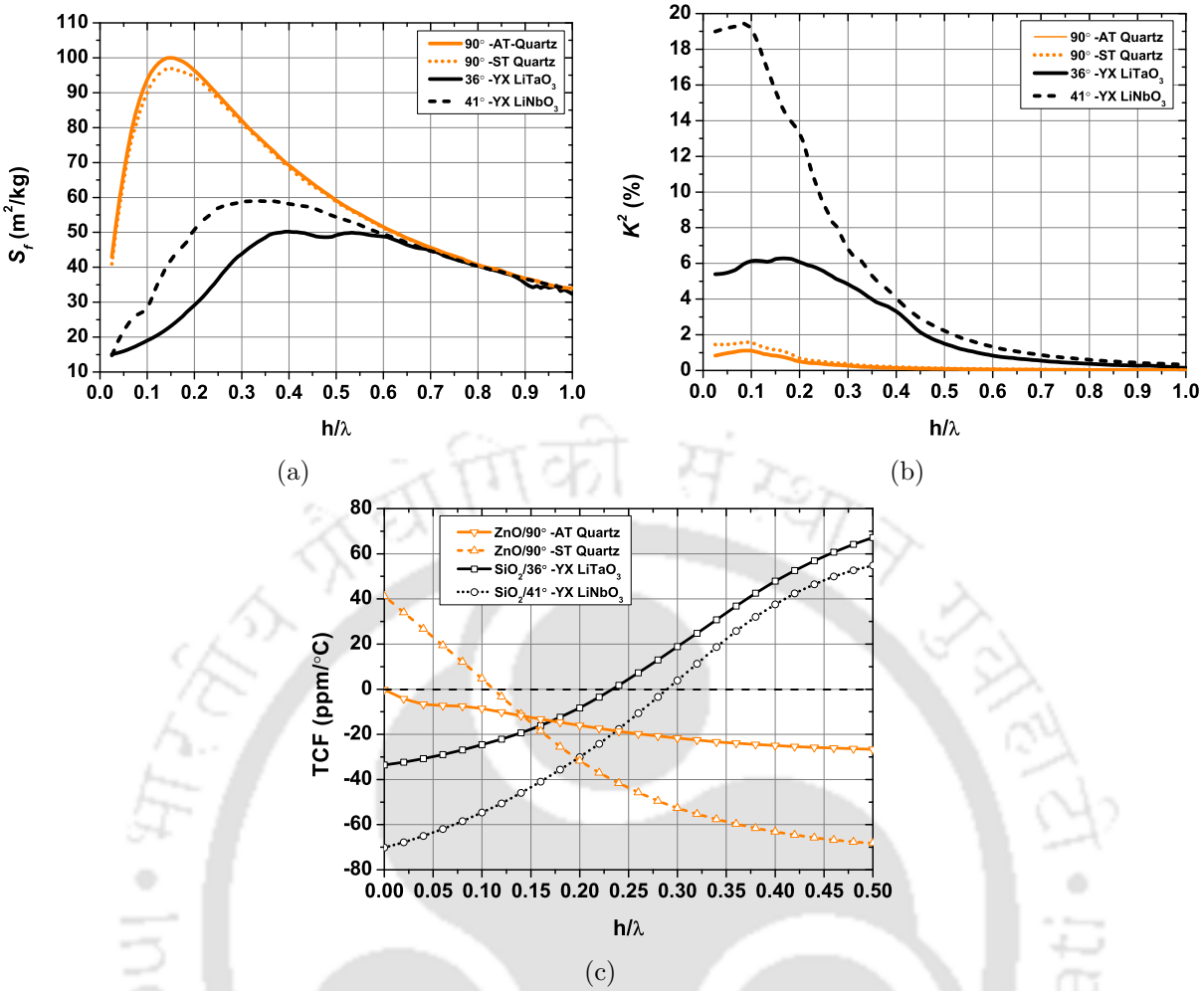

Figure 3.10: Variation in (a) mass sensitivity and (b) coupling coefficient of LW resonator with the normalized thickness of SiO_2 guiding layer considering different substrates. (c) Variation in TCF of LW resonator with the normalized thickness of guiding layer for different substrates. ZnO is considered as guiding layer for quartz while SiO_2 is selected for $LiTaO_3$ and $LiNbO_3$ substrates.

As listed in Table 2.2, 36°-YX $LiTaO_3$ and 41°-YX $LiNbO_3$ possess large negative TCF of -34 and -71 ppm°C^{-1} respectively. 90°-AT quartz has TCF close to zero while 90°-ST quartz has positive TCF of 39 ppm°C^{-1}. SiO_2 layer has a positive temperature coefficient. Thus, it can be coated on 36°-YX $LiTaO_3$ and 41°-YX $LiNbO_3$ substrates so that negative TCF can be brought to zero [165]. Similarly, ZnO has a negative temperature coefficient, and it can be coated on quartz substrates to design a zero TCF LW device [166]. Equations (1.11) and (2.56) along with the values of temperature coefficients of SiO_2 and ZnO, given in Table A.4 (Appendix A) are used to calculate the TCF of LW device. Fig. 3.10c shows the change in TCF of LW device with the normalized thickness of guiding layer, considering different substrates. Zero TCF for $LiTaO_3$ and $LiNbO_3$ based LW device with the SiO_2 guiding layer is achieved at h/λ of 0.23 and 0.29 respectively. Zero TCF for 90°-ST quartz-based LW device with ZnO guiding layer is attained at h/λ of 0.11.

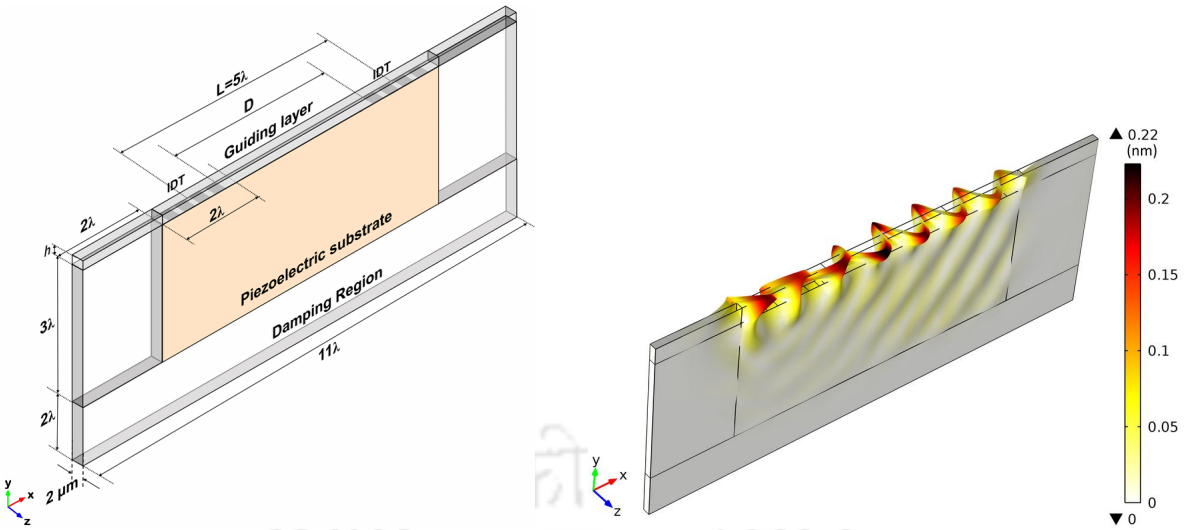

(a) (b)

Figure 3.11: (a) 3D simulation geometry of LW delay line device. (b) Time response simulation showing displacement profile and propagation of LW at $t = 20$ ns.

3.4 LW delay line

The geometry employed for 3D FE simulation of LW delay line device is shown in Fig. 3.11a. A SiO_2 guiding layer of thickness $h = 4.7$ µm is made on a 36°-YX $LiTaO_3$ piezoelectric substrate. Massless input and output IDT fingers of aluminum with zero thickness and 3 µm width are rendered on the substrate that generates surface wave of $\lambda = 12$ µm. The center-to-center separation L between input and output IDT is 5λ. The delay line path length D is 39 µm. Periodic boundary conditions are kept along the z axis to realize IDTs of an infinite aperture that helps to minimize the size of simulation geometry. A critically damped region of size 2λ is made on the either side and bottom of the device to avoid reflections from the edges. The simulation settings are same as described in section 2.6.1. The time response is obtained for 50 ns with a time step of 1 ps. Insertion loss is calculated by taking the FFT of the obtained impulse response of the device. The *added mass* feature is used to simulate the mass loading of the device by applying an incremental surface mass density Δm, from 2×10^{-5} $\mathrm{kg\,m^{-2}}$ to 6×10^{-5} $\mathrm{kg\,m^{-2}}$ on the delay line surface of length 3λ. Mass loading causes a time shift Δt in the output voltage waveforms. The resulting phase shift $\Delta\phi$ can be obtained by comparing the instantaneous phase (ϕ) of the two voltage waveforms by employing the Hilbert transform [167]. Mass sensitivity is calculated from the slope of the graph of normalized phase shift versus incremental surface mass density [21]. The frequency and phase mass sensitivities are then obtained using (1.7) and (1.8) respectively.

3.4.1 Time response

The delay line device generates LW with SH wave motion as shown in the 3D displacement profile of Fig. 3.11b. The shear horizontal nature of the wave is confirmed from the variation in displacement components u_x, u_y, and u_z with time as shown in Fig. 3.12a. The shear

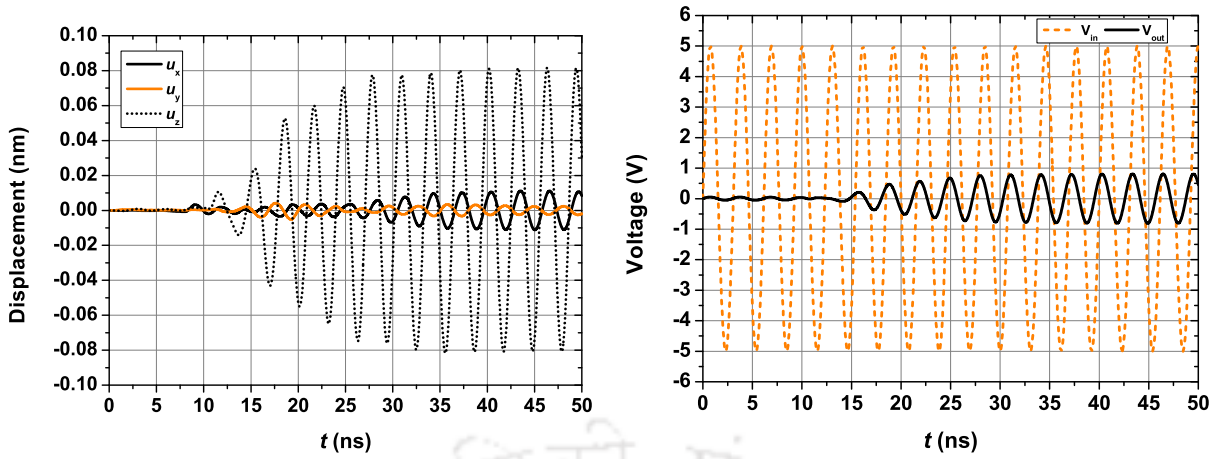

(a) (b)

Figure 3.12: (a) Time response of LW delay line composed of SiO_2 guiding layer and 36°-YX $LiTaO_3$ showing the variation of (a) displacement components u_x, u_y and u_z, and (b) input and output voltage with time.

Surface mass density (Δm) ($\mathbf{kg\,m^{-2}}$)	**Time delay (Δt) (ns)**	**Phase shift ($\Delta\phi$) (rad)**
2×10^{-5}	0.017	0.035
3×10^{-5}	0.024	0.049
4×10^{-5}	0.032	0.065
5×10^{-5}	0.04	0.082
6×10^{-5}	0.049	0.1

Table 3.4: Time delay and phase shifts obtained in output signal upon mass loading

displacement component u_z attains a maximum value of 0.08 nm while the vertical displacement component u_y stays well below 0.01 nm. The variation of input and output voltages of the device with time is shown in Fig. 3.12b. Application of 5 V sinusoidal signal at the input IDT generates a stable 0.9 V sinusoidal output.

3.4.2 Mass sensitivity

Application of mass on the LW delay line surface causes a change in velocity of the wave which in turn produces a shift in time or phase of the wave. Fig. 3.13a shows the variation in output voltage with and without mass loading when a 5 V sinusoidal signal of 325 MHz is applied to the input IDT. It is noted that mass loading with 6×10^{-5} $\mathrm{kg\,m^{-2}}$ produces a time shift of 0.049 ns (or phase shift of 0.1 rad). Table 3.4 shows the values of time delay and phase shift obtained due to incremental mass loading at the sensor surface. The plot of $\Delta\phi/kD$ versus Δm shown in Fig. 3.13b results in a straight line with slope representing the phase mass sensitivity. Using (1.8) and (1.9), the calculated value of S_ϕ and S_f are 80 $\mathrm{m^2\,kg^{-1}}$ and 52 $\mathrm{m^2\,kg^{-1}}$. The frequency mass sensitivity value is consistent with the value obtained previously for the LW resonator case.

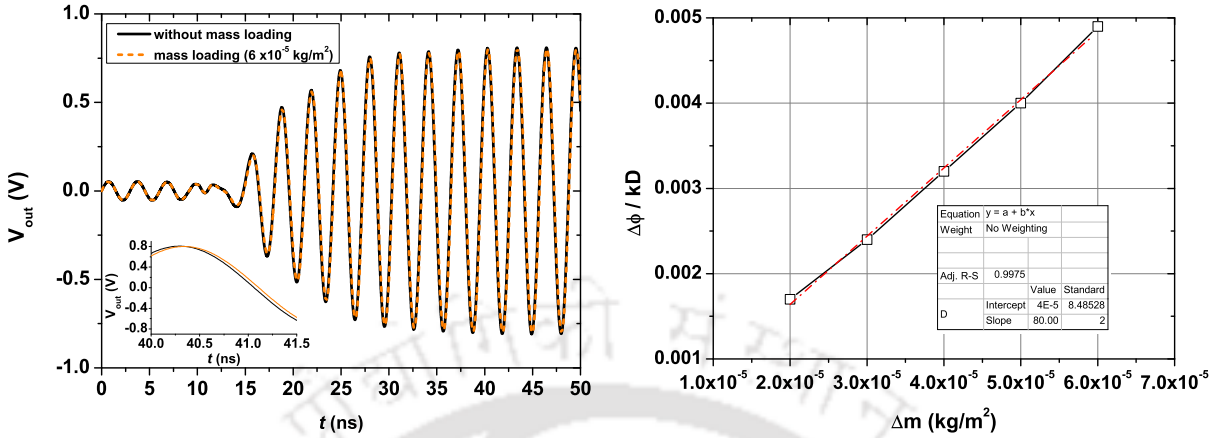

(a) (b)

Figure 3.13: (a) Time response of the output voltage with and without mass loading. Inset of the figure shows the magnified time response with Δt of 0.049 ns due to mass loading with Δm = 6×10^{-5} kg m^{-2}. (b) Plot showing the normalized phase shift ($\Delta\phi/kD$) versus incremental surface mass density Δm. The slope represents the phase mass sensitivity.

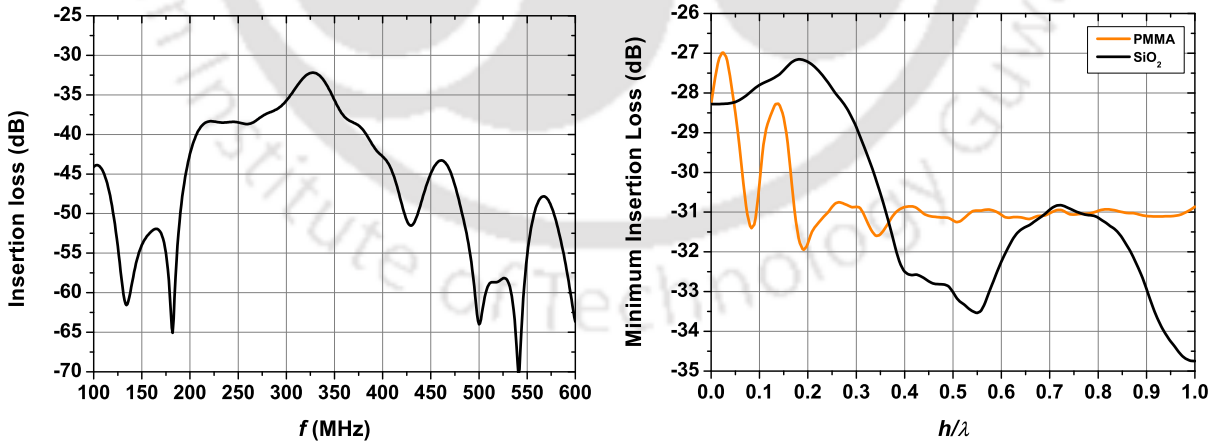

(a) (b)

Figure 3.14: (a) Insertion loss of LW delay line with SiO_2 guiding layer of thickness 4.7 µm. (b) Plot of minimum insertion loss of LW delay line versus normalized thickness of PMMA and SiO_2 as guiding layers.

3.4.3 Insertion loss

The insertion loss of LW device composed of a SiO_2 layer of 4.7 µm thickness and a 36°-YX $LiTaO_3$ substrate is obtained by taking FFT of the impulse response of the device. Fig. 3.14a shows the frequency response of LW device with SiO_2 guiding layer, displaying a minimum insertion loss of -32.2 dB at 327 MHz. The minimum insertion loss of LW device is plotted against the normalized thickness of PMMA and SiO_2 as guiding layer in Fig. 3.14b. As layer height increases, the insertion loss goes through a series of oscillations corresponding to the transition in the modes of vibration. PMMA being a polymer, because of its low density and low shear velocity shows rapid transitions in the mode as its thickness increases. For PMMA, a minimum insertion loss of -27, -28.3 and -30.8 dB is observed at h/λ of 0.025, 0.13, and 0.27, respectively. On the other hand, SiO_2 layer shows a slow transition in modes, offering a minimum insertion loss of -27.2 and -30.8 dB at h/λ of 0.18 and 0.72, respectively. The plot shows that increasing overlayer thickness initially improves the insertion loss of the device then degrades it substantially. The pattern repeats periodically with transition in the mode of vibration. These type oscillations in insertion loss were also observed experimentally by Mchale *et al.* [13] in the analysis of polymer coated LW device.

3.5 Summary

The chapter has presented analysis of LW device considering different guiding layer materials and substrates. LW is a type of shear horizontally polarized wave that can be produced in a SSBW device or leaky SAW device when an overlayer with an acoustic shear velocity less than that of substrate is deposited on the propagation path. The guiding layer slows down the propagating acoustic shear mode and confines the energy of the wave to the surface.

The v_p, v_g, and S_f of LW device are calculated by solving the dispersion equation of LW, and the results are compared with 3D FE simulation of LW resonator. Polymer layers such as polyimide, PMMA, and SU-8 give a maximum mass sensitivity of 868, 822, and 652 $m^2\,kg^{-1}$ at corresponding normalized thickness of 0.06, 0.07, and 0.14, respectively. The low density and low shear velocity of polymers cause stronger entrapment of acoustic energy on the surface leading to high mass sensitivity. The mass sensitivities of LW device with SiO_2, ZnO and gold layers typically lie between 20–50 $m^2\,kg^{-1}$. Polymer layers exhibit sharp rise and fall in K^2 values within a very narrow range of h/λ 0.03–0.1. To achieve significant K^2 with polymers, they need to be coated precisely over a narrow range of thickness. In comparison to polymers, ZnO and SiO_2 offer slow variation in K^2 over a wide range of h/λ. Operating the device at high frequency (lower wavelengths) can provide high sensitivity, but the fabrication of IDT with reduced electrode width becomes challenging. SiO_2 is often preferred as guiding layer material because of its inertness to chemicals, good mechanical stability, and sufficiently low shear velocity. Frequency response and depth displacement studies have also been performed for the LW resonator.

A comparative analysis of LW device with SiO_2 guiding layer considering different substrates

such as 36°-YX $LiTaO_3$, 41°-YX $LiNbO_3$, 90°-AT and ST quartz is performed. Quartz-based LW device offers high mass sensitivity of about 100 $m^2\,kg^{-1}$ at h/λ of 0.15, which is almost double the mass sensitivity provided by $LiTaO_3$ and $LiNbO_3$ based LW devices. However, LW devices based on $LiTaO_3$ and $LiNbO_3$ provide maximum K^2 of 6.3% and 19.5% at h/λ of 0.17 and 0.08 respectively, while quartz provides maximum K^2 of about 1.6% which is much lower. Zero TCF of LW device can be achieved by coating a guiding layer that has opposite sign of temperature coefficient than the underlying substrate.

Time response study has been performed for LW delay line composed of a 36°-YX $LiTaO_3$ substrate and 4.7 µm thick SiO_2 guiding layer. The shear displacement component u_z is about eight times the vertical displacement component u_y, which confirms the SH nature of the LW. Mass sensitivity is calculated by carrying out incremental mass loading on the active area of the device, which produces time or phase shift in output waveform. The calculated values of S_ϕ and S_f are 80 $m^2\,kg^{-1}$ and 52 $m^2\,kg^{-1}$, consistent with the result obtained for LW resonator. A minimum insertion loss of -32.2 dB is obtained at 327 MHz. As layer height is increased, the insertion loss goes through a series of oscillations corresponding to the transition in the modes of vibration.

Chapter 4

Coupled Resonance in Love wave device with ZnO nanorods

> If you want to find the secrets of the universe, think in terms of energy, frequency and vibration.
>
> Nikola Tesla

The previous chapter discussed the effect on mass sensitivity and coupling coefficient of the LW device considering different guiding layer materials. LW devices are the preferred choice for designing biosensors as they not only keep the energy of the propagating wave on the surface but also provide high mass sensitivity. Polymers are often used as guiding layer material in LW devices as they have low shear velocity and density and offer high mass sensitivity. However, polymer-based LW devices suffer from high insertion losses and low K^2 [68]. To design a device with high mass sensitivity and sufficiently high K^2, bilayer or multilayer LW devices have also been reported that combine the advantages of different guiding layers. Du *et al.* [168] performed the theoretical and experimental analysis of PMMA/SiO_2/Quartz based LW device and showed that the bilayer configuration offered better sensitivity and reduced TCF than its single layer counterpart. It has been shown that LW sensors with multiple viscoelastic layers comprising SU-8 and SiO_2 on quartz offer improved sensitivity and overall performance of the device [169].

The mass sensitivity of LW biosensor can also be improved by designing nanostructures that increase the surface area for the analyte to attach. Gold nanoparticles, graphene oxide, nanostructured PMMA and ZnO nanorods have been used on the surface of LW sensors for improving the mass sensitivity in detection of proteins, chemicals, and disease-causing pathogens [90], [103], [170], [171]. Coupled resonance can be achieved by making nano or microstructures of an appropriate aspect ratio on the LW or SH-SAW device. These structures will not only increase the active surface area of the sensor but also vibrate in unison with the device thereby offering high mass sensitivity. This chapter addresses the effect of varying the height of ZnO nanorods designed on the surface of the sensor on the performance of LW device through FE simulations.

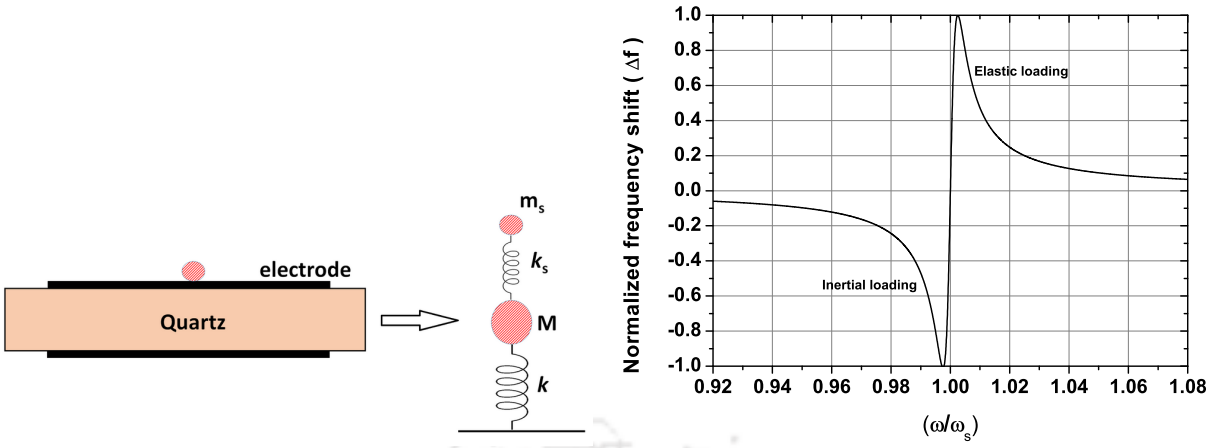

(a) (b)

Figure 4.1: (a) Spherical object adhering the surface of a quartz crystal microbalance. The sphere and the device together form a system of coupled resonator and is represented by an equivalent mechanical model. (b) Plot showing the variation in normalized frequency shift (Δf) with ω/ω_s. Positive and negative frequency shifts occurring because of inertial and elastic loading respectively [112], [173].

The phenomenon of coupled resonance showing the transition between inertial and elastic loading regimes is described using the Dybwad model. LW resonator composed of a SiO_2 guiding layer and ZnO nanorods is simulated to study the variation in resonance frequency, mass sensitivity, and coupling coefficient of the device with the height and packing density of rods. FE simulation of LW delay line is also performed by designing ZnO nanorods on the delay line path between input and output IDTs. The effect of nanorods on the time response, stress and insertion loss of the device is studied.

4.1 Coupled resonance

Acoustic resonators, especially QCM have been widely used for detection of various bio-analytes on an appropriately functionalized surface [172]. The QCM device consists of a thin piezoelectric plate usually made of quartz that is electrically excited using top and bottom metal electrodes to generate a thickness shear mode. For a QCM, the sensor response is described by the Sauerbrey relation as [32]

$$\frac{\Delta f^*}{f_0} = -\frac{-2f}{Z_q} m_A \tag{4.1}$$

where $\Delta f^* = \Delta f + \mathrm{i}\Delta\Gamma$ is the complex frequency shift, f_0 is the unperturbed resonance frequency, Γ is the half bandwidth at half maximum, Z_q is the acoustic impedance of quartz, and m_A is the mass per unit area deposited on the sensor surface. For the ideal inertial loading case, the frequency shift is real with no shift in bandwidth. As the analyte attaches to the sensor surface, the effective mass of the resonator increases which decreases the oscillation frequency of the resonator, and a negative shift in frequency is obtained.

In 1985 Dybwad explained a system of coupled resonator where gold particles of 10-50 µm

diameter size were put on a quartz substrate vibrating in a shear horizontal way [112]. Fig. 4.1a shows a small gold sphere adsorbed on the surface of QCM with its equivalent mechanical model. The quartz resonator is represented with mass M and spring constant k. The spherical object of mass m_s is assumed to be attached with a spring constant k_s to the resonator. The sphere in contact with the vibrating substrate forms a system of coupled resonator with the individual resonance frequency of $\omega_s = \sqrt{(k_s/m_s)}$ and $\omega = \sqrt{(k/M)}$, respectively. The frequency shift of the composite resonator upon mass loading depends on whether ω_s is greater or smaller than ω. When the size of the sphere is small, it is firmly attached to the surface with $\omega_s > \omega$. In this inertial loading regime, any increase in the size of the sphere increases the mass on the resonator which leads to decrease in the resonance frequency or a negative shift in the frequency as shown in Fig. 4.1b. At a certain size of the sphere, the resonance frequency of the sphere becomes less than that of resonator ($\omega_s < \omega$), causing a positive shift in the frequency known as the elastic loading regime. In this limit, the positive shift in the frequency is proportional to the stiffness of the contact and independent of the mass of the sphere [173]. Since the stiffness of the composite resonator increases, rather than its mass, the sphere remains immobile at the surface due to inertia and exerts a restoring force on the crystal which increases the oscillation frequency of the resonator. A more generalized form of Dybwad model considers an array of spheres present on the surface of the substrate causing coupled resonance. Presence of spheres on the crystal results in a frequency shift given by,

$$\frac{\Delta f^*}{f_0} \approx -\frac{n m_s \omega}{A \pi Z_c} \frac{1}{(1 - \frac{\omega^2}{\omega_s^2})} \tag{4.2}$$

where Δf^* is the complex frequency shift, $Z_c = \sqrt{\rho\mu}$ is the acoustic impedance of substrate, which depends on the shear modulus μ and density ρ of the crystal. Symbol n denotes the number of spheres over area A, m_s is the mass of each sphere attached to the crystal with spring constant k_s. Assuming small load approximation, the crystal surface undergoes a tangential shear motion, producing frequency shift proportional to acoustic load impedance Z_{aL} given by the ratio of area-averaged stress σ and speed $\dot{u}$ at the crystal surface represented as [173]

$$\frac{\Delta f + i\Delta\Gamma}{f_0} \approx \frac{i Z_{aL}}{\pi Z_c} = \frac{i}{\pi Z_c} \left\langle \frac{\sigma}{\dot{u}} \right\rangle_{area} \tag{4.3}$$

where i is the imaginary unit and the angled bracket $\langle\rangle$ denotes the average.

4.2 LW resonator with ZnO nanorods

Mass sensitivity can be enhanced by making nanostructures on the sensor surface as they provide large surface area for the analyte to attach. Many techniques involving fabrication of nanorods and nanowires require high temperatures, that may damage the piezoelectric properties of the substrate. Of all the nanostructures, ZnO nanorods can be easily fabricated at low temperatures by a chemical hydrothermal method, and their height can also be controlled [109], [110]. A vertically aligned array of ZnO nanorods can be grown over large areas by hydrothermal solution growth on a predeposited ZnO seed layer covered by lithographically patterned pho-

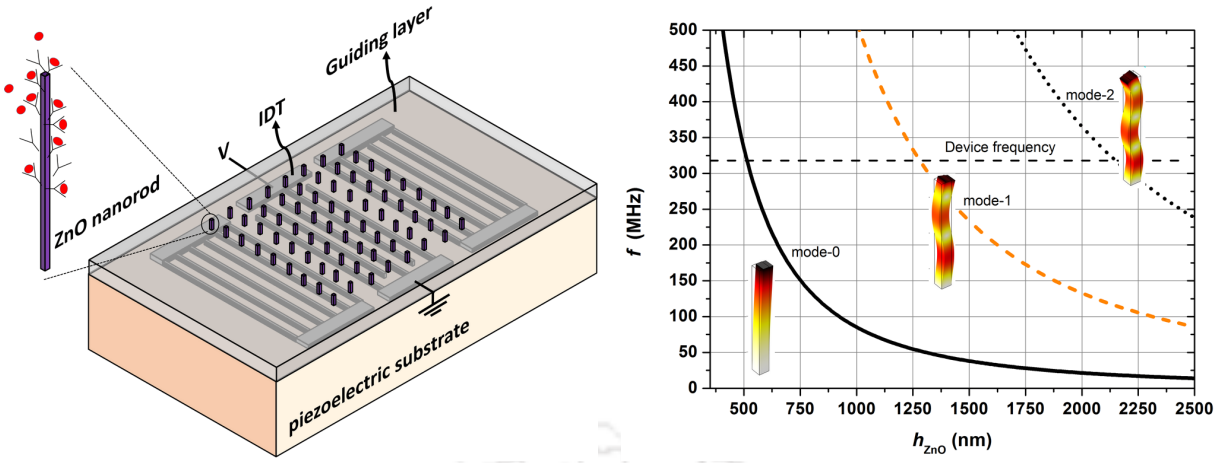

(a) (b)

Figure 4.2: (a) Proposed LW resonator with ZnO nanorods made on the active region of the device. (b) Variation in Eigenmode frequency of individual ZnO nanorod with its height along with the mode shapes. Longer nanorods can excite higher order modes.

toresist, acting as a template [111]. They offer high aspect ratio and large surface area for DNA immobilization [174]. Zhang *et al.* [90] have shown experimentally that ZnO nanotips of 500 nm height over $SiO_2/LiNbO_3$ SAW sensor could enhance the immobilization of DNA by a factor of 200 compared to the flat ZnO film. Reyes *et al.* [108] reported a nanostructured QCM device containing ZnO nanotips on the sensing area that provided ten-fold increase in mass sensitivity over the conventional QCM.

Coupled resonance in a QCM device with polymer micro-pillars has been extensively studied in the literature. Coupled resonance involves the presence of nano or microstructures of suitable aspect ratio on the QCM surface that vibrates in unison with the structure giving negative (inertial loading) and positive (elastic loading) frequency shifts upon mass loading [112], [173], [175]. Wang *et al.* carried out the numerical and experimental study of coupled resonance system composed of QCM device and PMMA micro-pillars in the presence and absence of liquid for biological detection [176] and humidity sensing [114]. The device offered high mass sensitivity at the critical height of micro-pillars. Kashan *et al.* [115] performed the simulation and experiment of a SU-8/QCM micro-pillar based coupled resonance system and discovered that the coupled resonance characteristics not only depend on the resonant structure dimensions but also on the location of contact regions in the acoustic device. The pillars offer elastic loading only when they are placed in the regions of maximum displacement. Ramakrishnan *et al.* [113] further investigated coupled resonance by employing high aspect ratio palladium resonant nano-pillars on a SAW device using FE simulation to detect a small concentration of hydrogen. The author has also reported experimental, and simulation results of mass loading by SU-8 micro-pillars made on the surface of SAW resonators [177], [178].

Fig. 4.2a shows the proposed LW resonator with ZnO nanorods made on the active region of the sensor. The nanorods can be grown on the SiO_2 guiding layer, and their height can be controlled using the low-temperature hydrothermal method. The nanorods can be silanized and chemically modified so that the desired analyte molecules can be selectively attached to the

sensing device. The presence of ZnO nanorods of a particular aspect ratio on the LW device not only increases the surface area for the analyte to attach but can also form a Dybwad system of coupled resonance. Such a system can be highly sensitive to the mass attachment which is the motivation of the current study. In chapter 3, section 3.3.1, it was shown that LW resonator operating at about 318 MHz (λ = 12 µm) composed of SiO_2 and 36°-YX $LiTaO_3$ substrate offers highest S_f at a SiO_2 thickness of 4.7 µm. The mass sensitivity of the device can be further increased by making ZnO nanorods of *resonant height* on the device. 3D FE eigenmode simulation of the resonator comprising ZnO nanorods with square cross section of size 100 nm and various heights was carried out to study the variation in frequency and modes with nanorod height h_{ZnO}. Fig. 4.2b shows that for a particular mode, as the nanorod height is increased the resonance frequency starts to decrease. Higher order modes appear when longer nanorods are considered. Coupled resonance can occur if the resonance frequency of the nanorod matches with the device frequency, at h_{ZnO} = 515, 1280 and 2150 nm for mode-0, mode-1 and mode-2, respectively.

4.2.1 Simulation methodology

3D FE simulation is performed for a LW resonator composed of a SiO_2 guiding layer of 4.7 µm thickness made on a 36°-YX $LiTaO_3$ substrate, operating at a wavelength of λ = 12 µm. The resonator can be regarded as an infinitely extended periodic structure of which one unit cell is shown in Fig. 4.3. Periodic and anti-periodic boundary conditions are applied along the z and x axis respectively with bottom surface kept fixed. Massless aluminum IDT of 3 µm finger width is made on the piezoelectric substrate. A substrate depth of 5λ is kept in the simulation. Eigenmode analysis is used to calculate the electromechanical coupling coefficient K^2 of the device from the metalized surface velocity v_m and free surface velocity v_f using (1.2). To study the effect of nanostructures on the device, ZnO nanorods are designed on the LW sensor with SiO_2 as guiding layer. ZnO nanorods with a square cross-section of size 100 nm are considered, and height h_{ZnO} is varied from 300 nm to 1800 nm. Surface nanorod density (SNRD), defined as the number of rods present on the unit area of the sensor surface is varied from 1 µm^{-2} to 25 µm^{-2}. As illustrated in Fig. 4.3, simulations are carried out for n equal to 6, 9, 12, 15, 18, 21, 24, 27 and 30 nanorods that corresponds to SNRD values of 1, 2.25, 4, 6.25, 9, 12.25, 16, 20.25, and 25 µm^{-2}, respectively. Considering time and memory usage, an *extra fine* tetrahedral mesh setting is used that generated more than 28,000 tetrahedral elements and 240,000 solvable degrees of freedom. The *added mass* feature of COMSOL Multiphysics™ is used to simulate mass loading of the device by applying incremental surface mass density Δm on the sensor surface (includes the top flat portion of the device and the five exposed surfaces of all the nanorods), increasing from 2×10^{-5} kg m^{-2} to 6×10^{-5} kg m^{-2}. The slope of the graph of relative change in frequency against change in surface mass density as per (1.7) gives the mass sensitivity value. The total force F_T at the surface is calculated using the relation

$$F_T = \sqrt{(F_x^2 + F_y^2 + F_z^2)} \tag{4.4}$$

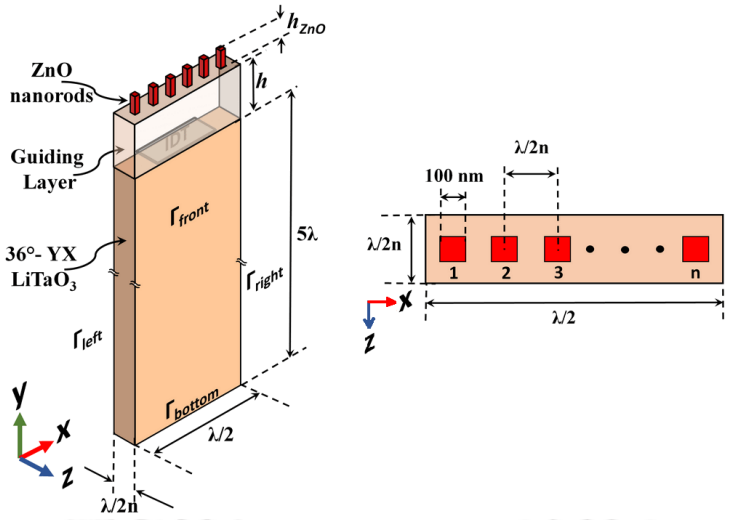

Figure 4.3: Geometry used for 3D FE simulation of Love wave resonator with ZnO nanorods. The top view of the sensor surface shows the distribution of ZnO nanorods.

where F_x, F_y, and F_z are the forces at the sensor surface considering the x, y, and z directions respectively. According to Fig. 4.3, the area averaged total stress $\overline{\sigma}_T$ at the surface is calculated from the total average force $\overline{F}_T$ as:

$$\overline{\sigma}_T = \frac{\overline{F}_T}{(\lambda/2n)(\lambda/2)} \tag{4.5}$$

4.2.2 Coupled resonance with ZnO nanorods

The SH vibrations of the LW device force the nanorods to vibrate in a particular mode depending on the height of nanorods. The variation in normalized values of frequency shift (Δf) with (ω/ω_s), obtained from (4.2) is plotted in Fig. 4.4a. At a critical height of nanorods, when $\omega \approx \omega_s$, both the crystal and the rods start to vibrate in unison causing a transition from inertial loading to elastic loading leading to a sharp swing in the frequency shift. As more nanorods are packed on the surface, the frequency shift becomes more pronounced. The coupled resonance behavior is also observed in FE simulation results shown in Fig. 4.4b. As SNRD is increased, the corresponding swing in the frequency associated with coupled resonance also increases. The first swing in the frequency is observed at $h_{ZnO} = 475$, 460 and 425 nm corresponding to SNRD of 1, 9, and 25 μm^{-2}, respectively. The next frequency swing is seen when h_{ZnO} is equal to 1240, 1190 and 1115 nm for SNRD of 1, 9, and 25 μm^{-2}, respectively.

4.2.3 Effect on mass sensitivity and coupling coefficient

The exact height at which transition from inertial to elastic loading takes place can be obtained by plotting the variation in K^2 with h_{ZnO} as shown in Fig. 4.5a. As h_{ZnO} increases, mode transition occurs when K^2 for mode-1 becomes greater than K^2 for mode-0, and again

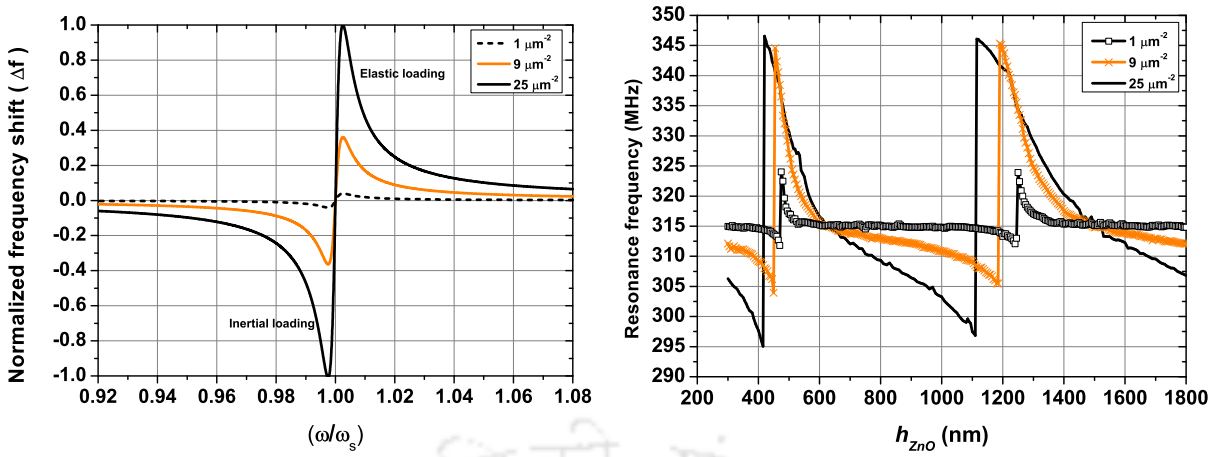

(a) (b)

Figure 4.4: (a) The normalized values of frequency shift (Δf) as a function of (ω/ω_s) obtained using (4.2) for SNRD of 1, 9 and 25 μm^{-2}. (b) Graph showing variation in resonance frequency with ZnO nanorod height for SNRD of 1, 9 and 25 μm^{-2} obtained through FE simulation.

when K^2 for mode-2 becomes greater than K^2 for mode-1. It is observed that, when SNRD is high (25 μm^{-2}), the K^2 values rise and fall sharply near the resonant height, attaining a maximum value of 4.4% at ZnO nanorod height of 475 nm. When SNRD is low (1 μm^{-2}), the K^2 value remains stable at about 2.8% over a wide range of nanorod heights. At coupled resonance, the electromechanical coupling coefficient of the device becomes low, attaining a value of 1.74, 1.31, and 1.05% at SNRD of 1, 9 and, 25 μm^{-2} respectively. This lowering of K^2 is an indication of increase in the losses in the device [179], [180]. Typical vibrational mode shapes for SNRD = 9 μm^{-2} showing mode-0, mode-1, and mode-2 at h_{ZnO} = 400, 1000, and 1600 nm, respectively are presented in Fig. 4.5b–4.5d.

SNRD	Non-coupled resonance			Coupled resonance							
				mode-0				mode-1			
	$S_{f_{max}}$ (m^2/kg)	K^2_{max} (%)	$\overline{\sigma}_T$ (MPa)	h_{ZnO} (nm)	$S_{f_{max}}$ (m^2/kg)	K^2_{max} (%)	$\overline{\sigma}_T$ (MPa)	h_{ZnO} (nm)	$S_{f_{max}}$ (m^2/kg)	K^2_{max} (%)	$\overline{\sigma}_T$ (MPa)
1	58	2.91	10.5	475	770	1.74	235	1240	710	1.46	215
2.25	71	2.73	12.6	470	835	1.57	300	1225	765	1.43	275
4	89	2.71	19.5	470	928	1.43	348	1210	840	1.38	315
6.25	113	2.5	27.5	465	1045	1.36	435	1200	935	1.34	389
9	135	2.6	30.7	460	1155	1.31	446	1190	1030	1.27	397
12.25	175	2.42	37.6	440	1227	1.28	538	1095	1180	1.25	480
16	221	2.4	41.2	435	1275	1.18	638	1165	1135	1.2	567
20.25	269	2.2	51.4	430	1310	1.09	724	1155	1142	1.18	631
25	291	2.1	55.6	425	1338	1.05	801	1150	1294	1.17	688

Table 4.1: Maximum values of mass sensitivity $S_{f_{max}}$, coupling coefficient K^2_{max} and area-averaged stress $\overline{\sigma}_T$ for different SNRD, in the absence of coupled resonance and in the presence of coupled resonance (mode-0 and mode-1).

The mass sensitivity of LW device is obtained by applying the equivalent surface mass density of double-stranded DNA uniformly over the sensor surface. ZnO nanorods of varying height and SNRD are made on the surface of the device. Fig. 4.5a shows the variation in mass sensitivity S_f

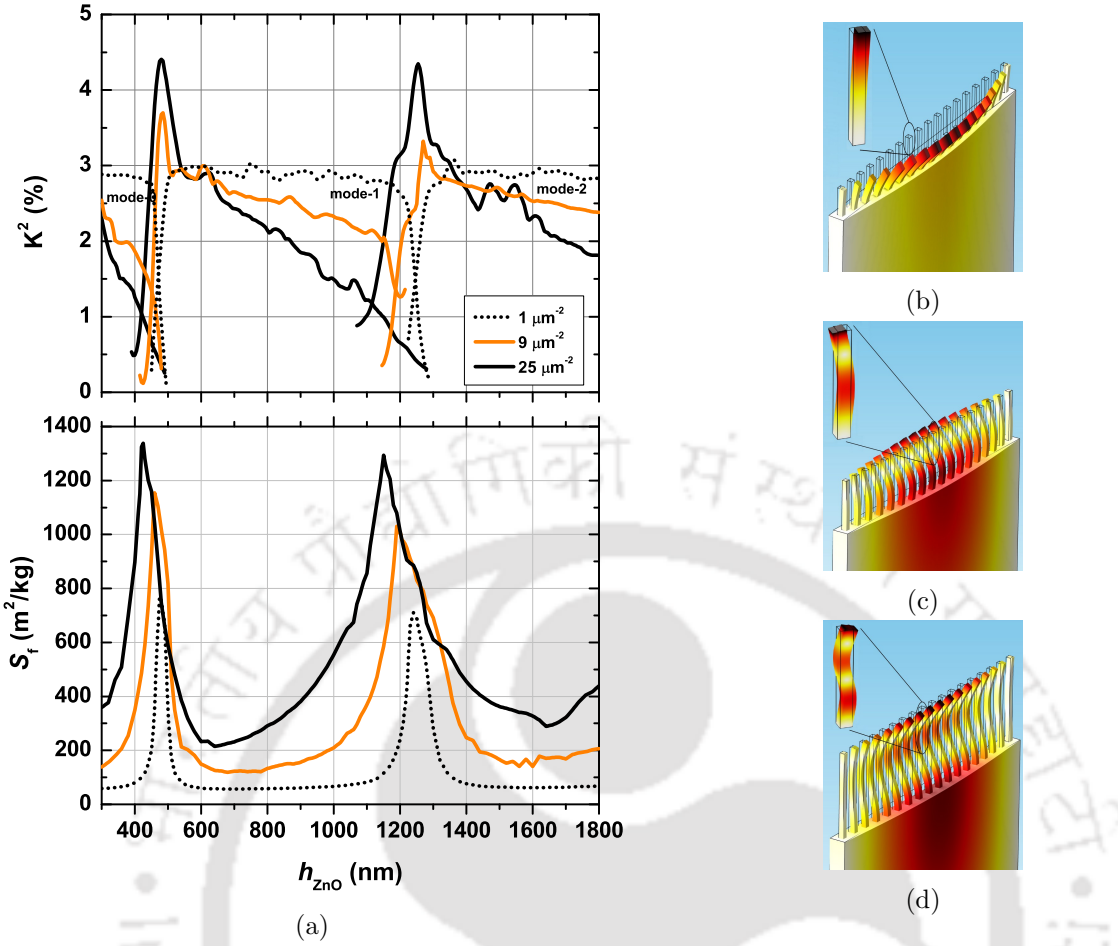

Figure 4.5: (a) Variation in coupling coefficient and mass sensitivity of LW resonator with ZnO nanorod height for SNRD = 1, 9, and 25 µm^{-2}. Illustration of the transition of modes in LW resonator as the height of ZnO nanorods increases. Typical vibrational mode shapes for (b) mode-0, (c) mode-1, and (d) mode-2 at h_{ZnO} = 400, 1000, and 1600 nm, respectively for SNRD = 9 µm^{-2} are shown.

versus ZnO nanorod height for SNRD of 1, 9, and 25 µm^{-2}. Considering the case when SNRD = 1 µm^{-2}, in the absence of coupled resonance (at h_{ZnO} = 800 nm) the mass sensitivity is about 58 m^2 kg^{-1} which is close to the mass sensitivity of a plain SiO_2 based LW device obtained in the previous chapter. However, in the presence of coupled resonance at nanorod heights of 475 and 1240 nm, mass sensitivity increases to 770 and 710 m^2 kg^{-1} respectively. As the nanorod packing density on the surface of the device increases, the mass sensitivity at coupled resonant height also rises.

The stress profile of the area of contact between nanorods and substrate with six ZnO nanorods corresponding to SNRD = 1 µm^{-2} is plotted in Fig. 4.6a and 4.6b for h_{ZnO} = 475 nm and 800 nm, respectively. The magnitude of total stress at the contact surface in the xz plane is represented in the form of color bars and normalized projections. Overall, the stress values at the edges of the contact area between nanorod and substrate, along the x direction are high in comparison to other regions. In the presence of coupled resonance at h_{ZnO} = 475 nm, the stress at the edges of the contact area goes above 26 GPa significantly greater than the stress

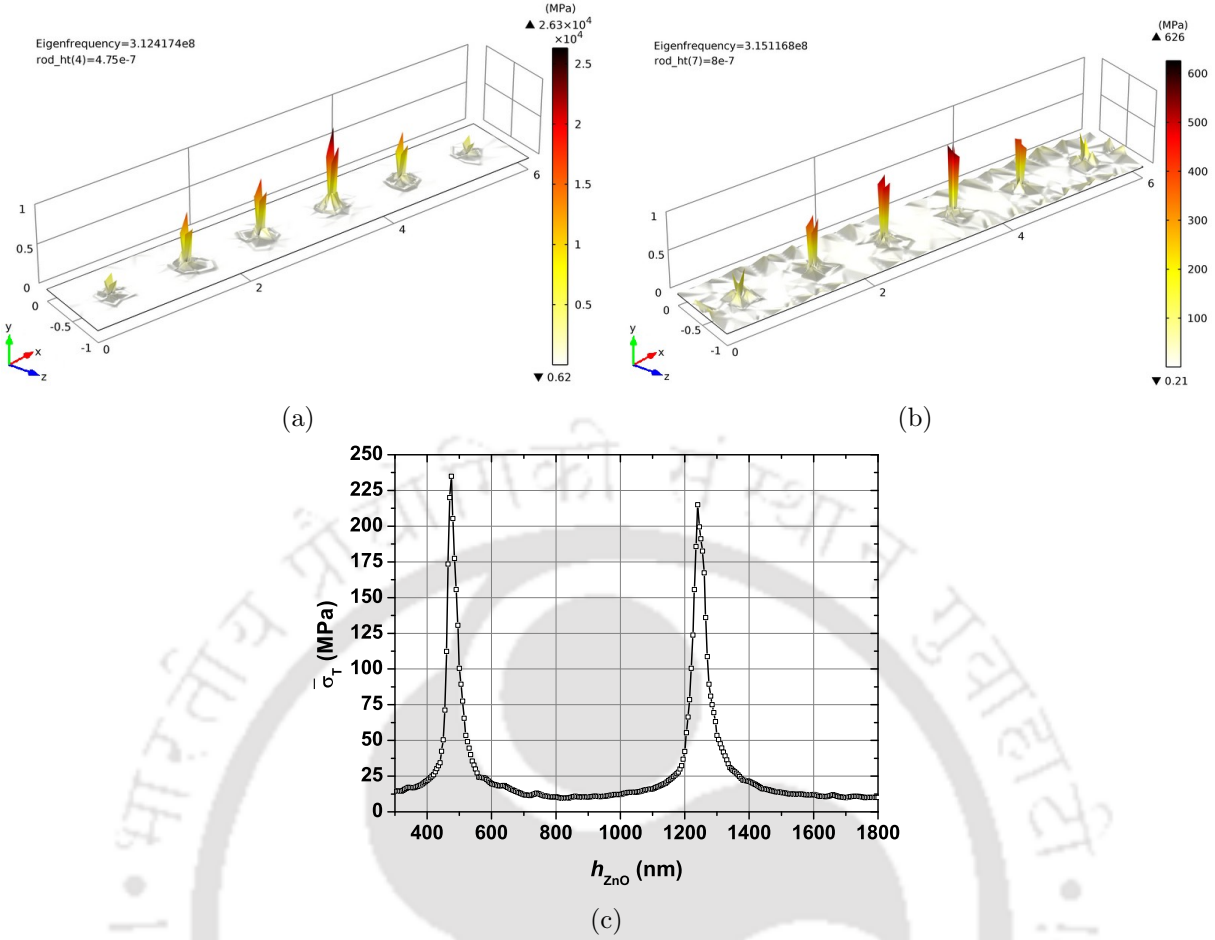

Figure 4.6: Stress profile of the active area of the sensor surface with six ZnO nanorods corresponding to SNRD = 1 µm^{-2}. The magnitude of total stress over the contact surface in the xz plane is represented in the form of color bars and normalized projections for (a) in the presence of coupled resonance ($h_{ZnO} = 475$ nm) and (b) in the absence of coupled resonance ($h_{ZnO} = 800$ nm). The figure shows large vertical stress at the edges of the contact area between nanorod and substrate and it greatly increases at the resonant height $h_{ZnO} = 475$ nm. (c) Plot of magnitude of total stress averaged over the entire top surface of the sensor versus ZnO nanorod height for SNRD of 1 µm^{-2}.

of 0.6 GPa observed in the absence of coupled resonance at $h_{ZnO} = 800$ nm. The magnitude of total stress *averaged* over the entire top surface area of the sensor ($\overline{\sigma}_T$) in the xz plane is calculated for SNRD of 1 µm^{-2} for varying heights of nanorods as shown in Fig. 4.6c. Away from the coupled resonance, the average stress on the surface is about 15 MPa, but near the resonant height, it reaches above 235 MPa.

The maximum values of mass sensitivity $S_{f_{max}}$, coupling coefficient K^2_{max} and area-averaged stress $\overline{\sigma}_T$ for different SNRD, in the presence of coupled resonance (mode-0 and mode-1), and in the absence of coupled resonance are listed in Table 4.1. It is noted that in the absence of coupled resonance, S_f increases with SNRD and attains a maximum value of 291 m^2 kg^{-1} for SNRD of 25 µm^{-2}, i.e. about six times greater than the mass sensitivity of a plain LW device. However, this rise is mainly due to the enhanced inertial mass loading caused by the increase in surface area provided by nanorods for the analyte to attach. On the other hand, in the presence

of coupled resonance, S_f increases to 1338 $m^2\,kg^{-1}$ for SNRD = 25 μm^{-2}, that is about 25 times greater than the mass sensitivity of a plain LW device (section 3.3.1, Table 3.1). The significant increase in the mass sensitivity due to coupled resonance can be attributed to the increase in the contact stiffness of the composite resonator. In the presence of coupled resonance, with increasing SNRD, the mass sensitivity of the device also increases considering both mode-0 and mode-1. Although the mass sensitivity and average stress at SNRD = 25 μm^{-2} are high, the coupling coefficient falls to a low value of 1.05 and 1.17 for mode-0 and mode-1 respectively. Thus, the increase in mass sensitivity comes at the cost of a decrease in coupling coefficient and increase in the losses in the device. The advantage of coupled resonance can be highlighted from the observation that even a low SNRD of 1 μm^{-2} can offer an increase in mass sensitivity by about fifteen times compared to a plain SiO_2 based LW device. The presence of ZnO nanorods of appropriate size on LW sensor will not only provide ample surface area but will also resonate in unison with the device to cause coupled resonance leading to an extremely sensitive biosensing device.

4.3 LW delay line with ZnO nanorods

The section presents the results of FE simulation involving coupled resonance with ZnO nanorods in LW delay line. ZnO nanorods of various heights are designed on the delay line path between input and output IDTs. Typical signature of the coupled resonance showing a negative and positive shift in the phase of the output voltage waveform is obtained. The effect of nanorods on the LW delay line is studied concerning time response, mode transition, mass sensitivity, stress, and insertion loss of the device.

4.3.1 Simulation methodology

The 3D geometry used for the simulation of LW delay line with ZnO nanorods is shown in Fig. 4.7a. Massless input and output IDTs of aluminum with zero thickness and 3 µm width are made on the piezoelectric substrate that generates SAW of wavelength λ = 12 µm propagating in the x direction. SiO_2 guiding layer of thickness 4.7 µm is made on the 36°-YX $LiTaO_3$ substrate. The center-to-center separation L between input and output IDT is 5λ. A damping region of size 2λ is implemented on the left, right and bottom of the delay line to avoid reflections from the edges of the device. Periodic boundary conditions are kept along the z axis to realize IDTs of an infinite aperture that helps to minimize the size of simulation geometry. Considering memory usage of the delay line geometry, only two SNRD values of 0.25 and 1 μm^{-2} are considered which corresponds to n = 18 and 36 nanorods respectively, designed on the top surface of the device. ZnO nanorods with square cross section of size 100 nm with height varying from 350 nm to 1400 nm are kept. The even fingers of the input IDT are connected and given a sinusoidal input voltage of $V_{in} = 5\sin\omega t$ while the odd fingers are connected and grounded. A signal of frequency f = 325 MHz is applied to the input IDT. The even fingers of output IDT are connected and are used as output V_{out} while the odd fingers are connected and grounded. The time response is obtained for 50 ns with a step size of 1 ps. The insertion loss (IL) of

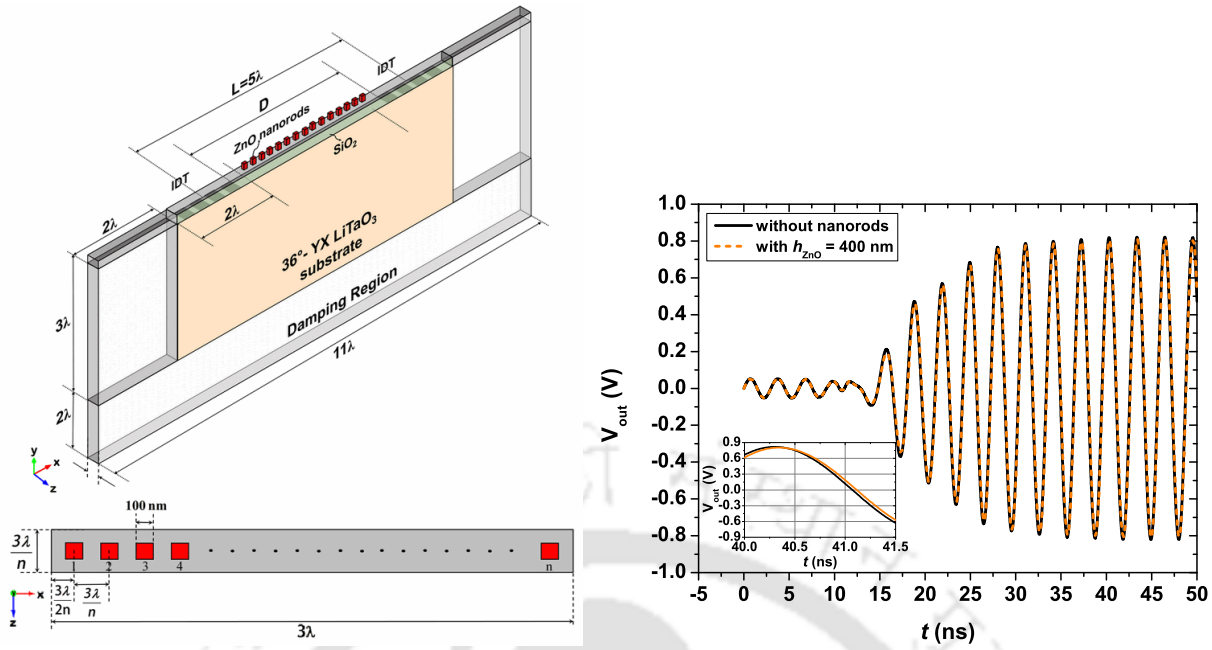

(a) (b)

Figure 4.7: (a) Simulation geometry of the LW delay line device showing the distribution of ZnO nanorods on the surface. (b) Time response showing the output voltage waveform for two cases, one with $h_{ZnO} = 400$ nm and the other without nanorods.

the device is calculated by taking the Fourier transform of the impulse response using (1.5). Mass loading of the device is simulated by applying an incremental surface mass density Δm, from $2{\times}10^{-5}$ kg m^{-2} to $6{\times}10^{-5}$ kg m^{-2} on the active area of the sensor surface. Mass loading causes a time shift Δt in the output voltage waveform. The resulting phase shift $\Delta\phi$ can be obtained by comparing the instantaneous phase (ϕ) of the two voltage waveforms by employing the Hilbert transform [167]. The slope of the graph plotted between relative normalized phase shift and incremental surface mass density gives the mass sensitivity value [21]. The phase mass sensitivity S_ϕ or frequency mass sensitivity S_f of the device is calculated using (1.7). The total force at the sensor surface is calculated using (4.4), and the total area averaged stress is given by

$$\overline{\sigma}_T = \frac{\overline{F}_T}{(3\lambda/n)(3\lambda)} \tag{4.6}$$

4.3.2 Coupled resonance with nanorods

Two LW delay line devices are considered, one comprising nanorods of a specific height and the other a plain LW device without nanorods. Time or phase difference between the output voltage signals of the two devices is then noted. Fig. 4.7b shows the output voltages for the two devices, one without nanorods and the other with nanorod height of 400 nm. It indicates the occurrence of a time delay of 0.041 ns between the two waveforms, equivalent to a phase difference of about 0.084 rad. Thus, the presence of nanorods on the device surface alters the transition time of the wave and produces a time difference in the wave reaching the output IDT.

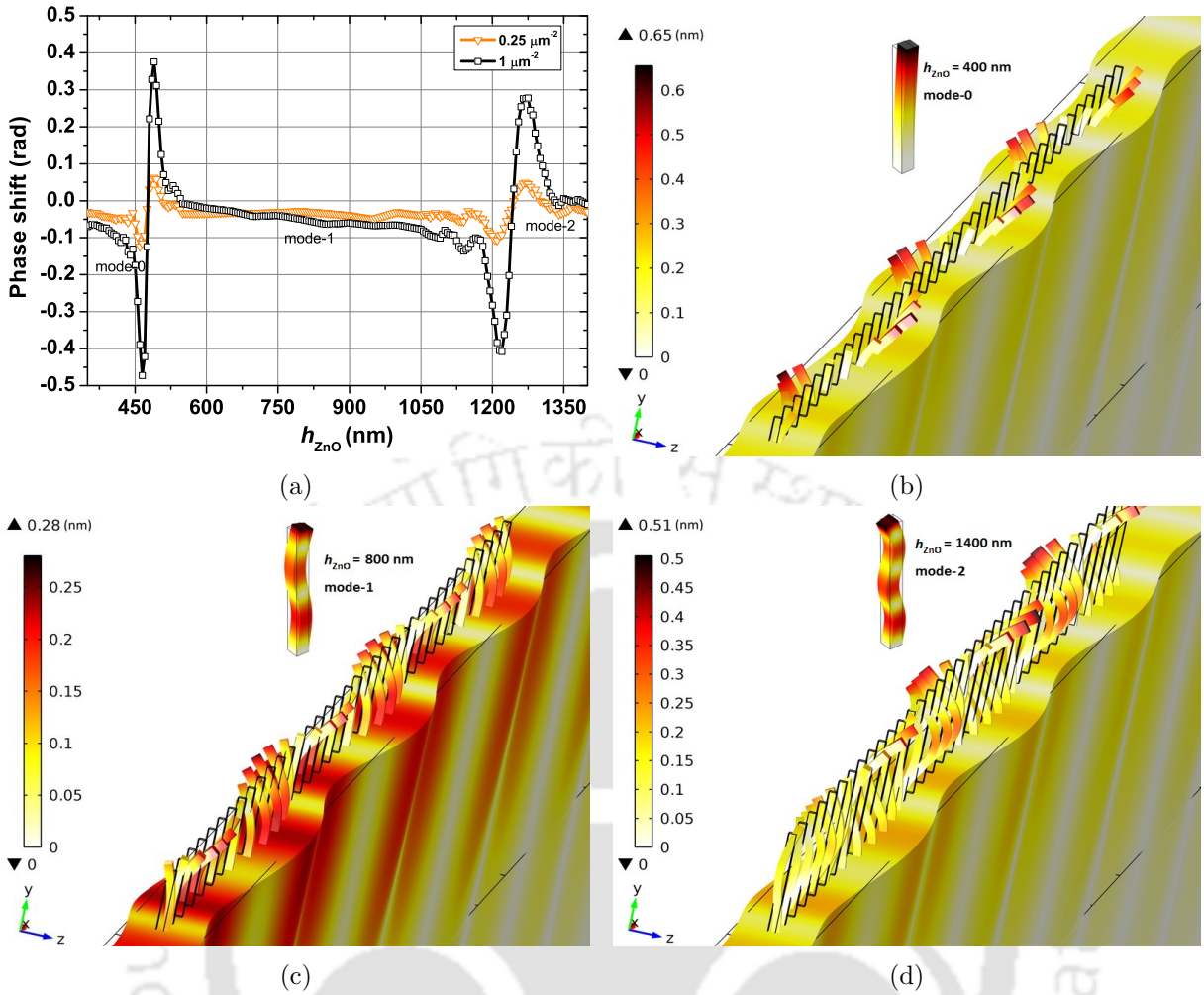

Figure 4.8: (a) Plot of phase shift versus nanorod height for SNRD = 0.25 and 1 µm^{-2}. The phase shift is calculated with respect to a plain device (without nanorods). Illustration of total displacement and mode of vibration for h_{ZnO} equal to (b) 400 nm (c) 800 nm, and (d) 1400 nm corresponding to mode-0, mode-1, and mode-2 respectively.

When the phase difference is plotted with nanorod height varying from 350 nm to 1400 nm, a typical signature of coupled resonance showing a sharp change in the phase difference from negative to positive is obtained as shown in Fig. 4.8a. In the inertial mass loading regime, as nanorod height is increased, the mass on the SAW delay line increases which results in larger time delays and a corresponding increase in the phase difference. Considering SNRD = 1 µm^{-2}, below h_{ZnO} of 460 nm, the nanorods vibrate in mode-0. At h_{ZnO} = 460 nm, the nanorods and substrate both vibrate in unison causing coupled resonance and any further increase in the height of the rods instigates elastic loading leading to a positive swing in the phase shift along with the transition in the mode of vibration from mode-0 to mode-1. As nanorod height is increased further, the phenomenon repeats at h_{ZnO} = 1210 nm indicating another change in mode of vibration from mode-1 to mode-2. The swing in the phase shift due to coupled resonance becomes prominent with a larger packing density of rods on the surface. Fig. 4.8b, 4.8c and 4.8d show the total displacement and mode of vibration of LW device at t = 50 ns, with ZnO nanorods of height 400, 800 and 1400 nm, respectively. The SH motion of LW force

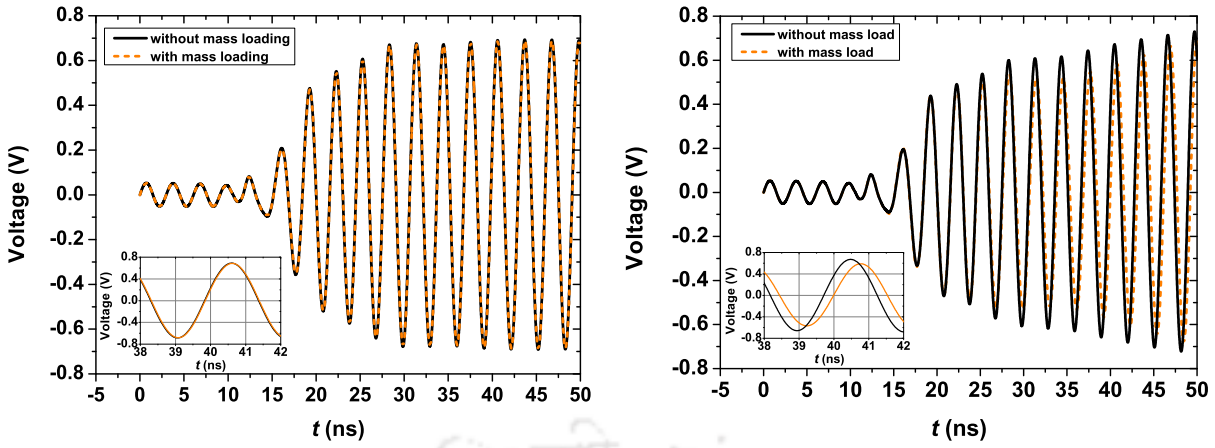

(a) (b)

Figure 4.9: Plot showing the output voltage waveform with and without mass loading for (a) h_{ZnO} = 800 nm and (b) h_{ZnO} = 460 nm. Mass loading is performed with surface mass density $\Delta m = 2{\times}10^{-5}$ kg m^{-2}. Inset of the figure shows the magnified time response with $\Delta t = 0.017$ and 0.28 ns obtained because of mass loading with h_{ZnO} = 800 and 460 nm, respectively.

the nanorods to vibrate in a particular mode depending on its height.

4.3.3 Effect of nanorods on mass sensitivity, stress and insertion loss

Simulation of mass loading is performed by applying an incremental surface mass density on the active area of the sensor, containing nanorods. Two LW devices containing nanorods of the same height are considered, one with added mass and the other without mass loading. Mass loading causes time delay (or phase shift) in the output voltage waveform of the two devices. Fig. 4.9a and 4.9b show the time shift due to mass loading with a surface mass density of $2{\times}10^{-5}$ kg m^{-2} for two different nanorod heights, 800 and 460 nm respectively. In the absence of coupled resonance, at h_{ZnO} = 800 nm, a negligible reduction in peak output voltage and a minimal time delay of 0.017 ns (equivalent to $\Delta\phi$ of 0.035 rad) is obtained upon mass loading. However, for the same mass loading in the presence of coupled resonance at h_{ZnO} = 460 nm, the output voltage gets reduced by about 0.08 V and a larger time delay of 0.28 ns (equivalent to $\Delta\phi$ of 0.57 rad) is obtained. Fig. 4.10a displays the relative change in phase ($\Delta\phi/kD$) occurring as a result of the change in incremental mass loading (Δm) for different nanorod heights considering SNRD = 1 µm^{-2}. The slope of the plot represents the phase mass sensitivity S_ϕ, and it greatly increases near the coupled resonant height (460 nm and 1210 nm). Fig. 4.10b shows the variation in frequency mass sensitivity S_f with nanorod height for SNRD = 0.25 and 1 µm^{-2}. For most of the nanorod heights, S_f remain between 40–80 m^2 kg^{-1}, which is close to the S_f of a plain LW device [141], [181]. However, at the coupled resonant height, high mass sensitivity is obtained. For SNRD = 1 µm^{-2}, at resonant height of 460 and 1210 nm, high mass sensitivity of 728 and 627 m^2 kg^{-1} is obtained respectively. The values of S_f obtained for the ZnO nanorod based LW delay line device is similar to the calculated values of S_f for the resonator case. Thus, for SNRD = 1 µm^{-2}, coupled resonance with ZnO nanorods increase the mass sensitivity by about 15 times compared to the conventional SiO_2 based LW device. The rise in mass sensitivity due

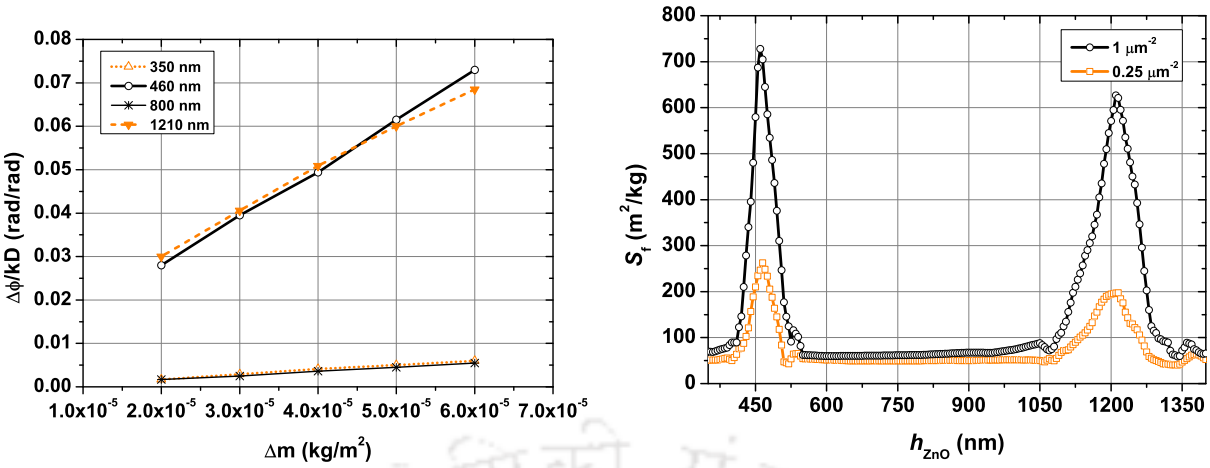

(a) (b)

Figure 4.10: (a) Plot of normalized phase shift ($\Delta\phi/kD$) versus incremental surface mass density (Δm) considering different nanorod heights. (b) Variation in mass sensitivity S_f of device with nanorod height h_{ZnO} for SNRD = 0.25 and 1 μm^{-2}.

to coupled resonance is further enhanced if the packing density of rods is increased.

The variation in area-averaged total stress $\overline{\sigma}_T$ as defined in (4.6) at the interface between nanorod and substrate with time is plotted in Fig. 4.11 for different nanorod heights. The stress at the interface increases with time and tends to stabilize after 30 ns. It is noted that coupled resonance causes a substantial increase in the contact stress. At h_{ZnO} = 460 and 1210 nm, i.e. in the presence of coupled resonance, the contact stress becomes greater than 2.8 MPa. On the other hand, in the absence of coupled resonance, at h_{ZnO} = 800 nm, the contact stress remains below 0.1 MPa.

The impulse response of the device is obtained by applying a unit impulse voltage signal of 1.5 ns duration at the input IDT. Fig. 4.11b shows the impulse response of device with nanorod height of 800 nm. The electromagnetic feed-through effect seen at the beginning of the impulse response is 100 times less than the applied unit impulse signal. The frequency response of the delay line was obtained by taking the Fourier transform of the impulse response voltage at the output IDT. Since the time response simulation contained a limited number of data points, the frequency response signal was improved by zero padding the output voltage signal [127]. Fig. 4.12a shows IL of device considering plain surface, h_{ZnO} = 460, 490, and 800 nm. The inset of the figure represents the magnified portion of IL between 310-345 MHz. For the plain SiO_2 surface the device shows a minimum insertion loss IL_{min} of -32.2 dB at 327 MHz. In the absence of coupled resonance, at h_{ZnO} = 800 nm the insertion loss increases marginally by about 0.1 dB, with IL_{min} = -32.3 dB at 326.8 MHz. However, in the presence of coupled resonance, at h_{ZnO} = 460 nm, IL_{min} of -33 dB is obtained at a decreased frequency of 319.5 MHz. Also, when h_{ZnO} = 490 nm increase in the frequency is observed with IL_{min} = -32.8 dB at 333.1 MHz. It shows that coupled resonance with ZnO nanorods of SNRD = 1 μm^{-2} causes an increase in the insertion loss by about 0.8 dB along with positive and negative frequency shifts around the resonant height. The variation of IL_{min} of the device with nanorod height for SNRD = 0.25 and 1 μm^{-2} is plotted in Fig. 4.12b. The device without nanorods offers IL_{min} of -32.2 dB.

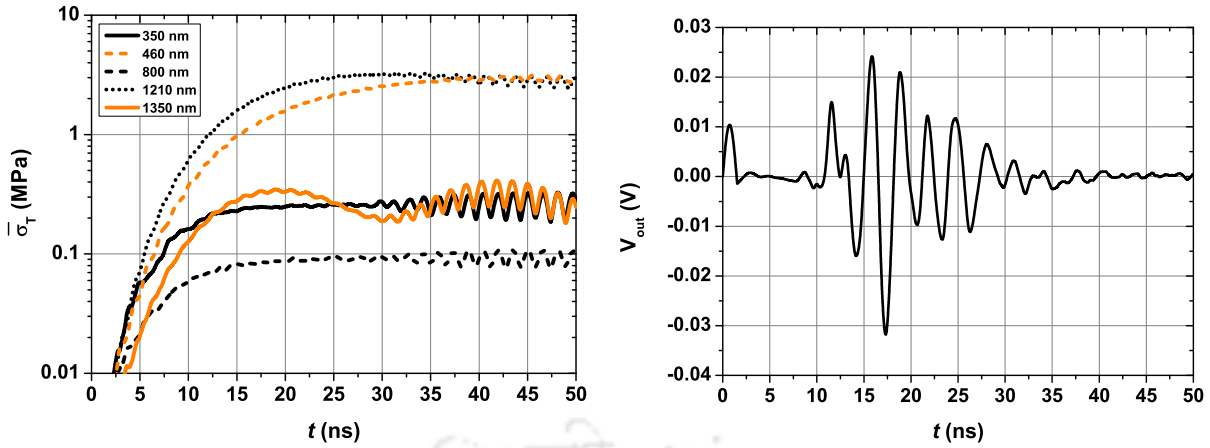

(a) (b)

Figure 4.11: (a) Time response of the area averaged total stress $\overline{\sigma}_{\mathrm{T}}$ at the top surface of the LW delay line device considering SNRD = 1 μm^{-2} and different nanorod heights. (b) Impulse response of the LW delay line device with h_{ZnO} = 800 nm.

Δm (kg m^{-2})	Δt (ns) for different values of h_{ZnO} (nm)				
	350 nm	460 nm	800 nm	1210 nm	1350 nm
2×10^{-5}	0.017	0.28	0.017	0.3	0.016
3×10^{-5}	0.029	0.395	0.025	0.406	0.034
4×10^{-5}	0.041	0.494	0.036	0.509	0.047
5×10^{-5}	0.05	0.615	0.045	0.6	0.055
6×10^{-5}	0.06	0.73	0.055	0.685	0.061
S_ϕ (m^2 kg^{-1})	107	1120	96	964	111
S_f (m^2 kg^{-1})	69.6	728	62.4	626.6	72.2
$\overline{\sigma}_T$ (MPa)	0.25	2.9	0.09	2.8	0.35
IL_{min} (dB)	-32.1	-33	-32.3	-32.9	-32.7

Table 4.2: Time delay due to mass loading, mass sensitivities, area averaged total stress and minimum insertion loss listed for different nanorod heights.

As nanorod height is increased, the IL starts to deteriorate and becomes maximum near the coupled resonant height. Further increase in the height of the nanorods cause mode transition (from mode-0 to mode-1) and IL again starts to improve. The rise and dip in the insertion loss are again observed when the transition occurs from mode-1 to mode-2. This type of swing in the IL_{min} was also observed by Mchale *et al.* [152] in the experimental analysis of quartz-based LW device with a polymer guiding layer. It is also noted that larger the packing density of rods, increased IL is obtained near the coupled resonance.

The time delay due to mass loading, mass sensitivities, stable values of area-averaged total stress and insertion loss for different nanorod heights are listed in Table 4.2. In the presence of coupled resonance, at h_{ZnO} = 460 and 1210 nm, significant time delays of about 0.28 and 0.3 ns (upon mass loading with 2×10^{-5} kg m^{-2}) along with high S_f of 728 and 627 m^2 kg^{-1} are obtained respectively. Coupled resonance also leads to increase in the area averaged stress values. Although coupled resonance provides high mass sensitivity, it comes at the cost of increased insertion losses in the device.

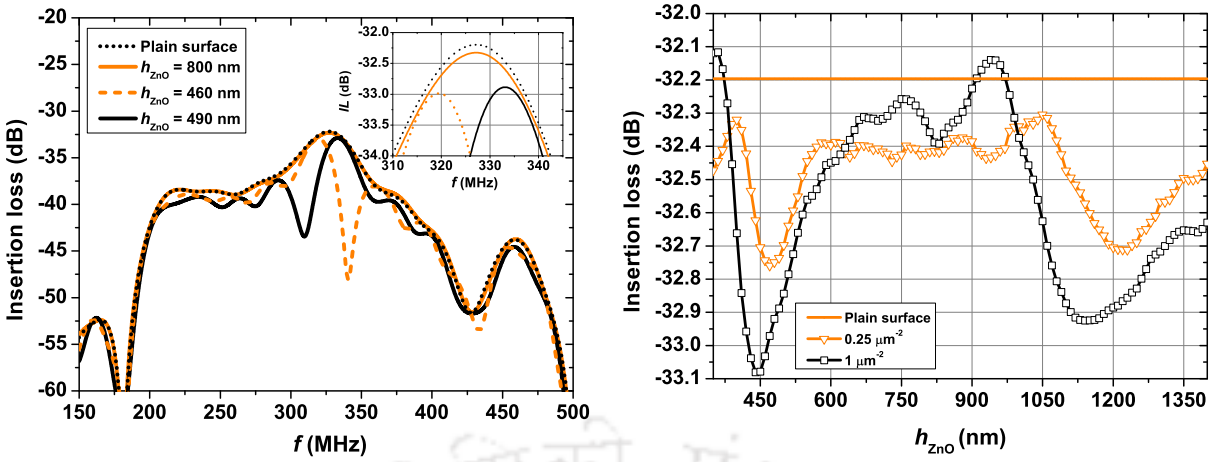

(a) (b)

Figure 4.12: (a) Insertion loss of delay line device considering plain surface, and h_{ZnO} = 460, 490, and 800 nm for SNRD = 1 μm^{-2}. The inset of the figure represents the magnified portion of insertion loss between 310–345 MHz. (b) Variation in minimum insertion loss of delay line device with nanorod height considering SNRD = 0.25 and 1 μm^{-2}

4.4 Summary

The chapter has presented 3D FE simulation of coupled resonance phenomenon with ZnO nanorods for both resonator and delay line configurations. ZnO nanorods of square cross section of various heights and SNRD are designed on the surface of the devices. At an appropriate size of nanorods, both the substrate and nanorods vibrate in unison causing a sharp swing in the frequency or phase shift of the device, leading to the transition from inertial to elastic loading.

Eigenmode analysis is performed for the LW resonator composed of 36°-YX $LiTaO_3$ and SiO_2 guiding layer with ZnO nanorods made on the surface of the device. The nanorods are of square dimension of size 100 nm with height varying from 300 to 1400 nm, and SNRD from 1 μm^{-2} to 25 μm^{-2}. The coupled resonance behavior is observed in FE simulation results. As SNRD is increased, the corresponding swing in the frequency associated with coupled resonance also increases. The first swing in frequency is observed at h_{ZnO} equal to 475, 460, and 425 nm corresponding to SNRD of 1, 9, and 25 μm^{-2}, respectively. The next frequency swing is seen when h_{ZnO} is equal to 1240, 1190, and 1115 nm for SNRD of 1, 9, and 25 μm^{-2}, respectively. At coupled resonance, the electromechanical coupling coefficient of the device becomes low, attaining a value of 1.74, 1.31, and 1.05% at SNRD of 1, 9, and 25 μm^{-2}, respectively. This lowering of coupling coefficient is an indication of an increase in the losses in the device. In the absence of coupled resonance, S_f increases with SNRD and attains a maximum value of 291 m^2 kg^{-1} for SNRD of 25 μm^{-2}, that is about six times greater than the mass sensitivity of a plain LW device. However, this rise is mainly due to the enhanced inertial mass loading caused by the increase in surface area provided by nanorods for the analyte to attach. On the other hand, in the presence of coupled resonance, S_f increases to 1338 m^2 kg^{-1} for SNRD = 25 μm^{-2}, that is about 25 times greater than the mass sensitivity of a plain LW device. The significant increase in mass sensitivity due to coupled resonance can be attributed to the increase in contact

stiffness of the composite resonator. Although the mass sensitivity and average stress at SNRD = 25 μm^{-2} are high, the coupling coefficient falls to a low value of 1.05 and 1.17 for mode-0 and mode-1, respectively. Thus, the increase in mass sensitivity comes at the cost of a decrease in coupling coefficient and increase in the losses in the device.

FE simulation of LW delay line containing ZnO nanorods is performed with SNRD = 0.25 and 1 μm^{-2}. The presence of nanorods on the device surface alters the transition time of the wave and produces a time difference in the wave reaching the output IDT. When the phase difference is plotted with nanorod height varying from 350 nm to 1400 nm, a typical signature of coupled resonance resulting in a sharp change in phase difference from negative to positive is obtained. Simulation of mass loading is performed by applying an incremental surface mass density on the active area of the sensor containing nanorods. In the presence of coupled resonance, at h_{ZnO} = 460 and 1210 nm, significant time delays along with high S_f of 728 and 627 $m^2\,kg^{-1}$, respectively are obtained. Coupled resonance also leads to increase in the area averaged stress at the interface between nanorod and the substrate. Although coupled resonance provides high mass sensitivity, the insertion loss of the device increases. The minimum insertion loss goes through oscillations, indicating the transition in the mode of vibration as nanorod height is varied.

Chapter 5

Coupled resonance in SH-SAW device with SiO_2 micro-ridges

> No problem is too small or too trivial if we can really do something about it.
>
> Richard Feynman

Shear horizontal surface acoustic wave (SH-SAW) devices generate a shear wave with vibration components perpendicular to the direction of wave propagation and parallel to the surface, and have been extensively used for biosensing purposes. Piezoelectric substrates such as 36°-YX $LiTaO_3$, 41°-YX $LiNbO_3$, 90°-AT and ST quartz are used for generating the SH wave. Hur *et al.* [182] have demonstrated SH-SAW sensor with sensing and reference channels in an oscillator configuration for DNA hybridization sensing. Bergaoui *et al.* [183] have experimentally estimated the sensitivity of gold coated 36°-YX $LiTaO_3$ based SH-SAW device by detecting different concentrations of streptavidin as an analyte. Detection of viral agents such as sin nombre virus (SNV) using SH-SAW device have also been reported [6]. Kwon *et al.* [184] have developed SH-SAW sensor to detect protein molecules and immunoglobulins in liquid solutions on the delay line SAW device. The sensitivity of SH-SAW device can be improved by coating a suitable guiding layer and converting it into a LW device. Micro-cavities filled with different materials, designed on SH-SAW delay line path for the reduction in insertion loss, improvement in power efficiency and enhancement of mass sensitivity were also studied through simulations and experiments in [133]–[135]. This chapter presents FE simulation of SH-SAW resonator and delay line device involving coupled resonance with SiO_2 micro-ridges made on the surface along the wave propagation direction. The ridges help to guide the SH wave, increase the sensor surface area and also cause coupled resonance at a particular size increasing the mass sensitivity of the device.

The structure of a SH-SAW device with SiO_2 micro-ridges made on a 36°-YX $LiTaO_3$ substrate is shown in Fig. 5.1. SiO_2 ridges 1 µm apart are made on the delay line path along the direction of wave propagation. The SiO_2 ridges can be biofunctionalized to detect DNA,

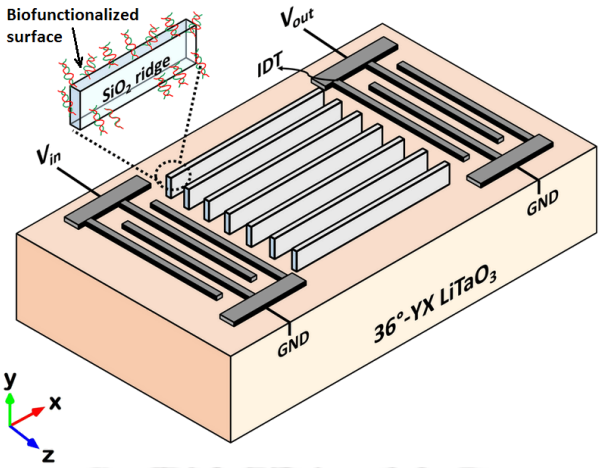

Figure 5.1: Diagram showing micro-ridges of SiO_2 made along the wave propagation direction on the surface of SH-SAW device.

protein or any other antibody/antigen combination. Two similar devices, one acting as a sensing channel and the other as a reference are made. The analyte to be detected is applied to both the devices and after PBS washing it would remain attached only on the sensing channel causing a phase and frequency shift between the two devices. At a certain height of the ridges, coupled resonance will occur causing the ridges to vibrate in unison with the device, leading to a significant increase in the mass sensitivity of the device. The chapter presents FE simulation of SH-SAW device with SiO_2 micro-ridges considering both resonator and delay line geometries. Eigenmode analysis is used to study the variation in the resonance frequency of the resonator and transition in the mode of vibration with increasing ridge height. FE simulation is carried out to calculate mass sensitivity, coupling coefficient and interface stress of the device. Effect of SiO_2 ridges on time response of SH-SAW delay line device is studied by varying the ridge height. Mass sensitivity of delay line is calculated by noting the time and phase shifts upon mass loading. FFT of the impulse response is used to calculate the insertion loss of the device.

5.1 SH-SAW resonator with SiO_2 micro-ridges

The 3D geometry used for FE simulation is shown in Fig. 5.2a. A one port resonator composed of 36°-YX $LiTaO_3$ substrate is designed with periodic and anti-periodic boundary conditions applied along the z and x axis respectively. The resonator generates a standing wave of $\lambda = 12$ µm. A substrate width of $\lambda/12$ is considered. The bottom surface is kept fixed. Massless aluminum IDT finger of size 3 µm is made on the substrate. Devices are simulated with SiO_2 ridges of width $w = 500$ nm, 1 µm apart and height h_t varying from 200 to 4000 nm made along the direction of wave propagation on the device surface. Extremely fine tetrahedral mesh setting is used for the simulation. Eigenmode study is used to calculate the resonance frequency, mode shapes, stress and electromechanical coupling coefficient of the device. The coupling coefficient is calculated using the relation (1.2). The total displacement of the SAW is given by $\sqrt{(|u_x|^2 + |u_y|^2 + |u_z|^2)}$ where u_x, u_y, and u_z are the particle displacements in the x, y, and z directions respectively. The mass sensitivity of the resonator is calculated as described in

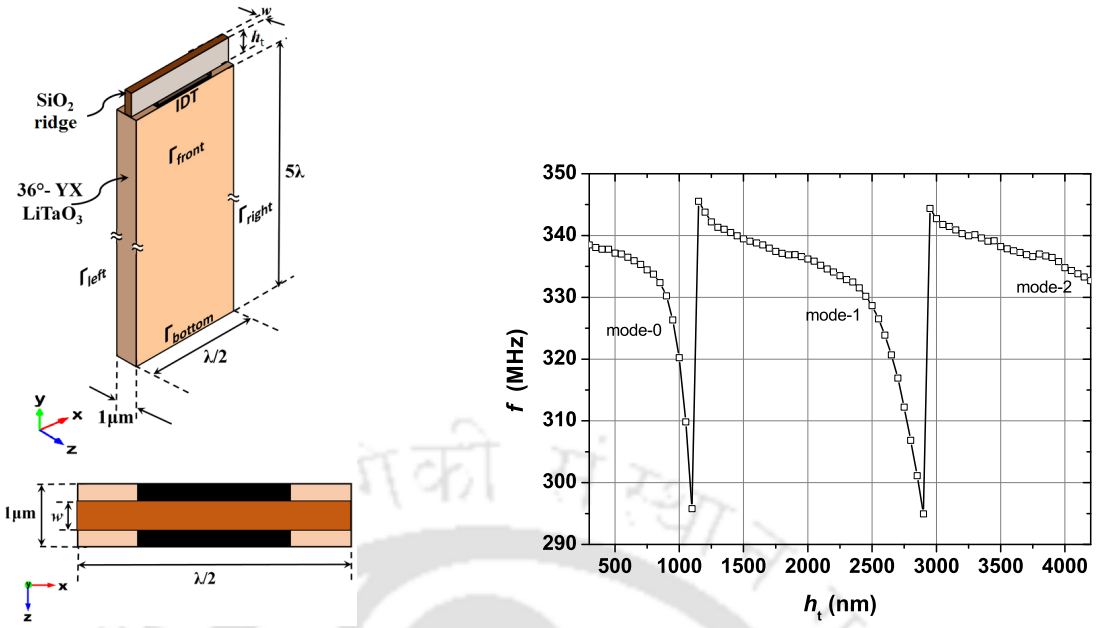

(a) (b)

Figure 5.2: (a) 3D FE simulation geometry of SH-SAW resonator with SiO_2 micro-ridges. (b) Plot showing the variation in the resonance frequency f with ridge height h_t.

section 4.2.1 about the LW resonator with nanorods by applying the incremental surface mass density on the top surface of the sensor. The total force at the sensor surface is given by 4.4, and the area averaged stress considering the interface between ridge and the substrate is given by the relation

$$\overline{\sigma}_T = \frac{\overline{F}_T}{(\lambda/2)(\lambda/12)} = \frac{\overline{F}_T}{\lambda^2/24} \tag{5.1}$$

5.1.1 Coupled resonance

The SH vibrations of the device force the ridges to vibrate in a particular mode depending on the height of the ridges. The variation in resonance frequency with ridge height is plotted in Fig. 5.2b. As the height of SiO_2 ridges increases, the resonance frequency of the device decreases due to inertial mass loading. At a critical ridge height h_t = 1150 and 2950 nm, both the substrate and the ridge start to vibrate in unison causing a transition from inertial loading to elastic loading leading to a sharp swing in the resonance frequency at mode transitions.

Fig. 5.3 shows the variation in shear displacement component u_z with the device depth for ridge heights 500, 2000 and 3500 nm along with their modes shapes. Shear displacement component is calculated along a line passing through the center of the device, starting from the top of the SiO_2 ridge to the bottom surface. When h_t = 500 nm, mode-0 is excited with a maximum shear displacement of about 90 nm observed at the topmost ridge surface in the $+z$ direction and decreases with the device depth (Fig. 5.3b). When h_t = 2000 nm, mode-1 is excited (Fig. 5.3c) with a maximum shear displacement magnitude of about 100 nm, changing

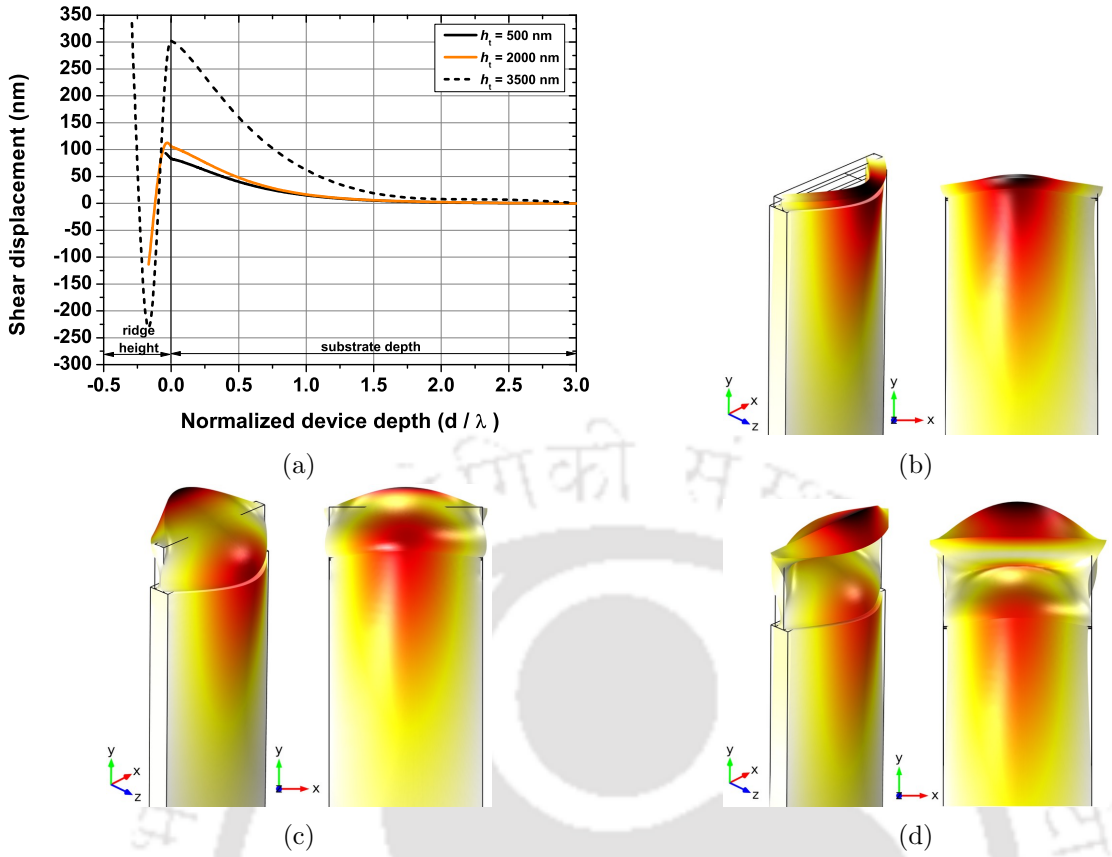

Figure 5.3: (a) Variation in shear displacement component with normalized device depth for ridge heights h_t = 500, 2000 and 3500 nm associated with mode-0, mode-1 and mode-2 respectively. (b) Mode shapes shown for ridge heights h_t (b) 500 nm (mode-0), (c) 2000 nm (mode-1), and (d) 3500 nm (mode-2).

from $-z$ to $+z$ direction along the ridge height. When h_t = 3500 nm, mode-2 is excited (Fig. 5.3d) with maximum shear displacement swinging sharply from $+z$ to $-z$ and again to $+z$ along the ridge height. It is noted that the change in shear displacement is very sharp along the ridge height than along the substrate depth. For all the modes, at a device depth of about one wavelength, most of the wave energy diminishes, and the shear displacement component reduces by about six times from its maximum value.

5.1.2 Effect on mass sensitivity and coupling coefficient

The exact height at which transition from inertial to elastic loading takes place can be obtained by plotting the variation in K^2 with h_t as shown in Fig. 5.4. As h_t increases, mode transition occurs when K^2 for mode-1 becomes greater than K^2 for mode-0, and again when K^2 for mode-2 becomes greater than K^2 for mode-1. It is observed that the K^2 values rise and fall sharply near the resonant height, attaining a maximum value of about 6.8%. However, at coupled resonance, the K^2 of the device becomes low attaining a value of 2.2% and 1.7% at h_t = 1150 and 2950 nm respectively. Low K^2 near coupled resonance is an indication of increase in the losses in the device.

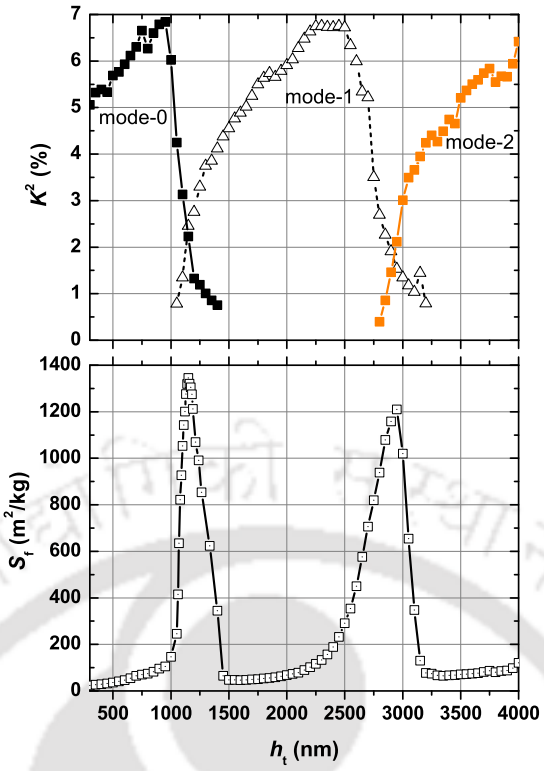

Figure 5.4: Variation in coupling coefficient and mass sensitivity of SH-SAW device with SiO_2 ridge height.

The mass sensitivity of the device is obtained by applying an incremental surface mass density uniformly on the sensor surface. SiO_2 micro-ridges of various heights are made on the device surface. Fig. 5.4 shows the variation in mass sensitivity S_f versus SiO_2 ridge height h_t. For most of the heights, in the absence of coupled resonance, the mass sensitivity value remains between 40–100 $m^2\,kg^{-1}$. However, in the presence of coupled resonance at ridge heights of 1150 and 2950 nm, mass sensitivity increases to 1345 and 1210 $m^2\,kg^{-1}$ respectively.

The stress profile of the area of contact between the micro-ridge and substrate is plotted in Fig. 5.5a and 5.5b for $h_t = 500$ and 1150 nm respectively. The magnitude of total stress at the contact surface in the xz plane is represented in the form of color bars and normalized projections. Overall, the stress values at the edges of the contact area between ridge and the substrate surface are high in comparison to other regions. In the presence of coupled resonance at $h_t = 1150$ nm, the stress at the edges of the contact area goes above 1400 MPa, significantly greater than the stress of 27 MPa observed in the absence of coupled resonance at $h_t = 500$ nm. The magnitude of total stress averaged over the entire top surface area of the sensor ($\overline{\sigma}_T$) in the xz plane is calculated for various heights of SiO_2 ridges as shown in Fig. 5.5c. Away from the coupled resonance, the average stress on the surface stays between 2.5–4 MPa, but at coupled resonance, it reaches around 165 MPa. The significant increase in the mass sensitivity due to coupled resonance can be attributed to the increase in the contact stiffness of the composite resonator. However, the increase in mass sensitivity comes at the cost of a decrease in coupling coefficient and increase in the losses in the device.

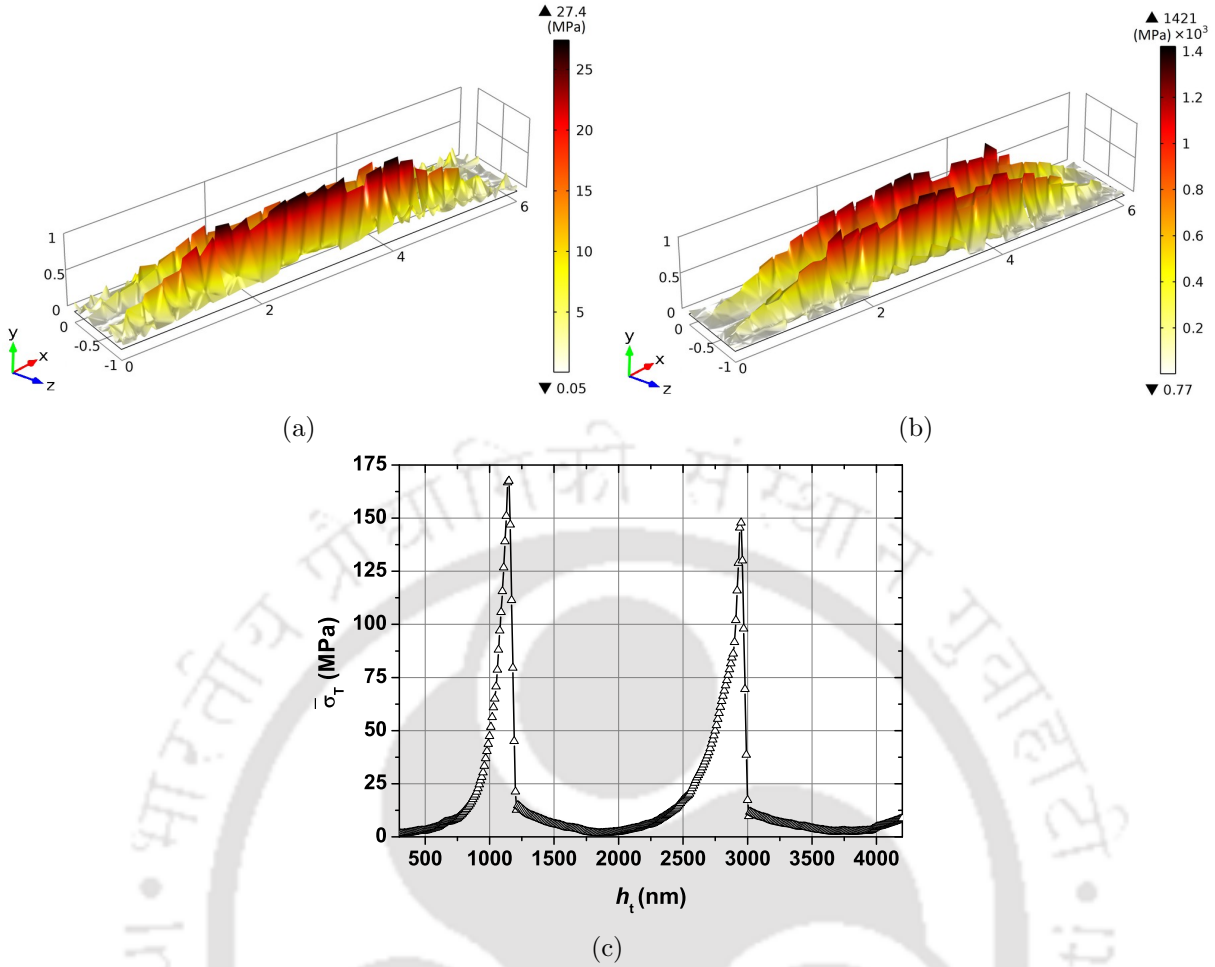

Figure 5.5: Stress profile of the active area of the sensor surface with SiO_2 micro-ridges. The magnitude of the total stress at the contact surface in the xz plane is represented in the form of color bars and normalized projections for (a) in the absence of coupled resonance ($h_t = 500$ nm) and (b) in the presence of coupled resonance ($h_{ZnO} = 1150$ nm). The figure shows large vertical stress at the edges of the contact area between ridge and the substrate and it greatly increases at the resonant height $h_t = 1150$ nm. (c) Plot of magnitude of the total stress averaged over the entire top surface of the sensor versus ridge height.

5.2 SH-SAW delay line with SiO_2 micro-ridges

The 3D geometry used for the simulation of SH-SAW delay line with SiO_2 micro-ridges is shown in Fig. 5.6a. Massless input and output IDT fingers of aluminum with zero thickness and 3 µm width are made on a 36°-YX $LiTaO_3$ substrate that generates SH-SAW of wavelength $\lambda = 12$ µm propagating in the x direction. A substrate width of $\lambda/12$ is considered. SiO_2 micro-ridges of width $w = 500$ nm and various heights h_t in the range of 500 to 3500 nm are made along the direction of wave propagation. The center-to-center separation L between the input and output IDT is 5λ. A damping region of size 2λ is implemented on the left, right and bottom of the delay line to avoid reflections from the edges of the device. Periodic boundary conditions are kept along the z axis to realize IDTs of an infinite aperture that helps to minimize the size of simulation geometry. The even fingers of the input IDT are connected and given a sinusoidal input voltage of $V_{in} = 5\ \sin\omega t$ while the odd fingers are connected and grounded. A

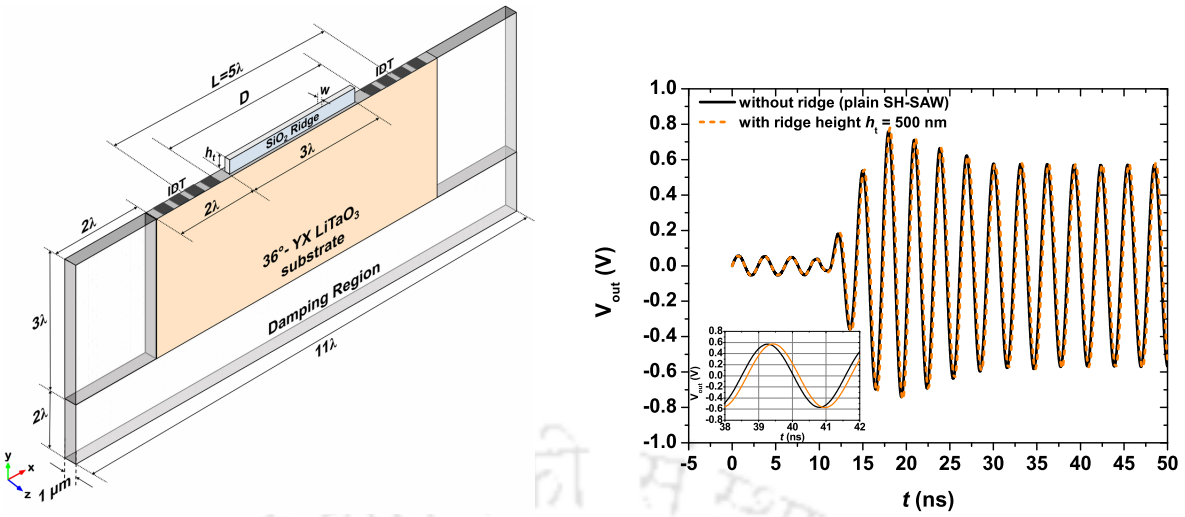

(a) (b)

Figure 5.6: (a) Simulation geometry of SH-SAW delay line device with an SiO_2 micro-ridge. (b) Time response showing the output voltage waveform for two cases, one with $h_t = 500$ nm and the other without ridges.

frequency of $f = 325$ MHz is applied to the input IDT. The even fingers of output IDT are connected and are used as output V_{out} while the odd fingers are connected and grounded. The time response is obtained for 50 ns with a step size of 1 ps. The insertion loss (IL) of the device is calculated by taking the Fourier transform of the impulse response using (1.5). Mass loading of the device is simulated by applying an incremental surface mass density Δm, from $2{\times}10^{-5}$ kg m^{-2} to $6{\times}10^{-5}$ kg m^{-2} on the sensor surface. Mass loading causes a time shift Δt in the output voltage waveforms. The resulting phase shift $\Delta\phi$ can be obtained by comparing the instantaneous phase ϕ of the two voltage waveforms by employing the Hilbert transform. Mass sensitivity is calculated from the slope of the graph of normalized phase shift versus incremental surface mass density. The phase mass sensitivity S_ϕ or frequency mass sensitivity S_f of the device is calculated using (1.7). The total force F_T at the sensor surface is calculated using (4.4), and the area averaged stress $\overline{\sigma}_T$ is given by the relation

$$\overline{\sigma}_T = \frac{\overline{F}_T}{(\lambda/12)(3\lambda)} = \frac{\overline{F}_T}{\lambda^2/4} \tag{5.2}$$

5.2.1 Coupled resonance

Two SH-SAW delay line devices are considered, one with SiO_2 ridges of specific height and the other a plain SH-SAW device (without ridges). Time or phase difference between the output voltage signals of the two devices is then noted. Fig. 5.6b shows the output voltages for two devices, one without ridges and the other with ridge height of 500 nm. It indicates the occurrence of a time delay of 0.16 ns between the two waveforms, equivalent to a phase difference of about 0.33 rad. Thus, the presence of ridges on the device surface alters the transition time of the wave

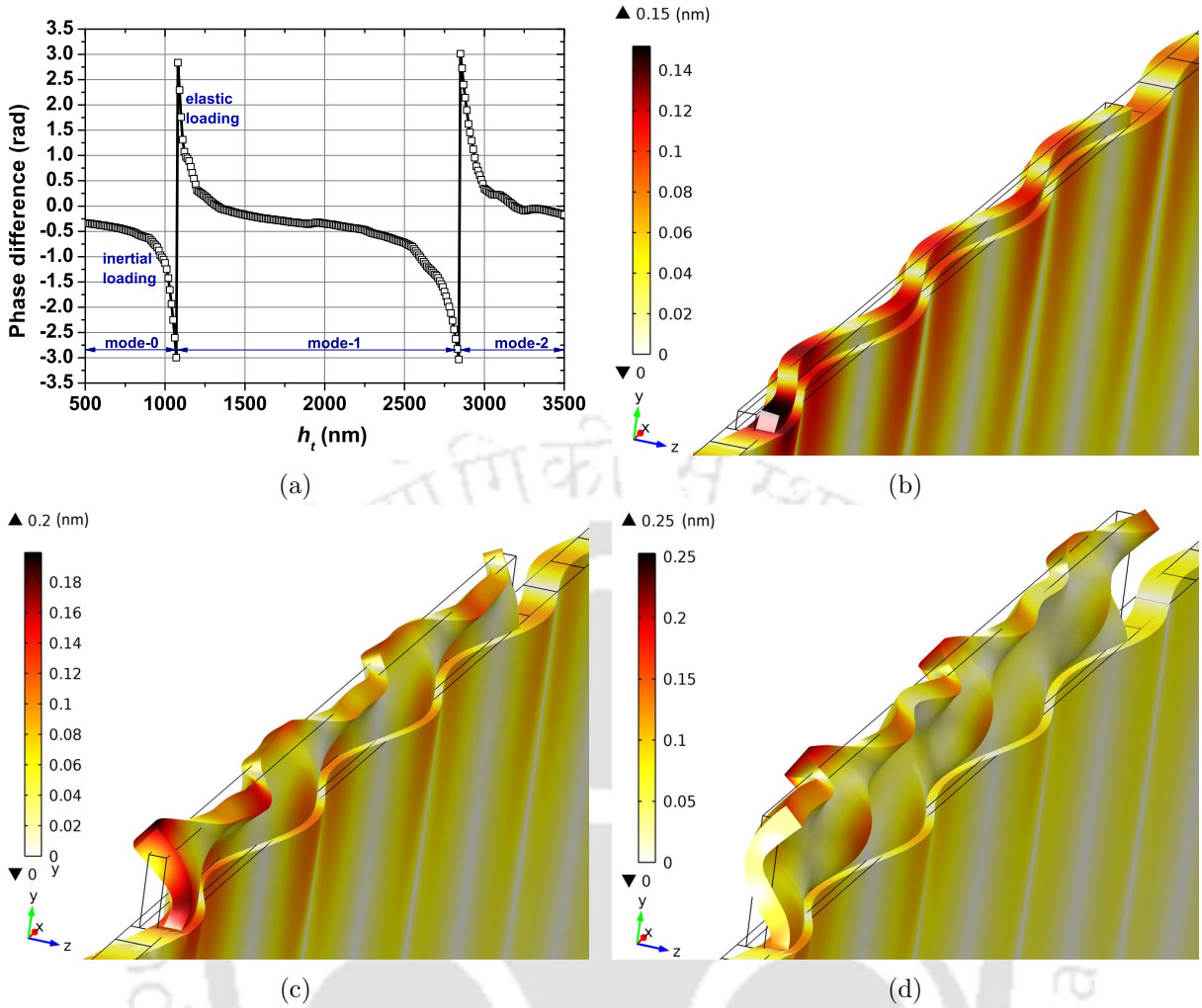

Figure 5.7: (a) Plot of phase difference versus SiO_2 ridge height. The phase difference is calculated with respect to a plain device without ridges. Illustration of total displacement and mode of vibration for h_t equal to (b) 500 nm (c) 2000 nm and, (d) 3500 nm corresponding to mode-0, mode-1, and mode-2, respectively.

and produces a time difference in the wave reaching the output IDT. When the phase difference is plotted with ridge height varying from 500 to 3500 nm, a typical signature of coupled resonance resulting in a sharp change in phase difference from negative to positive is obtained as shown in Fig. 5.7a. In the inertial mass loading regime, as ridge height is increased, the mass on the SAW delay line increases which results in larger time delays and a corresponding increase in phase difference. Below $h_t = 1050$ nm the ridges vibrate in mode-0. Any further increase in the height of the ridge causes transition in the mode of vibration from mode-0 to mode-1 and instigates elastic loading leading to a positive swing in the phase shift. As ridge height is increased further, the phenomenon repeats at $h_t = 2850$ nm indicating another change in the mode of vibration from mode-1 to mode-2. The total displacement and the mode of vibration for $h_t = 500$, 2000, and 3500 nm corresponding to mode-0, mode-1 and mode-2 are shown in Fig. 5.7b–5.7d respectively.

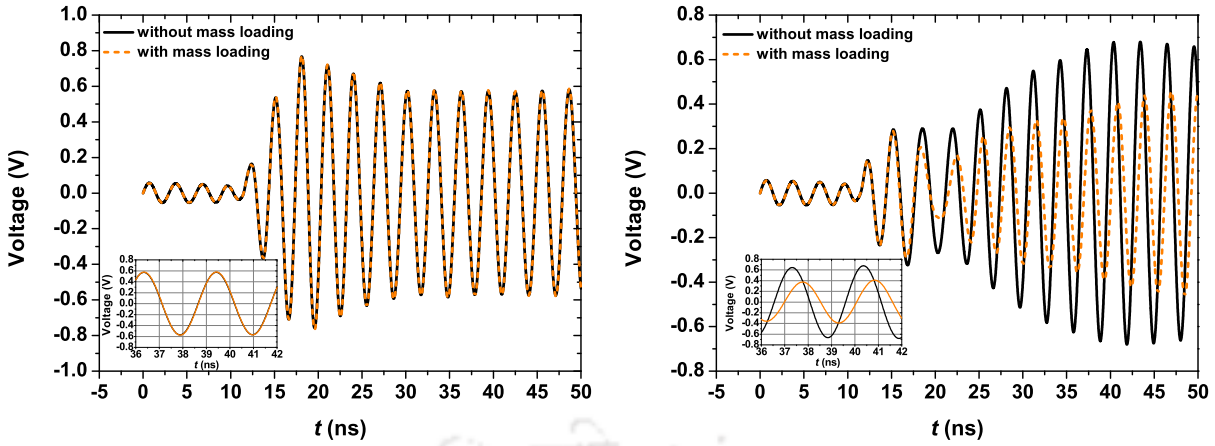

(a) (b)

Figure 5.8: Plot showing the output voltage waveforms with and without mass loading for (a) h_t = 2000 nm and (b) h_t = 1050 nm. Mass loading is performed with surface mass density Δm = $2{\times}10^{-5}$ kg m^{-2}. Inset of the figure shows the magnified time response with Δt = 0.01 and 0.55 ns obtained due to mass loading with h_t = 2000 and 1050 nm, respectively.

5.2.2 Effect of SiO_2 ridges on mass sensitivity, insertion loss and stress

Simulation of mass loading in SH-SAW delay line device is performed by applying an incremental surface mass density on the delay path containing SiO_2 ridges. Two identical SH-SAW devices containing ridges of the same height are considered, one with added mass and the other without mass loading. Mass loading causes time delay (or phase shift) between the output voltage waveforms of the two devices. Fig. 5.8a and 5.8b shows the time shift due to mass loading with a surface mass density of $2{\times}10^{-5}$ kg m^{-2} for two different ridge heights, 2000 and 1050 nm respectively. In the absence of coupled resonance at h_t = 2000 nm, mass loading causes negligible reduction in the peak output voltage and a time delay of 0.01 ns (equivalent to $\Delta\phi$ of 0.02 rad). However, for the same mass loading in the presence of coupled resonance at h_t = 1050 nm, the output voltage reduces by about 0.27 V and a considerable time delay of 0.55 ns (equivalent to $\Delta\phi$ of 1.12 rad) is obtained. Fig. 5.9a displays the normalized phase shift ($\Delta\phi$/kD) caused by incremental mass loading (Δm) for different ridge heights. The slope of the plot represents the phase mass sensitivity S_ϕ and it increases greatly near the coupled resonant height (1050 and 2850 nm). Fig. 5.9b shows the variation in frequency mass sensitivity S_f with ridge height. For most of the ridge heights, S_f remain between 30–70 m^2 kg^{-1}, which is close to the S_f of a plain LW device. However, at the coupled resonant heights 1050 and 2850 nm, a high mass sensitivities of 1295 and 1084 m^2 kg^{-1} are obtained respectively. The values of S_f obtained for the SiO_2 ridge based SH-SAW delay line device is similar to the calculated values of S_f for the resonator case discussed in section 5.1.2.

The variation in area-averaged total stress $\overline{\sigma}_T$ as defined in (5.2) at the interface between ridge and substrate with time is plotted in Fig. 5.10 for different ridge heights. The stress at the interface increases with time and tends to stabilize after 30 ns. It is noted that coupled resonance causes a substantial increase in the contact stress. At h_t = 1050 and 2850 nm, in the presence of coupled resonance, the contact stress increases to a value of 8.6 and 5.4 MPa. On

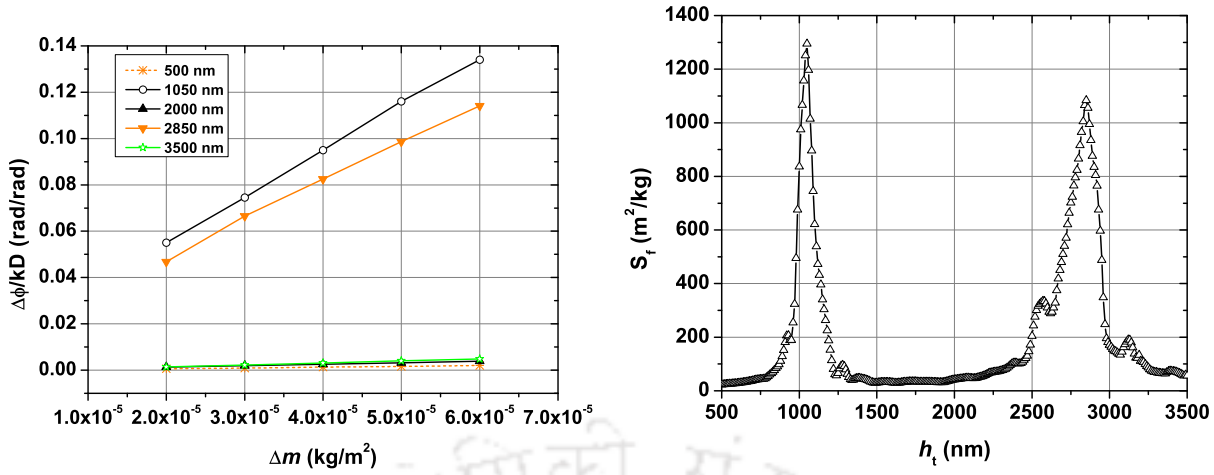

(a) (b)

Figure 5.9: (a) The change in normalized phase shift ($\Delta\phi$/kD) with increasing surface mass density (Δm) plotted for different ridge heights. (b) Variation in mass sensitivity S_f of device with ridge height h_t.

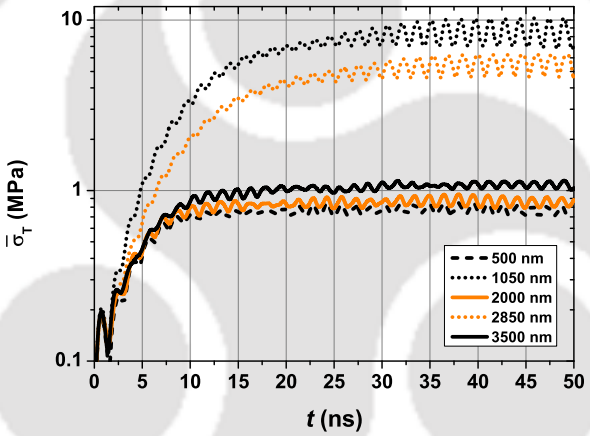

Figure 5.10: Time response of the area averaged total stress $\overline{\sigma}_T$ of the SH-SAW delay line device with SiO_2 ridge height.

the other hand, in the absence of coupled resonance, at $h_t = 500$, 2000 and 3500 nm the contact stress remains close to or lower than 1 MPa.

The frequency response of the delay line was acquired by taking the Fourier transform of the impulse response voltage obtained at the output IDT. Since the time response simulation contained a limited number of data points, the frequency response signal was improved by zero padding the output voltage signal. Fig. 5.11a shows the insertion loss (IL) of the device considering ridge heights $h_t = 800$, 1050, 2000, and 2850 nm. In the absence of coupled resonance, at $h_t = 800$ and 2000 nm, a minimum insertion loss of about -26.1 dB at 358 MHz is obtained. However, in the presence of coupled resonance, at $h_t = 1050$ nm, minimum insertion loss of -32.3 dB is obtained at a decreased frequency of 326.5 MHz. Also, when $h_t = 2850$ nm, minimum insertion loss of -31 dB is obtained at an increased frequency of 360.3 MHz. An increase in the insertion loss by about 5 dB along with positive and negative frequency shifts are observed near the coupled resonance. The variation in minimum insertion loss IL_{min} of the device with

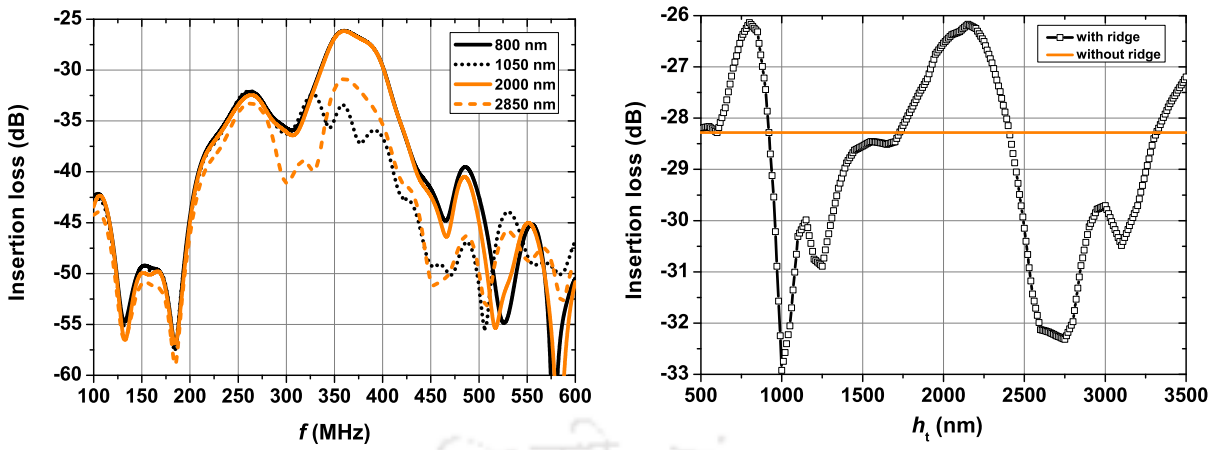

(a) (b)

Figure 5.11: (a) Insertion loss of SH-SAW delay line device considering different ridge heights h_t = 800, 1050, 2000 and 2850 nm. (b) Variation in minimum insertion loss of delay line device with ridge height.

Δm (kg m^{-2})	Δt (ns) for different values of h_t (nm)				
	500 nm	1050 nm	2000 nm	2850 nm	3500 nm
2×10^{-5}	0.006	0.55	0.013	0.468	0.014
3×10^{-5}	0.009	0.745	0.019	0.665	0.022
4×10^{-5}	0.013	0.95	0.025	0.825	0.031
5×10^{-5}	0.016	1.16	0.032	0.987	0.04
6×10^{-5}	0.02	1.34	0.039	1.141	0.048
S_ϕ (m^2 kg^{-1})	35	1995	65	1668	86
S_f (m^2 kg^{-1})	23	1295	42	1084	56
$\overline{\sigma_T}$ (MPa)	0.8	8.6	0.9	5.4	1.1
IL_{min} (dB)	-28.2	-32	-26.5	-31	-27.2

Table 5.1: Time delay due to mass loading, mass sensitivities, area averaged total stress, and minimum insertion loss for different ridge heights.

ridge height is plotted in Fig. 5.11b. For the plain SH-SAW device without ridges, the device shows IL_{min} of -28.2 dB. As ridge height is increased, the IL starts to deteriorate and becomes maximum near the coupled resonant height. The insertion loss increases by about 5 dB near the coupled resonant height. Further increase in the height of the ridges causes mode transition (from mode-0 to mode-1) and IL again starts to improve. The rise and dip in the insertion loss are again observed when the transition occurs from mode-1 to mode-2.

The time delay due to mass loading, mass sensitivities, stable values of area-averaged total stress, and insertion loss for different ridge heights are listed in Table 5.1. In the presence of coupled resonance, at h_t = 1050 and 2850 nm, significant time delays of about 0.55 and 0.47 ns (upon mass loading with 2×10^{-5} kg m^{-2}) along with high S_f of 1295 and 1084 m^2 kg^{-1} are obtained respectively. Coupled resonance also leads to increase in the area averaged stress values. Although coupled resonance provides high mass sensitivity, it comes at the cost of increased insertion losses in the device.

5.3 Summary

The chapter has presented 3D FE simulation of coupled resonance phenomenon with SiO_2 micro-ridges for both the resonator and delay line configurations. Micro-ridges of fixed width and various heights are designed on the surface of the device. At an appropriate size of the ridge, both the substrate and the ridge vibrate in unison causing a sharp swing in the resonance frequency or phase of the device, leading to a transition between inertial and elastic loading regimes.

Eigenmode analysis is performed for the SH-SAW resonator composed of 36°-YX $LiTaO_3$ and SiO_2 micro-ridges made on the surface of the device. The ridges are of 500 nm width and the height is varied from 200 to 4000 nm. A sharp swing in the resonance frequency is observed in the simulation results at the critical ridge heights. In the presence of coupled resonance at ridge heights of 1150 and 2950 nm, mass sensitivity increases to 1345 and 1210 $m^2\,kg^{-1}$ respectively. The significant increase in mass sensitivity due to coupled resonance can be attributed to the increase in the contact stiffness of the composite resonator. However, the electromechanical coupling coefficient of the device becomes low, attaining a value of 2.2 and 1.7% respectively at the coupled resonant heights, indicating an increase in the losses of the device.

FE simulation of SH-SAW delay line comprising SiO_2 micro-ridges is performed. The presence of ridges on the device surface alters the transition time of the wave and produces a phase difference in the output. When the phase difference is plotted with various ridge heights, a typical signature of coupled resonance resulting in a sharp change in the phase difference is obtained. Simulation of mass loading is performed by applying an incremental surface mass density on the surface area of the sensor containing ridges. The presence of coupled resonance results in significant time delays along with high S_f of 1295 $m^2\,kg^{-1}$ about 25 times greater than the mass sensitivity of a SiO_2 based LW device (Table 3.1). Coupled resonance also leads to increase in the area averaged stress at the interface between ridges and the substrate. Although coupled resonance provides high mass sensitivity, the insertion loss of the device increases. The minimum insertion loss goes through oscillations, changing by about 5 dB, indicating transitions in the mode of vibration as ridge height is varied.

Chapter 6

Fabrication and characterization of Love wave device

> Don't read success stories you will, get only message...Read failure stories, You will get some ideas to get success!
>
> Dr. A.P.J. Abdul Kalam

The chapter presents micro-fabrication process and characterization of the proposed SiO_2 based LW devices and fabrication of ZnO nanorods on the surface of devices. The SAW resonator and delay line devices are designed and fabricated on 36°-YX $LiTaO_3$ substrate using standard UV-photolithography. SAW devices are then coated with SiO_2 which acts as a guiding layer. Both LW resonator and delay line devices are characterized using network analyzer by connecting appropriate matching circuits. Input reflection coefficient S_{11} and insertion loss S_{21} are measured for the resonator and delay line devices, respectively.

To test the growth of ZnO nanorods, RF sputtered ZnO film is deposited on the substrate, and subsequently annealed to form nano-sized grains on the surface. The film acts as a seed layer for nanorod growth. Different methods such as direct growth, polyethylenimine (PEI) assisted growth, and fabrication through e-beam template were attempted on the samples to control the height and orientation of the nanorods. The device fabrication process is carried out at Center for nanoscience & engineering (CeNSE), IISc Bangalore under the Indian nanoelectronics user program (INUP).

6.1 Fabrication process flow

The process flow for the fabrication of the proposed device is illustrated in Fig. 6.1. Firstly, a 36°-YX $LiTaO_3$ wafer is taken and cleaned using acetone and isopropyl alcohol (IPA). Next, the IDT pattern with required dimensions is designed on the photoresist coated wafer using UV-lithography. Gold is deposited on the substrate surface through RF sputtering, and IDT

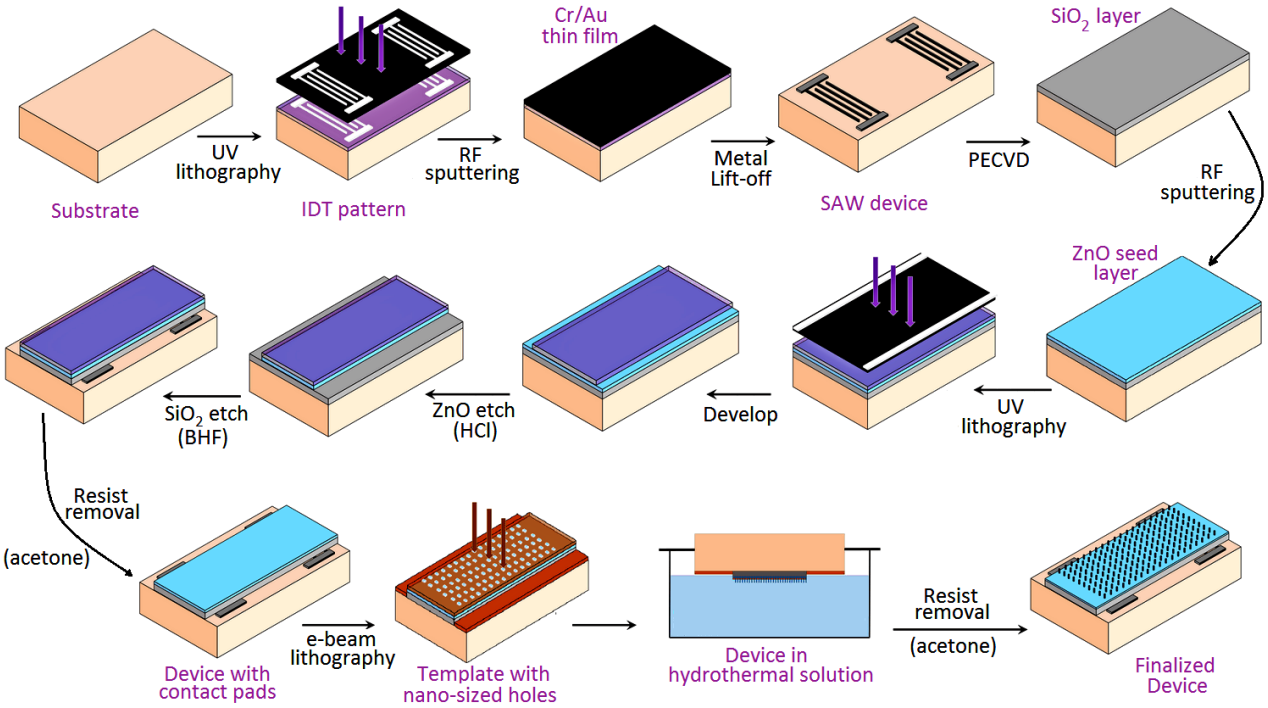

Figure 6.1: Proposed fabrication process flow.

structure is realized by metal lift-off in acetone. Once the SAW device with IDT is made, SiO_2 is deposited on the surface using plasma enhanced chemical vapour deposition (PECVD) followed by RF sputtering of a thin film of ZnO. SiO_2 acts as a guiding layer while the ZnO layer functions as a seed layer for nanorod growth. A second stage photolithography is performed followed by wet etching of SiO_2 and ZnO to expose the metal bond pads for wire connection. Lastly, e-beam lithography is carried out on the device to create nano-sized holes acting as a template for the nanorods to grow. The device is dipped upside down in a hydrothermal solution for ZnO nanorod fabrication [111]. After the growth is completed, the resist is stripped in acetone, and the device is ready for biofunctionalization and sensor measurements.

6.2 Fabrication of Love wave device

In electronic industry, SAW devices are fabricated using photolithography to design IDT pattern either by etching or by lift-off techniques. Out of the two, the lift-off process is more suitable for the development of uniform IDT pattern having feature size less than 5 µm, because precise control of etching time is challenging to maintain for realizing small feature size. Inadequate etching time causes undeveloped pattern and large etching time causes undercut that can be significant enough to wash out the complete IDT structure [185]. Hence, the lift-off process is employed in the development of uniform IDT in the proposed SAW devices. IDT with finger width of 5 µm is considered because below this value, the accuracy of fabrication and resolution control becomes practically difficult with UV lithography process. The necessary steps involved in the fabrication of SAW devices on the piezoelectric substrate involves layout design, mask preparation, photolithography, and metal deposition on the wafer for lift-off process. Next, SiO_2

Device	a	p	W	N_p	N_g	L_g	L
One-port resonator	$\lambda/4$	$\lambda/2$	120λ	20	251	$250\lambda/2$	-
Delay line	$\lambda/4$	$\lambda/2$	120λ	20	-	-	200λ

Table 6.1: Dimensions used for the fabrication of LW one-port resonator and LW delay line considering $\lambda = 20$ µm.

and ZnO are deposited followed by photolithography and wet etching to expose the metal bond pads.

36°-YX $LiTaO_3$ substrate is used as it offers reasonably high K^2 and low insertion loss. Single side polished $LiTaO_3$ wafers of 3" diameter are ordered from Hangzhou Freqcontrol Electronic Technology Ltd, China. The thickness of the substrate is 500 µm which is sufficient in terms of penetration depth of a SAW having wavelength $\lambda = 20$ µm. IDT dimensions with desired 50 Ω impedance are designed using equivalent circuit model for one port resonators and delay line device as described in the second chapter. ZnO films on the substrate are deposited using 3" diameter ZnO sputtering target of 99.99% purity with an ionic bonded copper backing plate, procured from Vinkarola Instruments, U.S.A.

6.2.1 Layout design

The layout of the IDT and SiO_2 layer are graphically designed using the CleWin software. Bi-layered design with standard alignment marks is chosen to accomplish the layout of both the IDT structure and patterned SiO_2 layer. Fig. 6.2a shows the arrangement of LW devices on a 3" wafer diameter with multiple alignment marks. Fig. 6.2b shows the layout of one port SAW resonator with design pattern of SiO_2 guiding layer present above the IDT and reflector gratings. Ground-source-ground (GSG) contacts of 100 µm pitch for probe station connection, and additional square metal pads of size 2 mm are made for wired connection. Fig. 6.2c depicts the layout of LW delay line with metallized delay path between input and output IDT covered by SiO_2 guiding layer. Fig. 6.2d shows the magnified view of the uniform IDT and reflector grating having equal finger width and spacing of 10 µm.

Some of the essential criteria considered in the fabrication of SAW devices on $LiTaO_3$ are as follows:

- One-port resonators and LW delay line devices on a $LiTaO_3$ substrate with the patterned SiO_2 film are designed with $\lambda = 20$ µm and h/λ of 0.39 which gives highest mass sensitivity observed in simulation results given in Table 3.1. The IDT is designed to match with the 50 Ω impedance of coaxial connector of the network analyzer at the corresponding resonance frequency of 208 MHz using the equivalent circuit model described in chapter 2, section 2.2.3. A metallization ratio of 0.5 is kept for the IDT design. Table 6.1 lists all the sizes and dimensions used for the fabrication of SAW devices. IDT finger width, pitch, and aperture are denoted by a, p, and W respectively. N_p is the number of finger pairs in the IDT while N_g represents the number of fingers in the reflector grating. The length of the grating $L_g = (N_g - 1)p$. The center to center distance between input and output IDT of

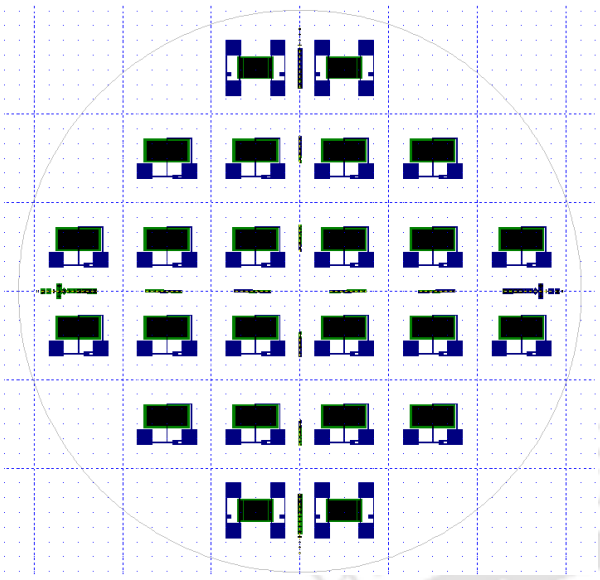

(a)

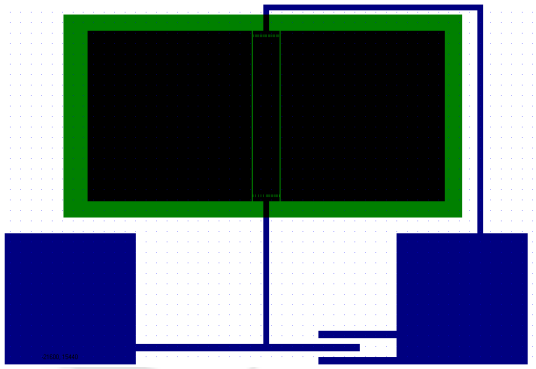

(b)

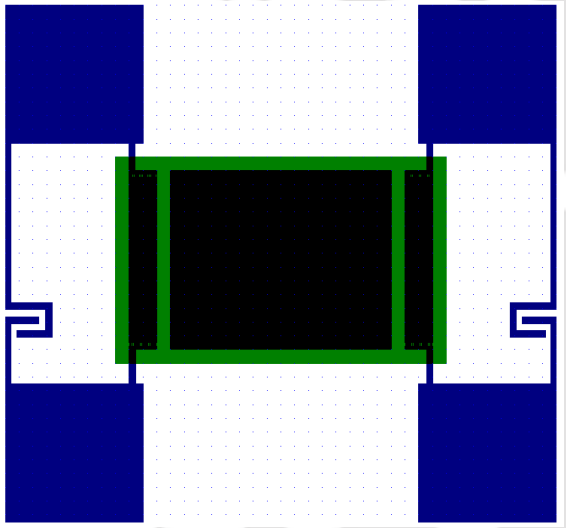

(c)

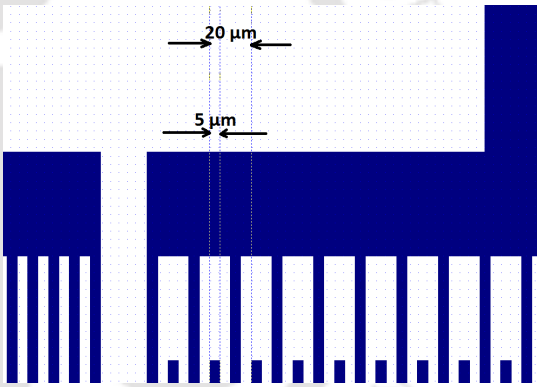

(d)

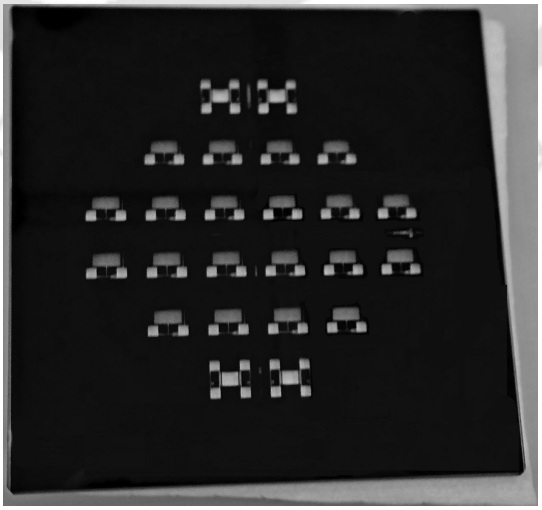

(e)

Figure 6.2: (a) Mask layout made using CleWin software, (b) schematic of one port LW resonator, (c) schematic of LW delay line, (d) magnified view of the layout of the resonator showing the dimensions of IDT, and (e) image of the prepared chromium mask plate.

the delay line is denoted by L.

- Bond pads are designed according to the dimensions of conventional GSG probes with 100 µm pitch to facilitate the characterization of fabricated SAW devices using RF probe station and network analyzer. External square bond pads of 2 mm are also designed for wire connection and soldering if required. The width of the bus bar connecting the fingers of the IDT is of 50 µm.
- To verify the occurrence of coupled resonance with ZnO nanorods, a large number of plain LW resonator devices are fabricated so that devices with different ZnO nanorod heights can be grown by varying the duration of hydrothermal process. The design layout consists of twenty resonator devices and four delay line devices. The layout is organized to fit a maximum number of devices in the mask design.
- A minimum spacing of 3 mm is provided between adjacent devices to ensure the possibility of dicing of the processed wafer.
- Adequate space is given at both ends of the device so that the generated SAW will decay eventually or absorbing materials can be coated at the edge of the device.

6.2.2 Mask preparation

Direct laser writing can be employed over a photoresist-coated wafer to make IDT patterns with high accuracy. As the devices are to be fabricated on a 3" wafer, direct laser writing will consume a significant amount of time. Hence laser writer is used to prepare chromium mask plate which is then used for UV lithography process. Standard alignment markers are included in the layout to facilitate second layer lithography for patterning the SiO_2 film. The 4" chrome mask plates with 3" active area are prepared using laser writer µPG 501 (Heidelberg Instruments, Germany).

The chromium coated mask plate with positive photoresist is loaded into the laser writer, and the desired dimensions are engraved using a standard lens. The laser written chrome mask plates are developed using MF-26A developer (MicroChem, USA). The exposed chromium region is etched using chrome etchant solution. Chrome etchant solution contains, ceric ammonium nitrate $(NH_4)_2Ce(NO_3)_6$ or sulfate $(NH_4)_4Ce(SO_4)_4{\cdot}2H_2O$, with small amounts of HNO_3 [186]. The unwanted photo-resist is removed using acetone, followed by piranha cleaning process for 30 s. Fig. 6.2e shows the image of chromium mask used for the first stage photolithography.

6.2.3 Wafer cleaning

The $LiTaO_3$ wafer is cleaned by standard solutions of acetone and IPA. The wafer is first dipped in the acetone solution for two minutes followed by immersion in IPA for the same time. The wafer is then washed with deionized (DI) water. Lastly, the wafer is dried with filtered nitrogen gas for about 30 s.

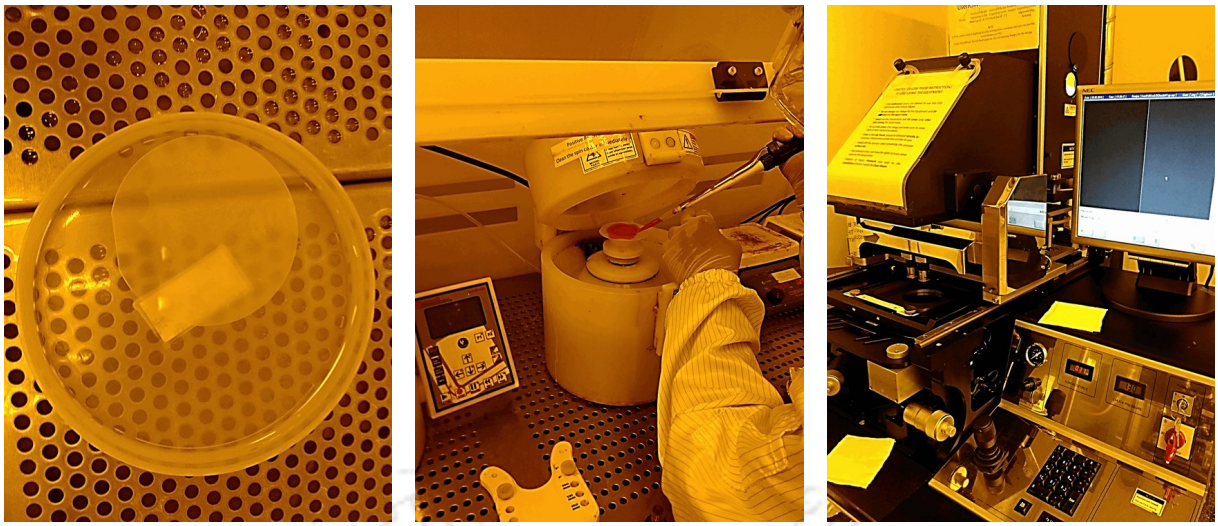

(a) (b) (c)

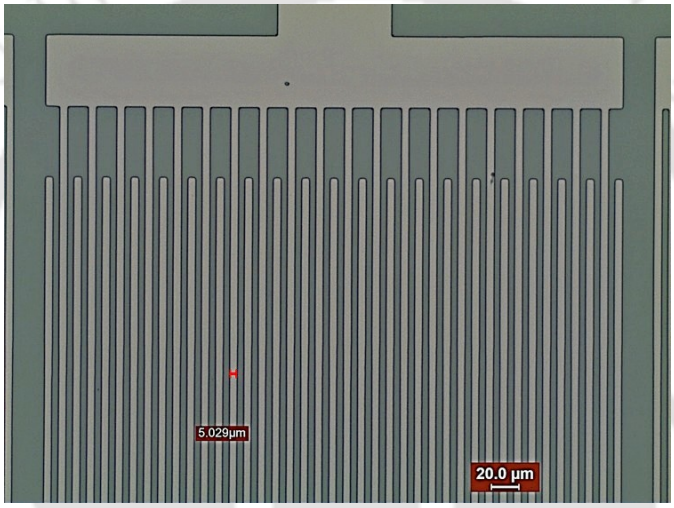

(d)

Figure 6.3: (a) Wafer dipped in acetone for cleaning, (b) spin coating the wafer with positive resist (AZ 5214E), (c) UV exposure using the mask aligner MJB4 lithography equipment, and (d) IDT pattern designed in the photoresist after UV exposure showing the obtained line width of 5 µm.

First stage photolithography			
Step no.	**Process**	**Temperature**	**Time**
1	Wafer cleaning	RT	~5 min
2	Dehydration bake	110 °C	10 min
3	Spin coat HMDS primer (4000 rpm)	RT	40 s
4	Primer baking	110 °C	1 min
5	Spin coat AZ 5214E resist (4000 rpm)	RT	40 s
6	Softbake	110 °C	1 min
7	UV exposure dosage ($45\ \mathrm{mJ\,cm^{-2}}$)	RT	5 s
8	Develop in MF-26A	RT	~10 s

Table 6.2: Steps and parameters used for first stage photolithography.

6.2.4 First stage photolithography

After the cleaning process, the wafer is given a dehydration bake for 10 min at 110 °C to remove all the moisture and water content from the surface. Next, the hexamethyldisilazane (HMDS) primer is spin coated on the wafer at 4000 rpm for 40 s followed by primer baking at 110 °C for 1 min. The wafer is spin-coated with positive photoresist for the development of IDT pattern. It is ensured that the center of the wafer is precisely aligned with the center of the spin coater to obtain uniform photoresist thickness. AZ 5214E photoresist (AZ Electronic Materials, UK) is dispensed from the bottle and spread all over the wafer, ensuring that no bubbles form on the surface. The wafer is spun for 40 s at 4000 rpm to get a resist thickness of 1.4 µm. Photoresist coated sample is softbaked on the hot plate at a temperature of 110 °C for 1 min. To avoid wafer getting stuck to the hot plate surface, aluminum foil is placed between the wafer and the hot plate. The wafer is placed in the mask aligner MJB4 (SUSS MicroTech) with 4-inch substrate chuck. The setup parameters such as wafer thickness, the separation between mask plate and wafer, wedge correction, and alignment of the substrate are performed manually, and UV exposure dosage of 45 mJ cm^{-2} for 5 s is finalized after three trials. The exposed samples are developed in MF-26A solution for about 10 s. The sample is regularly inspected in the optical microscope while developing the IDT pattern to avoid over-development or under-development of features on the resist. Each time the development time varies slightly, due to intermediate cleaning of the wafer with DI water for inspection under the microscope. Fig. 6.3a–6.3c show images of wafer cleaning, photoresist spin coating on the wafer, and UV exposure, respectively. Fig. 6.3d shows the developed IDT pattern on the wafer having a line width of about 5 µm as designed. Table 6.2 shows all the steps and parameters used in the first stage lithography.

6.2.5 Metal sputtering and lift-off

Gold thin film of 100 nm thickness is used as electrode material for designing the IDT structure. A thin chromium under-layer of 10 nm is used to promote the adhesion between gold and $LiTaO_3$ substrate. The sputtering parameters for gold and chromium metals are listed in Table 6.3. After metal deposition, the samples are placed in a petri dish with acetone, and the dish is placed in ultra-sonication for 10–15 minutes for the lift-off process. Acetone strips-off the resist as well as the metal layer deposited just over it, leaving the patterned metal electrodes on the surface. The gold lift-off process is shown in Fig. 6.4a. Once the lift-off is completed the wafer is washed with IPA and DI water to remove any metal debris remaining on the surface of the wafer. The processed wafer after metal lift-off is shown in Fig. 6.4b. The optical microscope image of the IDT structure and reflector grating after the lift-off process is presented in Fig. 6.5a, showing the metal width of about 4.6 µm. Atomic force microscopy (AFM) image of a particular section of the IDT of 50 µm × 50 µm size is shown in Fig. 6.5b. Line profile of the image shows the obtained metal thickness of about 150 nm and pitch of 10 µm.

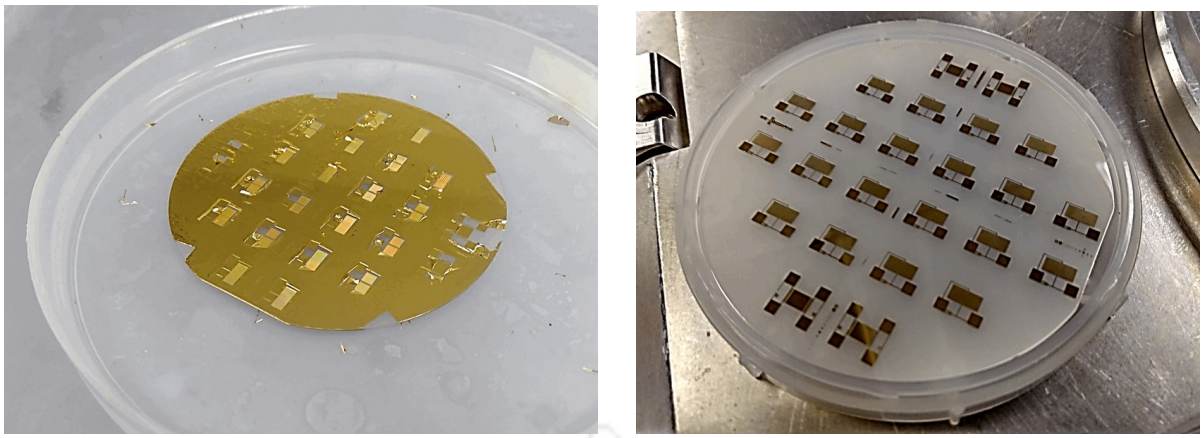

(a) (b)

Figure 6.4: (a) Gold film getting stripped-off from the surface of the wafer during the lift-off process. (b) Final structure of devices on the wafer after lift-off is completed.

Metal RF Sputtering		
Specifications	**Chromium (Cr)**	**Gold (Au)**
Desired thickness	10 nm	100 nm
Power	25 W	100 W
Pre-sputter time	30 s	600 s
Deposition time	250 s	22 s
Base presuure	5×10^{-6} torr	
Working pressure	7.5×10^{-3} torr	
Distance between target and substrate	7.5 cm	
Gas used	Ar (13 sccm)	
Temperature	RT	

Table 6.3: Parameters used for RF sputtering of chromium and gold.

6.2.6 Deposition of SiO_2 and ZnO layers

After the IDTs are made, the wafer is deposited with SiO_2 layer using PECVD process. As discussed in chapter 3 (Table 3.1), considering SiO_2 guiding layer, a normalized thickness of 0.39 gives maximum mass sensitivity. For a device with $\lambda = 20$ µm, it turns out to be a thickness of 7.8 µm. The fabrication limitation of the facility allowed to deposit a thickness up to 3 µm only. Deposition of SiO_2 was performed using the PlasmaLab machine (Oxford Instruments, UK) as shown in Fig. 6.6a. The wafer was kept on the sample holder on a silicon carrier wafer along with some support pieces so that the wafer does not move while the deposition is going on. Since deposition is uniform, a small sample wafer piece was kept beside the main wafer so that thickness can be measured. The recipe for PECVD process is shown in Table 6.4. The deposition rate was 43.32 $\mathrm{nm\,min^{-1}}$, and the machine was used for about 70 min to acquire a thickness of about 3 µm as verified by the profilometer data shown in Fig. 6.6b.

A 3-inch target of ZnO is used for deposition of ZnO thin film in Anelva SPF 332H RF sputtering machine. The target is attached to the bottom section while the wafer is fixed using Kapton tape on the top of the column with the active surface facing downwards. The distance

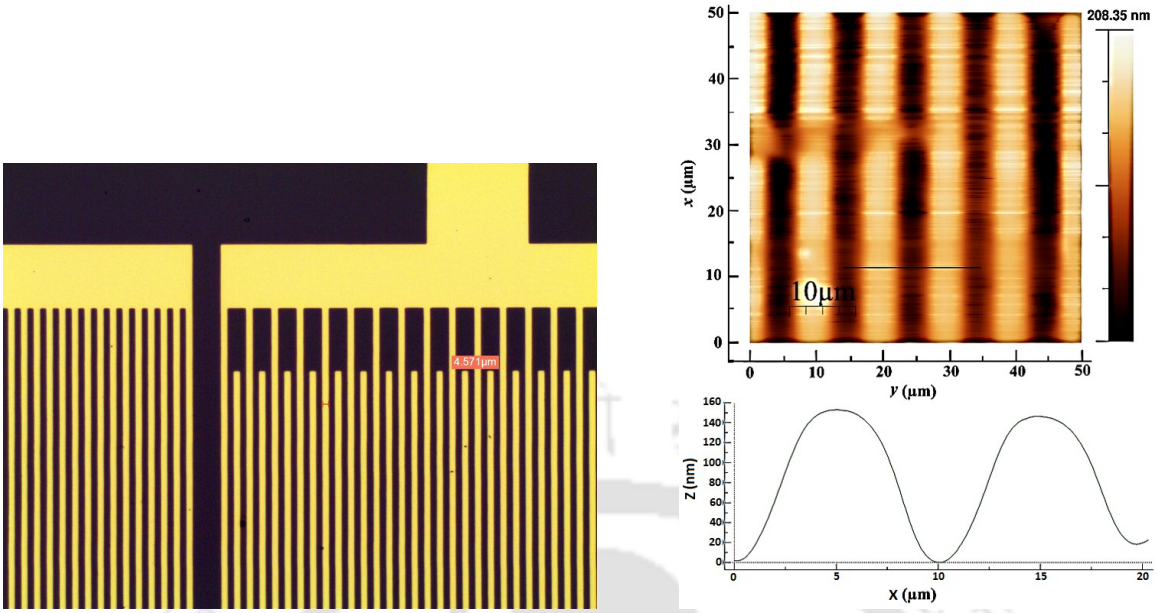

(a) (b)

Figure 6.5: (a) Optical microscope image of the gold IDT and reflector grating showing a finger width of about 4.6 µm. (b) AFM image and line profile of a particular section of the IDT.

PECVD of SiO_2			
Gases	SiH_4 : 8.5 sccm N_2O : 710 sccm N_2 : 161 sccm	**Pressure**	100 mtorr, 13.56 MHz
RF power	10 W, 13.56 MHz	**Deposition rate**	43.32 nm/min
Time	70 min	**Thickness**	3 µm

Table 6.4: Parameters used for PECVD deposition of SiO_2.

ZnO RF Sputtering	
Specifications	**Values**
Input/Reflected power	95 W/ 10 W
Plate voltage/ Plate current	1.5 kV/ 105 mA
Presputter time	15 min
Deposition time	8 min
Base pressure	5×10^{-6} torr
Working pressure	8×10^{-3} torr
Distance between target and substrate	5.2 cm
Gas used	Ar (13 sccm)
Thickness	~300 nm

Table 6.5: Parameters used for RF sputtering of ZnO film.

(a)

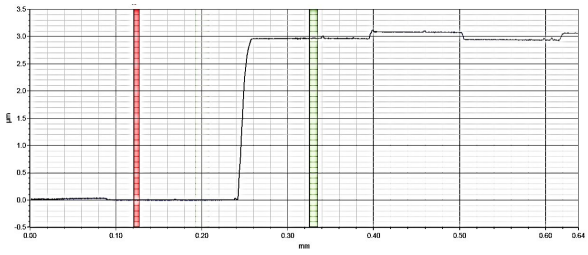

(b)

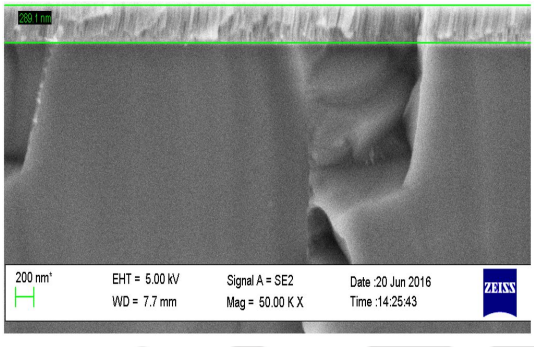

(c)

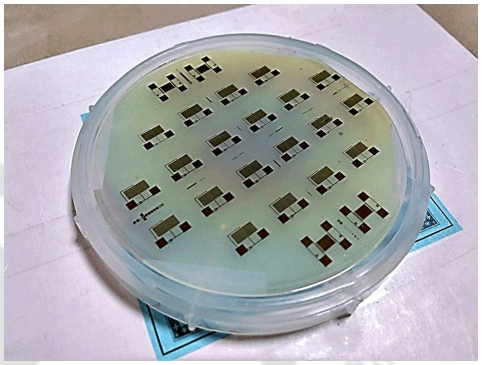

(d)

Figure 6.6: (a) PlasmaLab System used for PECVD of SiO_2. (b) Profilometer showing SiO_2 film of 3 µm thickness deposited on the wafer. (c) FESEM image showing ZnO film of thickness 290 nm deposited on the wafer. (d) Wafer after SiO_2 and ZnO deposition.

between the target and wafer is kept at 5.2 cm. Three test samples were used and the sputtering time was varied from 5 to 15 min to find the thickness of the film obtained. Cross section image of the test sample was acquired using field emission scanning electron microscope (FESEM) to verify the thickness of the deposited film. Fig. 6.6c shows a 290 nm thick ZnO film deposited in about 8 min. The details of the process are listed in Table 6.5. The final wafer after SiO_2 and ZnO deposition is shown in Fig. 6.6d.

6.2.7 Second stage photolithography

A second lithography step ensures that the resist stays only over the active region of the device and the developed portions are etched out to expose the metal bond pads. After the film deposition steps are completed, the wafer is again cleaned with acetone, IPA, and DI water, and given a dehydration bake at 110 °C for 10 min. Negative photoresist AZ nLOF 2070 is spin coated on the wafer at 4000 rpm for 40 s giving a thickness of about 6 µm. After softbaking, alignment marks are used to match the pattern created in the first lithography step, and the wafer is given UV exposure dose of 65 $mJ\,cm^{-2}$. Fig. 6.7a shows mask-aligner being used to match the pattern before exposing with UV energy. Postbaking the wafer at 110 °C for 90 s cross-links the UV-exposed areas of the resist. Developing the wafer in AZ 726MIF solution removes the non-exposed areas but retains the UV-exposed portions due to cross-linking of photoresist. The resist is then hard baked at 130 °C for 3 min. The details of the process are

Second stage photolithography			
Step no.	**Process**	**Temperature**	**Time**
1	Wafer cleaning	RT	∼5 min
2	Dehydration bake	110 °C	10 min
3	Spin coat negative resist AZ nLOF2070 (4000 rpm)	RT	40 s
4	Soft baking	110 °C	1 min
5	UV-exposure by mask aligner (65 mJ cm^{-2})	RT	5 s
6	Postbake (cross-linking)	110 °C	90 s
7	Develop in solution (AZ 726MIF)	RT	40 s
8	Hardbake	130 °C	3 min

Table 6.6: Steps and parameters used for second stage photolithography.

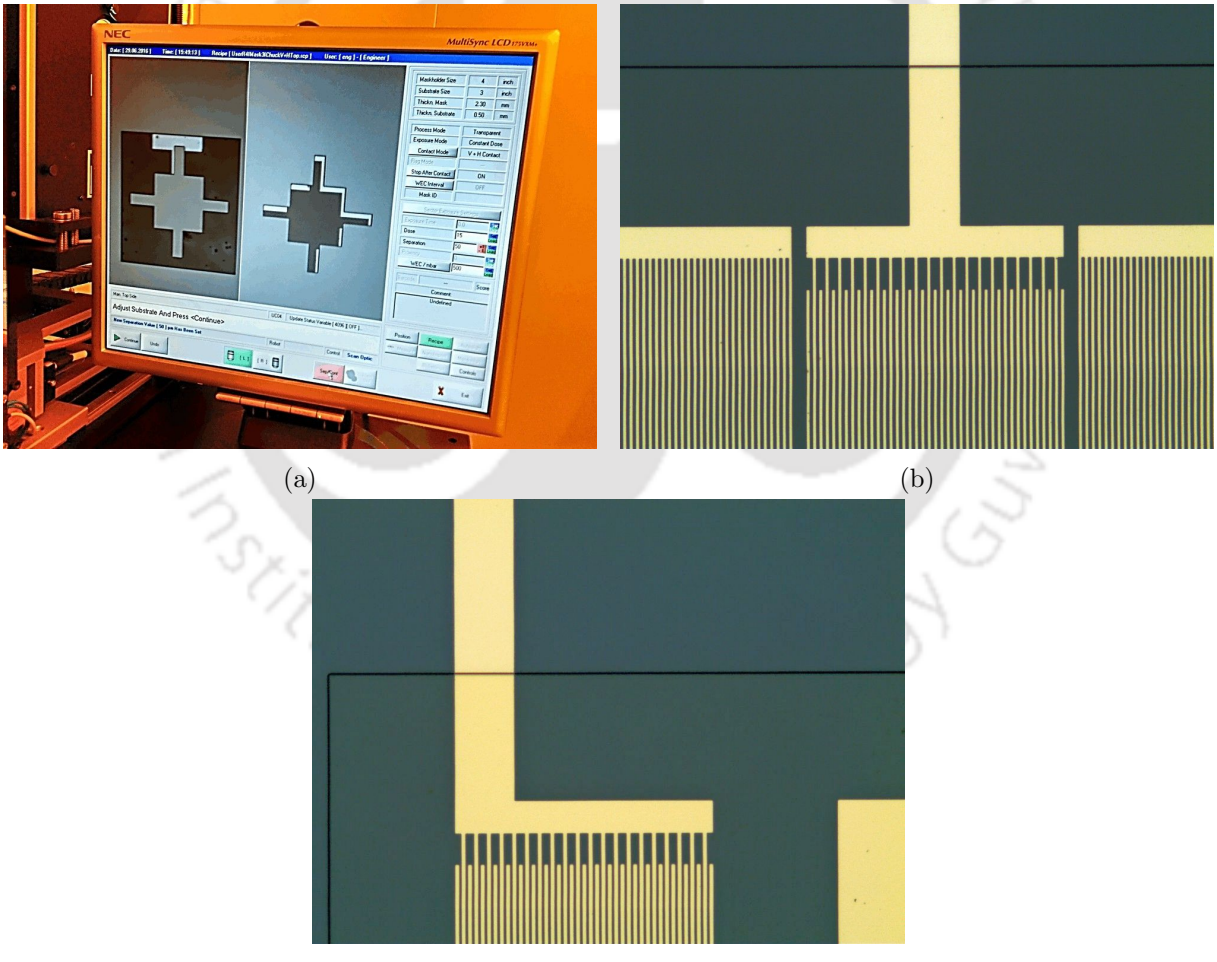

(a) (b)

(c)

Figure 6.7: (a) Use of alignment marks in mask-aligner equipment for the second stage lithography. Microscopic image of the developed pattern after etching showing the guiding layer covering the active region of (b) resonator and (c) delay line device.

listed in Table 6.6.

6.2.8 Etching

A layer of negative resist protects the SiO_2 and ZnO film present on the active central region of the device. The rest of the areas are etched away using traditional wet etching methods. For etching the ZnO film, many acidic solutions such as nitric acid, phosphoric acid, hydrochloric acid, and acetic acid can be used [187]. Here, HCl solution was used to remove the ZnO film while buffered hydrofluoric acid (BHF) solution was employed to etch the SiO_2 layer. ZnO was etched by dipping the wafers in 1% HCl solution for 30 s. The etch rate was about 15 $nm\,s^{-1}$. SiO_2 was etched by dipping samples in 13:2 BHF solution for 17 min giving an etch rate of about 180 $nm\,min^{-1}$. After completion of wet etching, the negative resist present on the central region of the device is removed using TechniStrip NI555 resist remover. Optical microscope image of a resonator and delay line device with guiding layer present in the central region is shown in Fig. 6.7b and 6.7c respectively.

6.2.9 Dicing

A semi-automatic wafer dicer (MTI Corporation) was used to separate the devices. The back side of the wafer containing the fabricated devices was coated with a gel known as Crystal-Bond-509 and placed on a glass wafer by heating at 120 °C for 5 min. At room temperature, the gel is solid, but upon heating it becomes viscous, and this allows the back-side of the wafer to get stuck on the glass plate upon cooling. The glass plate with the attached wafer is placed on the machine for dicing. The blade used for cutting was 0.3 mm thick. The samples were cut at a rate of 10 $mm\,s^{-1}$ using straight lines and square pieces were diced out. Once dicing is completed, the wafer is again kept on the hot plate at 130 °C so that the gel underneath melts and wafer pieces can be taken out. The separated devices are again cleaned with acetone, IPA, and DI water.

6.3 FE simulation

Since the devices were fabricated with SiO_2 guiding layer of thickness $h = 3$ µm instead of 7.8 µm because of the fabrication limitation, FE simulation was again performed using the fabricated dimensions, $\lambda = 20$ µm and $h = 3$ µm. The new values of the resonance frequency of the resonator and the height of the ZnO nanorods at which coupled resonance is expected to occur are found. The simulation geometry used is similar to Fig. 3.3 shown in Chapter 3. The frequency response of the device is shown in Fig. 6.8a. The resonance (f_r) and anti-resonance frequency (f_{ar}) were obtained at 199.7 and 205.5 MHz respectively. Ten ZnO nanorods with square cross section of size 100 nm, 1 µm apart were made on the surface of the guiding layer with SNRD = 1 μm^{-2} and simulation was performed to study coupled resonance. The sharp

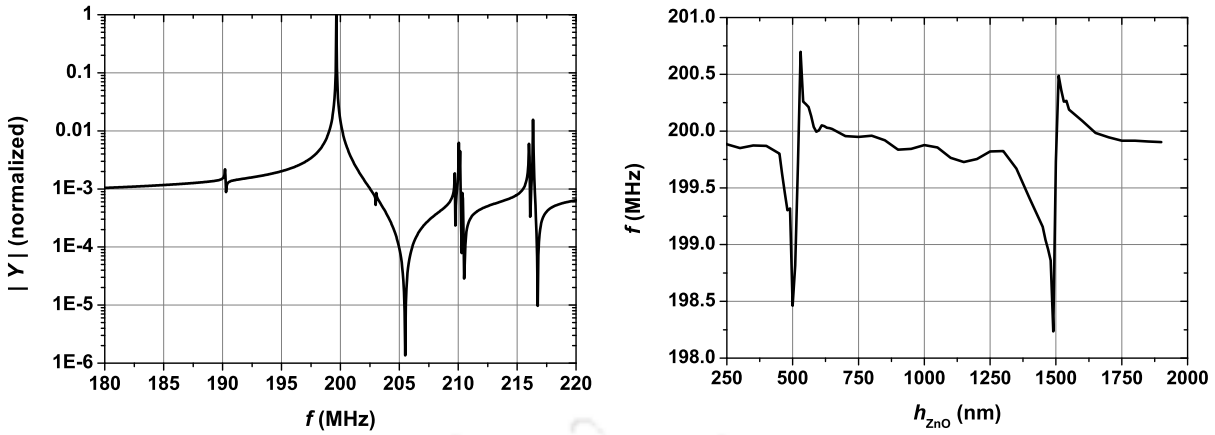

(a) (b)

Figure 6.8: (a) Frequency response of LW device consisting of SiO_2 guiding layer of thickness 3 µm, operating at $\lambda = 20$ µm. The resonance (f_r) and anti-resonance frequency (f_{ar}) are obtained at 199.7 and 205.5 MHz respectively. (b) Simulation showing coupled resonance at $h_{ZnO} = 600$ and 1600 nm.

swing in the frequency indicating coupled resonance was observed at $h_{ZnO} = 600$ and 1600 nm. Therefore, fabrication of ZnO nanorods of the desired dimensions was attempted.

6.4 Characterization of Love wave devices

A SAW transducers is often designed with input impedance close to 50 Ω (characteristic impedance Z_0) so that it can be connected to a signal source without suffering any return loss. However, because of the large capacitance of the IDT structure, presence of multiple layers on the device, and fabrication inconsistencies the exact impedance matching is difficult to achieve. Usually, a two-component L-section matching network is used between the signal source and SAW device [11]. Once the matching is done, maximum power from the source is transferred to the SAW device minimizing the reflection of the signal. Consider a SAW device with load impedance $Z_L = R_L + jX_L$. The L-section matching network can be designed by using a combination of series and parallel reactance as shown in Fig. 6.9a and 6.9b for the cases $R_L > Z_0$ and $R_L < Z_0$, respectively. Considering $R_L > Z_0$, the net impedance is found by looking into the network using circuit analysis. The values of B and X is given by [188]

$$\begin{aligned} B &= \frac{X_L \pm \sqrt{R_L/Z_0}\sqrt{R_L^2 + X_L^2 - Z_0 R_L}}{R_L^2 + X_L^2} \\ X &= \frac{1}{B} + \frac{X_L Z_0}{R_L} - \frac{Z_0}{B R_L}. \end{aligned} \tag{6.1}$$

Similarly for the case of $R_L < Z_0$, the values are given by the equations

$$\begin{aligned} B &= \pm\frac{\sqrt{(Z_0 - R_L)/R_L}}{Z_0} \\ X &= \pm\sqrt{R_L(Z_0 - R_L)} - X_L. \end{aligned} \tag{6.2}$$

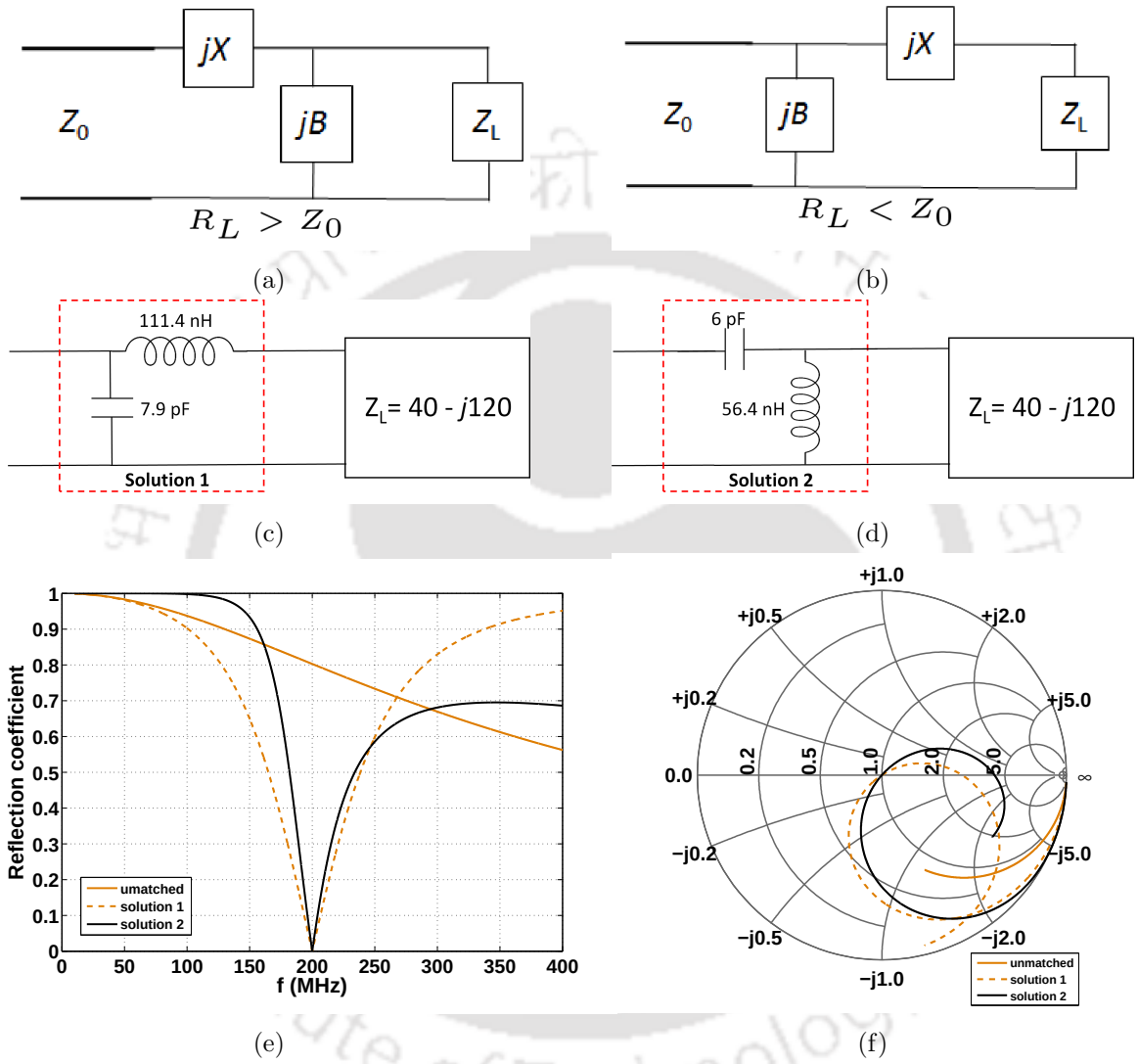

Figure 6.9: Possible L-section matching network connections of SAW device with load impedance $Z_L = R_L + jX_L$ for the case (a) $R_L > Z_0$ and (b) $R_L < Z_0$. Two Matching network solutions for $Z_L = 40 - j120$ using (c) shunt capacitor and series inductor and (d) series capacitor and shunt inductor. Variation in (e) reflection coefficient with frequency and (f) Smith chart plot shown for the unmatched case, solution 1 and solution 2.

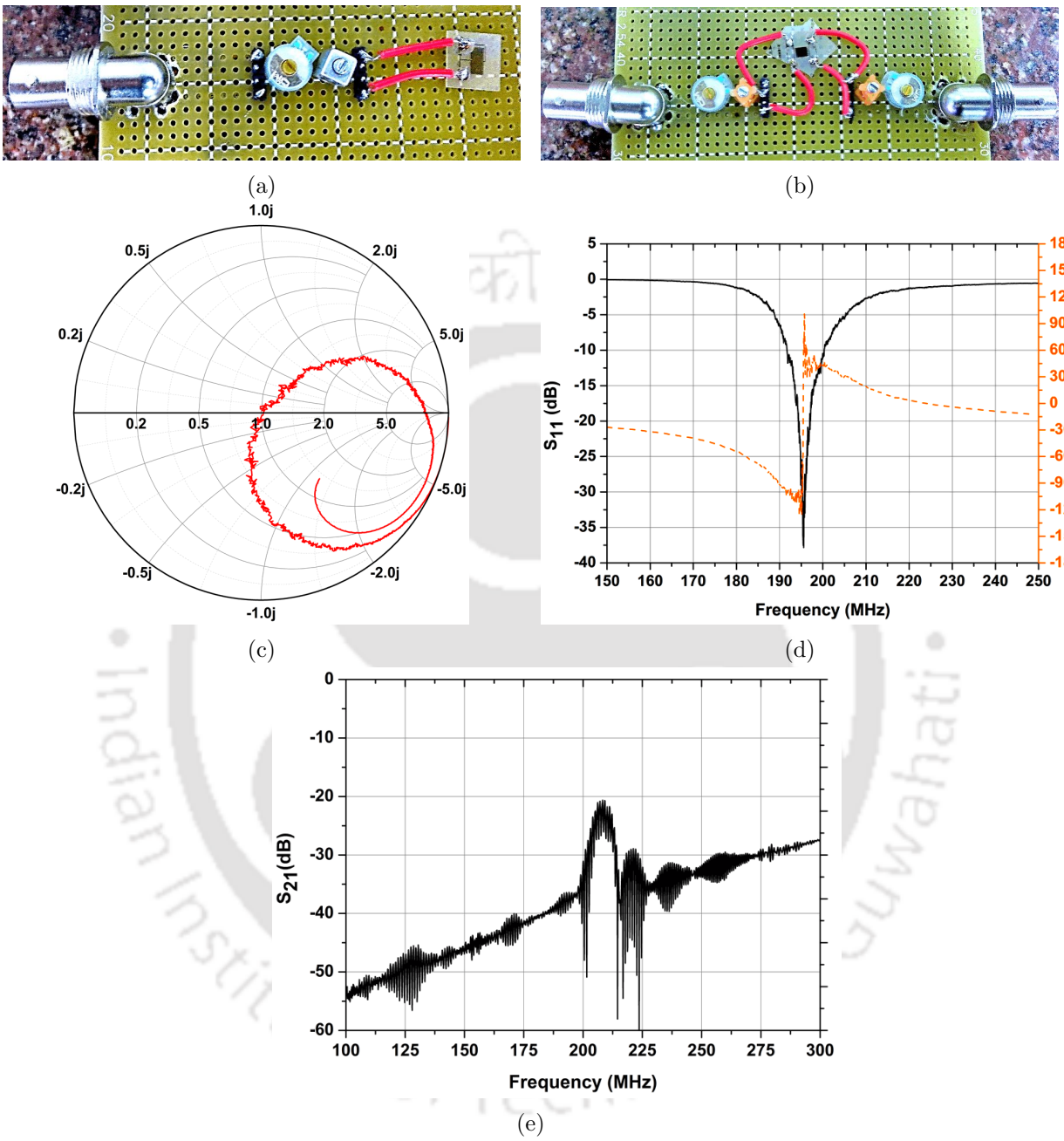

Figure 6.10: (a) LW resonator and (b) LW delay line device with connected matching circuit. Matching is achieved by connecting a variable series capacitor and a variable shunt inductor ($C \approx 3$ pF and $L \approx 80$ nH). (c) Smith chart showing the successful matching of the resonator. (d) Frequency response showing S_{11} of LW resonator showing resonance occurring at 195.5 MHz. (e) Frequency response of LW delay line showing minimum insertion loss of -20.6 dB at 208.2 MHz.

The equations indicate that for a given case, both positive and negative values of X and B are possible. Positive and negative X implies an inductor and capacitor respectively, while positive and negative values of B implies a capacitor and an inductor respectively. For an unmatched SAW device with $Z_L = 40 - j120$, operating at $f = 200$ MHz, two L-section matching solutions exists as shown in Fig. 6.9c and 6.9d respectively. Fig. 6.9e shows the variation in reflection coefficient for the unmatched case and the two possible matching solutions. The reflection coefficient becomes close to zero near the operating frequency for the matched case, indicating that the undesirable reflections are eliminated. Smith chart can also be used to verify the matching attained for load Z_L. The Smith chart shows the normalized impedances, with the upper and lower half of the circle representing the normalized inductive and capacitive reactances respectively. The rightmost point indicates an open circuit with infinite impedance while the leftmost point indicates a short circuit. Fig. 6.9f shows that if the load is matched correctly, the frequency response curve passes through the center of the Smith chart where the normalized impedance is unity. A small program is written in MATLAB using equations (6.1) and (6.2) to calculate the correct values of L and C required for designing the matching circuit for a given load impedance of SAW device.

Fig. 6.10a and 6.10b show the LW resonator and delay line devices with matching circuit connected between the coaxial connector and the device. The matching is achieved by connecting a series variable capacitor and a shunt variable inductor ($C \approx 3$ pF and $L \approx 80$ nH). Rohde & Schwarz ZVA24 vector network analyzer (VNA) was used to characterize the device. Firstly, the device was connected without matching circuit to calculate the load impedance Z_L at the operating frequency. Next, the required values of C and L were calculated and then implemented in the circuit. The matching was verified by plotting the Smith chart as shown in Fig. 6.10c. Variation in S_{11} (dB) and phase with frequency of the LW resonator is plotted in Fig. 6.10d, indicating the resonance occurring at 195.5 MHz. The matching circuit was connected on either side of the two port LW delay line device. A minimum insertion loss of -20.6 dB is obtained at $f = 208.2$ MHz as shown in Fig. 6.10e.

6.5 ZnO nanorod fabrication

ZnO nanorods are fabricated using various methods such as Metal-organic chemical vapor deposition (MOCVD) [189], thermal evaporation [190], hydrothermal solution growth, vapor phase transport process [191], and chemical vapour deposition (CVD) [192]. Most of these growth techniques are complicated and temperatures used for the nanorod growth are quite high (> 400 °C), that may damage the piezoelectric properties of the substrate. The hydrothermal method [193] has attracted considerable attention because of its unique advantages: it is a simple, low temperature (60–100 °C), and high yield process.

The process usually involves deposition of ZnO seed layer by RF sputtering, thermal or sol-gel methods. The film is then annealed to induce the formation of nano-sized grains on the surface. Fig. 6.11a shows small wafer pieces placed on a quartz boat for annealing the ZnO film in the furnace. Annealing was performed at 350 °C for 30 min in argon gas. X-ray diffraction

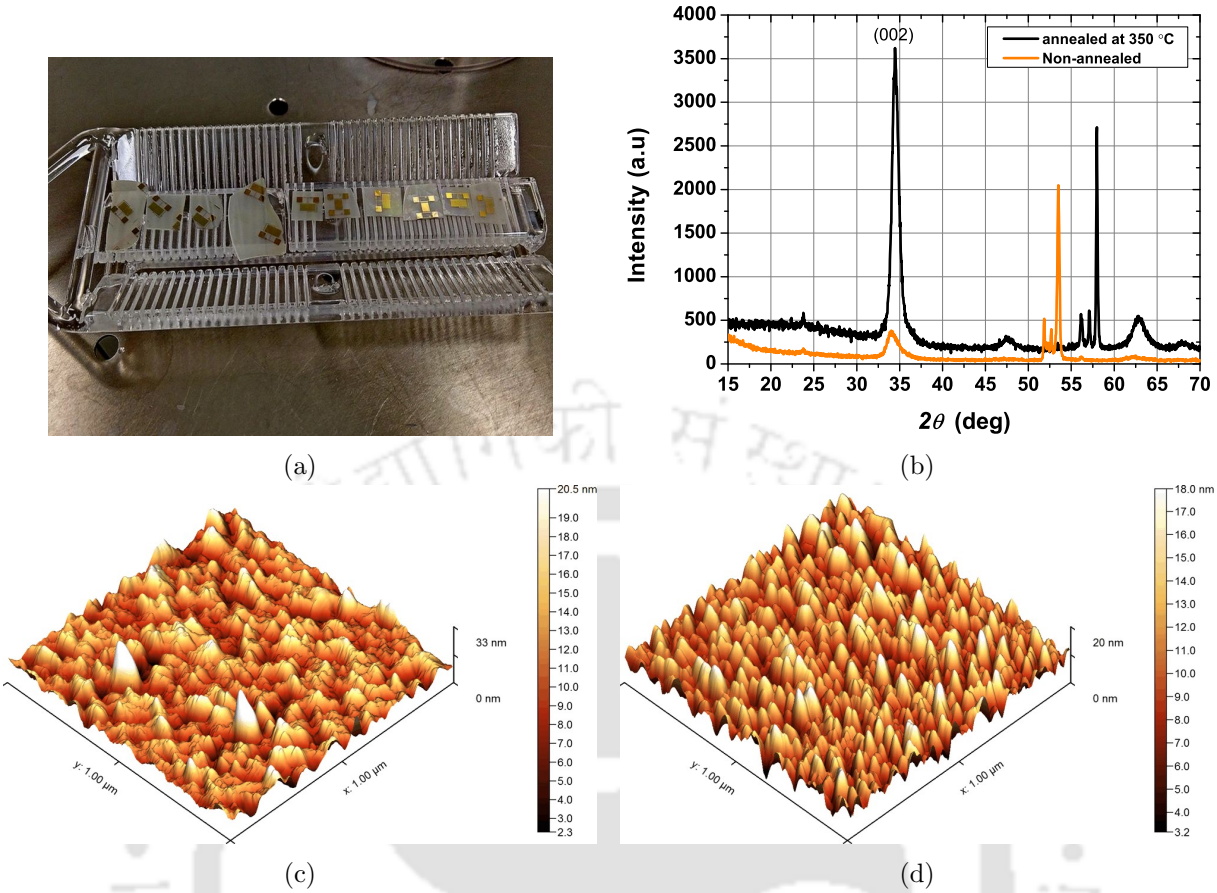

Figure 6.11: (a) Small wafer pieces kept on a quartz boat for annealing the ZnO thin film in the furnace. (b) XRD plot of ZnO thin film before and after annealing at 350 °C. AFM images showing the surface morphology of ZnO film (c) before annealing and (d) after annealing.

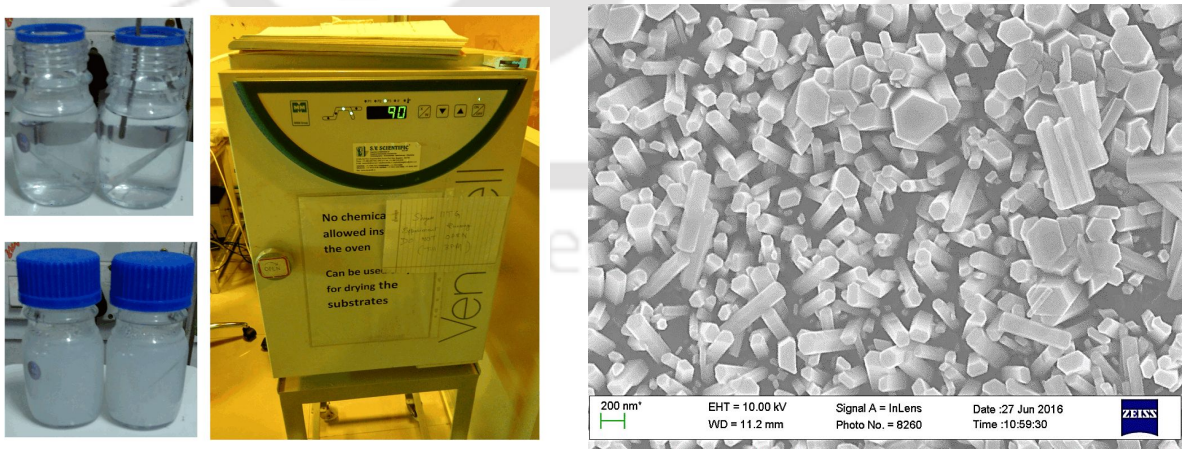

Figure 6.12: (a) ZnO nanorods grown in a sealed glass bottle containing hydrothermal solution at 90–95 °C by sticking the sample on a glass slide and keeping it upside down. As the reaction proceeds, color of the solution changes to white. (b) ZnO nanorods grown by direct method at 95 °C for 3 hours in 0.05 M solution.

(XRD) measurement was carried out to investigate the crystalline property of the ZnO thin film, and the results are shown in Fig. 6.11b. Annealing leads to preferential orientation of the film along the c-axis representing the (002) plane of wurtzite hexagonal structure of ZnO. AFM image displaying the surface morphology of the film before and after annealing is shown in Fig. 6.11c and 6.11d respectively. The plain film has a low grain density of about 30 μm^{-2}, but annealing increases the grain density to about 90 μm^{-2}. The size of ZnO nano-grains is about 40–50 nm. Equimolar concentration of zinc nitrate hexahydrate ($Zn(NO_3)\cdot 6H_2O$) and hexamethylenetetramine (HMTA) ($C_6H_{12}N_4$) are mixed, and the solution is heated to 90–95 °C for a few hours to start the growth of ZnO nanorods on the surface. ZnO nanorods of about 100 nm diameter and different heights can be made on the device surface by varying the duration of hydrothermal growth process. Growth trials were conducted on some test samples. Three methods namely, direct growth, PEI assisted growth, and e-beam template growth were attempted.

6.5.1 Direct growth

Annealed samples were stuck to the glass slide upside down, and the slides were placed in a sealed glass bottle containing hydrothermal solution as shown in Fig. 6.12a. The bottles were placed in an oven at 90–95 °C for a few hours. As the reaction proceeds, the solution turns white. The mechanism of the reaction is explained below

$$\begin{aligned} &C_6H_{12}N_4 + 6H_2O \rightarrow 4NH_3 + 6HCHO \\ &NH_3 + H_2O \rightarrow NH_4^+ + OH^- \\ &Zn(NO_3)\cdot 6H_2O \rightarrow Zn^{2+} + 2NO_3^- \\ &Zn^{2+} + 2OH^- \rightarrow Zn(OH)_2 \rightarrow ZnO + H_2O \end{aligned} \tag{6.3}$$

HMTA decomposes to provide four NH_3 molecules and six HCHO molecules, where the HCHO molecules do not take part in the nanorod growth. The OH^- ions are produced via the protonation of NH_3. The Zn^{2+} ions are released by $Zn(NO_3)\cdot 6H_2O$ in water which reacts with OH^- to form $Zn(OH)_2$, causing the solution to become turbid white. $Zn(OH)_2$ is further decomposed under heat to form ZnO nanorods. FESEM image of the ZnO nanorods grown by the direct method at 95 °C for 3 hours in 0.05 M solution is shown in Fig. 6.12b. The diameter of the nanorods depend on the solution concentration, and the growth rate depends on the temperature. Directly grown nanorods have less height, tend to merge and have low aspect ratio.

6.5.2 PEI assisted growth

It has been reported that PEI has a prominent effect on controlling the aspect ratio of ZnO nanorods grown by the hydrothermal solution [194]. Without the addition of PEI, as-grown ZnO nanorods possess wider diameter and shorter length along the *c*-axis direction. PEI sticks to the side walls of the nanorods during growth and inhibits the lateral expansion of the rods,

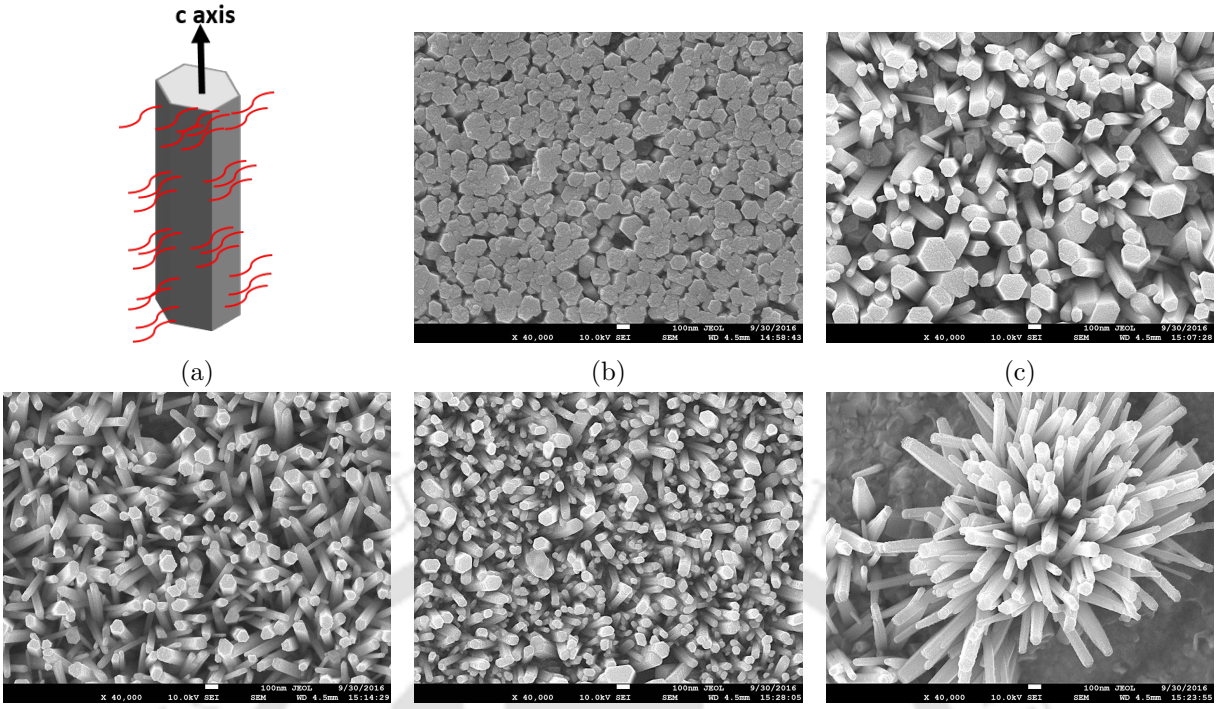

Figure 6.13: (a) Schematic of ZnO nanorod growing along the *c* direction with PEI sticking to the sides of the nanorod to inhibit the lateral growth. ZnO nanorods grown in 80 mL, 0.025 M hydrothermal solution for 3 h by adding different volumes of PEI (b) 0.1 mL, (c) 0.2 mL, (d) 0.5 mL, (e) 1 mL, and (f) 1.5 mL.

thereby increasing the aspect ratio as shown in Fig. 6.13a. ZnO nanorods were grown at 90 °C for 3 h in a sealed glass bottle containing 80 mL of 0.025 M hydrothermal solution by adding different amounts of PEI. The diameter of the rods progressively decreased from 250 nm to under 100 nm, and the rods tend to become longer with increasing PEI concentration as shown in Fig. 6.13b–6.13f. In 2–3 h, nanorod height of 1–2 µm can be attained. However, acquiring the cross-section image of nanorods and measuring the exact height in FESEM was difficult. Moreover, the nanorods tend to branch out and with poor orientation control.

6.5.3 E-beam template growth

E-beam lithography (EBL) was performed on few test samples to make pattern comprising of holes of 100 nm size, 2 µm apart in the PMMA resist using the Raith eLine lithography equipment. The details of the process are shown in Table 6.7. Firstly, the samples are dipped in IPA solution for 1 min, followed by drying in N_2. Next, the sample is spin coated with e-beam resist (950 PMMA A4) at 6000 rpm for 1 min. The wafer is then baked at 180 °C for 3 min, followed by e-beam exposure with a dosage of 250 µC cm^{-2}. Square holes of size 100 nm, 2 µm apart were made on a 1 mm area of the resist. Methyl isobutyl ketone (MIBK) solvent is the key ingredient in the developer that controls the solubility and swelling of the resist, while IPA is the alcohol (non-solvent). PMMA resist is developed using MIBK:IPA (1:3) solution.

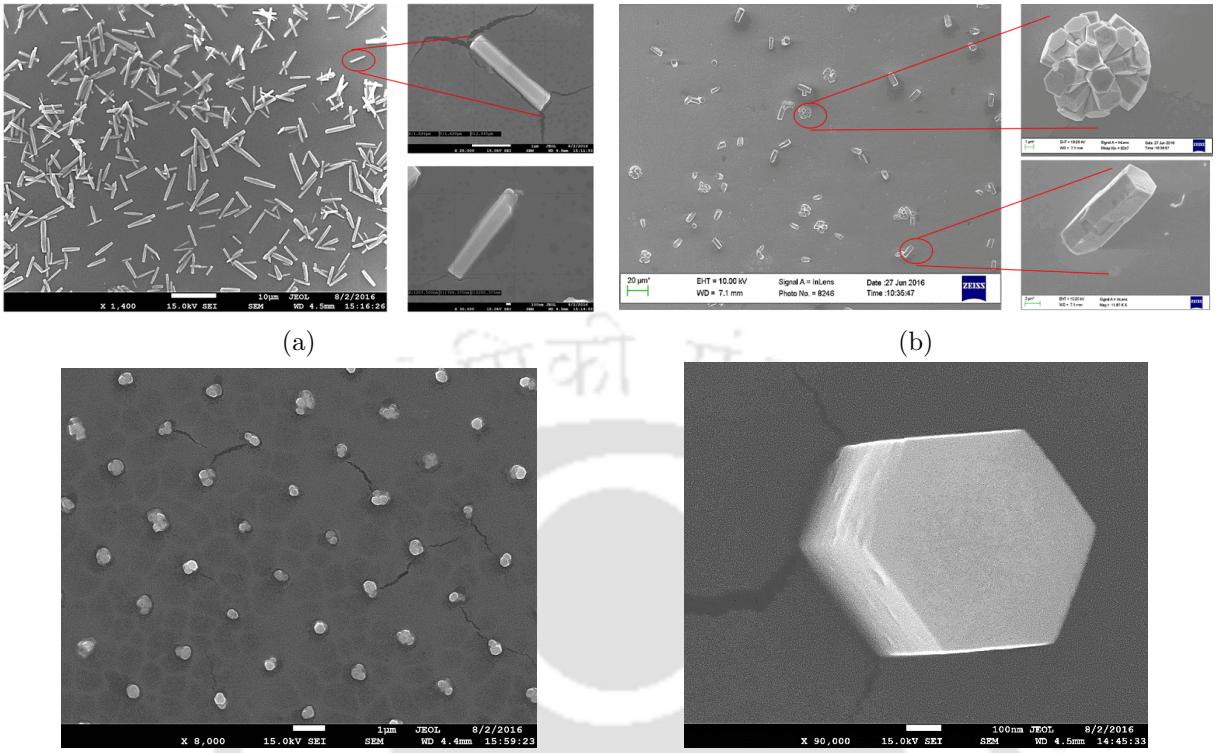

Figure 6.14: ZnO nanorod grown in a 0.05 M solution at 90 °C using e-beam template containing 100 nm holes for different times (a) 2.5 h, (b) 4 h, and (c) 1.5 h. (d) Hexagonal shape of nanorod.

E-beam lithography		
Step	**Process**	**Details**
1	Cleaning	IPA dip for 1 min, drying with nitrogen
2	Spin coat resist (950 PMMA A4)	6000 rpm for 1 min
3	Baking	180 °C for 3 min
4	E-beam exposure	Dosage : 250 µC/cm^2 Beam current : 360 pA Aperture: 30 µm
5	Develop	MIBK:IPA (1:3) for 40 sec

Table 6.7: Process and parameters used in E-beam lithography.

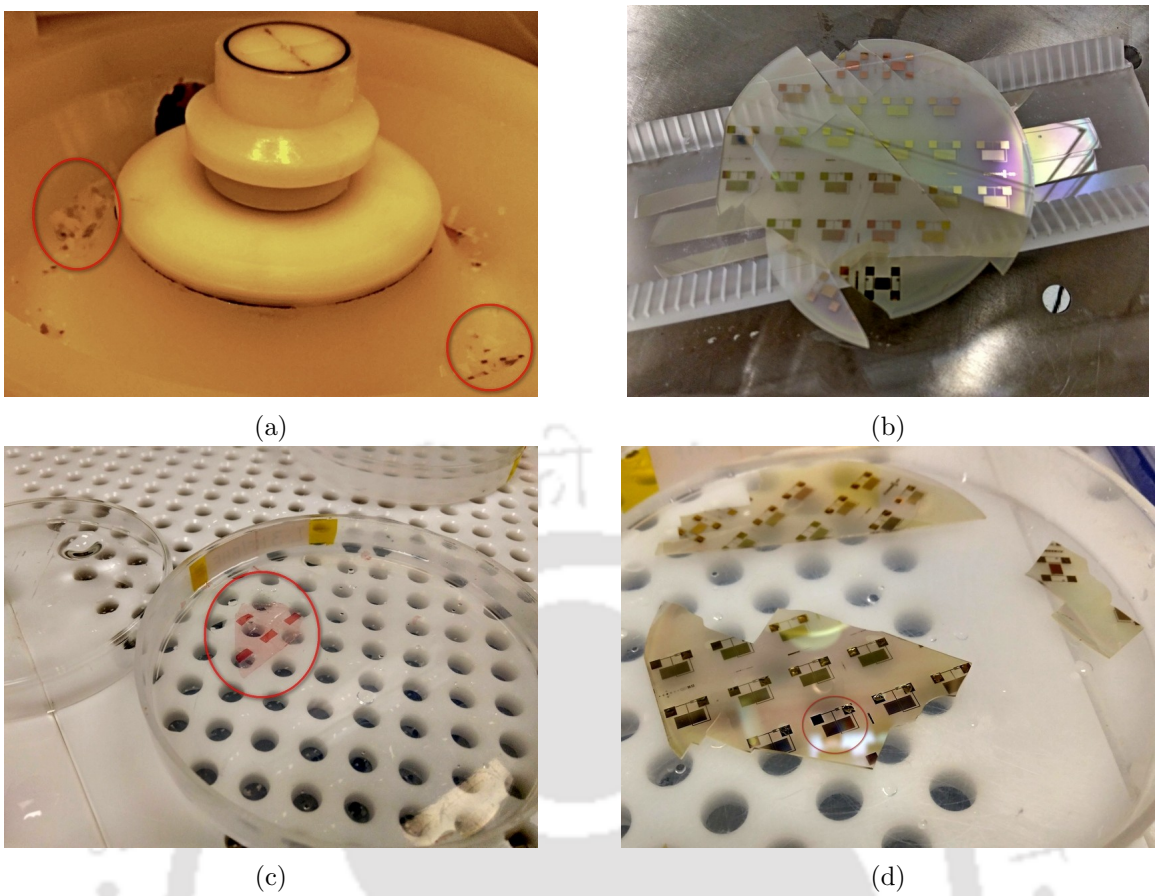

(a) (b)

(c) (d)

Figure 6.15: (a) Wafer shattered during spin coating. (b) Image showing cracked wafer during ZnO film annealing process. (c) Negative resist still remaining after improper second stage photolithography. (d) Manual etching performed using a pointed soft bud to expose metal bond pads.

FESEM images of nanorods grown in a 0.05 M solution at 90 °C using the e-beam template are shown in Fig. 6.14. Nanorods grown for a duration of 2.5 and 4 h tend to merge, become thick and micron-sized. In some cases, the nanorods do not come out vertically but grow horizontally over the resist (Fig. 6.14a). Although the patterned holes were of 100 nm size, nanorods tend to laterally increase in size after coming out and form micron-sized nanoflower structures (Fig. 6.14b). The uniformity of the nanorod growth was found to be difficult to control and reproduce. Although some level of uniformity was attained as shown in Fig. 6.14c when ZnO nanorods 2 µm apart were grown on the resist for 1.5 h. The growing nanorods have the tendency to merge.

6.6 Difficulties faced in fabrication

Some difficulties were faced in the micro-fabrication process of LW devices during photolithography, etching, annealing and nanorod growth attempts.

- Brittle nature of $LiTaO_3$ substrate gave some problems in handling of wafer during various processes. Minor cracks developed due to sudden heating/cooling or mishandling led to shattering of wafer during spin coating (Fig. 6.15a).

- The deposited ZnO thin film on the wafer had to be annealed at 350 °C to create nano-sized grains in the ZnO layer. As shown in Fig. 6.15b, the wafer got cracked after it was taken out from the furnace for cooling causing loss of many devices. Thus, the wafer should be diced before annealing.
- The wafer should not be diced using a standard hand-held glass cutter, generally used to for cutting silicon wafer because of the brittle nature of $LiTaO_3$. The samples had to be taken out of the clean room and diced using semi-automatic wafer dicer.
- Optimizing energy dosage and time for the second stage lithography using AZ nLOF 2070 resist required a lot of effort. After completion of lithography, the wafer was kept in a 10:1 BHF solution for etching SiO_2 for a long time but etching did not begin. This happened because a very thin layer of resist remained on the wafer even after development. Fig. 6.15c shows that upon pouring concentrated HF on the device the undeveloped resist came out like a thin sheet, indicating failure of second stage photolithography.
- The wafers that got cracked or suffered improper lithography had to be manually etched using a pointed soft bud to remove the ZnO and SiO_2 layers for exposing the metal bond pads (Fig. 6.15d).
- Hydrothermal ZnO nanorod growth was attempted through several methods. The nanorods tend to merge, and it is difficult to control the orientation and uniformity of rods on the device surface required to achieve coupled resonance.

6.7 Summary

The chapter has presented the details and processes required for the fabrication and characterization of LW resonator and delay line devices. The devices consist of patterned IDT structure with electrode width of 5 µm, operating at $\lambda = 20$ µm. Two chromium masks with proper alignment marks were prepared using the design layout created by CleWin software. Standard photolithography is performed on clean wafers followed by metal deposition and lift-off to realize the IDT pattern. The dimensions and the thickness of the IDTs are verified using optical microscope and AFM. SiO_2 guiding layer of 3 µm thickness is deposited on the wafer using PECVD. A thin ZnO film is sputtered on the wafer that acts as a seed layer for the nanorods to grow. A second stage photolithography is performed on the wafer using the previously created alignment marks to retain the guiding layer in the active region of the device and etch out the remaining areas to expose the metal bond pads. The devices are connected to a network analyzer via an appropriate L-section matching circuit for characterization. The frequency response of the device is studied by plotting S_{11} and S_{21} of LW resonator and delay line device, respectively. The resonance frequency of the LW resonator is obtained at 195.5 MHz. For the LW delay line device, a minimum insertion loss of -20.6 dB is obtained at 208.2 MHz.

Test samples were put in the furnace at 350 °C for annealing the ZnO film. Annealing not only creates nano-sized grains but also increases the grain density. Hydrothermal growth of ZnO nanorods was carried out in a sealed glass bottle by keeping the samples upside down in

an equimolar solution of zinc nitrate hexahydrate and HMTA at 90–95 °C. Direct growth, PEI assisted, and e-beam template growth were attempted. The diameter of the nanorods depends on the solution concentration, and the growth rate depends on the temperature. Directly grown nanorods have less height, tend to merge and have low aspect ratio. The aspect ratio of the rods can be increased by using PEI in the growth solution. PEI sticks to the side of the rods and inhibits their lateral growth, thereby making the rods thinner and longer. E-beam holes were created, and nanorod growth was attempted, but nanorods tend to merge and sometimes grow non-uniformly to form micron-sized nanoflower type structure with poor orientation. In conclusion, it is difficult to control the orientation and uniformity of ZnO nanorods grown by the bottom-up hydrothermal solution on the device surface required to achieve coupled resonance.

Chapter 7

SH-SAW resonator with S1813 polymer ridges as biosensor

> The proper method for inquiring after the properties of things is to deduce them from experiments.
>
> Issac Newton

The chapter presents fabrication, characterization, bio-functionalization and sensor measurements of SH-SAW resonator comprising S1813 polymer ridges. The ridges are made on the resonator surface along the direction of wave propagation, perpendicular to the IDT aperture. In the previous chapter, fabrication and characterization of LW resonator and growth of ZnO nanorods using the low-temperature hydrothermal method have been discussed. It is found that the height, uniformity in growth and orientation of nanorods are challenging to control and reproduce necessary to attain coupled resonance in the device. However, fabrication of microstructures using top-down approach is easier regarding controlling the aspect ratio of structures. Micro-pillars of polymer materials such as SU-8 and PMMA with precise dimension control have been designed on QCM resonators for various sensing applications [114], [115], [176]. Experimental and simulation results of coupled resonance concerning mass loading effect of SU-8 micro-pillars on the surface of SAW resonators have also been reported in [177], [178].

LW devices using polymer as guiding layer material have been used for designing biosensors. The thickness of the polymer layers can be controlled by varying the spin speed during spin-coating. The low density and low shear velocity of the polymers helps to confine the LW to the surface of the device, thereby providing high mass sensitivity at an optimum layer thickness [195]. Commercially available polymer photoresists such as PMMA, AZ 5214E, SU-8, and S1813 are often used for microfabrication process for designing required patterns on the substrate. Their surface can be chemically modified for biosensing. Joshi *et al.* [196] reported silanization of SU-8 micro-cantilevers followed by immobilization of human immunoglobulin. Fabrication of protein micro-arrays on AZ 5214E polymeric films coated on silicon chips was used to demon-

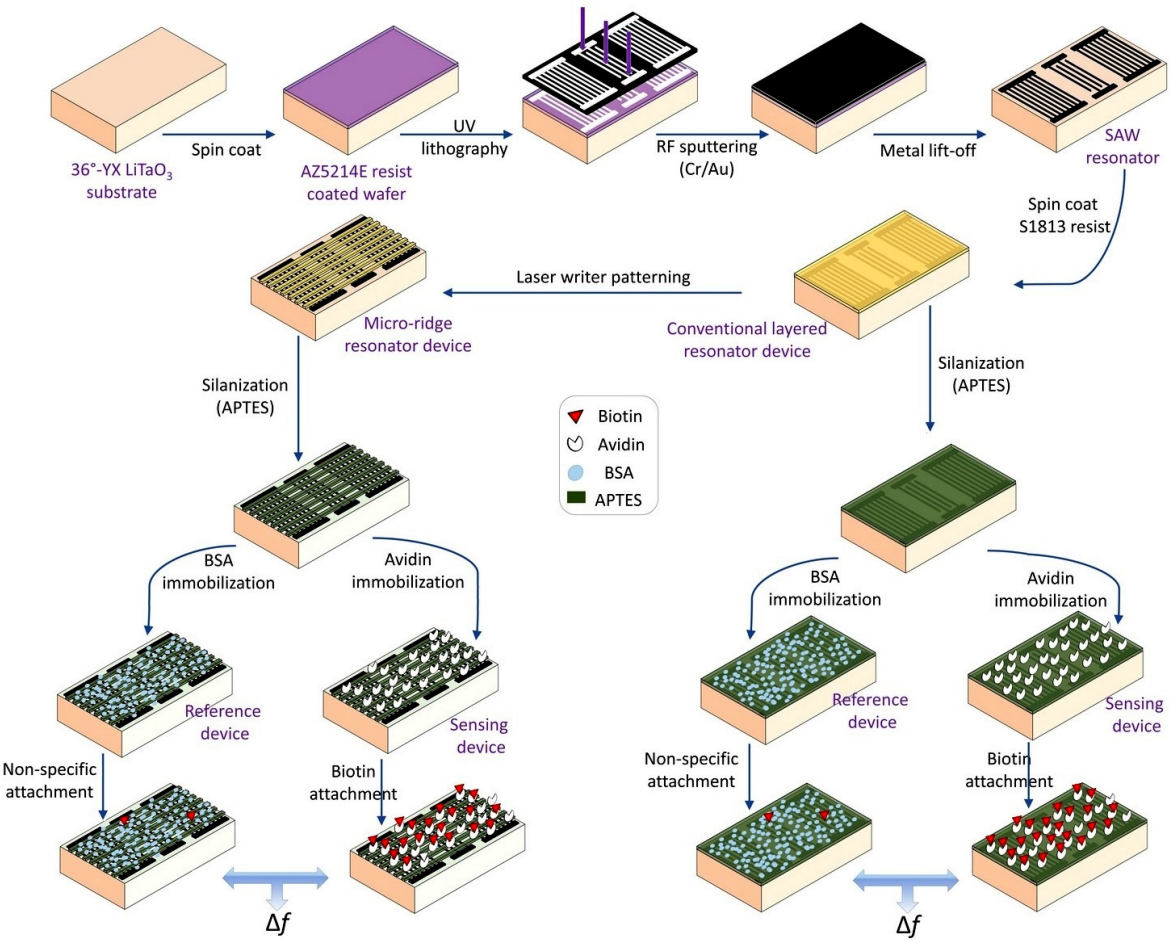

Figure 7.1: Process flow for device fabrication and biofunctionalization

strate highly efficient and repeatable protein binding process [197]. Goudar *et al.* [198] used fluorescence microscopy to confirm attachment of bovine serum albumin (BSA) and avidin on the S1813 positive resist using aminopropyltriethoxysilane (APTES) solution. The present work concerns with FE simulation and experiments of SH-SAW resonator comprising S1813 polymer micro-ridges designed on the surface of the device. The height of the ridges is varied by changing the spin speed during spin coating of the polymer. The ridges are biofunctionalized by silanization and proteins such as BSA and avidin are attached to the surface. The attachment is confirmed by confocal microscopy and AFM. Two devices, one acting as a sensing device and the other as a reference are designed, and different concentrations of biotin are detected along with measurement of mass sensitivity and LOD of the device. The mass sensitivity of the proposed device is compared with a conventional layered SH-SAW (LW) device experimentally.

7.1 Materials and methods

The section presents the details of materials used and process flow of the device fabrication. The geometry used for FE simulation and the methods used for frequency analysis of the device are described. The steps required for device characterization, biofunctionalization of the sensor

surface, and biosensor measurement are also presented.

7.1.1 Device fabrication

The device fabrication process flow of the conventional layered SH-SAW device and ridge-based device is illustrated in Fig. 7.1. The process begins by cleaning the 36°-YX $LiTaO_3$ wafer with acetone, IPA and DI water followed by spin coating with AZ 5214E positive resist (Microchemicals GmbH). The wafer is soft baked at 110 °C for 1 min and given an UV-exposure of 45 mJ cm^{-2} using EVG 620 mask aligner. The substrate is then developed in MF-26A solution (Dow Chemicals) to design the IDT pattern on the resist. A thin film of chromium and gold metal (Cr/Au) of thickness (20/100 nm) is RF sputtered on the wafer and lift off is performed in acetone to realize metal electrodes on the substrate. The completed devices on the wafer are then separated by dicing. Fig. 6.5 (Chapter 6) shows the fabricated resonator device with IDT pattern having an IDT finger width of about 5 µm. The device is expected to resonate at 200 MHz with $\lambda = 20$ µm. The electrode width and aperture of the IDT are kept at $\lambda/4$ and 120λ, respectively. IDT with 20 electrode pairs and reflector grating with 251 electrodes are used in the design.

Two conventional layered SH-SAW (LW) device, one as a reference device and the other as a sensing device are fabricated by spin coating the S1813 resist of thickness 2000 nm. The steps for biofunctionalization and characterization of the conventional device are the same as described for the proposed device with S1813 ridges in the following sections.

The micro-ridge pattern is designed on the device surface by spin-coating with the S1813 positive resist (MicroChem Corp). Each device is kept inside the Dilase 250 laser writer (KLOE, France) and aligned by matching any three corner positions of the device in an optical microscope with the coordinate positions in the design layout. The devices are exposed to UV energy dose of 15%. S1813 micro-ridges of 10 µm width are made along the wave propagation direction on the device surface by developing with MF-26A solution. The variation in height of S1813 ridges is attained by varying the spin speed during spin-coating the resist, as per data sheet of the photoresist [199] (Fig. 7.2a). The optical microscope image and the FESEM image of the S1813 ridges designed on the resonator surface are shown in Fig. 7.2b and 7.2c, respectively.

7.1.2 Surface preparation and characterization

The surface modification and biofunctionalization process used is described in [198]. Once the ridges are designed, both the sensing and reference devices are cleaned using the UV-ozone technique to make the surface rich in –OH bonds. The devices are silanized by immersing them in 3% solution of APTES in toluene for 1 h. The devices are rinsed with toluene to remove unattached APTES and dried on the hot plate. Proteins like BSA (Bovine serum albumin), fluorescein isothiocyanate (FITC)-conjugated BSA, biotin, and avidin from egg white were all procured from Sigma Aldrich. Separate BSA and avidin solutions of 1 mg/ml concentration were prepared in phosphate-buffered saline (PBS). The reference and sensing devices were incubated

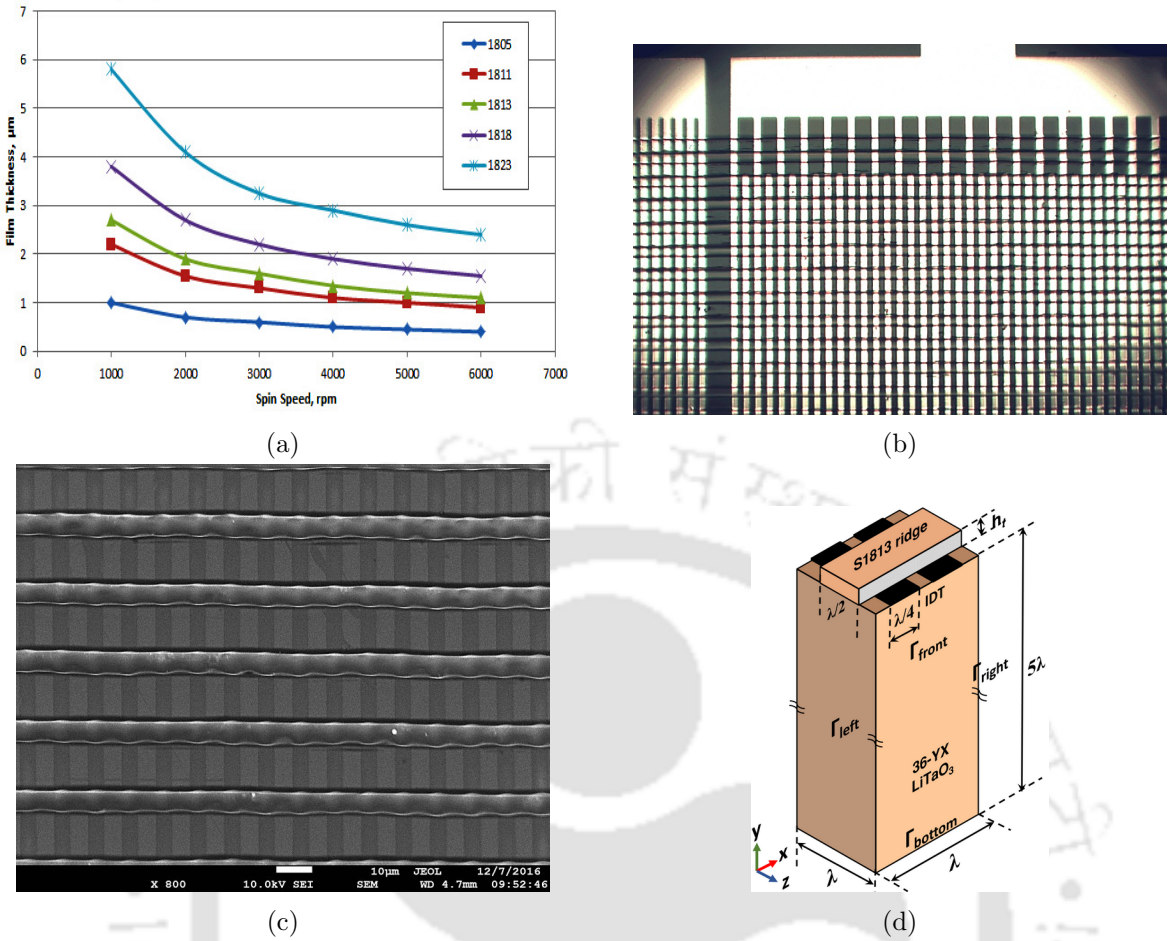

Figure 7.2: (a) Spin speed curves for MICROPOSIT S1813 positive photoresist, (b) optical microscope image showing the developed S1813 ridges on the resonator surface, (c) FESEM image showing the S1813 ridges of width 10 µm, and (d) Simulation geometry used for FE simulation of SH-SAW resonator.

with 30 µL solution of BSA and avidin, respectively for 1 h and rinsed with PBS. The protein attachment test on the device surface was done by attaching FITC-BSA on the sample and observing the fluorescence in confocal microscope and surface morphology in FESEM. AFM images of the bare sample, after silanization and after protein attachment were also taken.

The devices after biofunctionalization were connected to a vector network analyzer VNA (ZVA24, Rohde & Schwarz) via an LC matching circuit using a variable series capacitor of 3–20 pF and a variable parallel inductor of 40–60 nH (Coilcraft Inc.). The matching circuit was used to match the input impedance of SAW device with the characteristic impedance of 50 Ω and minimize the input port reflections. The active area of both the sensing and the reference devices containing ridges were incubated with 30 µL of biotin solution of different concentrations (10, 50, 100, 200 and 400 µg/mL), and then washed with PBS and dried. Biotin selectively attaches on the avidin-functionalized sensing device and not on the BSA coated reference device, producing a frequency shift between the two devices. The slope of the graph of frequency shift versus concentration gives the mass sensitivity S_f while the limit of detection LOD $= 3\sigma/S_f$, where σ is the standard deviation obtained in the frequency measurement of the reference device under

stable conditions.

7.1.3 Simulation methodology

3D FE simulation of a SH-SAW resonator comprising S1813 ridges, operating at $\lambda = 20$ µm is carried out using COMSOL Multiphysics. Fig. 7.2d shows the simulation geometry of the resonator composed of 36°-YX $LiTaO_3$ and S1813 ridges of width $\lambda/2$ made along the direction of wave propagation on the device surface. The ridges are equidistant with their centers λ apart from each other. Massless IDT finger of width $\lambda/4$ is defined on the substrate surface. Periodic boundary conditions are applied along the x and z-axis to simulate one-full wavelength of the SH wave. The bottom surface is kept fixed. A rotated coordinate system with Euler angles (0°, -54°, 0°) is used to simulate the crystal with the correct orientation. An extra-fine mesh of tetrahedral elements is used to mesh the geometry that generates about 20,000 elements and over 120,000 solvable degrees of freedom during simulation. Material properties of S1813 such as density $\rho = 1180\ \mathrm{kg\,m^{-3}}$, Youngs modulus $E = 8$ GPa, and Poisson's ratio $\nu = 0.33$ are used in the simulation. The variation in the frequency of the resonator with ridge height h_t is calculated by using the Eigenmode analysis as ridge height is varied from 100 nm to 3000 nm. Frequency response analysis is also performed to calculate the resonance f_r and the anti-resonance frequency f_{ar} of the device.

Using the small load approximation [173], [200], the frequency shift due to coupled resonance can be written in terms of acoustic load impedance Z_L of the device as

$$\frac{\Delta f^*}{f_0} \approx \frac{i}{\pi}\frac{Z_L}{Z_c} = \frac{i}{\pi Z_c}\left\langle \frac{\sigma}{\dot{u}} \right\rangle_{area} \tag{7.1}$$

where $Z_c = \sqrt{\mu\rho}$ is the acoustic impedance depending on the density ρ and shear modulus μ of the substrate. The load impedance is given by the ratio of the *area-averaged* tangential stress σ and lateral speed $\dot{u}$ at the device surface. The magnitude of the normalized specific acoustic impedance $|Z_s|$ of the device is calculated from the ratio of Z_L and Z_c as

$$|Z_s| = \frac{\left|\left(\int_A \sigma dA\right) / \left(\int_A \dot{u} dA\right)\right|}{Z_c} \tag{7.2}$$

where A denotes the area of the interface between the ridge and the substrate. The gravimetric mass sensitivity S_f of the device is calculated using the *added mass* feature COMSOL by applying an incremental surface mass density Δm from 2×10^{-5} kg/m^2 to 5×10^{-5} kg/m^2 on the exposed surfaces of the polymer ridge. Mass loading causes a shift in the Eigenmode frequency of the device. The mass sensitivity is calculated from the slope of the graph plotted between relative change in frequency $(\Delta f/f_0)$ and incremental surface mass density Δm and is given by the relation [48]

$$S_f = \lim_{\Delta m \to 0} \frac{\Delta f/f_0}{\Delta m} \tag{7.3}$$

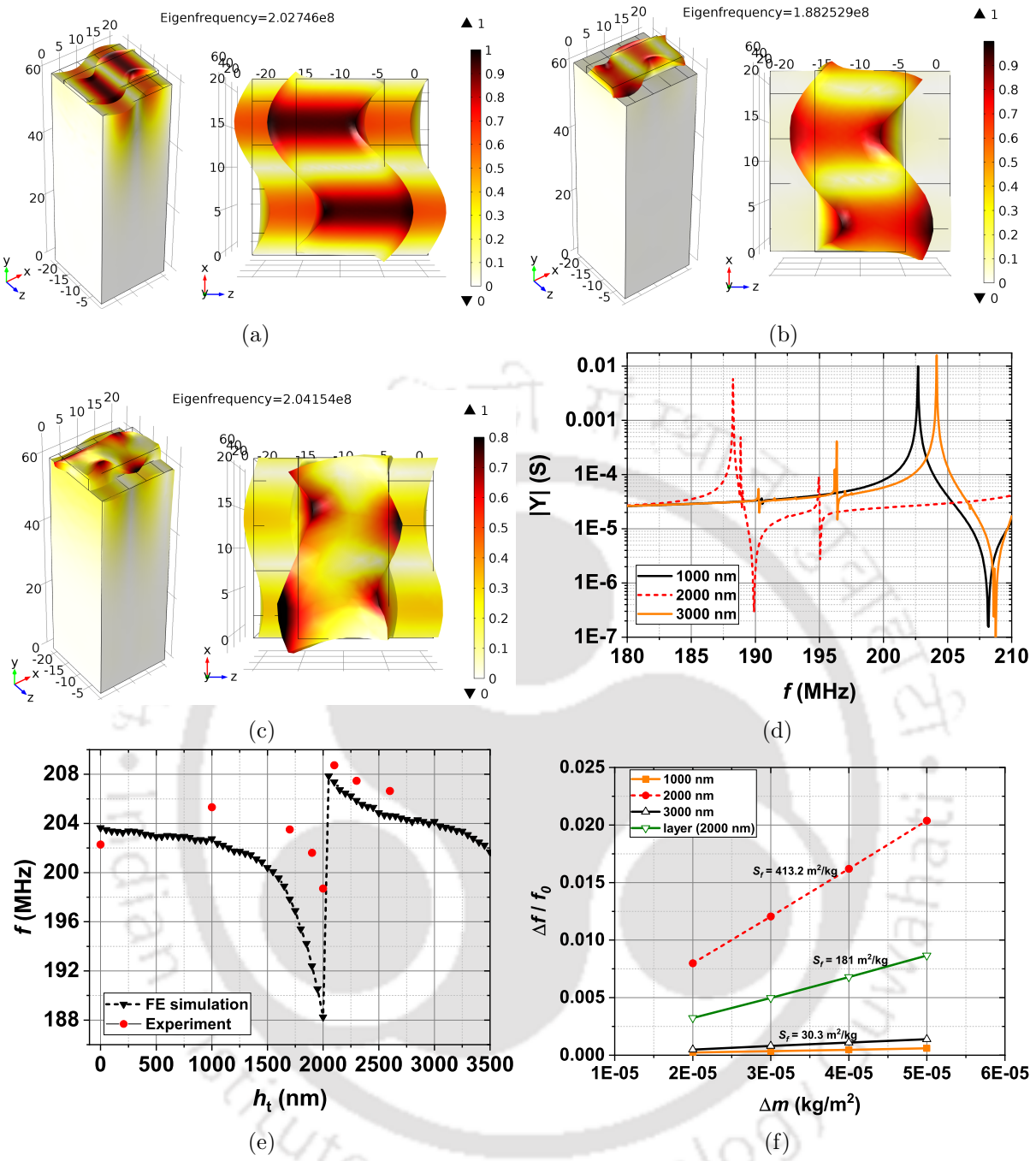

Figure 7.3: Eigenmode analysis of the resonator showing the anti-symmetric mode shape and normalized displacement profile in 3D and in the xz plane for (a) 1000 nm, (b) 2000 nm, and (c) 3000 nm ridge height. (d) The frequency response of the resonator for h_t = 1000 nm, 2000 nm, and 3000 nm showing resonance at 202.7 MHz, 204.2 MHz, and 188.3 MHz, respectively. (e) Variation in the resonance frequency of the device with ridge height indicating occurrence of the coupled resonance near h_t = 2000 nm through both FE simulation and experiment. (f) The plot of relative shift in the frequency versus incremental surface mass density for the layered case and three different ridge heights.

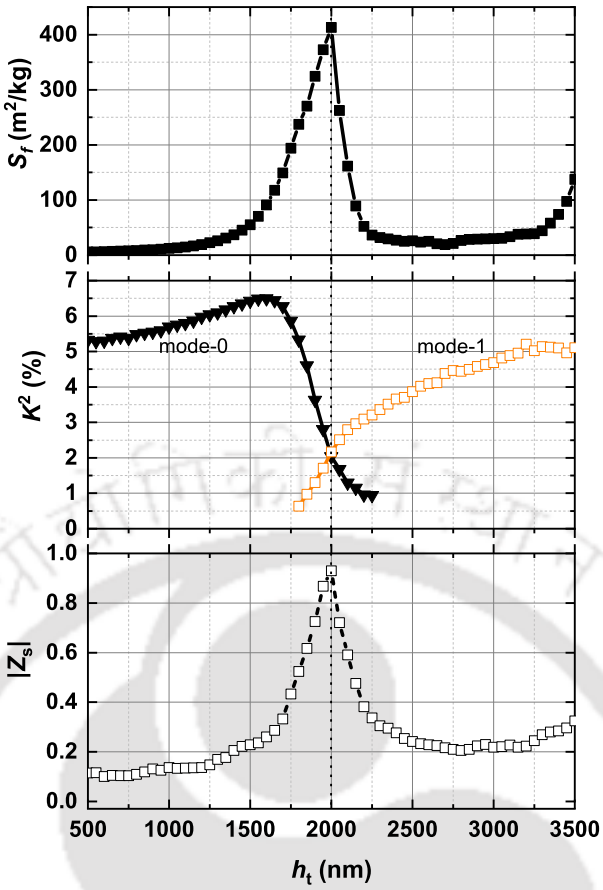

Figure 7.4: Variation in mass sensitivity, coupling coefficient and magnitude of the normalized specific acoustic impedance of the device with ridge height.

7.2 Results and discussions

The section presents the results of FE simulation and experiments concerning coupled resonance in SH-SAW resonator with S1813 ridges. The verification of biofunctionalization with confocal microscopy along with FESEM and AFM study of sensor surface after silanization and protein attachment is also presented. Lastly, frequency measurements of the sensing and reference devices are performed using a VNA for detection of biotin.

7.2.1 Coupled resonance with polymer micro-ridges

Eigenmode analysis of SH-SAW resonator comprising S1813 ridges on the device surface is carried out. Fig. 7.3a, 7.3b, and 7.3c show the Eigenmode shape and normalized displacement profile in 3D and in the xz plane for h_t = 1000 nm, 2000 nm, and 3000 nm, respectively. The mode shapes indicate that the resonator generates a standing wave with SH vibrations at the surface. Below a critical ridge height of 2000 nm, the resonator vibrates in the fundamental mode (mode-0, Fig. 7.3a). Any further increase in the height of the ridges causes a transition to the next higher order mode of vibration (mode-1, Fig. 7.3c). The frequency response of the resonator with h_t = 1000 nm, 2000 nm, and 3000 nm is shown in Fig. 7.3d. The frequency at which the admittance of the device becomes maximum is called as the resonance frequency. At

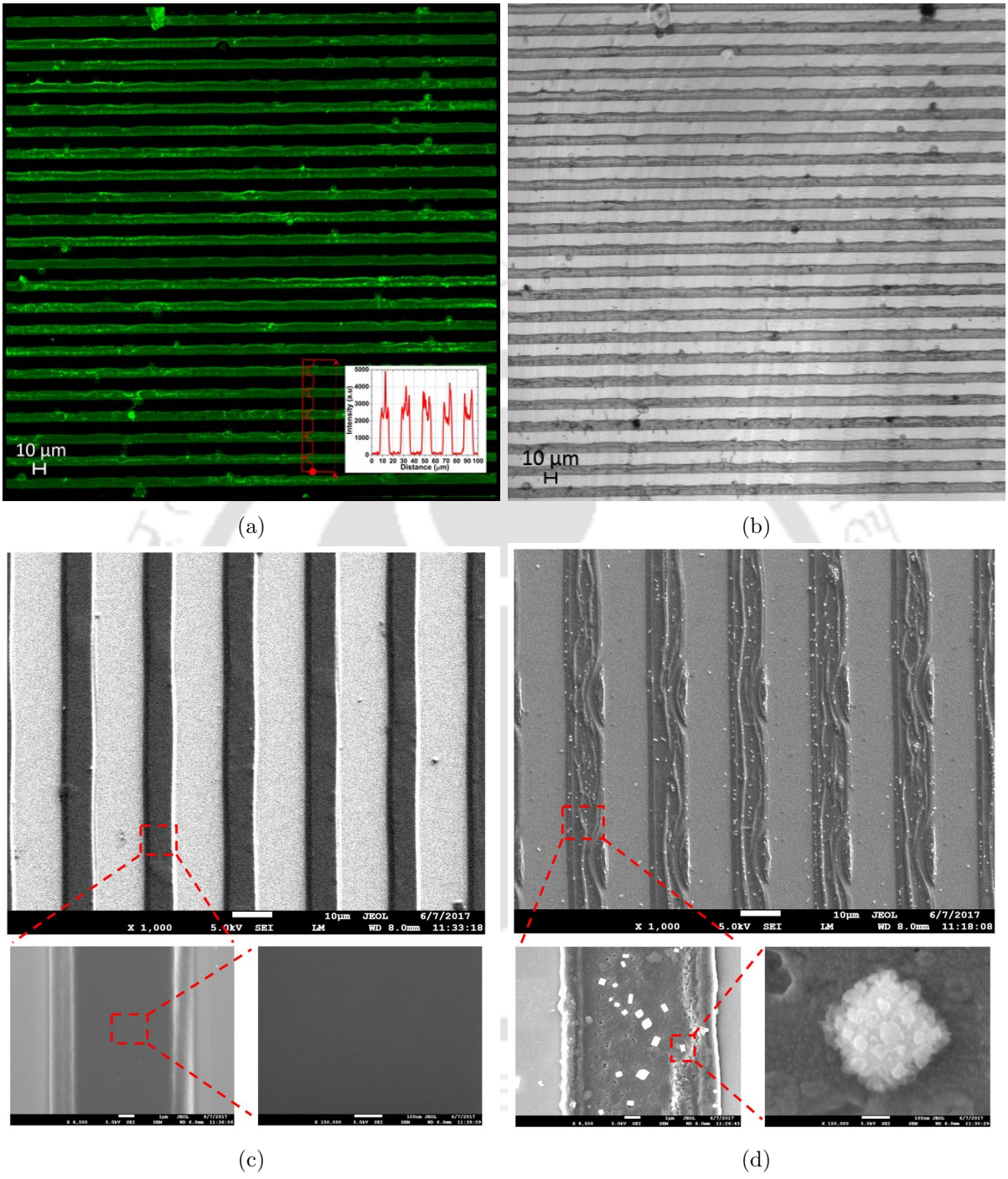

Figure 7.5: (a) Fluorescence and the corresponding (b) bright field image showing the attachment of FITC-BSA protein on the silanized S1813 ridge surface. The variation in fluorescence intensity along the red colored line in the figure indicates uniform protein attachment on the micro-ridges. FESEM image showing the S1813 ridge pattern along with the magnified images of the portions of the ridge considering (c) bare surface and (d) silanized surface with attached FITC-BSA. Agglomerates of BSA protein can be seen attached preferentially on the ridge surface.

Spin speed (rpm)	S1813 thickness (µm)	Resonance frequency (MHz)
0	0	202.28
7000	1.0	205.32
2500	1.7	203.51
2000	1.9	201.61
1850	2.0	198.70
1700	2.1	208.74
1500	2.3	207.47
1000	2.6	206.64

Table 7.1: Variation in S1813 resist thickness with spin speed and the corresponding measured resonance frequencies of the resonator device.

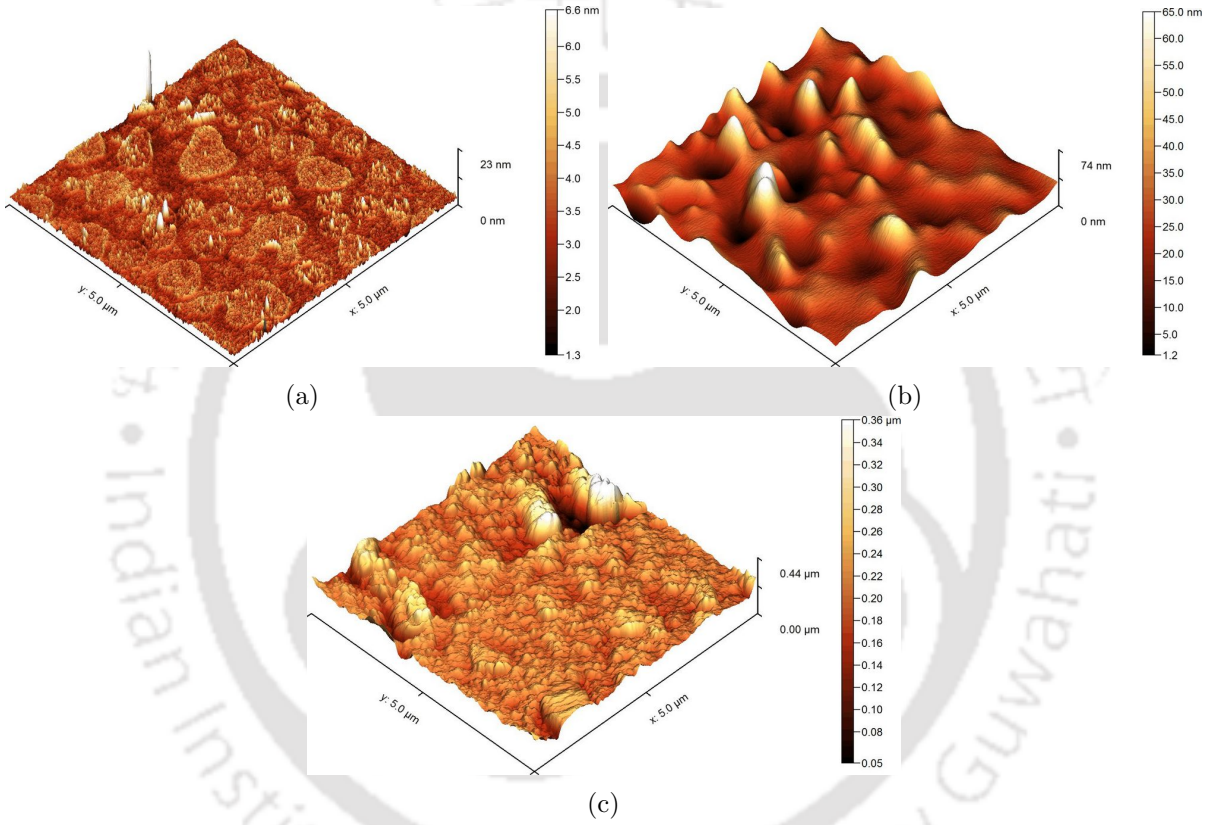

Figure 7.6: AFM images of a portion of S1813 ridge showing the (a) bare, (b) silanized, and (c) BSA attached surface.

h_t = 1000 nm and 3000 nm, resonance frequencies of 202.7 MHz and 204.2 MHz are obtained, respectively. However, at critical h_t = 2000 nm, the resonance frequency shifts to 188.3 MHz. The resonance frequency of the device containing ridges is measured by connecting it to the VNA. After measurement, the resist is stripped off by putting the device in acetone and ridges of different height are again made on the device surface. Table 7.1 shows different thicknesses of S1813 resist attained by varying the spin speed and the corresponding measured resonance frequency. Fig. 7.3e shows the variation in resonance frequency of the device with ridge height indicating the occurrence of coupled resonance near h_t = 2000 nm through both Eigenmode analysis and experiment. When higher spin speeds are employed, ridges of lower thickness are made on the device. As spin speed is reduced, the thickness of the ridges increase leading

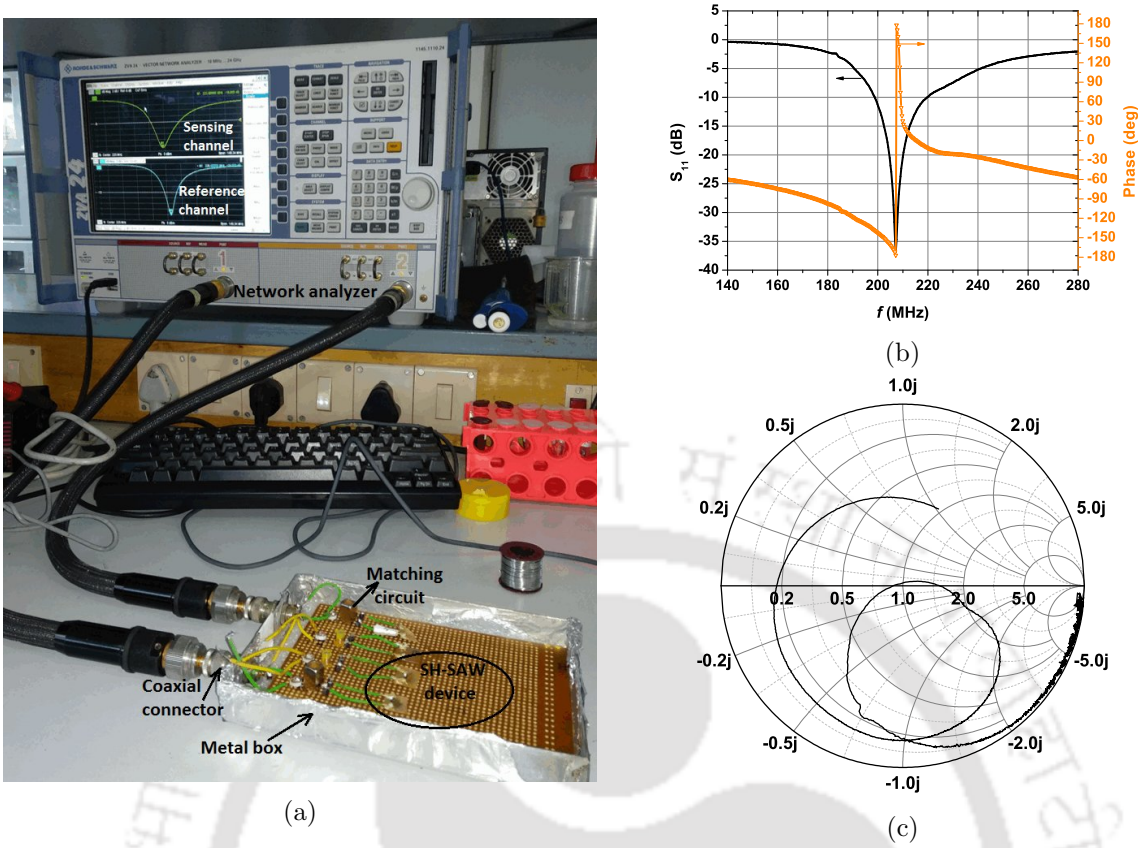

Figure 7.7: (a) SH-SAW devices connected to the VNA through a matching circuit comprising a series variable capacitor and a shunt variable inductor. The frequency shift is measured by monitoring the S_{11} of the sensing and reference devices. (b) Frequency response showing the S_{11} (dB) and phase of the reference device measured after the matching process with resonance occurring at 207.2 MHz. (c) Matching verified by the Smith chart.

to a decrease in the resonance frequency of the device due to inertial loading. Near coupled resonance, sharp rise in the measured resonance frequency from 198.8 MHz to 208.7 MHz is seen indicating a transition from inertial to elastic loading.

Fig. 7.3f shows the plot of relative shift in frequency of the SH-SAW device with incremental mass loading for the layered case and three different ridge heights. At h_t = 1000 nm and 2000 nm, S_f of 12.1 m^2/kg and 30.3 m^2/kg are obtained, respectively. Coupled resonance at h_t = 2000 nm increases the mass sensitivity to 413.2 m^2/kg which is more than twice the mass sensitivity offered by the layered device of the same thickness. Fig. 7.4 shows the variation in sensitivity, coupling coefficient and magnitude of the normalized specific acoustic impedance with ridge height. The mass sensitivity of the device becomes maximum at the coupled resonant height but it remains below 50 m^2/kg for most of the other ridge heights. When the height of the ridges is low, the K^2 of the device tends towards the K^2 value of 36°-YX $LiTaO_3$ substrate (4.8%) [11]. As ridge height increases, the K^2 of the fundamental mode (mode-0) also increases reaching a maximum value of 6.5% at h_t = 1600 nm. Transition in the mode of vibration occurs at critical ridge height where the K^2 of the next higher order mode (mode-1) becomes greater than the K^2 of mode-0. Although the S_f of the device increases at coupled resonant height, the K^2 of the device reduces to a low value of about 2%. The variation in $|Z_s|$ with ridge

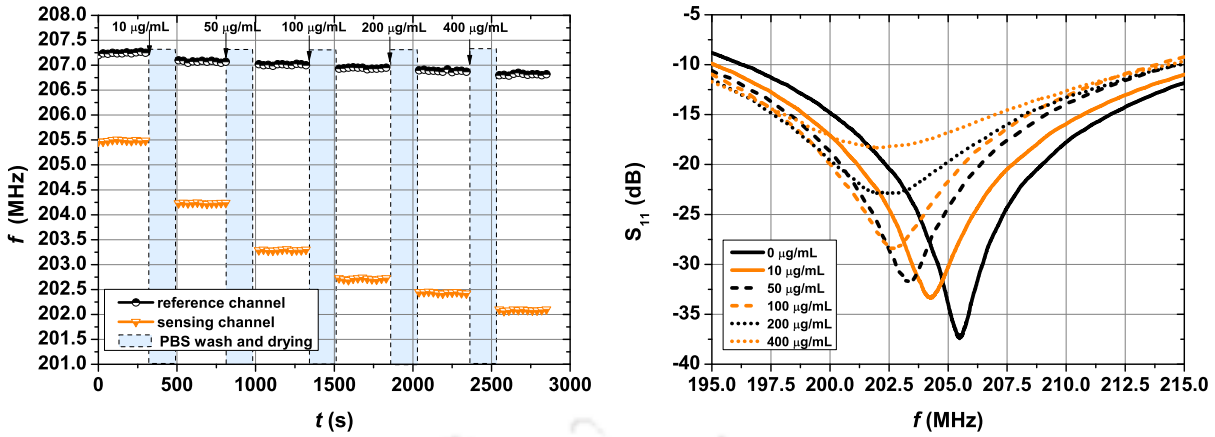

(a) (b)

Figure 7.8: (a) Variation in the resonace frequency of the sensing and reference devices with time upon mass loading with different concentrations of biotin. The sensing and the reference devices are immobilized with avidin and BSA, respectively. (b) Variation in S_{11}(dB) of the sensing device with frequency on adding different concentrations of biotin.

height follows a trend similar to the mass sensitivity of the device. At coupled resonance, the contact stiffness increases, the ridges get clamped by inertia and exert a restoring force back on the substrate [200]. This raises the specific acoustic impedance and the area-averaged stress between the ridge-substrate interface and such a system produces large frequency shifts upon mass loading.

7.2.2 Biofunctionalization

The protein attachment test is done by applying FITC-tagged BSA on the silanized S1813 ridges and observing in the confocal microscope. Fig. 7.5a and 7.5b show the fluorescence and the corresponding bright field image of the FITC-BSA attached to the 10 µm ridge pattern, respectively. The green-colored fluorescence seen from the ridge-pattern indicates the selective attachment of FITC-BSA on to the S1813 micro-ridges and not on the substrate. The S1813 positive photoresist is essentially based on a cresol-novolac resin containing –OH group in the repeating unit of the polymer chain. These –OH groups react with APTES and get silanized which subsequently leads to attachment of protein on the surface of the photoresist [198], [201]. The bold red colored line in Fig. 7.5a shows the variation in fluorescence intensity along the line, indicating uniform protein attachment on the micro-ridges.

Change in the surface morphology after BSA attachment is observed using FESEM and AFM. Fig. 7.5c and 7.5d show the FESEM images of S1813 ridge pattern before and after attachment of BSA respectively along with the magnified images of the resist region. The bare surface with no protein binding is smooth, but after protein attachment the ridges becomes rough. Agglomerates of BSA of about 350 nm size can be seen preferentially sitting on the ridge surface than on the substrate indicating attachment of BSA on the polymer. AFM images showing a portion of the bare S1813 ridge surface, silanized ridge surface, and BSA-attached ridge surface are presented in Fig. 7.6a, 7.6b, and 7.6c, respectively. The bare surface of the

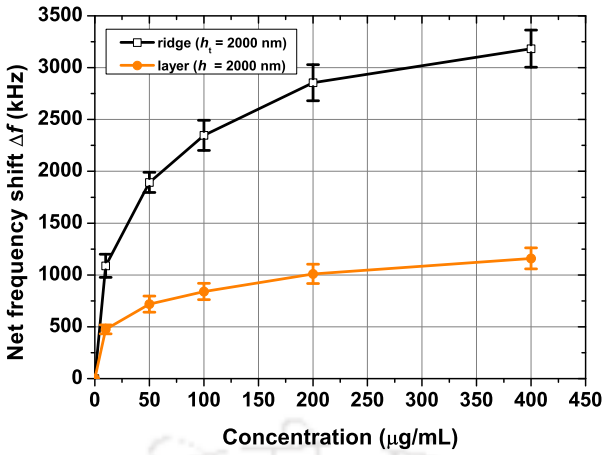

Figure 7.9: Net frequency shift because of mass loading with different concentrations of biotin considering two devices, one with ridges of height 2000 nm and the other consisting of layer of the same height. Three independent measurements were performed. The error bars represent the standard deviation.

photoresist after the spin coating is very smooth with a RMS roughness of about 0.6 nm. The surface roughness increases to 8 nm after silanization, and up to 33 nm after BSA immobilization on the surface.

7.2.3 Sensor measurements

SH-SAW devices with polymer ridges of width 10 µm and height about 2000 nm are fabricated. The surfaces of the reference and sensing devices are chemically modified by silanization, and immobilized with BSA and avidin, respectively. After biofunctionalization, the devices are connected to the VNA and matched by tuning the variable capacitor and inductor so that the resonance frequencies of both the devices are close to each other. Fig. 7.7a shows the SH-SAW resonators and the associated matching circuit, placed in a metal box and connected to the VNA using coaxial connectors. The S_{11} of the reference and the sensing devices are monitored simultaneously on the split screen of the VNA. Fig. 7.7b shows the measured value of S_{11}(dB) and phase of the reference device. At the resonance frequency of 207.2 MHz, the S_{11} of the device displays a minimum value of -36.8 dB with sharp phase reversal. The Smith chart plot crossing the normalized unit impedance at the resonance frequency in Fig. 7.7c indicates the attained matching.

Fig. 7.8a shows the variation in the resonance frequency of the reference and sensing device with time for increasing concentrations of biotin applied on the sensor surface. Before adding biotin, the reference and the sensing devices are matched at about 207.2 MHz and 205.5 MHz, respectively. The measured standard deviation σ in the frequency of the reference device under stable conditions was about 12 kHz. Both the devices were disconnected from VNA and incubated with 30 µL of 10 µg/mL of biotin solution for 2 min. Next, the devices are washed with PBS, dried and then reconnected to measure the stable value of the resonance frequency, and the corresponding frequency shift Δf between them. The process is repeated for different biotin

Concentration (µg/mL)	S1813 ridge (h_t = 2000 nm)				S1813 layer (h = 2000 nm)			
	Δf (kHz)			Mean (kHz)	Δf (kHz)			Mean (kHz)
	Exp. 1	Exp. 2	Exp. 3		Exp. 1	Exp. 2	Exp. 3	
0	0	0	0	0	0	0	0	0
10	970	1105	1190	1088.3	429	480	515	474.7
50	1895	1990	1795	1893.3	655	695	805	718.3
100	2200	2490	2350	2346.7	912	855	755	840.7
200	2800	2715	3050	2855	917	1010	1105	1010.7
400	3350	2995	3205	3183.3	1275	1085	1120	1160

Table 7.2: Frequency shifts obtained for the ridge and the layered case with increasing concentration of biotin solution.

Year/Author	Layer/Substrate	f (MHz)	Detection	Sensitivity kHz/(µg/ml)	LOD
2002/ Barie *et al.*[202]	Polyimide/36°-YX LT	380	Mouse-Ig	1.56	7 pg/mm^2
2004/ Kwon *et al.*[184]	Gold/36°-YX LT	100	Human Ig	0.06	10.8 ng/mL/Hz
2009 Lee *et al.*[80]	SiO_2/36°-YX LT	200	Heaptitus B	0.76	< 10 pg/µL
2010/ Cheng *et al.*[203]	Gold/ST-90°X	178	Arbin	5.2	-
2011/ Feng *et al.*[204]	PMMA/64°-YX LN	112	IgG	7.3	-
2015/Zhang *et al.*[205]	SiO_2/36°-YX LT	198	Prostate antigen	-	10 ng/mL
This work	S1813 ridge/36°-YX LT	200	Biotin	6.4	<6 µg/mL

Table 7.3: Comparison of sensitivity and LOD with other reported work.

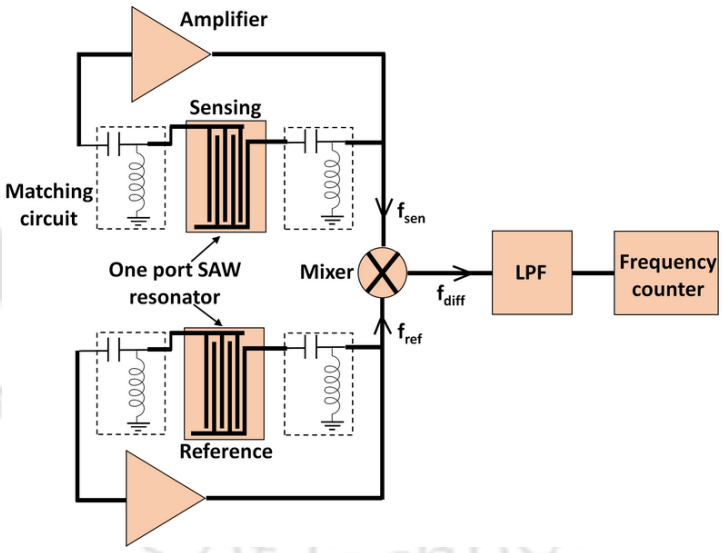

Figure 7.10: Dual channel oscillator configuration for SAW sensor.

concentrations i.e. 50, 100, 200, and 400 µg/mL. Since the reference device is immobilized with BSA, biotin does not attach to the ridge surface and gets washed away with PBS solution causing a negligible shift in the frequency. However, biotin attaches to the sensing device immobilized with avidin leading to a more significant shift in the resonance frequency. Fig. 7.8b shows the S_{11} curves of the sensing device upon mass loading with different concentrations of biotin. The frequency of the sensing device decreases, return losses increase, and the curves become broader with increasing biotin concentration.

Fig. 7.9 shows the net frequency shift obtained by adding different concentrations of biotin

for two cases i.e. one with device composed of ridges of h_t = 2000 nm and the other a plain LW device with S1813 guiding layer of same thickness. Three independent experiments were performed and the frequency shifts obtained for the ridge and the layered cases are listed in Table 7.2. The frequency shift increases with increasing concentration of biotin and tends to saturate at higher concentrations. The device with ridges of h_t = 2000 nm offers a LOD of $<$ 6 µg/mL and a mass sensitivity of 6.4 kHz/(µg/mL) which is about three times the mass sensitivity of layered SH-SAW device. The outcome of the experiment is also compared with some other reported results in Table 7.3. The device was connected to the matching circuit via plain wires that caused noise in the system. The standard deviation (σ) obtained in the measured frequency of the device was large (12 kHz). The LOD can be improved if the device is connected on a pre-designed PCB, packaged and shielded. Also, the response would improve further if a basic flow cell was designed for automatic insertion of liquids rather than drop casting the sample on the active area.

7.3 Practical considerations for system design

A practical and reasonably priced sensor system can be realized by designing a PCB consisting of sensing and reference devices in a dual-channel oscillator configuration avoiding the use of network analyzer as shown in Fig. 7.10. The one-port SAW resonator is connected in the feedback loop of the amplifier. The frequencies of the sensing and the reference device are tuned with the help of the matching circuit. Upon specific attachment of the analyte, a frequency difference between the sensing and reference devices ($f_{diff} = f_{ref} - f_{sen}$) is measured with help of a frequency counter. Further reduction in cross-talk, noise along with temperature compensation can be achieved by using a micro controller-based phase-locked loop system reported in [206]. In addition, chemical modification at the surface should be made in such a way that the active area of the sensor can be reused upon washing. Materials cost can be further reduced by using a silicon substrate with a piezoelectric thin film.

Coupled resonance requires microstructures of specific aspect ratio to be present on the surface of the resonator. Achieving the accuracy required for coupled resonance through microfabrication is challenging. Once the microstructures are fabricated, the structural properties of the microstructures get fixed. Thus, it is more practical to adjust the SAW device frequency to match with the natural vibration frequency of the fabricated microstructures. It can be achieved by fine tuning the matching circuit till coupled resonance condition is met.

The system can be extended in making a point-of-care device by making the sensors detachable. The output data (frequency shift) is fed to a nearby data processing unit (mobile) for rapid analysis.

7.4 Summary

The chapter has presented FE simulation and experiments to analyze the coupled resonance effect in SH-SAW resonator comprising micro-ridges of S1813 photoresist. The chapter also presents biosensing experiments using SH-SAW devices with conventional sensing film and with micro-ridges in place of the film as proposed. Equidistant ridges of width 10 µm positioned perpendicular to the IDT aperture were designed using lithography and the height variation was achieved by varying the spin speed during spin-coating the polymer photoresist. Coupled resonance with micro-ridges is attained when the height of the ridges is close to 2000 nm. Two SH-SAW devices, one acting as a sensing device immobilized with avidin and the other as a reference device immobilized with BSA were connected to the VNA for frequency measurements via a matching circuit. S1813 resist being rich in –OH bond was silanized by APTES followed by confirmation of specific attachment of FITC-tagged BSA protein on the ridges by confocal microscope. The change in the surface morphology before and after protein attachment is studied using AFM and FESEM. Different concentrations of biotin are applied on the surface of the sensor, and the resulting frequency shifts are measured. The device with a critical ridge height of $h_t = 2000$ nm offers LOD of < 6 µg/mL and a produces large frequency shifts upon mass loading leading to a sensitivity of 6.4 kHz/(µg/mL), about three times greater than the conventional layered device. The results show that devices utilizing coupled resonance with microstructures offer great potential for various biosensing applications requiring high sensitivity.

Chapter 8

Conclusion and recommendations

> One never notices what has been done; one can only see what remains to be done.
>
> Marie Curie

The thesis mainly investigates coupled resonance in an LW device with ZnO nanorods and an SH-SAW device with SiO_2/polymer micro-ridges made on the top surface and its application for biosensing. Presence of nano or microstructures of appropriate size on the device generating SH waves leads to coupled resonance causing a transition between inertial and elastic vibration modes. At coupled resonance, the device and the nano/microstructure both vibrate in unison causing a large change in the resonance frequency of the system. Such a system is sensitive to mass attachments, producing large frequency shifts upon mass loading. At coupled resonance, the device offers high mass sensitivity and increased interface stress, but decease in electromechanical coupling coefficient as the losses in the device increase. Extensive FE simulations are performed to study coupled resonance in both resonator and delay line configurations of LW and SH-SAW devices. Experiments are carried out for verification of coupled resonance and its application for biosensing. LW devices based on 36°-YX $LITaO_3$ substrate and SiO_2 guiding layer were fabricated using standard photolithography and characterized using a network analyzer. ZnO nanorod fabrication via hydrothermal growth was attempted on the sensor surface, but the control of aspect ratio and orientation of the nanorods required for attaining coupled resonance proved to be challenging. SH-SAW resonator consisting of 10 µm wide S1813 polymer ridges along the direction of wave propagation were fabricated. The height of the ridges was varied by changing the spin speed during spin coating the resist, and the occurrence of coupled resonance is verified experimentally and found to be consistent with simulated results. The surface of the ridges was biofunctionalized after silanization, and the potential use of the device as a biosensor was demonstrated by detecting different concentrations of biotin on avidin functionalized surface.

The major contributions of the thesis are as follows:

- 3D FE analysis of a Y-cut $LiTaO_3$ is performed to study leaky and non-leaky SAW gener-

ated by the substrate as Euler angle θ is varied. Eigenmode analysis is done to calculate the free surface velocity, metalized surface velocity, coupling coefficient, and TCF of the substrates generating SH-wave such as 36°-YX $LiTaO_3$, 41°-YX $LiNbO_3$, 90°-AT and ST quartz. The obtained values are consistent with those reported in literature.

- Analytical calculations of phase velocity, group velocity and mass sensitivity of LW devices are performed by solving the dispersion equation of LW. Different guiding layers such as SiO_2, ZnO, gold, SU-8, PMMA, and polyimide are considered, and the results of FE simulation are compared with the analytically obtained values. Polymer layers offer high mass sensitivity but large K^2 is observed only within a narrow range of layer thickness, therefore they need to be coated precisely.

- A comparative analysis of LW devices with SiO_2 guiding layer considering different substrates such as 36°-YX $LiTaO_3$, 41°-YX $LiNbO_3$, 90°-AT and ST quartz is performed. Quartz-based LW devices offer higher mass sensitivity than $LiTaO_3$ and $LiNbO_3$ based LW devices. However, they suffer from poor K^2.

- LW resonator composed of a SiO_2 guiding layer and ZnO nanorods is simulated to study the variation in resonance frequency, mass sensitivity, and coupling coefficient with height and packing density of rods. FE simulation of LW delay line is also performed by designing ZnO nanorods on the delay line path between input and output IDTs. The effect of nanorods on the time response, stress and insertion loss of the device is studied. Coupled resonance with ZnO nanorods made on the LW device offers high mass sensitivity but at the cost of increased insertion losses and decreased K^2.

- FE simulation of SH-SAW resonator and delay line device involving coupled resonance with SiO_2 micro-ridges made along the wave propagation direction is performed. The ridges help to guide the SH wave, increase the sensor surface area, and also cause coupled resonance at a particular size increasing the mass sensitivity of the device.

- Large number of LW resonators and delay line devices composed of 36°-YX $LiTaO_3$ substrate and SiO_2 guiding layer are fabricated using the standard UV-photolithography, metal lift-off methods and PECVD deposition techniques. The devices are connected to a network analyzer via an appropriate L-section matching circuit for characterization. For a wavelength of $\lambda = 20$ µm of the LW resonator, a resonance frequency of 195.5 MHz is obtained. For the LW delay line device of $\lambda = 20$ µm, a minimum insertion loss of -20.6 dB is obtained at 208.2 MHz. Attempts were made to grow ZnO nanorods by a low-temperature chemical hydrothermal method. It was difficult to control the orientation and uniformity of rods on the device surface required to achieve coupled resonance.

- Experiments to verify coupled resonance were performed on SH-SAW resonators composed of 36°-YX $LiTaO_3$ substrate and S1813 photoresist micro-ridges made on the top surface of the devices.

- The S1813 polymer ridges were biofunctionalized after silanization, and the protein attachment was verified through confocal and AFM. The sensing and reference devices were immobilized with avidin and BSA respectively, and different concentrations of bi-

otin were detected. The device provided mass sensitivity and LOD of 6.4 kHz/µg mL^{-1} and 6 µg mL^{-1}, respectively.

The present work introduces a technique based on coupled resonance for the development of LW or SH-SAW devices highly sensitive to mass loading. Proper design of the device can lead to improved sensitivity and selectivity of the sensor, and the packaged setup can be useful for biosensing.

This research work can be extended in the following directions:

- Apart from ZnO nanorods, some other nanostructures such as nanowires, nanopillars, nanotubes that have a better possibility of controlled aspect ratio growth via EBL, laser interference lithography (LIL), and nanoimprint lithography (NIL) can be designed on the surface of the sensor to attain coupled resonance for high mass sensitivity.
- SAW devices operating at high frequencies may be investigated for sensors as the height of the pillars in the sensing medium could be reasonably small at high resonance frequencies.
- For CMOS compatibility, the device can be designed on a silicon wafer with piezoelectric ZnO thin film on the top surface and nanorods can be grown on via high-temperature CVD growth for better orientation control of the rods.
- In this thesis work, biotin was used as biomolecule for detection. In practice, a practically relevant bio-analyte such as disease-causing antigens, pathogens, and cancer bio-markers can be chosen for detection purposes, and sensitivity and selectivity can be studied.
- In addition to biosensors, coupled resonance phenomenon can be explored in designing highly tunable filters, sensitive gas sensors, UV sensors, and devices for photonic and signal processing applications.

Appendix A

Material constants

Elastic, piezoelectric and dielectric constants

$LiTaO_3$ and $LiNbO_3$ (Trigonal system class 32)

$$\begin{bmatrix} c_{11} & c_{12} & c_{13} & c_{14} & 0 & 0 \\ c_{12} & c_{11} & c_{13} & -c_{14} & 0 & 0 \\ c_{13} & c_{13} & c_{33} & 0 & 0 & 0 \\ c_{14} & -c_{14} & 0 & c_{44} & 0 & 0 \\ 0 & 0 & 0 & 0 & c_{44} & c_{14} \\ 0 & 0 & 0 & 0 & c_{14} & \frac{1}{2}(c_{11}-c_{12}) \end{bmatrix} \quad \begin{bmatrix} 0 & 0 & 0 & 0 & e_{15} & -e_{22} \\ -e_{22} & e_{22} & 0 & e_{15} & 0 & 0 \\ e_{31} & e_{31} & e_{33} & 0 & e_{15} & -e_{22} \end{bmatrix} \quad \begin{bmatrix} \epsilon_{11} & 0 & 0 \\ 0 & \epsilon_{11} & 0 \\ 0 & 0 & \epsilon_{33} \end{bmatrix}$$

Quartz (Trigonal system class 3m)

$$\begin{bmatrix} c_{11} & c_{12} & c_{13} & c_{14} & 0 & 0 \\ c_{12} & c_{11} & c_{13} & -c_{14} & 0 & 0 \\ c_{13} & c_{13} & c_{33} & 0 & 0 & 0 \\ c_{14} & -c_{14} & 0 & c_{44} & 0 & 0 \\ 0 & 0 & 0 & 0 & c_{44} & c_{14} \\ 0 & 0 & 0 & 0 & c_{14} & \frac{1}{2}(c_{11}-c_{12}) \end{bmatrix} \quad \begin{bmatrix} e_{11} & -e_{11} & 0 & e_{14} & 0 & 0 \\ 0 & 0 & 0 & 0 & -e_{14} & -e_{11} \\ 0 & 0 & 0 & 0 & 0 & 0 \end{bmatrix} \quad \begin{bmatrix} \epsilon_{11} & 0 & 0 \\ 0 & \epsilon_{11} & 0 \\ 0 & 0 & \epsilon_{33} \end{bmatrix}$$

Substrate	ρ	c_{11}	c_{12}	c_{13}	c_{14}	c_{33}	c_{44}	e_{11}	e_{14}	e_{15}	e_{22}	e_{31}	e_{33}	ϵ^s_{11}	ϵ^s_{33}
$LiTaO_3$	7450	232.96	46.89	80.23	-11.03	275.36	93.9	-	-	2.6	1.59	0.08	1.88	40.9	43.3
$LiNbO_3$	4700	202.9	52.92	74.91	9	243.08	59.90	-	-	3.7	2.54	0.19	1.31	43.6	29.16
Quartz	2651	86.73	6.99	11.91	17.91	107.19	57.95	-0.2	-0.12	-	-	-	-	4.41	4.68

Table A.1: Elastic, piezoelectric and dielectric constants of $LiTaO_3$, $LiNbO_3$, and quartz represented in stress-charge form. Density (ρ) is given in units of $\mathrm{kg\,m^{-3}}$, elastic constants c_{ij} in GPa, piezoelectric constants e_{ij} in $\mathrm{C\,m^{-2}}$ and permittivity ϵ_{ij} in ($\epsilon_0 \times 10^{-11}$ $\mathrm{F\,m^{-1}}$). The material constants are taken from COMSOL material library and are also available in [116], [138].

Material constants	First order temperature coefficients ($\times 10^{-4}$ °C^{-1})		
	$LiTaO_3$	$LiNbO_3$	Quartz
c_{11}	-1.03	-1.74	-0.44
c_{12}	-3.41	-2.52	-29.3
c_{13}	-0.50	-1.59	-4.92
c_{14}	6.67	-2.14	0.98
c_{33}	-0.96	-1.53	-1.88
c_{44}	-0.43	-2.04	-1.72
c_{66}	-0.47	-1.43	1.8
e_{15}	-1.32	1.47	-
e_{22}	-0.6	0.79	-
e_{31}	0.87	2.21	-
e_{11}	1.54	8.87	-

Table A.2: First order temperature coefficients for $LiTaO_3$, $LiNbO_3$ and quartz [140], [207].

Material	Shear modulus μ (GPa)	Density ρ (kg m^{-3})	Poisson's ratio ν	Shear velocity v (m s^{-1})
SiO_2	26	2200	0.17	3438
ZnO	40	5720	0.33	2650
Gold	28.5	19300	0.44	1216
PMMA	1.2	1180	0.35	1017
Polyimide	0.9	1420	0.34	809
SU-8	1.64	1190	0.22	1810

Table A.3: Material properties [68], [159], [208], [209].

Material constants	First order temperature coefficients ($\times 10^{-4}$ °C^{-1})	
	SiO_2	ZnO
c_{11}	2.39	-1.12
e_{13}	5.84	-1.61
c_{33}	2.39	-1.23
e_{44}	1.51	-0.70

Table A.4: First order temperature coefficients for SiO_2 and ZnO [166].

Appendix B

Matrix transformation using Euler angles

The properties of the piezoelectric crystal depends upon the orientation of the substrate plane. The matrix transformation method originally developed by W.L. Bond [139], uses the Euler angles (ϕ, θ, ψ), to transform the original (non-rotated) stiffness matrix $[c]$, piezoelectric matrix $[e]$, and permittivity matrix $[\epsilon]$ into new matrices $[c]_n$, $[e]_n$, and $[\epsilon]_n$. The transformation process is achieved using a coordinate transformation matrix $[a]$, and bond matrix $[M]$ by employing the following equations:

$$\begin{aligned} [c]_n &= [M][c][M]^{'} \\ [e]_n &= [a][e][M]^{'} \\ [\epsilon]_n &= [a][\epsilon][a]^{'} \end{aligned} \tag{B.1}$$

where the coordinate transformation matrix $[a]$ is given as

$$\begin{aligned} [a] &= \begin{bmatrix} a_{11} & a_{12} & a_{13} \\ a_{21} & a_{22} & a_{23} \\ a_{31} & a_{32} & a_{33} \end{bmatrix} \\ &= \begin{bmatrix} \cos\psi\cos\phi - \cos\theta\sin\phi\sin\psi & \cos\psi\sin\phi + \cos\theta\cos\phi\sin\psi & \sin\psi\sin\theta \\ -\sin\psi\cos\phi - \cos\theta\sin\phi\cos\psi & -\sin\psi\sin\phi + \cos\theta\cos\phi\cos\psi & \cos\psi\sin\theta \\ \sin\theta\sin\phi & -\sin\theta\cos\phi & \cos\theta \end{bmatrix} \end{aligned} \tag{B.2}$$

and the bond matrix $[M]$ is written as

$$[M] = \begin{bmatrix} a_{11}^2 & a_{12}^2 & a_{13}^2 & 2a_{12}a_{13} & 2a_{13}a_{12} & 2a_{11}a_{12} \\ a_{21}^2 & a_{22}^2 & a_{23}^2 & 2a_{22}a_{23} & 2a_{23}a_{21} & 2a_{21}a_{22} \\ a_{31}^2 & a_{32}^2 & a_{33}^2 & 2a_{32}a_{33} & 2a_{33}a_{31} & 2a_{31}a_{32} \\ a_{23}a_{31} & a_{22}a_{31} & a_{23}a_{33} & a_{22}a_{11} + a_{23}a_{32} & a_{21}a_{33} + a_{23}a_{31} & a_{22}a_{31} + a_{21}a_{32} \\ a_{23}a_{31} & a_{22}a_{12} & a_{33}a_{13} & a_{12}a_{33} + a_{13}a_{32} & a_{13}a_{31} + a_{11}a_{33} & a_{11}a_{32} + a_{12}a_{21} \\ a_{11}a_{21} & a_{12}a_{22} & a_{13}a_{23} & a_{12}a_{23} + a_{13}a_{22} & a_{13}a_{21} + a_{11}a_{23} & a_{11}a_{22} + a_{12}a_{21} \end{bmatrix} \tag{B.3}$$

Bibliography

[1] R. Lec and P. Lewin, "Acoustic wave biosensors," *Proceedings of the 20th Annual International Conference of the IEEE Engineering in Medicine and Biology Society. Vol.20 Biomedical Engineering Towards the Year 2000 and Beyond (Cat. No.98CH36286)*, vol. 6, pp. 2779–2784, 1998.

[2] D. Ivnitski, I. Abdel-Hamid, P. Atanasov, and E. Wilkins, "Biosensors for detection of pathogenic bacteria," *Biosensors and Bioelectronics*, vol. 14, no. 7, pp. 599–624, 1999.

[3] J. W. Gardner and V. K. Varadan, *Microsensors, Mems and Smart Devices*. New York, NY, USA: John Wiley & Sons, Inc., 2001.

[4] G. Harding, J. Du, P. Dencher, D. Barnett, and E. Howe, "Love wave acoustic immunosensor operating in liquid," *Sensors and Actuators A: Physical*, vol. 61, no. 1-3, pp. 279–286, Jun. 1997.

[5] D. A. Powell, K. Kalantar-Zadeh, W. Wlodarski, and S. J. Ippolito, "Layered surface acoustic wave chemical and biosensors," *Encycl. Sens*, vol. 4, pp. 245–262, 2006.

[6] M. Bisoffi, B. Hjelle, D. C. Brown, D. W. Branch, T. L. Edwards, S. M. Brozik, V. S. Bondu-Hawkins, and R. S. Larson, "Detection of viral bioagents using a shear horizontal surface acoustic wave biosensor.," *Biosensors and Bioelectronics*, vol. 23, no. 9, pp. 1397–403, Apr. 2008.

[7] D. M. Ştefănescu, "Handbook of Force Transducers: Principles and Components," in. Berlin, Heidelberg: Springer Berlin Heidelberg, 2011, ch. Acoustic Force Transducers, pp. 251–274.

[8] I. Voiculescu and A. N. Nordin, "Acoustic wave based MEMS devices for biosensing applications.," *Biosensors and Bioelectronics*, vol. 33, no. 1, pp. 1–9, Mar. 2012.

[9] M.-I. Rocha-Gaso, C. March-Iborra, A. Montoya-Baides, and A. Arnau-Vives, "Surface generated acoustic wave biosensors for the detection of pathogens: A review.," *Sensors (Basel, Switzerland)*, vol. 9, no. 7, pp. 5740–69, Jan. 2009.

[10] D. Royer and E. Dieulesaint, *Elastic Waves in Solids I: Free and Guided Propagation*. Springer Science & Business Media, 1999.

[11] D. Morgan, *Surface acoustic wave filters: With applications to electronic communications and signal processing*. Academic Press, 2010.

[12] O. Novotny, "Seismic surface waves," *Bahia, Salvador: Instituto de Geociencias*, 1999.

[13] G. McHale, M. I. Newton, F. Martin, E. Gizeli, and K. a. Melzak, "Resonant conditions for Love wave guiding layer thickness," *Applied Physics Letters*, vol. 79, no. 21, p. 3542, 2001.

[14] R. Wicander and J. Monroe, *Essentials of physical geology*. Nelson Education, 2008.

[15] R. M. White and F. W. Voltmer, "Direct piezoelectric coupling to surface elastic waves," *Applied Physics Letters*, vol. 7, no. 12, pp. 314–316, 1965.

[16] D. Royer and E. Dieulesaint, *Elastic waves in solids II: generation, acousto-optic interaction, applications*. Springer Science & Business Media, 1999.

[17] T. Nomura, A. Saitoh, Y. Horikoshi, and S. Furukawa, "Liquid sensing system based on two port SH-SAW resonator," in *1999 IEEE Ultrasonics Symposium. Proceedings. International Symposium (Cat. No.99CH37027)*, vol. 1, Oct. 1999, 477–480 vol.1.

[18] C. Campbell, *Surface acoustic wave devices and their signal processing applications*. Academic press, 1989.

[19] A. Ricco, S. Martin, and T. Zipperian, "Surface acoustic wave gas sensor based on film conductivity changes," *Sensors and Actuators*, vol. 8, no. 4, pp. 319–333, 1985.

[20] B. Jakoby and M. J. Vellekoop, "Properties of Love waves: applications in sensors," *Smart Materials and Structures*, vol. 6, no. 6, p. 668, 1997.

[21] M.-I. Rocha-Gaso, R. Fernandez-Diaz, A. Arnau-Vives, and C. March-Iborra, "Mass sensitivity evaluation of a Love wave sensor using the 3D Finite Element Method," *IEEE International Frequency Control Symposium*, pp. 228–231, Jun. 2010.

[22] S. Li, Y. Wan, Y. Su, C. Fan, and V. R. Bhethanabotla, "Gold nanoparticle-based low limit of detection Love wave biosensor for carcinoembryonic antigens," *Biosensors and Bioelectronics*, vol. 95, pp. 48–54, 2017.

[23] Q. Zhang, T. Han, G. Tang, J. Chen, and K.-Y. Hashimoto, "SAW characteristics of AlN/SiO_2/3C-SiC layered structure with embedded electrodes," *IEEE Transactions on Ultrasonics, Ferroelectrics, and Frequency Control*, vol. 63, no. 10, pp. 1608–1612, 2016.

[24] A. Sharma and K. R. Rogers, "Biosensors," *Measurement Science and Technology*, vol. 5, no. 5, p. 461, 1994.

[25] A. J. Cunningham, *Introduction to bioanalytical sensors*. John Wiley & Sons, New York, 1998.

[26] V. Tjong, L. Tang, S. Zauscher, and A. Chilkoti, "'Smart' DNA interfaces," *Chem. Soc. Rev.*, vol. 43, pp. 1612–1626, 5 2014.

[27] C. D. Bain, E. B. Troughton, Y. T. Tao, J. Evall, G. M. Whitesides, and R. G. Nuzzo, "Formation of monolayer films by the spontaneous assembly of organic thiols from solution onto gold," *Journal of the American Chemical Society*, vol. 111, no. 1, pp. 321–335, 1989.

[28] C. Heise and F. F. Bier, "Immobilization of DNA on microarrays," in *Immobilisation of DNA on Chips II*. Berlin, Heidelberg: Springer Berlin Heidelberg, 2005, pp. 1–25.

[29] S. Tombelli and M. Mascini, "Piezoelectric quartz crystal biosensors: Recent immobilisation schemes," *Analytical Letters*, vol. 33, no. 11, pp. 2129–2151, 2000.

[30] G. L. Cote, R. M. Lec, and M. V. Pishko, "Emerging biomedical sensing technologies and their applications," *IEEE Sensors Journal*, vol. 3, no. 3, pp. 251–266, Jun. 2003.

[31] C. Köblinger, E. Uttenthaler, S. Drost, F. Aberl, H. Wolf, G. Brink, A. Stanglmaier, and E. Sackmann, "Comparison of the QCM and the SPR method for surface studies and immunological applications," *Sensors and Actuators B: Chemical*, vol. 24, no. 1, pp. 107–112, 1995.

[32] G. Sauerbrey, "Verwendung von Schwingquarzen zur Wägung dünner Schichten und zur Mikrowägung," *Zeitschrift für Physik*, vol. 155, no. 2, pp. 206–222, Apr. 1959.

[33] R. M. Lec, "Piezoelectric biosensors: recent advances and applications," in *Frequency Control Symposium and PDA Exhibition, 2001. Proceedings of the 2001 IEEE International*, IEEE, 2001, pp. 419–429.

[34] C. March, J. Manclús, Y. Jiménez, A. Arnau, and A. Montoya, "A piezoelectric immunosensor for the determination of pesticide residues and metabolites in fruit juices," *Talanta*, vol. 78, no. 3, pp. 827–833, 2009.

[35] B. Lee, "Review of the present status of optical fiber sensors," *Optical fiber technology*, vol. 9, no. 2, pp. 57–79, 2003.

[36] E. Hawkins and M. Cooper, "Acoustic detection technology in the analysis of biomolecular interactions," *Innovations in Pharmaceutical Technology*, vol. 21, pp. 30–34, 2006.

[37] I. Ben-Dov, I. Willner, and E. Zisman, "Piezoelectric immunosensors for urine specimens of chlamydia trachomatis employing quartz crystal microbalance microgravimetric analyses," *Analytical Chemistry*, vol. 69, no. 17, pp. 3506–3512, 1997.

[38] X. Zhou, L. Liu, M. Hu, L. Wang, and J. Hu, "Detection of hepatitis B virus by piezoelectric biosensor," *Journal of Pharmaceutical and Biomedical Analysis*, vol. 27, no. 1, pp. 341–345, 2002.

[39] Y. S. Fung and Y. Y. Wong, "Self-assembled monolayers as the coating in a Quartz piezoelectric crystal immunosensor to detect salmonella in aqueous solution," *Analytical Chemistry*, vol. 73, no. 21, pp. 5302–5309, 2001.

[40] M. Stobiecka, J. M. Cieśla, B. Janowska, B. Tudek, and H. Radecka, "Piezoelectric sensor for determination of genetically modified soybean roundup ready (R) in samples not amplified by PCR," *Sensors*, vol. 7, no. 8, pp. 1462–1479, 2007.

[41] Z. Lin, C. M. Yip, I. S. Joseph, and M. D. Ward, "Operation of an ultrasensitive 30-MHz quartz crystal microbalance in liquids," *Analytical Chemistry*, vol. 65, no. 11, pp. 1546–1551, 1993.

[42] R. Gabl, E. Green, M. Schreiter, H. Feucht, H. Zeininger, R. Primig, D. Pitzer, G. Eckstein, and W. Wersing, "Novel integrated FBAR sensors: a universal technology platform for bio-and gas-detection," in *Sensors, 2003. Proceedings of IEEE*, IEEE, vol. 2, 2003, pp. 1184–1188.

[43] G. Wingqvist, J. Bjurström, L. Liljeholm, V. Yantchev, and I. Katardjiev, "Shear mode AlN thin film electro-acoustic resonant sensor operation in viscous media," *Sensors and Actuators B: Chemical*, vol. 123, no. 1, pp. 466–473, 2007.

[44] H. Zhang and E. S. Kim, "Micromachined acoustic resonant mass sensor," *Journal of Microelectromechanical Systems*, vol. 14, no. 4, pp. 699–706, Aug. 2005.

[45] J. Weber, W. M. Albers, J. Tuppurainen, M. Link, R. Gabl, W. Wersing, and M. Schreiter, "Shear mode FBARs as highly sensitive liquid biosensors," *Sensors and Actuators A: Physical*, vol. 128, no. 1, pp. 84–88, 2006.

[46] C. Déjous, M. Savart, D. Rebière, and J. Pistré, "A shear-horizontal acoustic plate mode (SH-APM) sensor for biological media," *Sensors and Actuators B: Chemical*, vol. 27, no. 1, pp. 452–456, 1995, Eurosensors VIII.

[47] F. Bender, F. Meimeth, R. Dahint, M. Grunze, and F. Josse, "Mechanisms of interaction in acoustic plate mode immunosensors," *Sensors and Actuators B: Chemical*, vol. 40, no. 2, pp. 105–110, 1997.

[48] K. Länge, B. E. Rapp, and M. Rapp, "Surface acoustic wave biosensors: A review," *Analytical and bioanalytical chemistry*, vol. 391, no. 5, pp. 1509–19, Jul. 2008.

[49] C. Evans, S. Stanley, C. Percival, G. McHale, and M. Newton, "Lithium tantalate layer guided plate mode sensors," *Sensors and Actuators A: Physical*, vol. 132, no. 1, pp. 241–244, 2006, The 19th European Conference on Solid-State Transducers.

[50] D. Ballantine Jr, R. M. White, S. J. Martin, A. J. Ricco, E. Zellers, G. Frye, and H. Wohltjen, *Acoustic wave sensors: theory, design and physico-chemical applications*. Academic press, 1996.

[51] J. W. Grate, S. J. Martin, and R. M. White, "Acoustic Wave Microsensors," *Analytical Chemistry*, vol. 65, no. 21, 940A–948A, 1993.

[52] R. M. White, P. J. Wicher, S. W. Wenzel, and E. T. Zellers, "Plate-mode ultrasonic oscillator sensors," *IEEE Transactions on Ultrasonics, Ferroelectrics, and Frequency Control*, vol. 34, no. 2, pp. 162–171, 1987.

[53] M. Vellekoop, G. Lubking, P. Sarro, and A. Venema, "Integrated-circuit-compatible design and technology of acoustic-wave-based microsensors," *Sensors and Actuators A: Physical*, vol. 44, no. 3, pp. 249–263, 1994.

[54] L. Rayleigh, "On Waves Propagated along the Plane Surface of an Elastic Solid," *Proceedings of the London Mathematical Society*, vol. s1-17, no. 1, pp. 4–11, 1885.

[55] H. Wohltjen and R. Dessy, "Surface acoustic wave probe for chemical analysis. I. Introduction and instrument description," *Analytical Chemistry*, vol. 51, no. 9, pp. 1458–1464, 1979.

[56] A. Arnau, *Piezoelectric transducers and applications*. Springer, 2004, vol. 2004.

[57] Y. Fu, J. Luo, X. Du, A. Flewitt, Y. Li, G. Markx, A. Walton, and W. Milne, "Recent developments on ZnO films for acoustic wave based bio-sensing and microfluidic applications: a review," *Sensors and Actuators B: Chemical*, vol. 143, no. 2, pp. 606–619, 2010.

[58] K. Nakamura, "SH-type and Rayleigh-type surface waves on rotated Y-cut $LiTaO_3$," *Ultrasonics Symposium*, pp. 819–822, 1977.

[59] T. Nishikawa, A. Tani, K. Shirai, and C. Takeuchi, "SH-type surface acoustic waves on rotated Y-cut quartz," in *34th Annual Frequency Control Symposium*, 1980, pp. 286–291.

[60] M. Lewis, "Surface Skimming Bulk Wave, SSBW," in *1977 Ultrasonics Symposium*, Oct. 1977, pp. 744–752.

[61] S. Shiokawa and T. Moriizumi, "Design of SAW sensor in liquid," *Japanese Journal of Applied Physics*, vol. 27, no. S1, p. 142, 1988.

[62] V. L. Strashilov and V. M. Yantchev, "Surface transverse waves: properties, devices, and analysis," *IEEE Transactions on Ultrasonics, Ferroelectrics, and Frequency Control*, vol. 52, no. 5, pp. 812–821, May 2005.

[63] M. Tom-Moy, R. L. Baer, D. Spira-Solomon, and T. P. Doherty, "Atrazine measurements using surface transverse wave devices," *Analytical Chemistry*, vol. 67, no. 9, pp. 1510–1516, 1995.

[64] R. F. Milsom, N. Reilly, and M. Redwood, "Analysis of generation and detection of surface and bulk acoustic waves by interdigital transducers," *IEEE Transactions on Sonics Ultrasonics*, vol. 24, pp. 147–166, 1977.

[65] T. L. Bagwell and R. C. Bray, "Novel surface transverse wave resonators with low loss and high Q," in *IEEE 1987 Ultrasonics Symposium*, Oct. 1987, pp. 319–324.

[66] A. E. H. Love, *Some problems of geodynamics*. Cambridge University Press, 2015.

[67] J. Du, G. Harding, J. Ogilvy, P. Dencher, and M. Lake, "A study of Love-wave acoustic sensors," *Sensors and Actuators A: Physical*, vol. 56, no. 3, pp. 211–219, Sep. 1996.

[68] M. Gaso, Y. Jiménez, L. Francis, and A. Arnau, *Love wave biosensors: A review, state of the art in biosensors - General aspects*. InTech, 2013.

[69] K. Kalantar-Zadeh, W. Wlodarski, Y. Y. Chen, B. N. Fry, and K. Galatsis, "Novel Love mode surface acoustic wave based immunosensors," *Sensors and Actuators B: Chemical*, vol. 91, no. 1-3, pp. 143–147, Jun. 2003.

[70] S. Krishnamoorthy, A. A. Iliadis, T. Bei, and G. P. Chrousos, "An interleukin-6 $ZnO/SiO_2/Si$ surface acoustic wave biosensor," *Biosensors and Bioelectronics*, vol. 24, no. 2, pp. 313–318, 2008.

[71] H. Oh, Y. Lee, S. Lee, S. S. Yang, and K. Lee, "Development of novel Love wave biosensor for simultaneous detection of multi-analyte," *Procedia Engineering*, vol. 25, pp. 908–911, 2011, EurosensorsXXV.

[72] T. Song, S. Y. Song, H. C. Yoon, and K. Lee, "Development of a wireless Love wave biosensor platform for multi-functional detection," *Japanese Journal of Applied Physics*, vol. 50, no. 6S, 06GL09, 2011.

[73] M. Puiu, A.-M. Gurban, L. Rotariu, S. Brajnicov, C. Viespe, and C. Bala, "Enhanced sensitive Love wave surface acoustic wave sensor designed for immunoassay formats," *Sensors*, vol. 15, no. 5, pp. 10 511–10 525, 2015.

[74] S. Li, Y. Wan, Y. Su, C. Fan, and V. R. Bhethanabotla, "Gold nanoparticles amplified surface acoustic wave biosensors for immunodetection," in *2016 IEEE Sensors*, Oct. 2016, pp. 1–3.

[75] E. Howe and G. Harding, "A comparison of protocols for the optimisation of detection of bacteria using a surface acoustic wave (SAW) biosensor," *Biosensors and Bioelectronics*, vol. 15, no. 11, pp. 641–649, 2000.

[76] O. Tamarin, C. Déjous, D. Rebière, J. Pistré, S. Comeau, D. Moynet, and J. Bezian, "Study of acoustic Love wave devices for real time bacteriophage detection," *Sensors and Actuators B: Chemical*, vol. 91, no. 1-3, pp. 275–284, Jun. 2003.

[77] D. W. Branch and S. M. Brozik, "Low-level detection of a Bacillus anthracis simulant using Love-wave biosensors on 36°-YX $LiTaO_3$," *Biosensors and Bioelectronics*, vol. 19, no. 8, pp. 849–859, 2004.

[78] N. Moll, E. Pascal, D. H. Dinh, J.-P. Pillot, B. Bennetau, D. Rebière, D. Moynet, Y. Mas, D. Mossalayi, J. Pistré, and C. Déjous, "A Love wave immunosensor for whole E. coli bacteria detection using an innovative two-step immobilisation approach," *Biosensors and Bioelectronics*, vol. 22, no. 9, pp. 2145–2150, 2007, Selected Papers from the Ninth World Congress On Biosensors. Toronto, Canada 10 - 12 May 2006.

[79] N. Moll, E. Pascal, D. Dinh, J.-L. Lachaud, L. Vellutini, J.-P. Pillot, D. Rebière, D. Moynet, J. Pistré, D. Mossalayi, Y. Mas, B. Bennetau, and C. Déjous, "Multipurpose Love acoustic wave immunosensor for bacteria, virus or proteins detection," *IRBM*, vol. 29, no. 2, pp. 155–161, 2008.

[80] H. J. Lee, K. Namkoong, E. C. Cho, C. Ko, J. C. Park, and S. S. Lee, "Surface acoustic wave immunosensor for real-time detection of hepatitis B surface antibodies in whole blood samples," *Biosensors and Bioelectronics*, vol. 24, no. 10, pp. 3120–3125, 2009.

[81] O. Tigli, L. Bivona, P. Berg, and M. E. Zaghloul, "Fabrication and characterization of a Surface-acoustic-wave biosensor in CMOS technology for cancer biomarker detection.," *IEEE Transactions on Biomedical Circuits and Systems*, vol. 4, no. 1, pp. 62–73, Feb. 2010.

[82] P. Bröker, K. Lücke, M. Perpeet, and T. M. Gronewold, "A nanostructured SAW chip-based biosensor detecting cancer cells," *Sensors and Actuators B: Chemical*, vol. 165, no. 1, pp. 1–6, 2012.

[83] D. Matatagui, D. Moynet, M. Fernández, J. Fontecha, J. Esquivel, I. Gràcia, C. Cané, C. Déjous, D. Rebière, J. Santos, and M. Horrillo, "Detection of bacteriophages in dynamic mode using a Love-wave immunosensor with microfluidics technology," *Sensors and Actuators B: Chemical*, vol. 185, pp. 218–224, Aug. 2013.

[84] X. Zhang, Y. Zou, C. An, K. Ying, X. Chen, and P. Wang, "A miniaturized immunosensor platform for automatic detection of carcinoembryonic antigen in EBC," *Sensors and Actuators B: Chemical*, vol. 205, pp. 94–101, 2014.

[85] F. Zhang, S. Li, K. Cao, P. Wang, Y. Su, X. Zhu, and Y. Wan, "A microfluidic Love-wave biosensing device for PSA detection based on an aptamer beacon probe," *Sensors*, vol. 15, no. 6, pp. 13 839–13 850, 2015.

[86] Y. Jiang, C. Y. Tan, S. Y. Tan, M. S. F. Wong, Y. F. Chen, L. Zhang, K. Yao, S. K. E. Gan, C. Verma, and Y. J. Tan, "SAW sensor for Influenza A virus detection enabled with efficient surface functionalization," *Sensors and Actuators B: Chemical*, vol. 209, pp. 78–84, 2015.

[87] J. T. Baca, V. Severns, D. Lovato, D. W. Branch, and R. S. Larson, "Rapid detection of Ebola virus with a reagent-free, Point-of-Care biosensor," *Sensors*, vol. 15, no. 4, pp. 8605–8614, 2015.

[88] M. Bisoffi, V. Severns, D. W. Branch, T. L. Edwards, and R. S. Larson, "Rapid detection of human immunodeficiency virus types 1 and 2 by use of an improved piezoelectric biosensor," *Journal of clinical microbiology*, vol. 51, no. 6, pp. 1685–1691, 2013.

[89] M. D. Schlensog, T. M. Gronewold, M. Tewes, M. Famulok, and E. Quandt, "A Love-wave biosensor using nucleic acids as ligands," *Sensors and Actuators B: Chemical*, vol. 101, no. 3, pp. 308–315, Jul. 2004.

[90] Z. Zhang, N. W. Emanetoglu, G. Saraf, Y. Chen, P. Wu, J. Zhong, Y. Lu, J. Chen, O. Mirochnitchenko, and M. Inouye, "DNA immobilization and SAW response in ZnO nanotips grown on $LiNbO_3$ substrates.," *IEEE Transactions on Ultrasonics, Ferroelectrics, and Frequency Control*, vol. 53, no. 4, pp. 786–92, Apr. 2006.

[91] J. Sakong, Y. Roh, and H. Roh, "Saw sensor system with micro-fluidic channels to detect DNA molecules," *IEEE Ultrasonics Symposium*, pp. 548–551, 2006.

[92] C.-S. Chiu and S. Gwo, "Quantitative surface acoustic wave detection based on colloidal gold nanoparticles and their bioconjugates," *Analytical Chemistry*, vol. 80, no. 9, pp. 3318–26, May 2008.

[93] A. Tsortos, G. Papadakis, K. Mitsakakis, K. A. Melzak, and E. Gizeli, "Quantitative determination of size and shape of surface-bound DNA using an acoustic wave sensor," *Biophysical journal*, vol. 94, no. 7, pp. 2706–2715, 2008.

[94] G. Papadakis, A. Tsortos, and E. Gizeli, "Triple-helix DNA structural studies using a Love wave acoustic biosensor," *Biosensors and Bioelectronics*, vol. 25, no. 4, pp. 702–707, 2009.

[95] N. Fourati, M. Lazerges, C. Vedrine, J.-M. Fougnion, C. Zerrouki, L. Rousseau, P. Lepeut, J. J. Bonnet, and C. Pernelle, "Surface acoustic waves sensor for DNA-biosensor development," *Sensor Letters*, vol. 7, no. 5, pp. 847–850, 2009.

[96] H.-L. Cai, Y. Yang, Y.-H. Zhang, C.-J. Zhou, C.-R. Guo, J. Liu, and T.-L. Ren, "A high sensitivity wireless mass-loading surface acoustic wave DNA biosensor," *Modern Physics Letters B*, vol. 28, no. 07, p. 1 450 056, 2014.

[97] E. Gizeli, C. R. Lowe, M. Liley, and H. Vogel, "Detection of supported lipid layers with the acoustic Love waveguide device: application to biosensors," *Sensors and Actuators B: Chemical*, vol. 34, no. 1-3, pp. 295–300, 1996.

[98] E. Gizeli, "Design considerations for the acoustic waveguide biosensor," *Smart Materials and Structures*, vol. 6, no. 6, pp. 700–706, Dec. 1997.

[99] F. Josse, F. Bender, and R. W. Cernosek, "Guided shear horizontal surface acoustic wave sensors for chemical and biochemical detection in liquids," *Analytical Chemistry*, vol. 73, no. 24, pp. 5937–5944, Dec. 2001.

[100] L. E. Fissi, J. M. Friedt, V. Luzet, F. Cherioux, G. Martin, and S. Ballandras, "A Love-wave sensor for direct detection of biofunctionalized nanoparticles," in *2009 IEEE International Frequency Control Symposium Joint with the 22nd European Frequency and Time forum*, Apr. 2009, pp. 861–865.

[101] I. Gammoudi, H. Tarbague, A. Othmane, D. Moynet, D. Rebière, R. Kalfat, and C. Dejous, "Love-wave bacteria-based sensor for the detection of heavy metal toxicity in liquid medium," *Biosensors and Bioelectronics*, vol. 26, no. 4, pp. 1723–1726, 2010.

[102] F. Fournel, E. Baco, M. Mamani-Matsuda, M. Degueil, B. Bennetau, D. Moynet, D. Mossalayi, L. Vellutini, J.-P. Pillot, C. Dejous, *et al.*, "Love wave biosensor for real-time detection of okadaic acid as DSP phycotoxin," *Sensors and Actuators B: Chemical*, vol. 170, pp. 122–128, 2012.

[103] I. Sayago, D. Matatagui, M. J. Fernández, J. L. Fontecha, I. Jurewicz, R. Garriga, and E. Muñoz, "Graphene oxide as sensitive layer in Love-wave surface acoustic wave sensors for the detection of chemical warfare agent simulants," *Talanta*, vol. 148, pp. 393–400, 2016.

[104] G. Kovacs, G. Lubking, M. Vellekoop, and A. Venema, "Love waves for (bio)-chemical sensing in liquids," in *Ultrasonics Symposium, 1992. Proceedings., IEEE 1992*, IEEE, 1992, pp. 281–285.

[105] E. Gizeli, N. J. Goddard, C. R. Lowe, and A. C. Stevenson, "A Love plate biosensor utilising a polymer layer," *Sensors and Actuators B: Chemical*, vol. 6, no. 1-3, pp. 131–137, 1992.

[106] L. A. Francis, J.-M. Friedt, and P. Bertrand, "Influence of electromagnetic interferences on the mass sensitivity of Love mode surface acoustic wave sensors," *Sensors and Actuators A: Physical*, vol. 123, pp. 360–369, 2005, Eurosensors XVIII 2004.

[107] J. Weber, M. Link, R. Primig, D. Pitzer, W. Wersing, and M. Schreiter, "Investigation of the scaling rules determining the performance of film bulk acoustic resonators operating as mass sensors," *IEEE Transactions on Ultrasonics, Ferroelectrics, and Frequency Control*, vol. 54, no. 2, 2007.

[108] P. I. Reyes, Z. Zhang, H. Chen, Z. Duan, J. Zhong, G. Saraf, Y. Lu, O. Taratula, E. Galoppini, and N. N. Boustany, "A ZnO nanostructure-based quartz crystal microbalance device for biochemical sensing," *IEEE Sensors Journal*, vol. 9, no. 10, pp. 1302–1307, 2009.

[109] Y. Wang, S.-Y. Zhang, F.-M. Zhou, L. Fan, Y.-t. Yang, and C. Wang, "Love wave hydrogen sensors based on ZnO nanorod film/36°-YX $LiTaO_3$ substrate structures operated at room temperature," *Sensors and Actuators B: Chemical*, vol. 158, no. 1, pp. 97–103, Nov. 2011.

[110] O. Akhavan, M. Mehrabian, K. Mirabbaszadeh, and R. Azimirad, "Hydrothermal synthesis of ZnO nanorod arrays for photocatalytic inactivation of bacteria," *Journal of Physics D: Applied Physics*, vol. 42, no. 22, p. 225 305, Nov. 2009.

[111] S. Wang, Y. Yang, J. Chai, K. Zhu, X. Jiang, and Z. Du, "Nanoimprint assisted transfer of different density vertically aligned ZnO nanorod arrays," *RSC Adv.*, vol. 6, pp. 64 332–64 337, 69 2016.

[112] G. L. Dybwad, "A sensitive new method for the determination of adhesive bonding between a particle and a substrate," *Journal of Applied Physics*, vol. 58, no. 7, pp. 2789–2790, 1985.

[113] N. Ramakrishnan, H. B. Nemade, and R. P. Palathinkal, "Finite element method simulation of a surface acoustic wave hydrogen sensor with palladium nano-pillars as sensing medium," *Sensor Letters*, vol. 8, no. 6, pp. 824–828, 2010.

[114] P. Wang, J. Su, C.-F. Su, W. Dai, G. Cernigliaro, and H. Sun, "An ultrasensitive quartz crystal microbalance-micropillars based sensor for humidity detection," *Journal of Applied Physics*, vol. 115, no. 22, p. 224 501, 2014.

[115] M. A. M. Kashan, V. Kalavally, H. W. Lee, and N. Ramakrishnan, "Resonant characteristics and sensitivity dependency on the contact surface in QCM micropillar based system of coupled resonator sensors," *Journal of Physics D: Applied Physics*, vol. 49, no. 19, p. 195 303, 2016.

[116] B. A. Auld, *Acoustic fields and waves in solids*. Wiley, 1973.

[117] C. S. Hartmann, D. T. Bell, and R. C. Rosenfeld, "Impulse model design of acoustic surface-wave filters," *IEEE Transactions on Microwave Theory and Techniques*, vol. 21, no. 4, pp. 162–175, Apr. 1973.

[118] W. R. Smith, H. M. Gerard, J. H. Collins, T. M. Reeder, and H. J. Shaw, "Analysis of interdigital surface wave transducers by use of an equivalent circuit model," *IEEE Transactions on Microwave Theory and Techniques*, vol. 17, no. 11, pp. 856–864, 1969.

[119] M. Thompson and D. C. Stone, *Surface Launched Acoustic Wave Sensors: Chemical Sensing and Thin-Film Characterization*. John Wiley & Sons,New York, NY, USA, 1997.

[120] V. Plessky and J. Koskela, "Coupling-of-modes analysis of SAW devices," *International Journal of High Speed Electronics and Systems*, vol. 10, no. 04, pp. 867–947, 2000.

[121] G. Tobolka, "Mixed matrix representation of SAW transducers," *IEEE Transactions on Sonics and Ultrasonics*, vol. 26, no. 6, pp. 426–427, Nov. 1979.

[122] S. Datta and B. J. Hunsinger, "Element factor for periodic transducers," *IEEE Transactions on Sonics and Ultrasonics*, vol. 27, no. 1, pp. 42–44, Jan. 1980.

[123] K.-Y. Hashimoto, *Surface acoustic wave devices in telecommunications*. Springer, 2000.

[124] K.-J. Bathe, *Finite element procedures*. Klaus-Jurgen Bathe, 2006.

[125] *COMSOL Multiphysics Reference Manual, version 4.4, comsol, inc, www.comsol.com.*

[126] R. Lerch, "Simulation of piezoelectric devices by two-and three-dimensional finite elements," *IEEE Transactions on Ultrasonics, Ferroelectrics, and Frequency Control*, vol. 37, no. 3, pp. 233–247, 1990.

[127] A. Abdollahi, Z. Jiang, and S. A. Arabshahi, "Evaluation on mass sensitivity of SAW sensors for different piezoelectric materials using finite-element analysis.," *IEEE Transactions on Ultrasonics, Ferroelectrics, and Frequency Control*, vol. 54, no. 12, pp. 2446–55, Dec. 2007.

[128] S. J. Ippolito, K. Kalantar-Zadeh, D. A. Powell, and W. Wlodarski, "A 3-dimensional finite element approach for simulating acoustic wave propagation in layered SAW devices," in *Ultrasonics, 2003 IEEE Symposium on*, IEEE, vol. 1, 2003, pp. 303–306.

[129] X. Wang and G. Xu, "Numerical study of the effects of film properties to the mass sensitivity of surface acoustic wave sensors," in *Proceedings of the 2005 IEEE International Frequency Control Symposium and Exposition, 2005.*, Aug. 2005, pp. 442–448.

[130] M. Z. Atashbar, B. J. Bazuin, M. Simpeh, and S. Krishnamurthy, "3D FE simulation of H_2 SAW gas sensor," *Sensors and Actuators B: Chemical*, vol. 111–112, no. 0, pp. 213–218, 2005, Eurosensors {XVIII} 2004 The 18th European Conference on Solid-State Transducers.

[131] M. M. EL Gowini and W. A. Moussa, "A finite element model of a MEMS-based surface acoustic wave hydrogen sensor," *Sensors*, vol. 10, no. 2, pp. 1232–1250, 2010.

[132] S. Rahman, M. Kataoka, C. Barnes, and H. Langtangen, "Numerical investigation of a piezoelectric surface acoustic wave interaction with a one-dimensional channel," *Physical Review B*, vol. 74, no. 3, p. 035 308, 2006.

[133] M. Richardson, S. K. R. S. Sankaranarayanan, and V. R. Bhethanabotla, "Low insertionl loss and highly sensitive SH-SAW sensors based on 36°-YX $LiTaO_3$ through the incorporation of filled microcavities," *IEEE Sensors Journal*, vol. 15, no. 2, pp. 787–796, Feb. 2015.

[134] S. Cular, S. K. R. S. Sankaranarayanan, and V. R. Bhethanabotla, "Enhancing effects of microcavities on shear-horizontal surface acoustic wave sensors: A finite element simulation study," *Applied Physics Letters*, vol. 92, no. 24, p. 244 104, 2008.

[135] S. Li, S. K. R. S. Sankaranarayanan, C. Fan, Y. Su, and V. R. Bhethanabotla, "Achieving lower insertion loss and higher sensitivity in a SAW biosensor via optimization of waveguide and microcavity structures," *IEEE Sensors Journal*, vol. 17, no. 6, pp. 1608–1616, Mar. 2017.

[136] K. Han and Y. J. Yuan, "Mass sensitivity evaluation and device design of a Love wave device for bond rupture biosensors using the finite element method," *IEEE Sensors Journal*, vol. 14, no. 8, pp. 2601–2608, Aug. 2014.

[137] J.-T. Luo, A.-J. Quan, G.-X. Liang, Z.-H. Zheng, S. Ramadan, C. Fu, H.-L. Li, and Y.-Q. Fu, "Love-mode surface acoustic wave devices based on multilayers of TeO_2/ZnO(1120)/Si(100) with high sensitivity and temperature stability," *Ultrasonics*, vol. 75, pp. 63–70, 2017.

[138] G. Kovacs, M. Anhorn, H. Engan, G. Visintini, and C. Ruppel, "Improved material constants for $LiNbO_3$ and $LiTaO_3$," *IEEE Symposium on Ultrasonics*, pp. 435–438, 1990.

[139] W. L. Bond, "The mathematics of the physical properties of crystals," *Bell Labs Technical Journal*, vol. 22, no. 1, pp. 1–72, 1943.

[140] F. Xu, W. Wang, J. Hou, and M. Liu, "Temperature effects on the propagation characteristics of love waves along multi-guide layers of SiO_2/SU-8 on ST-90°X quartz," *Sensors*, vol. 12, no. 6, pp. 7337–7349, 2012.

[141] N. Barié, T. Wessa, M. Bruns, and M. Rapp, "Love waves in SiO_2 layers on STW-resonators based on $LiTaO_3$," *Talanta*, vol. 62, no. 1, pp. 71–79, Jan. 2004.

[142] F. Herrmann, M. Weihnacht, and S. Buttgenbach, "Properties of shear-horizontal surface acoustic waves in different layered quartz-SiO_2 structures," *Ultrasonics*, vol. 37, no. 5, pp. 335–41, Jun. 1999.

[143] F. S. Hickernell and E. L. Adler, "Pseudo-SAW propagation on layered piezo-substrates: experiments and theory including film viscosity," in *1996 IEEE Ultrasonics Symposium. Proceedings*, vol. 1, Nov. 1996, 87–90 vol.1.

[144] K. Kalantar-Zadeh, D. A. Powell, W. Wlodarski, S. Ippolito, and K. Galatsis, "Comparison of layered based SAW sensors," *Sensors and Actuators B: Chemical*, vol. 91, no. 1, pp. 303–308, 2003.

[145] F. Herrmann and S. Büttgenbach, "Temperature-compensated shear-horizontal surface acoustic waves in layered Quartz/SiO_2 structures," *physica status solidi (a)*, vol. 170, no. 2, R3–R4, 1998.

[146] V. Ostasevicius and R. Dauksevicius, "Modeling and simulation of contact-type electrostatic microactuator," in *Microsystems Dynamics*. Dordrecht: Springer Netherlands, 2011, pp. 11–52.

[147] S. K. M. Richardson, V. R. Bhethanabotla, and S. K. R. S. Sankaranarayanan, "Design of SH-SAW phononic devices for highly sensitive and ultra-low power sensing applications," in *IEEE Sensors Proceedings*, Nov. 2014, pp. 213–216.

[148] J. Kondoh, Y. Okiyama, S. Mikuni, Y. Matsui, M. Nara, T. Mori, and H. Yatsuda, "Development of a shear horizontal surface acoustic wave sensor system for liquids with a floating electrode unidirectional transducer," *Japanese Journal of Applied Physics*, vol. 47, no. 5S, p. 4065, 2008.

[149] E. Gizeli, "Study of the sensitivity of the acoustic waveguide sensor," *Analytical chemistry*, vol. 72, no. 24, pp. 5967–5972, 2000.

[150] K. K. Zadeh, A. Trinchi, W. Wlodarski, and A. Holland, "A novel Love-mode device based on a ZnO/ST-cut quartz crystal structure for sensing applications," *Sensors and Actuators A: Physical*, vol. 100, no. 2, pp. 135–143, 2002.

[151] Z. Wang, J. D. N. Cheeke, and C. K. Jen, "Sensitivity analysis for Love mode acoustic gravimetric sensors," *Applied Physics Letters*, vol. 64, no. 22, p. 2940, 1994.

[152] G. McHale, M. I. Newton, and F. Martin, "Theoretical mass, liquid, and polymer sensitivity of acoustic wave sensors with viscoelastic guiding layers," *Journal of Applied Physics*, vol. 93, no. 1, p. 675, 2003.

[153] J. Liu and S. He, "Properties of Love waves in layered piezoelectric structures," *International Journal of Solids and Structures*, vol. 47, no. 2, pp. 169–174, Jan. 2010.

[154] J. Gore, Z. Bryant, M. Nöllmann, M. U. Le, N. R. Cozzarelli, and C. Bustamante, "DNA overwinds when stretched.," *Nature*, vol. 442, no. 7104, pp. 836–9, Aug. 2006.

[155] J. Marko and S. Cocco, "The micromechanics of DNA," *Phys. World*, pp. 37–41, 2003.

[156] R. Hartschuh, S. Wargacki, H. Xiong, J. Neiswinger, a. Kisliuk, S. Sihn, V. Ward, R. Vaia, and a. Sokolov, "How rigid are viruses," *Physical Review E*, vol. 78, no. 2, p. 021 907, Aug. 2008.

[157] J. W. Grate, S. J. Martin, and R. M. White, "Acoustic Wave Microsensors Part II," *Analytical Chemistry*, vol. 65, no. 22, 987A–996A, 1993.

[158] A. A. Vives, *Piezoelectric transducers and applications*. Berlin, Heidelberg: Springer Berlin Heidelberg, 2008, pp. 1–532.

[159] J. Zhao, C. Jiang, Y. Chen, H. Li, and S. He, "A study of Love wave sensors with SU-8 guiding layers," in *2008 IEEE Ultrasonics Symposium*, Nov. 2008, pp. 1120–1123.

[160] P. Roach, S. Atherton, N. Doy, G. McHale, and M. I. Newton, "SU-8 guiding layer for Love wave devices," *Sensors*, vol. 7, no. 11, pp. 2539–2547, 2007.

[161] H. Wu, X. Xiong, H. Zu, J. H.-C. Wang, and Q.-M. Wang, "Theoretical analysis of a Love wave biosensor in liquid with a viscoelastic wave guiding layer," *Journal of Applied Physics*, vol. 121, no. 5, p. 054 501, 2017.

[162] I. Nikolaou, H. Hallil, V. Conédéra, G. Deligeorgis, C. Dejous, and D. Rebière, "Inkjet-printed graphene oxide thin layers on Love wave devices for humidity and vapor detection," *IEEE Sensors Journal*, vol. 16, no. 21, pp. 7620–7627, Nov. 2016.

[163] D. Matatagui, J. Fontecha, M. Fernández, M. Aleixandre, I. Gràcia, C. Cané, and M. Horrillo, "Array of Love-wave sensors based on quartz/Novolac to detect CWA simulants," *Talanta*, vol. 85, no. 3, pp. 1442–1447, 2011.

[164] F. Herrmann, D. Hahn, and S. Büttgenbach, "Separate determination of liquid density and viscosity with sagittally corrugated Love-mode sensors," *Sensors and Actuators A: Physical*, vol. 78, no. 2, pp. 99–107, 1999.

[165] G. Kovacs, W. Ruile, M. Jakob, U. Rosler, E. Maier, U. Knauer, and H. Zoul, "A SAW duplexer with superior temperature characteristics for US-PCS," in *IEEE Ultrasonics Symposium, 2004*, vol. 2, Aug. 2004, 974–977 Vol.2.

[166] J. Luo, A. Quan, C. Fu, and H. Li, "Shear-horizontal surface acoustic wave characteristics of a (110) $ZnO/SiO_2/Si$ multilayer structure," *Journal of Alloys and Compounds*, vol. 693, no. Supplement C, pp. 558–564, 2017.

[167] M. Feldman, "Hilbert transform in vibration analysis," *Mechanical Systems and Signal Processing*, vol. 25, no. 3, pp. 735–802, 2011.

[168] J. Du and G. L. Harding, "A multilayer structure for Love-mode acoustic sensors," *Sensors and Actuators A: Physical*, vol. 65, no. 2, pp. 152–159, 1998.

[169] J. Liu, "A theoretical study on Love wave sensors in a structure with multiple viscoelastic layers on a piezoelectric substrate," *Smart Materials and Structures*, vol. 23, no. 7, p. 075 015, Jul. 2014.

[170] S. Li, Y. Wan, Y. Su, C. Fan, and V. R. Bhethanabotla, "Gold nanoparticle-based low limit of detection Love wave biosensor for carcinoembryonic antigens," *Biosensors and Bioelectronics*, vol. 95, no. Supplement C, pp. 48–54, 2017.

[171] M. Gianneli, K. Tsougeni, A. Grammoustianou, A. Tserepi, E. Gogolides, and E. Gizeli, "Nanostructured PMMA-coated Love wave device as a platform for protein adsorption studies," *Sensors and Actuators B: Chemical*, vol. 236, no. Supplement C, pp. 583–590, 2016.

[172] M. A. Cooper, *Label-free biosensors: techniques and applications*. Cambridge University Press, 2009.

[173] A. Pomorska, D. Shchukin, R. Hammond, M. A. Cooper, G. Grundmeier, and D. Johannsmann, "Positive frequency shifts observed upon adsorbing micron-sized solid objects to a quartz crystal microbalance from the liquid phase," *Analytical Chemistry*, vol. 82, no. 6, pp. 2237–2242, 2010.

[174] R. Niepelt, U. C. Schröder, J. Sommerfeld, I. Slowik, B. Rudolph, R. Möller, B. Seise, A. Csaki, W. Fritzsche, and C. Ronning, "Biofunctionalization of zinc oxide nanowires for DNA sensory applications.," *Nanoscale research letters*, vol. 6, p. 511, Jan. 2011.

[175] B. Du, A. M. König, and D. Johannsmann, "On the role of capillary instabilities in the sandcastle effect," *New Journal of Physics*, vol. 10, no. 5, p. 053 014, 2008.

[176] P. Wang, J. Su, L. Gong, M. Shen, M. Ruths, and H. Sun, "Numerical simulation and experimental study of resonance characteristics of QCM-P devices operating in liquid and their application in biological detection," *Sensors and Actuators B: Chemical*, vol. 220, no. Supplement C, pp. 1320–1327, 2015.

[177] N. Ramakrishnan, H. B. Nemade, and R. P. Palathinkal, "Mass Loading in Coupled Resonators Consisting of SU-8 Micropillars Fabricated Over SAW Devices," *IEEE Sensors Journal*, vol. 11, no. 2, pp. 430–431, Feb. 2011.

[178] N. Ramakrishnan, H. B. Nemade, and R. P. Palathinkal, "Resonant Frequency Characteristics of a SAW Device Attached to Resonating Micropillars," *Sensors*, vol. 12, no. 4, pp. 3789–3797, 2012.

[179] F. Herrmann, M. Weihnacht, and S. Buttgenbach, "Properties of sensors based on shear-horizontal surface acoustic waves in $LiTaO_3/SiO_2$ and quartz/SiO_2 structures," *IEEE Transactions on Ultrasonics, Ferroelectrics, and Frequency Control*, vol. 48, no. 1, pp. 268–273, Jan. 2001.

[180] H. Nakanishi, H. Nakamura, and R. Goto, "High electromechanical coupling coefficient SAW resonator on Ta_2O_5/Al/$LiNbO_3$ structure for wide duplex gap application," in *2009 IEEE International Ultrasonics Symposium*, Sep. 2009, pp. 2639–2642.

[181] J. A. Ogilvy, "The mass-loading sensitivity of acoustic Love wave biosensors in air," *Journal of Physics D: Applied Physics*, vol. 30, no. 17, p. 2497, 1997.

[182] Y. Hur, J. Han, J. Seon, Y. E. Pak, and Y. Roh, "Development of an SH-SAW sensor for the detection of DNA hybridization," *Sensors and Actuators A: Physical*, vol. 120, no. 2, pp. 462–467, May 2005.

[183] Y. Bergaoui, C. Zerrouki, J. Fougnion, N. Fourati, and A. Abdelghani, "Sensitivity estimation and biosensing potential of lithium tantalate shear horizontal surface acoustic wave sensor," *Sensor Letters*, vol. 7, no. 5, pp. 1001–1005, 2009.

[184] Y. Kwon and Y. Roh, "Development of SH-SAW sensors for underwater measurement," *Ultrasonics*, vol. 42, no. 1, pp. 409–411, 2004, Proceedings of Ultrasonics International 2003.

[185] M. J. Madou, *Manufacturing techniques for microfabrication and nanotechnology*. CRC press, 2011, vol. 2.

[186] P. Walker and W. H. Tarn, *CRC handbook of metal etchants*. CRC press, 1990.

[187] B.-H. Seo, S.-H. Lee, and J. H. Seo, "Study on the Wet Etch Behavior of a Zinc-Oxide Semiconductor in Acid Solutions," *Journal of the Korean Physical Society*, vol. 53, no. 1, pp. 402–405, Jul. 2008.

[188] D. M. Pozar, *Microwave engineering*. John Wiley & Sons, 2009.

[189] K.-S. Kim and H. W. Kim, "Synthesis of ZnO nanorod on bare Si substrate using metal organic chemical vapor deposition," *Physica B: Condensed Matter*, vol. 328, no. 3, pp. 368–371, 2003.

[190] Q. Wan, K. Yu, T. H. Wang, and C. L. Lin, "Low-field electron emission from tetrapod-like ZnO nanostructures synthesized by rapid evaporation," *Applied Physics Letters*, vol. 83, no. 11, pp. 2253–2255, 2003.

[191] J. Grabowska, K. K. Nanda, E. McGlynn, J. P. Mosnier, M. O. Henry, A. Beaucamp, and A. Meaney, "Synthesis and photoluminescence of ZnO nanowires/nanorods," *Journal of Materials Science: Materials in Electronics*, vol. 16, no. 7, pp. 397–401, Jul. 2005.

[192] T. Hirate, T. Kimpara, S. Nakamura, and T. Satoh, "Control of diameter of ZnO nanorods grown by chemical vapor deposition with laser ablation of ZnO," *Superlattices and Microstructures*, vol. 42, no. 1, pp. 409–414, 2007, E-MRS 2006 Symposium K: ZnO and Related Materials.

[193] D. Polsongkram, P. Chamninok, S. Pukird, L. Chow, O. Lupan, G. Chai, H. Khallaf, S. Park, and A. Schulte, "Effect of synthesis conditions on the growth of ZnO nanorods via hydrothermal method," *Physica B: Condensed Matter*, vol. 403, no. 19, pp. 3713–3717, 2008.

[194] H.-S. Choi, M. Vaseem, S. G. Kim, Y.-H. Im, and Y.-B. Hahn, "Growth of high aspect ratio ZnO nanorods by solution process: effect of polyethyleneimine," *Journal of Solid State Chemistry*, vol. 189, pp. 25–31, 2012.

[195] M. Gaso, Y. Jiménez, L. Francis, and A. Arnau, *Love wave biosensors: A review, state of the art in biosensors - General aspects*. InTech, 2013.

[196] M. Joshi, R. Pinto, V. R. Rao, and S. Mukherji, "Silanization and antibody immobilization on SU-8," *Applied surface science*, vol. 253, no. 6, pp. 3127–3132, 2007.

[197] P. S. Petrou, M. Chatzichristidi, A. M. Douvas, P. Argitis, K. Misiakos, and S. E. Kakabakos, "A biomolecule friendly photolithographic process for fabrication of protein microarrays on polymeric films coated on silicon chips," *Biosensors and Bioelectronics*, vol. 22, no. 9, pp. 1994–2002, 2007, Selected Papers from the Ninth World Congress On Biosensors. Toronto, Canada 10 - 12 May 2006.

[198] V. Goudar, S. Suran, and M. Varma, "Photoresist functionalisation method for high-density protein microarrays using photolithography," English, *Micro & Nano Letters*, vol. 7, 549–553(4), 6 Jun. 2012.

[199] MicroChem, "S1800 Data Sheet," *MICROPOSIT^{TM} S1800 Series Broadband Resists*, 2000.

[200] A. Peschel, A. Langhoff, and D. Johannsmann, "Coupled resonances allow studying the aging of adhesive contacts between a QCM surface and single, micrometer-sized particles," *Nanotechnology*, vol. 26, no. 48, p. 484 001, 2015.

[201] R. Dammel, *Diazonaphthoquinone-based resists*. SPIE press, 1993, vol. 11.

[202] N. Barie and M. Rapp, "Covalent bound sensing layers on surface acoustic wave (SAW) biosensors," *Biosensors and Bioelectronics*, vol. 16, no. 9, pp. 979–987, 2001.

[203] L. Cheng, H. l. Li, Y. Liang, S. t. He, and Z. y. Tong, "A Love wave biosensor using Aptamer sensitive layer," in *Proceedings of the 2010 Symposium on Piezoelectricity, Acoustic Waves and Device Applications*, Dec. 2010, pp. 532–535.

[204] C. T. Feng, C. J. Cheng, and M. Z. Atashbar, "PMMA/64°-YX-$LiNbO_3$ guided SH-SAW based immunosensing system," in *IEEE Sensors Proceedings*, Oct. 2011, pp. 308–311.

[205] F. Zhang, S. Li, K. Cao, P. Wang, Y. Su, X. Zhu, and Y. Wan, "A microfluidic love-wave biosensing device for PSA detection based on an aptamer beacon probe," *Sensors*, vol. 15, no. 6, pp. 13 839–13 850, 2015.

[206] Y.-T. Shen, C.-L. Huang, R. Chen, and L. Wu, "A novel SH-SAW sensor system," *Sensors and Actuators B: Chemical*, vol. 107, no. 1, pp. 283–290, 2005, Proceedings of the 7th European Conference on Optical Chemical Sensors and Biosensors.

[207] R. Smith and F. Welsh, "Temperature dependence of the elastic, piezoelectric, and dielectric constants of lithium tantalate and lithium niobate," *Journal of Applied Physics*, vol. 42, no. 6, pp. 2219–2230, 1971.

[208] C. Chen, Y. Shi, Y. Zhang, J. Zhu, and Y. Yan, "Size dependence of Young's modulus in ZnO nanowires," *Physical Review Letters*, vol. 96, no. 7, p. 075 505, Feb. 2006.

[209] S. Li, Y. Wan, C. Fan, and Y. Su, "Theoretical study of monolayer and double-layer waveguide love wave sensors for achieving high sensitivity," *Sensors*, vol. 17, no. 3, p. 653, 2017.

List of Publications

Journals

- S. Trivedi and H. Nemade, "Finite element simulation of Love wave resonator for DNA detection," *International Journal of Advances in Engineering Sciences and Applied Mathematics*, vol. 7, no. 4, pp. 210-218, Dec. 2015.
- S. Trivedi and H. Nemade, "Simulation of a Love wave device with ZnO nanorods for high mass sensitivity," *Ultrasonics*, vol. 84, pp. 150-161, Mar. 2018.
- S. Trivedi and H. Nemade, "Finite element simulation of a highly sensitive SH-SAW delay line sensor with SiO_2 micro-ridges," *Microsystem Technologies*, Feb. 2018.
- S. Trivedi and H. Nemade, "Coupled resonance in SH-SAW resonator with S1813 micro-ridges for high mass sensitivity biosensing applications," *Sensors and Actuators B: Chemical,* vol. 273, pp 288-297, June 2018.
- S. Trivedi and H. Nemade, "ZnO nanorod-based Love wave delay line for high mass sensitivity: A finite element analysis" (*Under review*).

Proceedings

- S. Trivedi and H. Nemade, "Finite Element Simulation of Love Wave based SAW Delay Line using COMSOL Multiphysics," *Excerpt from the Proceedings of the 2015 COMSOL Conference in Pune*, October 2015.
- S. Trivedi and H. Nemade, "Highly Sensitive SH-SAW Resonator with SiO_2 trenches for Biosensing Application," *Materials Today: Proceedings*, vol. 4, no. 9, pp. 10427-10431, 2017.

Conferences

- ZnO nanorod based Love Wave resonator for DNA detection, International Conference on MEMS and Sensors (ICMEMSS-2014), 18-20 December, IIT Madras **(Best Poster)**.
- Finite element simulation of Love wave based SAW delay line using COMSOL Multiphysics, COMSOL Conference, October 29-30, 2015, Pune.
- Finite element simulation of a sensitive SAW biosensor using ZnO Nanorods, 4th International Conference on Advanced Nanomaterials and Nanotechnology (ICANN-2015), December 8-11, 2015, IIT Guwahati.
- Finite element simulation of a highly sensitive SH-SAW delay line biosensor with SiO_2 ridges, International Conference on Recent trends in Engineering and Material Sciences (ICEMS-2016), March 17-19, 2016 Jaipur National University, Jaipur.
- SH-SAW resonator with S1813 micro-ridges as a sensitive biosensor, Research Conclave, Mar 8-11, 2018, IIT Guwahati, Guwahati **(Best Poster)**.